frontiers | Research Topics

Phase field method and integrated computing materials engineering

Edited by
Yu-Hong Zhao, Qingyan Xu, Jincheng Wang, Lei Chen and Qiang Du

Published in
Frontiers in Materials

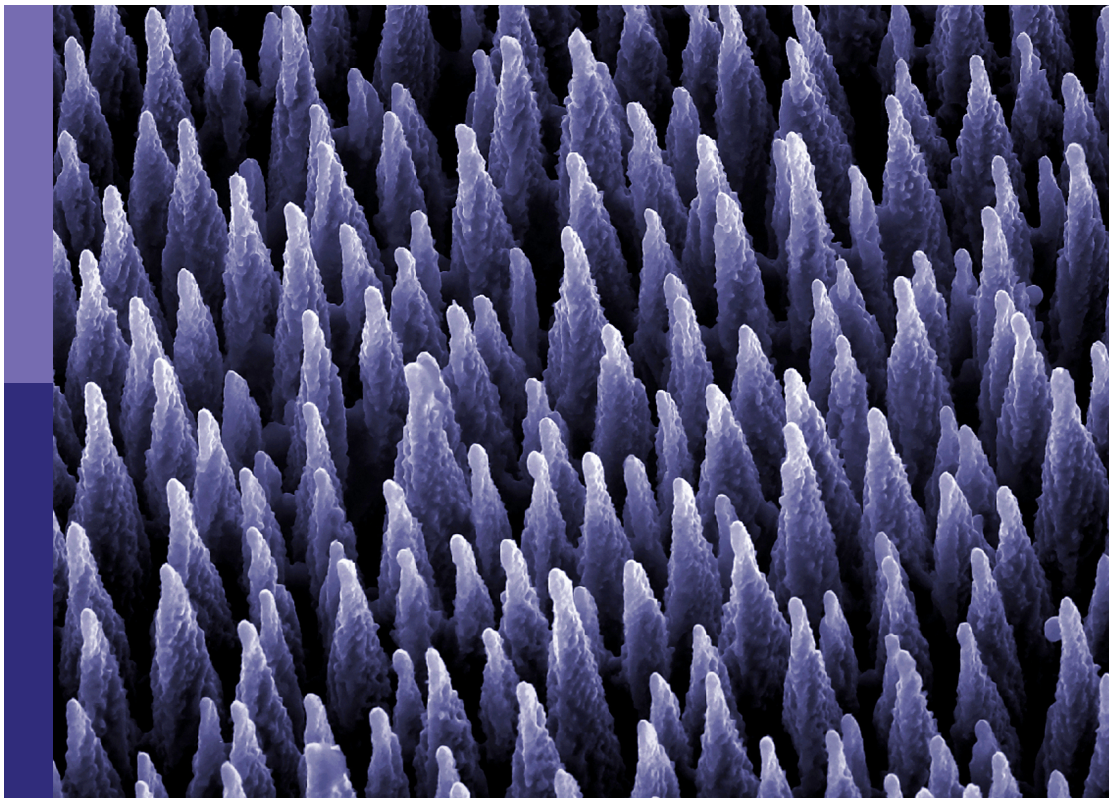

ISSN 1664-8714
ISBN 978-2-83251-737-6
DOI 10.3389/978-2-83251-737-6

About Frontiers

Frontiers is more than just an open access publisher of scholarly articles: it is a pioneering approach to the world of academia, radically improving the way scholarly research is managed. The grand vision of Frontiers is a world where all people have an equal opportunity to seek, share and generate knowledge. Frontiers provides immediate and permanent online open access to all its publications, but this alone is not enough to realize our grand goals.

Frontiers journal series

The Frontiers journal series is a multi-tier and interdisciplinary set of open-access, online journals, promising a paradigm shift from the current review, selection and dissemination processes in academic publishing. All Frontiers journals are driven by researchers for researchers; therefore, they constitute a service to the scholarly community. At the same time, the *Frontiers journal series* operates on a revolutionary invention, the tiered publishing system, initially addressing specific communities of scholars, and gradually climbing up to broader public understanding, thus serving the interests of the lay society, too.

Dedication to quality

Each Frontiers article is a landmark of the highest quality, thanks to genuinely collaborative interactions between authors and review editors, who include some of the world's best academicians. Research must be certified by peers before entering a stream of knowledge that may eventually reach the public - and shape society; therefore, Frontiers only applies the most rigorous and unbiased reviews. Frontiers revolutionizes research publishing by freely delivering the most outstanding research, evaluated with no bias from both the academic and social point of view. By applying the most advanced information technologies, Frontiers is catapulting scholarly publishing into a new generation.

What are Frontiers Research Topics?

Frontiers Research Topics are very popular trademarks of the *Frontiers journals series*: they are collections of at least ten articles, all centered on a particular subject. With their unique mix of varied contributions from Original Research to Review Articles, Frontiers Research Topics unify the most influential researchers, the latest key findings and historical advances in a hot research area.

Find out more on how to host your own Frontiers Research Topic or contribute to one as an author by contacting the Frontiers editorial office: frontiersin.org/about/contact

Phase field method and integrated computing materials engineering

Topic editors

Yu-Hong Zhao — North University of China, China
Qingyan Xu — Tsinghua University, China
Jincheng Wang — Northwestern Polytechnical University, China
Lei Chen — University of Michigan–Dearborn, United States
Qiang Du — SINTEF, Norway

Citation

Zhao, Y.-H., Xu, Q., Wang, J., Chen, L., Du, Q., eds. (2023). *Phase field method and integrated computing materials engineering*. Lausanne: Frontiers Media SA.
doi: 10.3389/978-2-83251-737-6

Table of contents

frontiers | Frontiers in Materials

TYPE Editorial
PUBLISHED 08 February 2023
DOI 10.3389/fmats.2023.1145833

OPEN ACCESS

EDITED AND REVIEWED BY
Roberto Brighenti,
University of Parma, Italy

*CORRESPONDENCE
Yu-Hong Zhao,
zhaoyuhong@nuc.edu.cn

SPECIALTY SECTION
This article was submitted to Computational Materials Science, a section of the journal Frontiers in Materials

RECEIVED 16 January 2023
ACCEPTED 30 January 2023
PUBLISHED 08 February 2023

CITATION
Zhao Y-H (2023), Editorial: Phase field method and integrated computing materials engineering.
Front. Mater. 10:1145833.
doi: 10.3389/fmats.2023.1145833

Editorial: Phase field method and integrated computing materials engineering

Yu-Hong Zhao[1,2]*

[1]Beijing Advanced Innovation Center for Materials Genome Engineering, University of Science and Technology Beijing, Beijing, China, [2]Collaborative Innovation Center of Ministry of Education and Shanxi Province, School of Materials Science and Engineering, North University of China, Taiyuan, China

KEYWORDS

integrated phase field methods, integrated computing materials engineering, materials processes, multi physical models, machine learning

Editorial on the Research Topic
Phase field method and integrated computing materials engineering

Nano- and meso-scale phase-field methods (PFM) have increasingly been used in a wide range of metallic materials, in addition to both inorganic and organic non-metallic materials. In the context of integrated computing materials and engineering (ICME), phase-field methods, together with other physical modeling or machine learning (ML) technologies, have become powerful tools for designing corresponding experiments and understanding material processes when dealing with the design and manufacturing of metals, alloys, or non-metallic materials. Solidification, precipitation, and deformation correspond to the casting, aging, forging, or additive manufacturing processes, etc., and controlling the microstructures in these processes is key for preparing high-performance materials or manufacturing components. The coupling of microscopic and mesoscale modeling during the design and manufacturing processes of materials or casting within the ICME framework is shown in Figure 1.

In this Research Topic of "PFM-ICME," the research work is unexpectedly included in this framework, showing the potential of PFM-ICME in the application of a variety of materials processes.

- H atom diffusion and void defects. Using the phase-field model, the grain structures and irradiated void defects of hydrogen (H) atoms in porous polycrystalline tungsten (W) are generated (Li et al., DOI: 10.3389/fmats.2022.935129). The effects of grain morphology and porosity on the effective diffusion coefficient of H in W alloy are investigated, providing a good way to understand the influence of complex microstructures on H diffusion and assisting in the design of W-based materials for the fusion reactor.
- Solid-state phase transformation (precipitation PFM). A macroscopic constituent redistribution phase-field model is developed by introducing the effect of irradiation on atom mobility and the effect of temperature on interface mobility (Wen et al.), and an expression of phase boundary width is proposed that applies to both microscopic and macroscopic scenarios. The interfacial parameters and Zr concentration distribution near the fuel surface in U-10wt% Zr metallic fuels are discussed. PFM combined with COSMAP software is used to investigate the precipitation of carbide $M_{23}C_6$ by surface quenching on GCr15 (Fe-Cr-C) alloy-bearing rings (Liu et al.).
- Additive manufacturing (solidification and precipitation PFM). A two-relaxation-time lattice Boltzmann model is proposed to simulate melt flows and free surface dynamics of Ti-6Al-4V alloy in an electron beam selective melting additive manufacturing process (Chen et al.). The model describes the dynamics of solid-liquid phase change and heat transfer and is employed

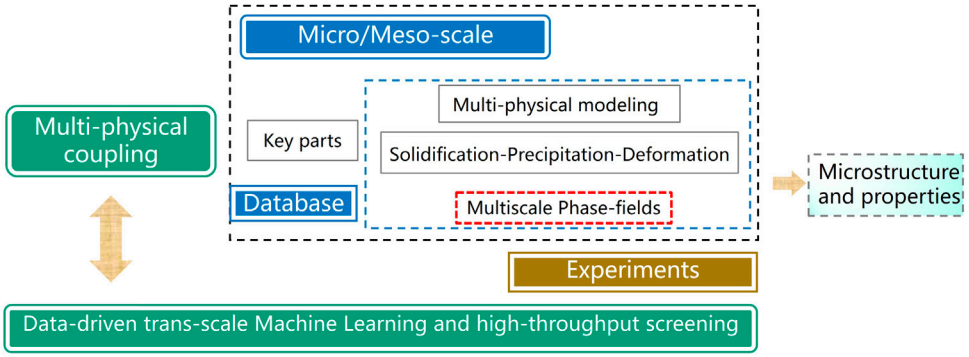

FIGURE 1
The design schematic of metallic materials processes in the PFM-ICME framework.

to simulate the influence of process parameters on single and multiple tracks of electron beam selective melting on a single layer of the powder bed. Another example (Chen et al.) is simulating the micro-structure evolution of Inconel 718 alloy homogenization during laser powder bed fusion (L-PBF).

- Precipitation of zirconium hydride blisters (corrosion PFM). The natural growth of hydride blisters and structural evolution after applying radial stress are investigated using a phase-field model coupled with anisotropic elastic, and the corrosion kinetics, stress distribution, and displacement changes are discussed (Wu et al.).
- Columnar to equiaxed transition (CET) (directional solidification PFM) (Zeng et al.) The transformation of columnar dendrites to equiaxed crystals during directional solidification of Al alloy in the convective environment of the actual roll casting process is investigated with the Kim-Kim-Suzuki (KKS) PFM, considering the microflow field and the roll casting experiment.
- Grain boundary dislocations in plastic deformation (phase field crystal, PFC). The dislocation arrangement and decomposition at grain-boundaries (GB) during constant-volume plastic deformation of the FCC bi-crystal system are studied by using the two-mode phase-field crystal (2PFC) method (Li et al.). The effects of different GB misorientations (GBMs) and tensile deformation directions are analyzed in terms of dislocation arrangement and decomposition. The atomic density profile changed periodically at equilibrium in three different symmetrical tilt GBs, but the initial GB dislocation arrangement remains almost the same when tensile deformation is applied in the x- or y-direction and is symmetrically arranged in a "bowknot" structure. Stress at GB is more concentrated with the increase in strain, and dislocation decomposition can reduce stress concentration.
- Coating growth (PFM in Materials Genome Engineering). Within the framework of Materials Genome Engineering (MGE), high-throughput 3D phase-field simulations for TiN coating growth during physical vapor deposition (PVD) combined with the multi-objective optimization strategy and the corresponding experiments are performed to screen the optimal coating properties (Dai et al.).

This Research Topic also includes a molecular dynamics simulation of the nano-crack closure mechanism and interface behaviors of polycrystalline austenitic steel (Chen et al.), demonstrating the modeling variety of ICME. Phase field methods, first principles, molecular dynamic simulations, machine learning technologies, macroscopic multi-physical field simulations, numerical algorithms, and corresponding experiments are often coupled together to solve many materials processes. As a result, the "Integrated phase-field methods (IPFM)", rather than a single PFM, will have greater application potential in the future design of high-performance metallic or non-metallic materials, and in the manufacturing of castings and other components. IPFM is becoming one of the most important and promising core parts within the scope of ICME.

Author contributions

The author confirms being the sole contributor of this work and has approved it for publication.

Acknowledgments

The author would like to thank Prof. Jian-Xin Xie of the University of Science and Technology Beijing and Prof. Long-Qing Chen of Pennsylvania State University for their help in the discussions of integrated phase-field methods (IPFM) and ICME. The author also thanks for the financial support of National Natural Science Foundation of China (No. 52074246), the National Defense Basic Scientific Research Program of China (No. JCKY2020408B002), and the Key Research and Development Program of Shanxi Province (202102050201011), which have given the author more time to work on IPFM and ICME.

Conflict of interest

The author declares that the research was conducted in the absence of any commercial or financial relationships that could be construed as a potential conflict of interest.

Publisher's note

frontiers | Frontiers in Materials

ORIGINAL RESEARCH
published: 29 April 2022
doi: 10.3389/fmats.2022.885481

A Two-Relaxation-Time Lattice Boltzmann Model for Electron Beam Selective Melting Additive Manufacturing

*Daoliang Chen[1], Wei Chen[2], Yanfei Liu[3] and Dongke Sun[1]**

[1]School of Mechanical Engineering, Southeast University, Nanjing, China, [2]Power Beam Processing Laboratory, AVIC Manufacturing Technology Institute, Beijing, China, [3]R and D Department, China Academy of Launch Vehicle Technology, Beijing, China

Electron beam selective melting is a rapidly developing additive manufacturing technology for industry and engineering. A two-relaxation-time lattice Boltzmann model is proposed to simulate melt flows and free surface dynamics in an EBSM additive manufacturing process. The model also describes the dynamics of solid-liquid phase change and heat transfer, and it is validated by several simulations of classical benchmarks. The model was applied to further simulate single and multiple tracks of electron beam selective melting on a single layer of powder bed and to analyze the influence of process parameters. The results demonstrate significant potentials of the present model for the study of additive manufacturing processes.

Keywords: lattice Boltzmann method, phase change, heat transfer, melt flows, electron beam selective melting

OPEN ACCESS

Edited by:
Yu-Hong Zhao,
North University of China, China

Reviewed by:
Lijun Zhang,
Central South University, China
Houbing Huang,
Beijing Institute of Technology, China

****Correspondence:***
Dongke Sun
dksun@seu.edu.cn

Specialty section:
This article was submitted to Computational Materials Science, a section of the journal Frontiers in Materials

Received: *28 February 2022*
Accepted: *08 March 2022*
Published: *29 April 2022*

Citation:
Chen D, Chen W, Liu Y and Sun D (2022) A Two-Relaxation-Time Lattice Boltzmann Model for Electron Beam Selective Melting Additive Manufacturing. Front. Mater. 9:885481. doi: 10.3389/fmats.2022.885481

1 INTRODUCTION

The electron beam selective melting (EBSM) additive manufacturing with higher energy density electron beam as the heat source can improve the quality and efficiency of metal parts additive manufacturing and reduce the molding cost. The metal powders are melted and solidified layer by layer to form the desired metal components by selective heating. EBSM has attached great attention in recent years as it is widely used in aerospace (Blakey-Milner et al., 2021), biomedical (Tamayo et al., 2021) and other crucial fields (Vafadar et al., 2021) to fabricate complex structural products. However, EBSM is a non-equilibrium physical process accompanied by various complex phenomena such as melt convection, heat transfer, solute transport, and phase change. In-depth investigation of melt's complex behavior during the melt pool evolution process is significant in improving the process manufacturing level and enhancing the product quality. As the rapid evolution of the melt pool during EBSM is difficult to observe, the general experimental approach can only obtain information on its formation through continuous trial and error, making it difficult to reveal its complex formation mechanism. Numerical simulation has become an essential part of scientific research about additive manufacturing, effectively reducing the time as well as the economic cost of traditional experimental means (Hashemi et al., 2021).

At present, the numerical studies on EBSM have attracted great attention. Cheng et al. (2014) developed a three-dimensional (3D) thermal model based on the finite element method (FEM) to predict the temperature distribution of the EBSM process and stated that the powder porosity is critical to the thermal characteristics of the melt, with the size of the melt pool increasing as the powder porosity increases. Riedlbauer et al. (2017) researched the experimental measurement

and macroscopic thermal simulation of melt pool in EBSM of Ti-6Al-4V based on FEM, obtained that a good agreement was between experimental and simulation results, and the existence time of the melt pool was proportional to the line energy. In contrast, the dimensions and line energy showed a nonlinear relationship. Jamshidinia et al. (2013) applied numerical simulation to compare the difference between the pure thermal model and the convective heat transfer model and concluded that the convection heat transfer model has a larger weld pool width and a longer length, but the penetration distance is shallower. Further, there are an increasing number of further studies on the evolution of the melt pool at the powder scale. A powder-scale model based on the finite volume method (FVM) was designed to effectively simulate the formation of defects such as the balling effect and analyze the surface morphology formation mechanism in EBSM (Yan et al., 2017). Wu et al. (2021) intensively developed an FVM-based 3D multiple-layer mesoscale model to investigate the side roughness of Ti-6Al-4V parts fabricated by EBSM and revealed the leading cause of track shape fluctuation. Zhao et al. (2020, 2021) investigated the effect of the thermal properties of the powder bed (i.e., emissivity, thermal conductivity) and the environmental conditions on the energy absorption and heat transfer of the EBSM process based on CtFD simulations. The results indicated the necessity to improve the process parameters according to the fineness of the powder to ensure the molded quality.

Combined with the above research status, it is known that the numerical simulation methods to predict and control the flow field of the molten pool have a high guiding significance for the actual EBSM process. However, most of the methods have certain limitations on the calculation of complex interfaces with relatively low computational efficiency. The lattice Boltzmann method (LBM) has been widely used in simulating heat transfer, and fluid flows for its simplicity in the algorithm, ease of implementation, and effectiveness in solving partial differential equations. Körner developed a two-dimensional model for EBSM, firstly employing LBM and successfully modeled surface tension and wetting phenomena (Körner et al., 2013; Ammer et al., 2014). Zheng et al. (2019) proposed a height function-LBM coupling model to study the melt pool dynamics of selective laser melting. Zakirov et al. (2020) implemented a high-performance tool called FaSTLaB for simulation of the powder bed fusion additive manufacturing process, which fits the framework of the single-relaxation-time scheme LBM. However, the single-relaxation-time scheme is less stable in some specific conditions. The LBM with multiple-relaxation-time lattice Boltzmann equations suffers from algorithmic complexity and computational consumption.

The present work aims at developing a three-dimensional (3D) two-relaxation-time (TRT) LBM-based mass and heat transfer model to study the melt pool evolution process during EBSM. The fluid dynamics and heat transfer in the model are validated by simulating thermal convection and phase change processes in a square cavity as well as the simulation of bead-on-plate. The powder bed fusion EBSM process under different process parameters is investigated. The analysis of the melt pool flow pattern provides an understanding of melt pool formation.

2 MATHEMATICAL MODEL

2.1 Modeling of Melt Flows During Phase Change

Melt flows during phase change in EBSM is described by the two-relaxation-time lattice Boltzmann equation (Ginzburg et al., 2008) as

$$f_i\left(\boldsymbol{x}+\boldsymbol{c}_i\delta t, t+\delta t\right)-f_i(\boldsymbol{x},t)=-\frac{1}{\tau_f^+}\left[f_i^+(\boldsymbol{x},t)-f_i^{\mathrm{eq}+}(\boldsymbol{x},t)\right] -\frac{1}{\tau_f^-}\left[f_i^-(\boldsymbol{x},t)-f_i^{\mathrm{eq}-}(\boldsymbol{x},t)\right]+F_i^*\delta t \quad (1)$$

with

$$f_i^+=\frac{f_i+f_{\bar{i}}}{2},\ f_i^-=\frac{f_i-f_{\bar{i}}}{2},\ f_i^{\mathrm{eq}+}=\frac{f_i^{\mathrm{eq}}+f_{\bar{i}}^{\mathrm{eq}}}{2},\ f_i^{\mathrm{eq}-}=\frac{f_i^{\mathrm{eq}}-f_{\bar{i}}^{\mathrm{eq}}}{2}, \quad (2)$$

where $f_i(\boldsymbol{x},t)$ is the density distribution function at $(\boldsymbol{x},t)$, $f_i^{\mathrm{eq}}(\boldsymbol{x},t)$ is the equilibrium density distribution function, τ_f^+ and τ_f^- indicate the symmetric dimensionless relaxation time and the anti-symmetric relaxation time, and F_i^* is the force term. Here, $\boldsymbol{c}_i$ is the discrete velocity in direction i, $\bar{i}$ represents the opposite direction of i, and δt is the time interval. The f_i^+ and f_i^- are referred to the symmetric and antisymmetric density distribution functions.

The $f_i^{\mathrm{eq}}(\boldsymbol{x},t)$ is given as

$$f_i^{\mathrm{eq}}=\omega_i\rho\left[1+\frac{\boldsymbol{c}_i\cdot\boldsymbol{u}}{c_s^2}+\frac{(\boldsymbol{c}_i\cdot\boldsymbol{u})^2}{2c_s^4}-\frac{|\boldsymbol{u}|^2}{2c_s^2}\right] \quad (3)$$

where ω_i is the weight coefficient, ρ is the density, $\boldsymbol{u}$ represents fluid velocity and c_s is the sound speed in relation to the lattice velocity, $c=\delta x/\delta t$ and $c=\sqrt{3}c_s$.

The F_i^* is introduced by the body force F_i described by Guo (Guo et al., 2002; Mao et al., 2022):

$$F_i^*=\left(1-\frac{1}{2\tau_f^+}\right)\frac{F_i+F_{\bar{i}}}{2}+\left(1-\frac{1}{2\tau_f^-}\right)\frac{F_i-F_{\bar{i}}}{2} \quad \text{and}$$
$$F_i=\omega_i\left(\frac{\boldsymbol{c}_i-\boldsymbol{u}}{c_s^2}+\frac{\boldsymbol{c}_i\cdot\boldsymbol{u}}{c_s^4}\boldsymbol{c}_i\right)\cdot\boldsymbol{F}, \quad (4)$$

where $\boldsymbol{F}$ is the force exerted on the melts. In EBSM, $\boldsymbol{F}$ includes the thermal buoyancy, the surface tension, the Marangoni force and the recoil pressure. Based on the boussinseuq approximation, the thermal buoyancy $\boldsymbol{F}_b$ is

$$\boldsymbol{F}_b=\rho\boldsymbol{g}\beta_T(T-T_m), \quad (5)$$

where $\boldsymbol{g}$ is the gravitational acceleration, β_T is the thermal expansion coefficient, T is the temperature and T_m is the melting temperature. The surface tension can be described as

$$\boldsymbol{F}_s=\sigma\kappa\boldsymbol{n}|\nabla\phi_l|\frac{2\rho}{\rho_l+\rho_g}, \quad (6)$$

where σ is the surface tension coefficient, κ is the local curvature, $\boldsymbol{n}$ is the unit normal vector dueto the forces acting on the

surface of the liquid, ϕ_l is the liquid phase fraction at the gas-liquid interface, ρ_l and ρ_g are the densities of liquid and gas phase (Brackbill et al., 1992). The Marangoni effect occurs because of the gradient of surface tension caused by non-uniform temperature distributions, and the Marangoni force can be calculated by

$$\boldsymbol{F}_M = \beta_M \left[\nabla T - (\boldsymbol{n}\cdot\nabla T)\,\boldsymbol{n}\right] |\nabla\phi_l| \frac{2\rho}{\rho_l+\rho_g}, \tag{7}$$

where β_M is the temperature coefficient of surface tension. The recoil pressure is an important driving force that acts on the surface of the melt, which is generated by vapor flux and defined as (Zhao et al., 2020)

$$\boldsymbol{F}_r = 0.54 P_0 \exp\left[\frac{L_v M\left(T-T_v\right)}{RTT_v}\right] \boldsymbol{n}|\nabla\phi_l| \frac{2\rho}{\rho_l+\rho_g}, \tag{8}$$

where P_0 is the ambient pressure, L_v is the enthalpy of metal vapor, M represents the molar mass, T_v is the vapor temperature of the metal and R is the universal gas constant.

The D3Q19 model is selected to model the present 3D-EBSM process in the present work. Therefore, the weight coefficient is given as

$$\omega_i = \begin{cases} 1/3 & i=0 \\ 1/18 & i=1,\ldots,6 \\ 1/36 & i=7,\ldots,18 \end{cases}, \tag{9}$$

and the discrete velocity in direction i is

$$[\boldsymbol{c}] = \begin{bmatrix} 0 & c & -c & 0 & 0 & 0 & 0 & c & -c & c & -c & c & -c & c & -c & 0 & 0 & 0 & 0 \\ 0 & 0 & 0 & c & -c & 0 & 0 & c & -c & -c & c & 0 & 0 & 0 & 0 & c & -c & c & -c \\ 0 & 0 & 0 & 0 & 0 & c & -c & 0 & 0 & 0 & 0 & c & -c & -c & c & c & -c & -c & c \end{bmatrix}. \tag{10}$$

In **Eq. 1**, the two dimensionless relaxation times τ_f^+ and τ_f^- can be calculated by using the magic number Λ_f, which is defined as

$$\Lambda_f = \left(\tau_f^+ - \frac{1}{2}\right)\left(\tau_f^- - \frac{1}{2}\right). \tag{11}$$

Here, the symmetric dimensionless relaxation time are described as

$$\tau_f^+ = \tau_f = \frac{\nu}{c_s^2\delta t} + \frac{1}{2}, \tag{12}$$

where ν is the kinetic viscosity. The macroscopic density ρ and velocity $\boldsymbol{u}$ are calculated as

$$\rho = \sum_{i=0}^{18} f_i, \quad \rho\boldsymbol{u} = \sum_{i=0}^{18} \boldsymbol{c}_i f_i + \frac{\delta t}{2}\rho\boldsymbol{F}. \tag{13}$$

The immersed moving boundary scheme (Noble and Torczynski, 1998) is introduced to account for the effects of partially solidified areas. The evolution of the density distribution function f_i includes the solid collision operator Ω_i^s and the fluid collision operator Ω_i^l, given by

$$f_i\left(\boldsymbol{x}+\boldsymbol{c}_i\delta t, t+\delta t\right) - f_i(\boldsymbol{x},t) = (1-\beta)\,\Omega_i^l + \beta\Omega_i^s \tag{14}$$

with

$$\Omega_i^l = -\frac{1}{\tau_f}\left[f_i(\boldsymbol{x},t) - f_i^{\mathrm{eq}}(\boldsymbol{x},t)\right] \quad \text{and}$$
$$\Omega_i^s = -\left(f_i(\boldsymbol{x},t) - f_i^{\mathrm{eq}}(\rho,\boldsymbol{u}_s)\right) + \left(f_{\bar{i}}(\boldsymbol{x},t) - f_{\bar{i}}^{\mathrm{eq}}(\rho,\boldsymbol{u})\right), \tag{15}$$

where β is weight function. It is described as

$$\beta = \frac{\left(1-\phi_l\right)\left(\tau_f - 0.5\right)}{\phi_l + \left(\tau_f - 0.5\right)}, \tag{16}$$

where ϕ_l is the liquid phase fraction at the liquid-solid interface. $\boldsymbol{u}_s$ is the solid velocity, $\boldsymbol{u}_s = \boldsymbol{0}$ in the subsequent simulations.

2.2 Modeling of the Liquid-Solid Phase Change

The evolution of enthalpy in the phase change system is governed by

$$h_i\left(\boldsymbol{x}+\boldsymbol{c}_i\delta t, t+\Delta t\right) = h_i(\boldsymbol{x},t) - \frac{1}{\tau_h}\left[h_i(\boldsymbol{x},t) - h_i^{\mathrm{eq}}(\boldsymbol{x},t)\right] + \omega_i\dot{Q}\delta t, \tag{17}$$

where h_i is distribution function for enthalpy of the phase change system, τ_h is the dimensionless relaxation time and $h_i^{\mathrm{eq}}(\boldsymbol{x},t)$ is the equilibrium enthalpy distribution function. The h_i^{eq} is given as

$$h_i^{\mathrm{eq}} = \omega_i c_p T\left[1 + \frac{\boldsymbol{c}_i\cdot\boldsymbol{u}}{c_s^2} + \frac{\left(\boldsymbol{c}_i\cdot\boldsymbol{u}\right)^2}{2c_s^4} - \frac{|\boldsymbol{u}|^2}{2c_s^2}\right] + \left(H - c_p T\right)\delta_{i0}, \tag{18}$$

where δ_{ij} is the Kronecker function. The source term $\dot{Q}$ includes the electron beam heat source, the evaporation heat loss and the radiation heat loss. The electron beam heat flux is generally independent of material state, whose generic form is typically

$$\dot{Q}_S = \eta P_B I_{xy} I_z, \tag{19}$$

where η is the energy absorption rate, P_B is the electron beam's power, which is depends on the process parameters, the accelerating voltage, U_B and the beam current, I_B. I_{xy} is the Gaussian distribution of energy in planes, where the maximum power intensity is at the centre with the power intensity decreasing as the width increase, as follow

$$I_{xy} = \frac{1}{2\pi\sigma_b^2}\exp\left\{-\frac{\left[(x-x_0)^2 + (y-y_0)^2\right]}{2\sigma_b^2}\right\}, \tag{20}$$

where σ_b is the standard deviation of beam width, (x_0, y_0) locates the center of the electron beam, which constantly changes as the heat source moves. I_z is the energy's vertical distribution, whose commonly used form is given as (Zäh and Lutzmann, 2010)

$$I_z = \frac{1}{z_s}\left(1 - \frac{z}{z_s}\right)\left(1 + \frac{3z}{z_s}\right), \tag{21}$$

where z_s is the penetration distance, for which a fairly common relationship is as follows (Knapp et al., 2019)

$$z_s = 2.1\times10^{-11}\frac{U_B^2}{\rho} \quad \text{for} \quad 10\text{kV} < U_B < 100\text{kV}. \tag{22}$$

The most electrons beam penetrate into the material and are absorbed, so reflections are not considered in the model.

The main sources of heat loss in the EBSM process are the thermal loss radiated to the atmosphere and the heat removed from the melt pool due to high temperature evaporation. The total heat flux due to radiation can be expressed as

$$\dot{q}_r = -\sigma_b \varepsilon \left(T^4 - T_{\text{ref}}^4\right), \tag{23}$$

where σ_b is the Stefan-Boltzmann constant, ε is the emissivity and T_{ref} is the ambient temperature. The model ignores the mass loss due to evaporation phenomena and only considers the heat loss which is sufficiently significant. The heat flux due to evaporation can be expressed as

$$\dot{q}_v = -\frac{0.82 L_v M}{\sqrt{2\pi MRT}} P_0 \exp\left[\frac{L_v M\left(T - T_v\right)}{RTT_v}\right]. \tag{24}$$

After the powder spreading process, there is a pre-treatment process to avoid powder smoke effect (Leung et al., 2019), where the metal powder is sintered at a high pre-heating temperature. Therefore the powder particles are considered fixed in the EBSM process.

In the D3Q19 model, the relationship between τ_h and the thermal diffusivity α is described as

$$\tau_h = \frac{\alpha}{c_s^2 \delta t} + \frac{1}{2}. \tag{25}$$

The temperature T can be determined by

$$T = \begin{cases} \dfrac{H}{c_p} & H \le H_s \\ T_s + \dfrac{H - H_s}{H_l - H_s}\left(T_l - T_s\right) & H_s < H < H_s, \\ T_l + \dfrac{H - H_l}{c_p} & H \ge H_l \end{cases} \quad \text{and} \quad H = \sum_{i=0}^{18} h_i. \tag{26}$$

where H_l and H_s are the total enthalpy corresponding to the solidus temperatures T_s and liquidus temperatures T_l, respectively. The liquid phase fraction ϕ_l can be updated according to $H = c_p T + \phi_l L_m$, where L_m represents the latent heat.

2.3 Tracking Evolution of Liquid/Gas Interface

The evolution of the liquid/gas (L/G) interface is described by using a mass-exchange method with the mediation of f_i and ϕ_l across L/G interface. The movement of the L/G interface is implemented by relabelling of cell types including gas cells, L/G interface cells and liquid cells based on the mass exchange. The liquid mass in a cell is related to the liquid phase fraction and the local density, defined as

$$m(\boldsymbol{x}, t) = \rho(\boldsymbol{x}, t)\, \phi_l(\boldsymbol{x}, t). \tag{27}$$

The cell's mass is updated according to

$$m(\boldsymbol{x}, t + \delta t) = m(\boldsymbol{x}, t) + \sum_{i=0}^{18} \Delta m_i \tag{28}$$

with the direction-dependent exchange mass

$$\Delta m_i = \begin{cases} f_{\bar{i}}(\boldsymbol{x} + \boldsymbol{c}_i \delta t) - f_i(\boldsymbol{x}) & (\boldsymbol{x} + \boldsymbol{c}_i \delta t) \in \text{L} \\ \dfrac{\phi_l(\boldsymbol{x} + \boldsymbol{c}_i \delta t) + \phi_l(\boldsymbol{x})}{2}\left[f_{\bar{i}}(\boldsymbol{x} + \boldsymbol{c}_i \delta t) - f_i(\boldsymbol{x})\right] & (\boldsymbol{x} + \boldsymbol{c}_i \delta t) \in \text{L/G} \cdot \\ 0.0 & (\boldsymbol{x} + \boldsymbol{c}_i \delta t) \in G \end{cases} \tag{29}$$

The L/G interface cell converts to the liquid cell when $m(\boldsymbol{x}, t) \ge \rho(\boldsymbol{x}, t)$ and the gas cell when $m(\boldsymbol{x}, t) \le 0$. The accuracy of the simplified advection scheme based on the mass exchange principle has been validated in the literature (Bogner et al., 2016). This model does not take into account the gas dynamics, so the distribution functions streamed from the gas phase is unknown. The particle distribution functions are reconstructed as (Körner et al., 2005)

$$f_{\bar{i}}(\boldsymbol{x}, t + \delta t) = f_{\bar{i}}^{\text{eq}}(\rho_0, \boldsymbol{u}_0) + f_i^{\text{eq}}(\rho_0, \boldsymbol{u}_0) - f_i(\boldsymbol{x}, t), \tag{30}$$

where ρ_0 is the reference density in the simulation and $\boldsymbol{u}_0$ represents the fluid velocity at the L/G interface. And the curvature estimation in the interface is performed using the height function method, which can guarantee second-order accuracy in curvature calculations (Ferdowsi and Bussmann, 2008; Afkhami and Bussmann, 2009).

3 RESULTS AND DISCUSSION

3.1 Validation

3.1.1 Convective Phase Change Problem

Numerical simulations are carried out to test the present model. Firstly, a square-cavity convective phase change problem is selected to make the validation. In this simulation, a two-dimensional cavity of length L is filled with homogeneous solid substance at the melting temperature T_0. The left wall is set at a constant temperature, T_h, above the melting temperature, and the right wall is set at T_0. Other walls are adiabatic. Two cases with different Rayleigh numbers Ra of 2.5×10^4 and 2.5×10^5 are simulated. The Stefan number defined as $St = c_p(T_h - T_0)/L$ is set to be 0.01 and the Prandtl number defined as $\text{Pr} = \nu/\alpha$, equals to 0.02 in the simulation. The average Nusselt number along the left wall, defined as $Nu = \int_0^L q_l dy/[\lambda(T_h - T_0)]$, and the liquid phase fraction of the square cavity, ϕ_l^{cavity}, are selected to characterize the problem quantitatively. **Figure 1A**; **Figure 1B** shows the Nusselt number and liquid phase fraction at different times for $Ra = 2.5 \times 10^4$ and $Ra = 2.5 \times 10^5$ respectively. Here, the Fourier number is introduced, which is defined as $Fo = \alpha t/L^2$. When $Ra = 2.5 \times 10^4$, Nu keeps oscillating at high frequencies as time progresses. The position of the solid-liquid interface at different moments is inscribed for the two cases, as shown in the **Figure 1C**; **Figure 1D** respectively. The results of the present simulations are both in high agreement with Mencinger's results inscribed by the dots (Mencinger, 2004).

3.1.2 Surface Tension and Wetting Effect

Surface tension and wetting have a significant effect on the melt pool formation. The shape of the droplets on the plate is simulated to compare with their theoretical shape to validate the surface tension and wetting effects in the model.

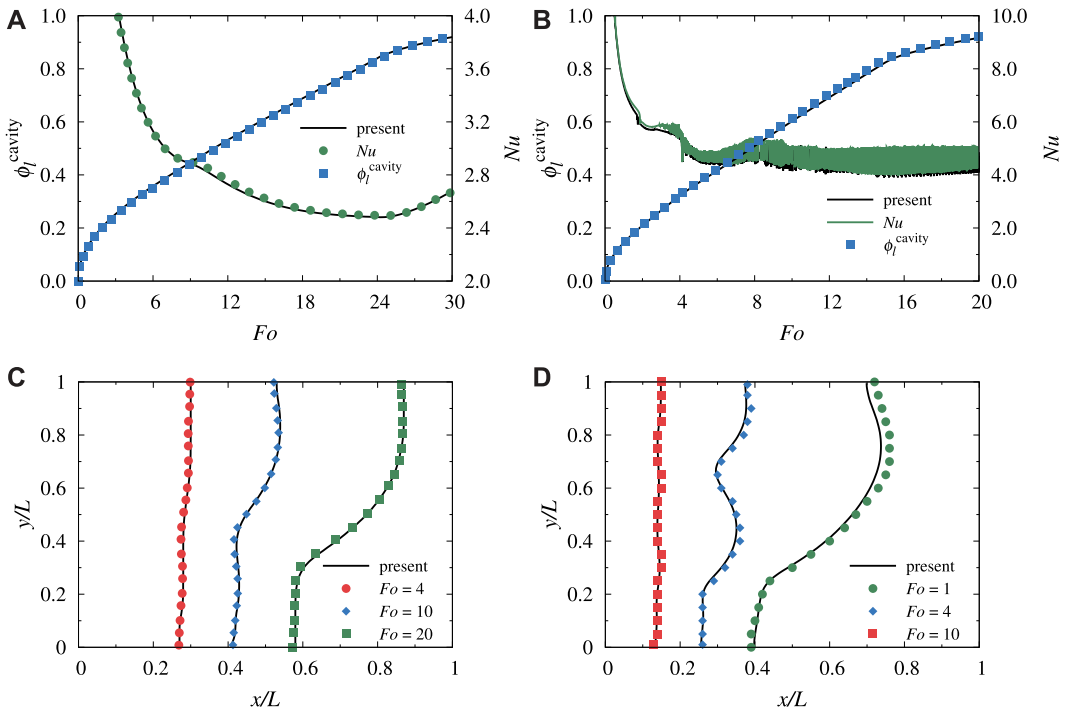

FIGURE 1 | The comparison of results for the average Nusselt number along the left wall *Nu* and the liquid phase fraction of the cavity ϕ_l^{cavity} versus the Fourier number *Fo* **(A)**: Ra = 2.5 × 10^4, **(B)**: Ra = 2.5 × 10^5), the position of the solid/liquid interface **(C)**: Ra = 2.5 × 10^4, **(D)**: Ra = 2.5 × 10^5).

In **Figure 2**, a semicircular droplet is placed on a flat wall with the initial contact angle of 90° and radius of *R*, which would be the equilibrium solution for neutral wetting conditions. For different wettability, assuming that the radius of the droplet at equilibrium is *r*, the volume of the droplet at equilibrium is

$$V^{eq} = \frac{2\pi r^3}{3}\left(2 - \cos\theta + \cos^2\theta\right). \tag{31}$$

With constant density, the relationship between the maximum height h_m and the initial radius R is obtained from the conservation of mass as

$$\frac{h_m}{R} = (1 - \cos\theta)\sqrt[3]{\frac{2}{2 - 3\cos\theta + \cos^3\theta}}. \tag{32}$$

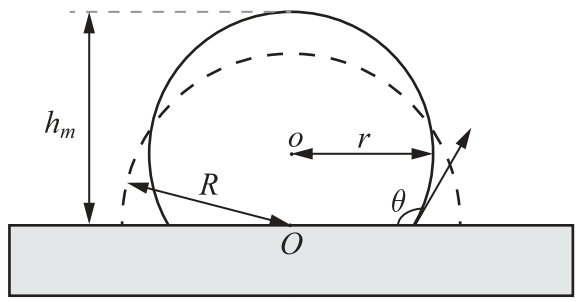

FIGURE 2 | Contact angle between the droplet and the plate.

Figure 3 gives the ratio of h_m and R at different wettability, which is in good agreement with the theoretical result. Curvature calculation based on the height function method is valid, and the present model can now effectively portray the phenomenon of melt wetting under surface tension.

3.1.3 Simulation of the Bead-on-Plate

The absorption of electron beam energy and melt-pool formation are the key factors for EBSM. The simulation of the

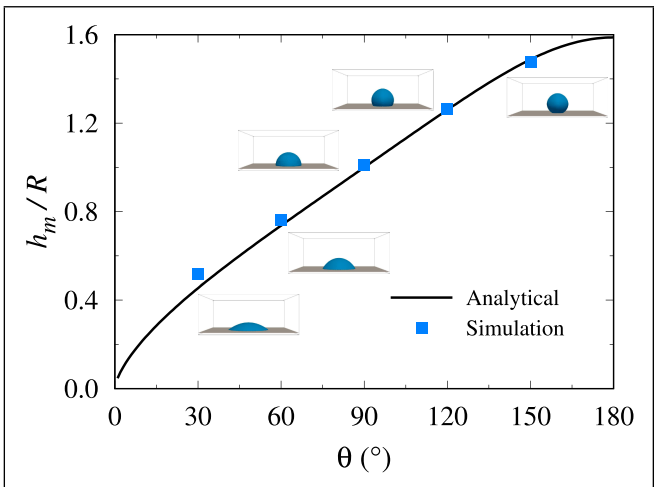

FIGURE 3 | Equilibrium profile and the ratio of h_m and *R* for five different contact angles.

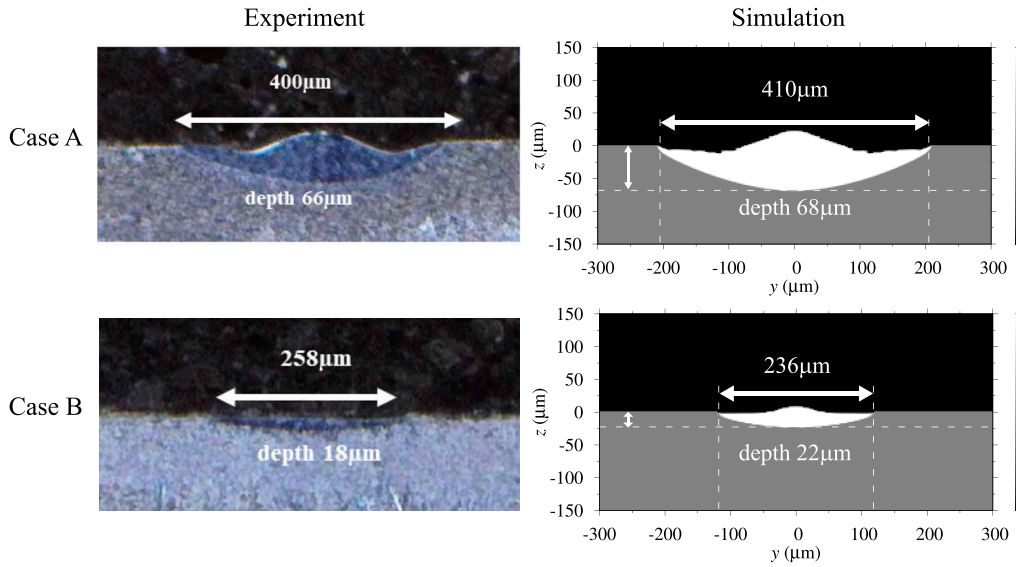

FIGURE 4 | The track cross-sections of the bead-on-plate for case A and case B.

bead-on-plate for the Ti-6Al-4V alloy was carried out to observe the evolution of the liquid phase. In this simulation, the accelerating voltage of 60 kV, the current of 5 mA, the beam spot size of 500 μ m, and the initial preheat temperature of 296 K are set. The scanning speed is 1,000 mm/s and 3,000 mm/s for cases A and B, as shown in **Figure 4**. The physical parameters used in the simulations (Lin et al., 2020; Wu et al., 2021) are given in **Table 1**. For the Ti-6Al-4V alloy, z_s is approximately 18.9 μm at $U_B = 60$ kV. Comparison of the melt-pool shapes in **Figure 4** demonstrates favorable agreement between the simulations and the experiments (Zakirov et al., 2020) in both the width and depth. It shows that the present model can well characterize the melt pool's interface evolution during EBSM.

3.2 Single Track on Powder-Bed

The powder bed with alloy powders of Ti-6Al-4V ranging from 45 to 105 μm is introduced in the simulation of the powder bed fusion EBSM. The layer thickness is about 100 μm. In this simulation, the initial preheat temperature is set to be 973 K. The beam spot size is 400 μm, the scanning speed is set to 0.5 m/s, and the accelerating voltage maintains at 60 kV.

TABLE 1 | Thermophysical properties of Ti-6Al-4V used in the simulation.

Parameters	Value	Parameters	Value
ρ	4,000 kg/m^3	μ	0.005 Pa·s
σ	1.68 N/m	β_M	2.6 × 10^{-4} N/(m·K)
M	0.446 kg/mol	R	8.314 J/(K·mol)
c_p	700 J/(K kg)	β	8.0 × 10^{-6} 1/K
P_0	1.013 × 10^5 Pa	T_v	3,315 K
T_l	1928 K	T_s	1,878 K
L_v	9.64 × 10^6 J/kg	L_m	2.86 × 10^5 J/kg
λ_l	30 W/(m·K)	λ_s	21 W/(m·K)
σ_b	2.56 × 10^{-8} W/(m^2·K^4)	ε	0.2

Figure 5 demonstrates the evolution process of the melt pool and its accompanying temperature field during single track melting with the electron beam current of 4 mA. The alloy powders are heated locally by the electron beam heat source, and their temperature continuously increases. When above their solidus line temperature, the powder particles melt to form a nearly circular melt pool, as shown in **Figure 5A**; **Figure 5B**. At this stage, the melt in the pool is mainly subject to thermal buoyancy, gravity, and surface tension. According to **Eq. 6**, the magnitude of the surface tension depends on the surface tension coefficient and the local curvature. Considering that the size of the melt pool was tiny, for alloy powders of Ti-6Al-4V with diameters in the range 45–105 μm, the complete melting was subject to the surface tension of approximately 8×10^{10}N/m^3, which is much greater than the other forces acting. Therefore, the surface tension is the primary motivation for the continuous convergence of the molten powder to form the melt pool. **Figure 5C** displays the changing morphology of the melt pool as the electron beam heat source traveled, elongating in the direction of the electron beam heat source. At the same time, the temperature distribution on the surface of the melt pool displays a more significant temperature gradient at the leading edge of the melt pool than at the tail end of the melt pool. During the rapid movement of the heat source, the tail end of the melt pool is out of the area heated by the electron beam. As the heat continuously transfers, the melt gradually cools and eventually solidifies. The continuous action of the electron beam heat source causes the temperature in the spot to rise by degrees, reaching the boiling point of the material at the current pressure, which leads to evaporation. The evaporation took away a large amount of heat and kept the maximum temperature in the melt pool at a relatively constant level. In addition, it provokes a recoil

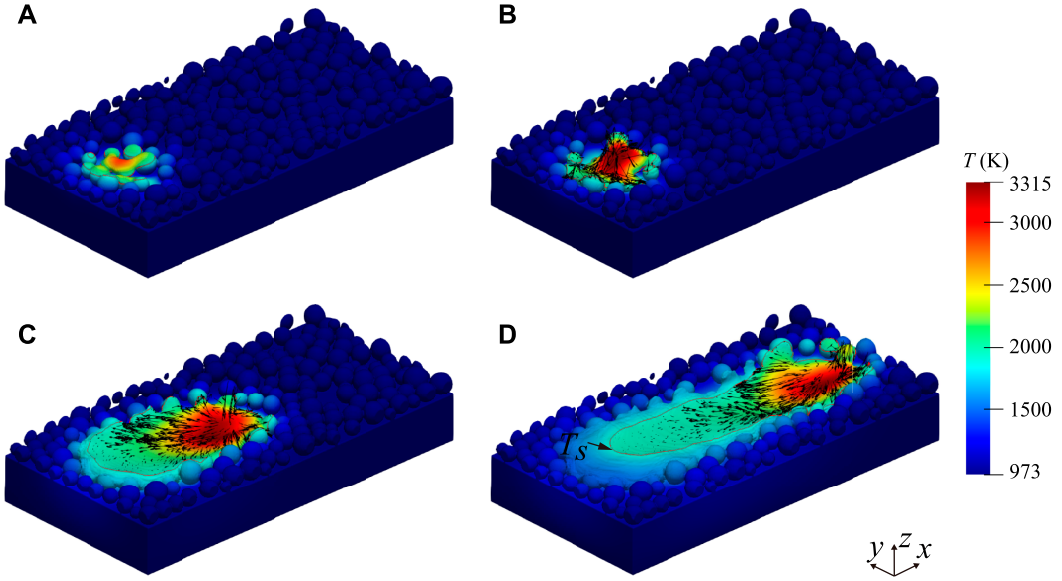

FIGURE 5 | The morphological characteristics and temperature distribution of the melt pool during electron beam scanning **(A)**: 0.1 ms, **(B)**: 0.2 ms, **(C)**: 1.2 ms, **(D)**: 2.4 ms.

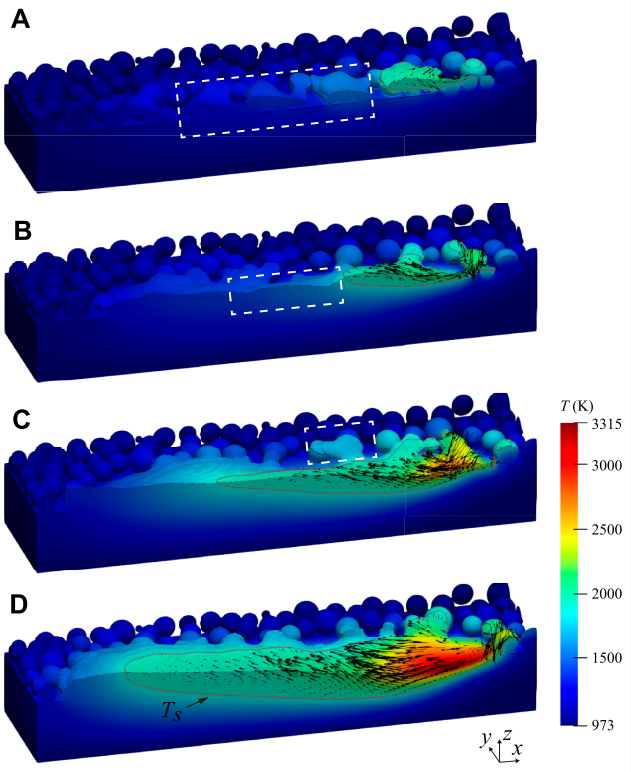

FIGURE 6 | The morphological characteristics and temperature distribution of the melt pool with an increase of the electron beam current in the longitude cross section view **(A)**: I_B = 1.0 mA, **(B)**: I_B = 1.5 mA, **(C)**: I_B = 2.5 mA, **(D)**: I_B = 4.0 mA). The dash squares mark the morphological features **(A)**: the balling effect, **(B)**: the fluctuation of the solidified track, **(C)**: the partially melted particles).

pressure at the interface, resulting in a distinct depression on the melt pool surface, as illustrated in **Figure 5D**. At the same time, it is evident that the melt flows from the center to the periphery owing to the Marangoni effect within the melt pool, which is due to the presence of tangential forces on the surface caused by temperature-dependent surface tension. Accordingly, this accelerates the convective cooling process and helps reduce the pool's temperature, which to some extent suggests that models without flow might overestimate the temperature values inside the pool.

Figure 6 shows the morphological characteristics and temperature distribution of the melt pool with an increase of the electron beam current from 1.0 to 4.0 mA at t = 2.4 ms. When the current is 1.0 mA, the melting track is discontinuous and appears to spherize, as illustrated in **Figure 6A**. When the heat input is relatively low, the melted powder tends to cluster under surface tension as the powder layer melts, and the substrate does not melt. As the power is increased to 90 W, the substrate gradually melts, and the melted powder spreads over the melted substrate to minimize the surface energy in **Figure 6B**. At this stage, the temperature in the melt pool is below the boiling point, and there is no significant depression, indicating that the pool is barely subject to recoil pressure. Due to inadequate substrate melting, the powders preferentially merge with each other after melting rather than entering the melt pool immediately. Due to the high solidification rate, the melt pool is not replenished by the melt in time for solidification to occur. The molten powder then fuses with the melt pool, and there is significantly more melt in the melt pool than before. This results in significant fluctuations in the surface of the solidified track. Some partially melted powder adheres to the melting track in **Figure 6C**. These particles are partially heated to full melting as they are away from the electron

beam heat source. This phenomenon contributes to the roughness of the melt track and is usually unavoidable. In practice, it may also increase the porosity, as discussed later. **Figure 6D** shows the melt flows towards the tail of the melt pool, creating a backward flow. In addition, a recirculation flow from the rear of the melt pool is generated. At this time, the electron beam power reaches 240W, the substrate is fully heated and melted, and the melted powder at the front of the melt pool can be replenished in time to provide sufficient melt for the reverse flow. This ensures that a flat surface is formed at the rear of the melt pool when it solidifies.

Figure 7A depicts the temperature along the surface of the melting track versus the distance from the electron beam at t = 2.4 ms. The position scale 0 indicates the position of the electron beam at the moment. As the electron beam power increases, the maximum temperature in the melt pool rises continuously. Furthermore, the position of the maximum temperature is not at the center of the electron beam but slightly off it. The electron beam has an apparent effect within a specific range. When the energy supplied by the electron beam to the metal powder or melt is higher than the heat lost by its heat transfer, the temperature keeps rising. The plateaus are noted

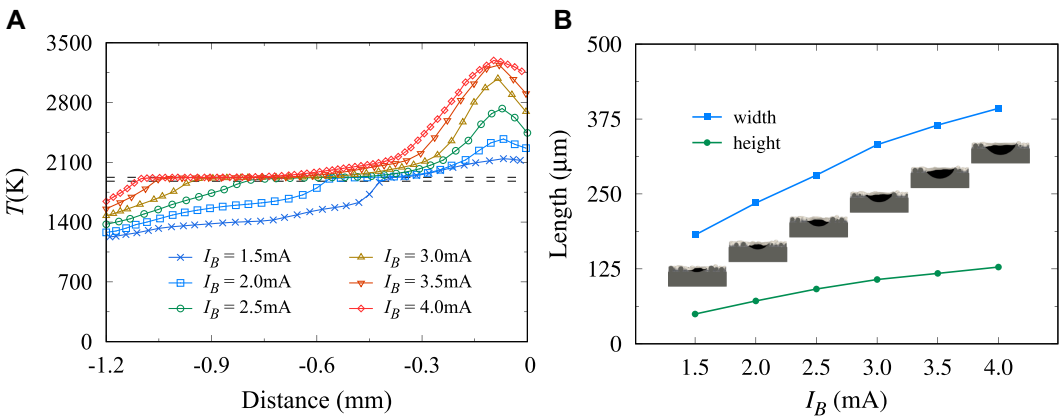

FIGURE 7 | (A) Temperature profile along the surface of the melt pool in the x-direction **(B)** The width and height of the solidified track.

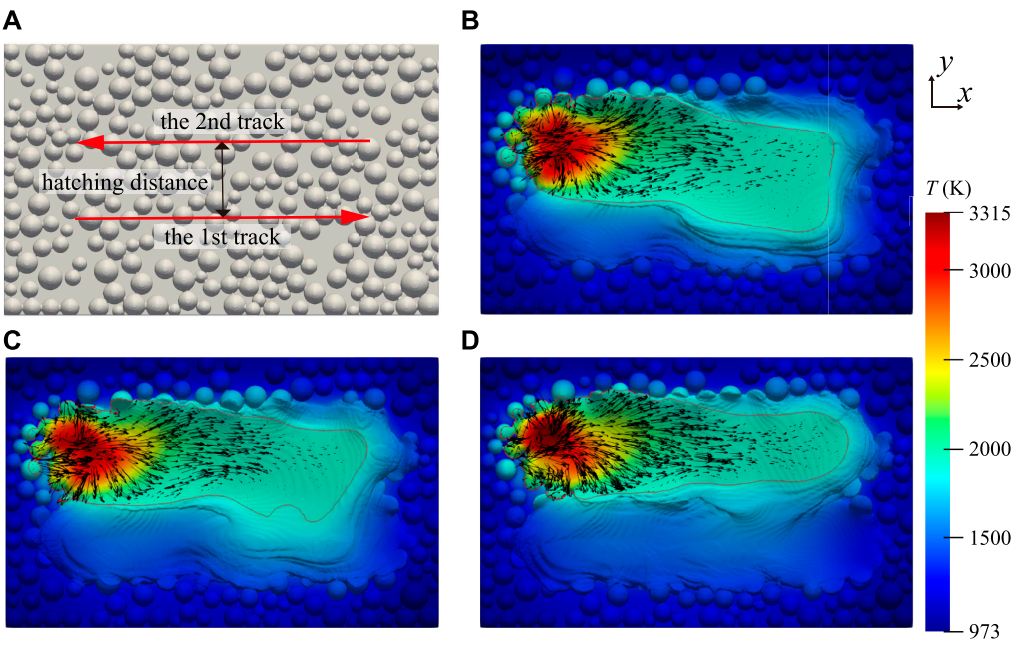

FIGURE 8 | (A) The scanning strategy **(B–D)** The temperature distribution of the melt pool with different hatching distance in the top view **(B)**: 0.28 mm, **(C)**: 0.32 mm, **(D)**: 0.36 mm.

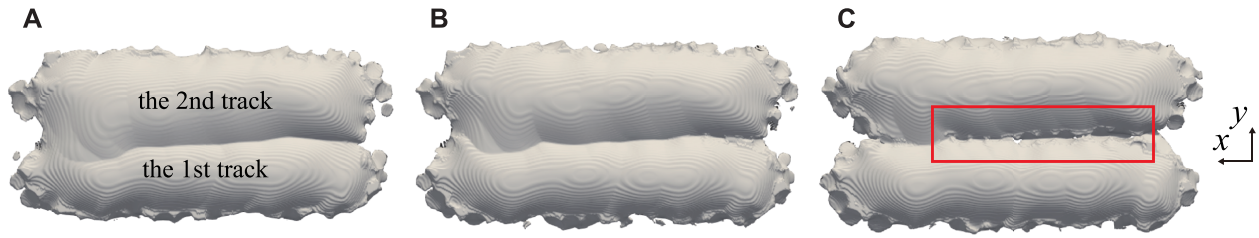

FIGURE 9 | The bottom morphology of the melt tracks with different hatching distance **(A)**: 0.28 mm, **(B)**: 0.32 mm, **(C)**: 0.36 mm.

corresponding to the latent heat for the phase change. At the position away from the electron beam, the melt solidifies and releases some heat, resulting in a slower temperature reduction. The temperature gradient around the pool is significantly lower than inside the pool but still reaches 1×10^5 K/m. The higher the electron beam power, the longer the plateau zone is in the figure, which indicates that the higher the electron beam energy density, the lower the solidification rate. **Figure 7B** shows the geometric characteristics of the single track, including the average width and height of the tracks in relation to the electron beam current. The average value is based on measurements from three cross-sections. Obviously, as the electron beam power increases, the width and height increase. At a power of 60 W, the average height is 49.73 m, which is nearly half the thickness of the powder layer. In this case, the substrate is not sufficiently melted, although the melt track is continuous. Simulation results indicate that the morphology of the melt pool is considerably dependent on the energy input parameters, and improper selection of process parameters may significantly reduce the part performance.

3.3 Multiple Tracks on Powder-Bed

The multiple tracks EBSM process is simulated to study the interaction between sequential tracks. In the simulation, the electron beam scanning speed is increased to 1 m/s, and the current is set to 4.5 mA. Other parameters are the same as before. The scanning strategy is an S-shaped path with no delays on the turns, as shown in **Figure 8A**. The hatching space l_h represents the distance between the first and second track. The hatching space is chosen as 0.28, 0.32, and 0.36 mm, respectively, where 0.36 mm is slightly more significant than the average width of the melt track.

Figures 8B–D show the morphological characteristics and temperature distribution of the melt pool for the multiple tracks. In **Figure 8B**; **Figure 8C**, the first solidified track appears to re-melt to some extent as the electron beam scans along the second track. The shorter the hatching distance, the larger the re-melted area. Before the first molten track has fully solidified, the powder on the second track melts and enters the previous molten pool, causing the rear of the melt pool to deviate from the scanning direction of the second electron beam. When the hatching space is 0.36 mm, some uneven protrusions are evident between the first and second track as illustrated in **Figure 8D**. In this case, the morphology of the melt pool differs from the previous two cases. **Figure 9** gives The bottom morphology of the melt tracks in these three cases. In **Figure 9C**, there are some apparent gaps between the first and second tracks, and the two tracks are almost independent of each other. This indicates that the hatching distance is selected according to the width of the single melt track. A reasonable distance ensures a good fusion joint between multiple tracks and reduces product defects.

4 CONCLUSION

A three-dimensional two-relaxation-times lattice Boltzmann model is developed to simulate the EBSM additive manufacturing process, including the dynamics of melt flows, heat transfer, phase changes, and effects of internal and external forces. The model is validated by simulations of convective phase change in a square-cavity and then applied to a bead-on-plate EBSM process. The results show that the present model can be used to accurately characterize the solid-liquid phase change and describe the formation of the melting pool in an EBSM additive manufacturing process.

For single track powder bed fusion, surface tension drives the convergence of the molten powder into a continuous melt. The Marangoni effect and recoil pressure induce backward flow within the melt pool, moving the melt away from the high-temperature region and thus creating a recirculation flow within the melt pool. At a constant electron beam voltage of 60 kV, the height and width of the melt track and the maximum temperature within the melt pool decrease continuously as the electron beam current decreases from 4 to 1.5 mA. When the energy input is relatively high, the powder and the substrate are sufficiently melted to form a continuous flat cladding layer. At a current of 15 mA, the melt pool is virtually immune to recoil pressure as the temperature is well below the boiling point, and the melt track surface is fluctuating due to inadequate substrate melting. When the current is further reduced to 10 mA, balling occurs in the track, resulting in the appearance of a significant area of voids. Excessive hatching distance for multiple tracks leads to many porosities, and partial remelting of the fusion track can reduce the porosity. Boosting energy input and reducing distance can effectively lower porosity to improve product quality.

DATA AVAILABILITY STATEMENT

The original contributions presented in the study are included in the article/Supplementary Material, further inquiries can be directed to the corresponding author.

AUTHOR CONTRIBUTIONS

DC: methodology, validation, writing–original draft, data curation and software. WC: conceptualization. YL: supervision. DS: conceptualization, methodology and manuscript revision.

REFERENCES

Afkhami, S., and Bussmann, M. (2009). Height Functions for Applying Contact Angles to 3d Vof Simulations. *Int. J. Numer. Meth. Fluids* 61, 827–847. doi:10.1002/fld.1974

Ammer, R., Markl, M., Ljungblad, U., Körner, C., and Rüde, U. (2014). Simulating Fast Electron Beam Melting with a Parallel thermal Free Surface Lattice Boltzmann Method. *Comput. Mathematics Appl.* 67, 318–330. doi:10.1016/j.camwa.2013.10.001

Blakey-Milner, B., Gradl, P., Snedden, G., Brooks, M., Pitot, J., Lopez, E., et al. (2021). Metal Additive Manufacturing in Aerospace: A Review. *Mater. Des.* 209, 110008. doi:10.1016/j.matdes.2021.110008

Bogner, S., Rüde, U., and Harting, J. (2016). Curvature Estimation from a Volume-Of-Fluid Indicator Function for the Simulation of Surface Tension and Wetting with a Free-Surface Lattice Boltzmann Method. *Phys. Rev. E* 93, 043302. doi:10.1103/PhysRevE.93.043302

Brackbill, J. U., Kothe, D. B., and Zemach, C. (1992). A Continuum Method for Modeling Surface Tension. *J. Comput. Phys.* 100, 335–354. doi:10.1016/0021-9991(92)90240-y

Cheng, B., Price, S., Lydon, J., Cooper, K., and Chou, K. (2014). On Process Temperature in Powder-Bed Electron Beam Additive Manufacturing: Model Development and Validation. *J. Manufacturing Sci. Eng.* 136. doi:10.1115/1.4028484

Ferdowsi, P. A., and Bussmann, M. (2008). Second-order Accurate Normals from Height Functions. *J. Comput. Phys. (Print)* 227, 9293–9302. doi:10.1016/j.jcp.2008.07.014

Ginzburg, I., Verhaeghe, F., and d'Humieres, D. (2008). Two-relaxation-time Lattice Boltzmann Scheme: About Parametrization, Velocity, Pressure and Mixed Boundary Conditions. *Commun. Comput. Phys.* 3, 427–478.

Guo, Z., Zheng, C., and Shi, B. (2002). Discrete Lattice Effects on the Forcing Term in the Lattice Boltzmann Method. *Phys. Rev. E* 65, 046308. doi:10.1103/PhysRevE.65.046308

Hashemi, S. M., Parvizi, S., Baghbanijavid, H., Tan, A. T., Nematollahi, M., Ramazani, A., et al. (2021). Computational Modelling of Process–Structure–Property–Performance Relationships in Metal Additive Manufacturing: a Review. *Int. Mater. Rev.* 67, 1–46. doi:10.1080/09506608.2020.1868889

Jamshidinia, M., Kong, F., and Kovacevic, R. (2013). Numerical Modeling of Heat Distribution in the Electron Beam Melting® of Ti-6al-4v. *J. Manufacturing Sci. Eng.* 135. doi:10.1115/1.4025746

Knapp, G. L., Raghavan, N., Plotkowski, A., and Debroy, T. (2019). Experiments and Simulations on Solidification Microstructure for Inconel 718 in Powder Bed Fusion Electron Beam Additive Manufacturing. *Additive Manufacturing* 25, 511–521. doi:10.1016/j.addma.2018.12.001

Körner, C., Bauereiß, A., and Attar, E. (2013). Fundamental Consolidation Mechanisms during Selective Beam Melting of Powders. *Model. Simulation Mater. Sci. Eng.* 21, 085011. doi:10.1088/0965-0393/21/8/085011

Körner, C., Thies, M., Hofmann, T., Thürey, N., and Rüde, U. (2005). Lattice Boltzmann Model for Free Surface Flow for Modeling Foaming. *J. Stat. Phys.* 121, 179–196. doi:10.1007/s10955-005-8879-8

Leung, C. L. A., Tosi, R., Muzangaza, E., Nonni, S., Withers, P. J., and Lee, P. D. (2019). Effect of Preheating on the thermal, Microstructural and Mechanical Properties of Selective Electron Beam Melted Ti-6al-4v Components. *Mater. Des.* 174, 107792. doi:10.1016/j.matdes.2019.107792

Lin, S., Gan, Z., Yan, J., and Wagner, G. J. (2020). A Conservative Level Set Method on Unstructured Meshes for Modeling Multiphase Thermo-Fluid Flow in Additive Manufacturing Processes. *Computer Methods Appl. Mech. Eng.* 372, 113348. doi:10.1016/j.cma.2020.113348

Mao, S., Wang, X., Sun, D., and Wang, J. (2022). Numerical Modeling of Dendrite Growth in a Steady Magnetic Field Using the Two Relaxation Times Lattice Boltzmann-phase Field Model. *Comput. Mater. Sci.* 204, 111149. doi:10.1016/j.commatsci.2021.111149

Mencinger, J. (2004). Numerical Simulation of Melting in Two-Dimensional Cavity Using Adaptive Grid. *J. Comput. Phys.* 198, 243–264. doi:10.1016/j.jcp.2004.01.006

Noble, D., and Torczynski, J. (1998). A Lattice-Boltzmann Method for Partially Saturated Computational Cells. *Int. J. Mod. Phys. C* 9, 1189–1201. doi:10.1142/s0129183198001084

Riedlbauer, D., Scharowsky, T., Singer, R. F., Steinmann, P., Körner, C., and Mergheim, J. (2017). Macroscopic Simulation and Experimental Measurement of Melt Pool Characteristics in Selective Electron Beam Melting of Ti-6al-4v. *Int. J. Adv. Manufacturing Technology* 88, 1309–1317. doi:10.1007/s00170-016-8819-6

Tamayo, J. A., Riascos, M., Vargas, C. A., and Baena, L. M. (2021). Additive Manufacturing of Ti6al4v alloy via Electron Beam Melting for the Development of Implants for the Biomedical Industry. *Heliyon* 7, e06892. doi:10.1016/j.heliyon.2021.e06892

Vafadar, A., Guzzomi, F., Rassau, A., and Hayward, K. (2021). Advances in Metal Additive Manufacturing: a Review of Common Processes, Industrial Applications, and Current Challenges. *Appl. Sci.* 11, 1213. doi:10.3390/app11031213

Wu, C., Zafar, M. Q., Zhao, H., Wang, Y., Schöler, C., Heinigk, C., et al. (2021). Multi-physics Modeling of Side Roughness Generation Mechanisms in Powder Bed Fusion. *Additive Manufacturing* 47, 102274. doi:10.1016/j.addma.2021.102274

Yan, W., Ge, W., Qian, Y., Lin, S., Zhou, B., Liu, W. K., et al. (2017). Multi-physics Modeling of Single/multiple-Track Defect Mechanisms in Electron Beam Selective Melting. *Acta Materialia* 134, 324–333. doi:10.1016/j.actamat.2017.05.061

Zäh, M. F., and Lutzmann, S. (2010). Modelling and Simulation of Electron Beam Melting. *Prod. Eng.* 4, 15–23. doi:10.1007/s11740-009-0197-6

Zakirov, A., Belousov, S., Bogdanova, M., Korneev, B., Stepanov, A., Perepelkina, A., et al. (2020). Predictive Modeling of Laser and Electron Beam Powder Bed Fusion Additive Manufacturing of Metals at the Mesoscale. *Additive Manufacturing* 35, 101236. doi:10.1016/j.addma.2020.101236

Zhao, Y., Aoyagi, K., Yamanaka, K., and Chiba, A. (2020). Role of Operating and Environmental Conditions in Determining Molten Pool Dynamics during Electron Beam Melting and Selective Laser Melting. *Additive Manufacturing* 36, 101559. doi:10.1016/j.addma.2020.101559

Zhao, Y., Koizumi, Y., Aoyagi, K., Yamanaka, K., and Chiba, A. (2021). Thermal Properties of Powder Beds in Energy Absorption and Heat Transfer during Additive Manufacturing with Electron Beam. *Powder Technology* 381, 44–54. doi:10.1016/j.powtec.2020.11.082

Zheng, M., Wei, L., Chen, J., Zhang, Q., Zhong, C., Lin, X., et al. (2019). A Novel Method for the Molten Pool and Porosity Formation Modelling in Selective Laser Melting. *Int. J. Heat Mass Transfer* 140, 1091–1105. doi:10.1016/j.ijheatmasstransfer.2019.06.038

Conflict of Interest: The authors declare that the research was conducted in the absence of any commercial or financial relationships that could be construed as a potential conflict of interest.

frontiers | Frontiers in Materials

ORIGINAL RESEARCH
published: 03 June 2022
doi: 10.3389/fmats.2022.916593

Phase-Field Model of Hydride Blister Growth Kinetics on Zirconium Surface

Shuai Wu[1,2,3], *Jie Sheng*[3], *Chao Yang*[1,2], *Xiaoming Shi*[1,2], *Houbing Huang*[1,2]*, *Yu Liu*[3]* and *Haifeng Song*[3]

[1]School of Materials Science and Engineering, Beijing Institute of Technology, Beijing, China, [2]Advanced Research Institute of Multidisciplinary Science, Beijing Institute of Technology, Beijing, China, [3]Laboratory of Computational Physics, Institute of Applied Physics and Computational Mathematics, Beijing, China

The precipitation of zirconium hydride blisters on the surface of zirconium alloy cladding destroys the integrity of the material and leads to material failure, which has serious potential safety hazards. To study the corrosion kinetics of zirconium hydride blisters, we established a phase-field model coupled with anisotropic elastic, which can reflect the microstructure evolution process of zirconium hydride blisters. The model studies the natural growth of hydride blister and the structural evolution process after applying radial stress and discusses the corrosion characteristics, stress distribution, and displacement changes. Zirconium hydride blisters tend to be semi-ellipsoidal in natural growth. Applying radial outward stress will promote the growth of blisters and aggravate the harm of corrosion. The stress state changes with applying stress, which affects the elastic driving force, resulting in the change of blister morphology. This work is helpful to understand the corrosion kinetic mechanism of hydride blisters.

Keywords: phase-field model, hydride blister, anisotropic elastic, microstructure evolution, applied stress

OPEN ACCESS

Edited by:
Yu-Hong Zhao,
North University of China, China

Reviewed by:
Lijun Zhang,
Central South University, China
Linyun Liang,
Beihang University, China
Dongke Sun,
Southeast University, China

***Correspondence:**
Houbing Huang
hbhuang@bit.edu.cn
Yu Liu
liu_yu@iapcm.ac.cn

Specialty section:
This article was submitted to Computational Materials Science, a section of the journal Frontiers in Materials

Received: *09 April 2022*
Accepted: *26 April 2022*
Published: *03 June 2022*

Citation:
Wu S, Sheng J, Yang C, Shi X, Huang H, Liu Y and Song H (2022) Phase-Field Model of Hydride Blister Growth Kinetics on Zirconium Surface. Front. Mater. 9:916593. doi: 10.3389/fmats.2022.916593

INTRODUCTION

Zirconium alloy has a low neutron absorption rate and good high-temperature corrosion resistance and is widely used in structural materials in fuel cladding of water-cooled reactors (Krishnan and Asundi, 1981; Bair et al., 2015; Motta et al., 2015). However, severe waterside corrosion reactions occur during use and storage, and its performance will also be limited (Hong et al., 2002; Han et al., 2019). During the corrosion process on the waterside, the outer layer of the zirconium alloy cladding is oxidized, releasing hydrogen atoms, and the hydrogen atoms migrate into the zirconium matrix. It moves along the hydrostatic stress gradient and moves against the thermal gradient (Kammenzind and Berquist, 2000; Reheman and Ståhle, 2018). In other words, hydrogen is attracted to high-stress areas and cold areas, or areas where the two interact together. When the hydrogen concentration exceeds the solid solution limit in the zirconium matrix, zirconium and solid solute hydrogen transform into the zirconium hydride phase (Ghosal et al., 2002; Bair et al., 2015; Reheman and Ståhle, 2018; Han et al., 2019). The formation of brittle hydride will not only cause the material to expand and increase its volume greatly, but also it is easy to initiate crack growth and penetrate the matrix (Kim et al., 2007; Puls, 2009; McRae et al., 2010). The hydride formed on the metal surface appears as a small bump, usually called a blister (Cheong et al., 2001; Singh et al., 2002). The growth of zirconium hydride blister is an important form of pitting corrosion. It is the main initiation point of fuel cladding failure in nuclear power plants, which will pose a serious threat to nuclear power safety. Therefore, the basic understanding of hydride blister growth behavior is of great significance for predicting material performance degradation and failure.

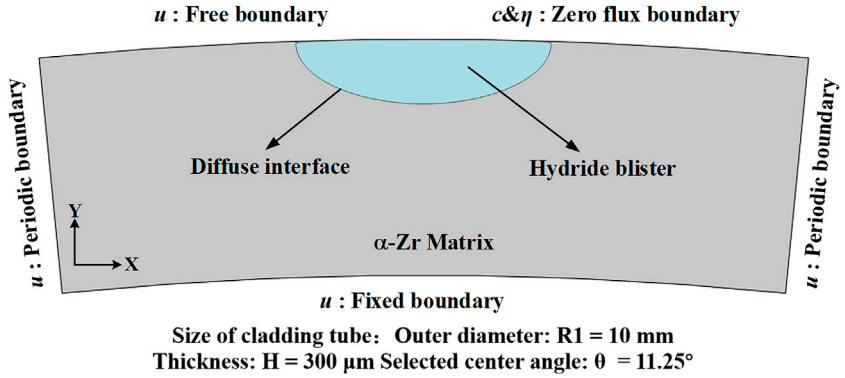

FIGURE 1 | Schematic diagram of zirconium-zirconium hydride blister model and boundary condition settings.

The size of the hydride blister is much larger than that of the single hydride, reaching the micrometer level (Cheong et al., 2001; Singh et al., 2002; Long et al., 2017; Kim et al., 2018). The formation of the hydride blister requires the existence of a cold spot in the surrounding environment, and the effect of cold spot aggregation on the growth of hydride blisters is also different (Singh et al., 2002). In the experiment of (Domizzi et al., 1996), the growth of blisters on the surface of the Zr-2.5% Nb alloy tube was studied. It divides the observed phenomenon into three areas (I) the main part of the zirconium hydride blister, whose growth is similar to that of a single hydride, and the anisotropic growth is ellipsoidal, (II) the radial hydride accumulation area, and (III) circumferential hydride accumulation area. The phase-field method has been widely used to study the microstructure changes such as hydride precipitation in Zr cladding materials (Bair et al., 2015; Bair et al., 2016; Bair and Zaeem, 2017; Bair et al., 2017; Han et al., 2019; Toghraee et al., 2021). Based on region (I) (Reheman and Ståhle, 2018), studies the growth and cracking of hydride blisters under elastic-plastic action by using the phase-field method, but its model is established based on isotropy, which can not represent the anisotropic growth of zirconium hydride blisters. In this work, we study the morphological evolution of zirconium hydride blisters by using the phase-field method coupled with anisotropic elastic strain energy. In addition, some studies (Cheong et al., 2001; Motta and Chen, 2012) show that during reactor operation, the fission gas and the helium filling gas in the cladding tube create a combined pressure that exposes the nuclear fuel cladding to constant stress. Even the swelling of nuclear fuel also produces a certain pressure on the zirconium alloy cladding tube (Rozhnov et al., 2011). Therefore, it is important to understand the evolution mechanism of zirconium hydride blisters under specific pressure. The evolution of hydride blisters under radial stress is considered in this work.

PHASE-FIELD MODEL

Combining the zirconium hydrogen phase diagram (Yu et al., 2020) and experimental research (Santisteban and Domizzi, 2009; Vicente Alvarez et al., 2011; Lin et al., 2016; Motta et al., 2019), it can be found that the hydrides in the zirconium hydride blister are all δ-hydrides, and the ratio varies approximately in the range of 60–85%, and the rest is the Zr matrix and impurities. Since the chemical energy parameters of the zirconium hydride blister are not clear yet, we simulate the zirconium hydride blister by using the chemical energy (Bair et al., 2016; Bair and Zaeem, 2017; Bair et al., 2017; Toghraee et al., 2021) and elastic parameters (Bair et al., 2017; Han et al., 2019) of the δ-hydride. The size of the cladding tube in the model is similar to some studies (Hong et al., 2002; Hellouin de Menibus et al., 2014), and 11.25-degree section is simulated. Since the longitudinal plane of the blister is usually observed in the experiment, we convert the data in the z-y direction of the coordinate axis to x-y. The whole calculation process is carried out in two dimensions. **Figure 1** shows the setting of the hydride blister growth model and boundary conditions. For the displacement field u, the top boundary is set as free boundary conditions, the left and right are periodic boundary conditions, and the bottom is fixed boundary conditions. The boundary settings of phase-field η and concentration field c are the same. All boundaries are set as zero flux boundary conditions, and hydride and the matrix phase are distinguished by the diffuse interface.

Governing Equations and Bulk Free Energy

Interfacial reaction, hydrogen transport driven by diffusion potential, and internal stress caused by precipitation and growth of zirconium hydride blister. Multi-physical field coupling based on dynamic equations can simulate these effects and reflect the dynamic characteristics (Shi et al., 2021; Liu et al., 2022; Shi et al., 2022). The phase field, hydrogen concentration field, and elastic strain energy field were coupled to establish the zirconium hydride blister growth model in this study. These fields are necessary to track the movement of the diffusion interface, calculate the diffusion/redistribution of hydrogen (Yang et al., 2021), and reveal the effect of radial stress on hydride growth. The advantage of the phase-field model in this study is that the shape of the grown precipitates can be calculated (Gao et al., 2021; Gao et al., 2022; Xu et al., 2022). The phase transition from metal to hydride is given by a

TABLE 1 | Model parameters and conditions used in the simulations.

Parameters	Symbol	Value	Unit
Temperature	T	600	K
Mesh size	dx	1e-6	m
The outer diameter of cladding tube Hong et al. (2002); Hellouin de Menibus et al. (2014)	$R1$	1e-2	m
The thickness of cladding tube	H	3e-3	m
Selected angle of cladding tube	θ	11.25	degree
Hydrogen concentration in matrix	c_α	0.05	—
Hydrogen concentration at stoichiometric ratio in blister	c_δ	0.6	—
Interface thickness	λ	1.4e-5	m
Gradient coefficient	κ_η	0.03675	J/m
Interface mobility Yang et al. (2021)	M	1.2158e-9	$m^3/(J{\cdot}s)$
Diffusion coefficient Han et al. (2019)	D	1.2302e-10	m^2/s
Gas constant	R	8.3145	J/(mol·K)
Molar volume Han et al. (2019)	V_m	14	cm^3/mol
A Constant in G_α	A_α	14	J/mol
A Constant in G_δ	A_δ	24.0388	J/mol
Elastic modulus of α-Zr Bair et al. (2017)	$C^\alpha_{11}, C^\alpha_{12}, C^\alpha_{13}, C^\alpha_{22}, C^\alpha_{33}, C^\alpha_{44}, C^\alpha_{55}, C^\alpha_{66}$,	155, 67, 65,155,155,40,40,44	GPa
Elastic modulus of blister (δ-hydride) Bair et al. (2017)	$C^\delta_{11}, C^\delta_{12}, C^\delta_{13}, C^\delta_{22}, C^\delta_{33}, C^\delta_{44}, C^\delta_{55}, C^\delta_{66}$,	63, 28, 44, 63, 65,93,93,101	GPa
Eigenstrain Singh et al. (2007); Tummala et al. (2018)	ε^{00}_{ij}	$\begin{bmatrix} 0.0528 & 0 & 0 \\ 0 & 0.0528 & 0 \\ 0 & 0 & 0.0781 \end{bmatrix}$	—

phase variable η that continuously covers a range of values, where the ends of the range represent pure metal or pure hydride, respectively. The analysis is based on totally free energy, including strain energy, chemical potential energy, and gradient energy describing the diffusion interface. In the phase-field model, both the diffusion of hydrogen atoms and the precipitation of hydrides are considered. The time evolution of the concentration c is determined by the Cahn-Hilliard diffusion equation (Kim et al., 2008), and the evolution of the microstructural parameter η is governed by the time-dependent Allen-Cahn equation (Allen and Cahn, 1979). In order to solve the evolution equation, the finite element method is adopted, and the mesh adaptive method is used to speed up the calculation.

$$\frac{\partial \eta}{\partial t} = -L\frac{\delta F_{\text{total}}}{\delta \eta} \tag{1}$$

$$\frac{\partial c}{\partial t} = \nabla \cdot M\nabla\frac{\delta F_{\text{total}}}{\delta c} \tag{2}$$

The driving force of the zirconium-hydride blister phase-field model comes from the minimization of the total free energy (F_{total}) of the system, which includes the uniform bulk chemical free energy (F_{bulk}) the interface gradient energy (F_{int}) and the elastic energy (F_{el}). For simplicity, it is assumed that the diffusion coefficients of hydrogen in the matrix and precipitate are the same.

$$F_{\text{total}} = F_{\text{bulk}} + F_{\text{int}} + F_{\text{el}} \tag{3}$$

Here, all the parameters used in this simulation are listed in **Table. 1** The bulk chemical free energy F_{bulk} is a function of the concentration c and the order parameter η at T = 600 k, while F_{int} is the gradient energy due to the inhomogeneity of the interface

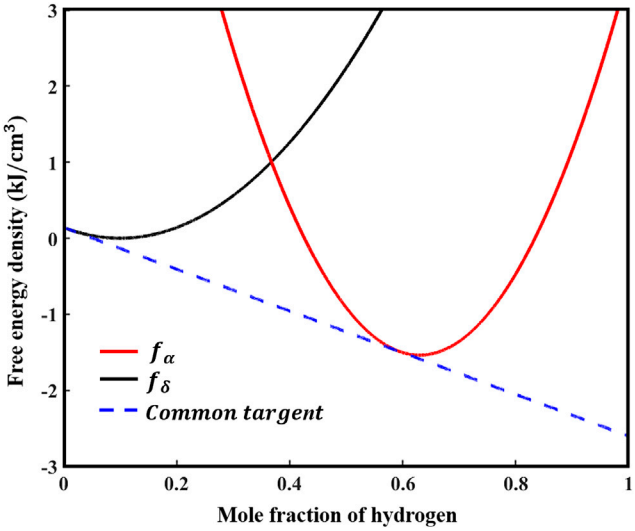

FIGURE 2 | Two-phase chemical free energy density curves of zirconium matrix and zirconium hydride blister.

and F_{el} is the elastic strain energy during the Zr matrix phase to the hydride phase transition.

$$F_{\text{bulk}} = \int_V f_{\text{bulk}} dV \tag{4}$$

The Kim-Kim-Suzuki (KKS) binary alloy model (Kim et al., 1999) is used to determine the expression form of bulk chemical free energy density. The KKS model assumes that each material point is considered to be a mixture of two or more phases with different concentrations, and the diffusion potentials of the same

concentration between different phases are equal. The assumption can be expressed as follows:

$$c = h(\eta)c_\alpha + [1 - h(\eta)]c_\delta \tag{5}$$

$$\frac{\partial f_\alpha(c_\alpha)}{\partial c_\alpha} = \frac{\partial f_\delta(c_\delta)}{\partial c_\delta} \tag{6}$$

$$f_{\text{bulk}}(c,\eta) = h(\eta)f_\alpha(c_\alpha) + [1 - h(\eta)]f_\delta(c_\delta) + wg(\eta) \tag{7}$$

where $h(\eta) = 3\eta^2 - 2\eta^3$ is the interpolation function, the double potential well function $g(\eta) = \frac{1}{2}(\eta^2 \times (1-\eta)^2)$, and w is the potential barrier. The free energy density in this study is constructed according to the quadratic fitting method adopted by (Bair et al., 2016; Bair and Zaeem, 2017; Bair et al., 2017; Toghraee et al., 2021). Taking advantage of the equal slope at the two-phase equilibrium point, the two-phase free energy curve can be constructed by using the artificial parameters A_α and c_α.

Two-phase molar free energy G_α and G_δ at $T = 600$ K can be expressed as:

$$G_\alpha = A_\alpha\left(c_\alpha - c_\delta^{'}\right)^2 \tag{8}$$

$$G_\delta = \Delta G_\delta^0\left(A_\delta\left(c_\delta - \left(c_\delta^{'} - 0.05\right)\right)^2 - 1\right) \tag{9}$$

$$\Delta G_\delta^0 = 46.37 - 0.0414T\left[\frac{KJ}{mol}\right] \tag{10}$$

$$c_\alpha^{'} = 3.27 \times 10^4 \exp\left(-\frac{25024}{RT}\right) \tag{11}$$

Here, c_α and c_δ are the molar fractions of atomic H in the matrix and blister. $c_\alpha^{'}$ is the concentration of maximum hydrogen solubility in the matrix before precipitation occurs (Une et al., 2009); $c_\delta^{'}$ is the hydrogen concentration in the hydride blister; ΔG_δ^0 is the molar Gibbs free energy of hydride blister formation. The constant A_α and A_δ are the contribution of the free energy of the two phases to the interface, which are determined by constructing a common tangent between the molar Gibbs free energy curves of the two phases (Yang et al., 2020; Yang et al., 2021; Sheng et al., 2022), from which an approximate expression of the free energy can be obtained. f_α and f_δ are the free energy densities of the zirconium matrix and hydride blister, respectively, as shown in **Figure 2** The blue dashed line is the common tangent when the two phases are in equilibrium.

$$f_\alpha = \frac{G_\alpha}{V_m} = 14c_\alpha^2 - 2.80c_\alpha + 0.14 \tag{12}$$

$$f_\delta = \frac{G_\delta}{V_m} = 36.9683c_\delta^2 - 46.5801c_\delta + 13.1349 \tag{13}$$

$$F_{\text{int}} = \int_V f_{\text{int}} dr \tag{14}$$

The interfacial energy density can generally be written as a function of the gradient of the phase-field variable,

$$f_{\text{int}} = \frac{1}{2}\kappa_\eta(\nabla\eta)^2 \tag{15}$$

where κ_η is the gradient energy coefficient related to the phase-field variable η.

Elastic Strain Energy and Applied Stress

When hydride blister precipitate and grow in the matrix, their elastic strain energy comes from the structural difference between hydride blister and matrix. The elastic strain energy F_{el} is expressed as follows:

$$F_{\text{el}} = \int_V f_{\text{el}} dr = \frac{1}{2}\int_V \sigma_{ij}\varepsilon_{ij}^{el} dr \tag{16}$$

where f_{el} is the mismatch elastic strain energy density, σ_{ij} and ϵ_{ij}^{el} are the stress and elastic strain, respectively. Considering that the cladding tube will be subjected to the radial outward stress from the swelling of nuclear fuel and so on, we add a new cylindrical coordinate system and add the radial outward stress σ_{app} to the model to study the evolution difference of the blister under different stresses. The radial stress σ_{app} is added through the stress coordinate conversion in elasticity.

$$\sigma_{ij} = \sigma_{app} + C_{ijkl}(\eta)\varepsilon_{ij}^{el} \tag{17}$$

$$\sigma_{app} = \begin{cases} \sigma_x = \dfrac{\sigma_r + \sigma_\varphi}{2} + \dfrac{\sigma_r - \sigma_\varphi}{2}cos\,2\varphi - \tau_{r\varphi}\,sin\,2\varphi \\ \sigma_y = \dfrac{\sigma_r + \sigma_\varphi}{2} - \dfrac{\sigma_r - \sigma_\varphi}{2}cos\,2\varphi + \tau_{r\varphi}\,sin\,2\varphi \\ \tau_{xy} = \dfrac{\sigma_r - \sigma_\varphi}{2}sin2\varphi + \tau_{r\varphi}\,sin\,2\varphi \end{cases} \tag{18}$$

σ_r and σ_φ are the radial stress and circumferential stress applied in the cylindrical coordinate system respectively. φ is the angle value in the cylindrical coordinate system. σ_x, σ_y, τ_{xy} are the stress value in the rectangular coordinate system.

$$\varepsilon_{ij}^{el} = \varepsilon_{ij}(r) - \varepsilon_{ij}^{00}(r) \tag{19}$$

$$\varepsilon_{ij}(r) = \frac{1}{2}\left(\frac{\partial u_i(r)}{\partial r_j} + \frac{\partial u_j(r)}{\partial r_i}\right) \tag{20}$$

$$\varepsilon_{ij}^{00}(r) = h(\eta)\varepsilon_{ij}^{00}(r)\delta_{ij} = \begin{bmatrix} h(\eta)\varepsilon_{11}^{00} & 0 & 0 \\ 0 & h(\eta)\varepsilon_{22}^{00} & 0 \\ 0 & 0 & h(\eta)\varepsilon_{33}^{00} \end{bmatrix} \tag{21}$$

The elastic strain ε_{ij}^{el} can be obtained from **Equation 19**, where $\varepsilon_{ij}(r)$ is the total strain represented by the components u_i and u_j of the displacement field variable u obtained by solving the mechanical equilibrium **Equation 23** and $\varepsilon_{ij}^{00}(r)$ is related to the lattice inherent strain ε_{ij}^{00}. Tummala (Tummala et al., 2018) and Singh (Singh et al., 2007) give the eigenstrain of hydride at different temperatures. The eigenstrain of the hydride blister at $T = 600$ k can be obtained.

$$\varepsilon_{ij}^{00} = \begin{cases} \varepsilon_{11}^{00} = \varepsilon_{22}^{00} = 0.03888 + 2.315 \times 10^{-5}T \\ \varepsilon_{33}^{00} = 0.06646 + 1.9348 \times 10^{-5}T \end{cases} \tag{22}$$

$$\frac{\partial \sigma_{ij}^{el}}{\partial r_j} = 0 \tag{23}$$

$$C_{ijkl}(\eta) = h(\eta)C_{ijkl}^{\delta} + [1 - h(\eta)]C_{ijkl}^{\alpha} = C_{ijkl}^{\delta} + h(\eta)\Delta C_{ijkl} \tag{24}$$

where $C_{ijkl}(\eta)$ is the elastic constant, a function of the order parameter η, C_{ijkl}^{α} and C_{ijkl}^{δ} are the elastic constants of the matrix and precipitate, respectively, and ΔC_{ijkl} is the difference between the elastic constants of C_{ijkl}^{α} and C_{ijkl}^{δ}.

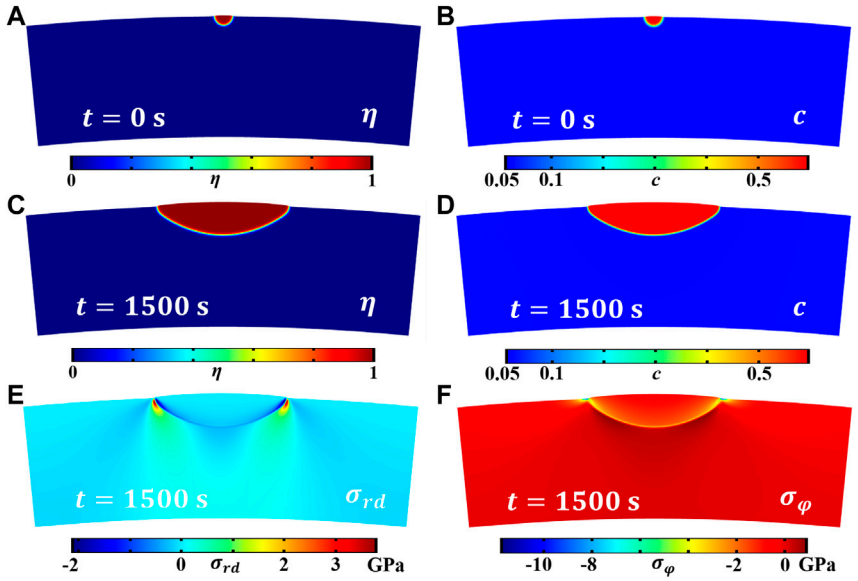

FIGURE 3 | The evolution results of the coupled anisotropic elastic energy zirconium hydride blister, where **(A)** and **(C)** are the morphology evolution results (order parameter field) of the hydride blister growth at t = 0 s and t = 1,500 s, **(B)**, and **(D)** is the distribution of hydrogen concentration field after t = 0 s and t = 1,500 s, **(E)** and **(F)** are the stress distribution of σ_{rd} (Radial stress) and σ_{φ} (Circumferential stress).

RESULTS AND DISCUSSION

The effect of anisotropic elastic energy on the growth morphology of hydride blisters is explored, as shown in **Figures 3A,C**, which are the evolution results of hydride blisters after initial state t = 0 s and final state t = 1500 s, respectively. Due to the effect of elastic energy, the corrosion width of hydride blister is greater than the corrosion depth, the growth characteristics of anisotropy appear, and the morphology is semi ellipsoid. In addition, there is a slight bulge at the top of the blister. The growth of the hydride blister is closely related to the intrinsic strain, and to minimize the elastic properties, different growth rates will appear in different directions. **Figures 3B,D** show that the concentration in the hydride blister is relatively high, and there is a diffusion area at the interface between the matrix and the hydride blister. **Figures 3E,F** are the stress distribution results in the radial and circumferential directions of the coupled anisotropic elastic energy, respectively. The hydride blisters in both directions are in a compressed state, and there are stress concentration area near the phase interface and the tips on both sides. The stress concentration will redirect the δ-hydrides around the hydride blisters, form more harmful radial hydride clusters, and even cause the initiation and propagation of microcracks.

Zirconium alloy cladding tube will be subjected to a certain radial outward stress during operation, which will have a great impact on the formation and growth of hydride. We applied stress of 1, 2, and 3 GPa along the radial direction in this model. Because this model is established under the ideal condition of no defects, the applied stress is much greater than that of the actual cladding tube. We can qualitatively study the effect of radial stress on the growth morphology of hydride blisters. The evolution results after t = 1,500 s are shown in **Figure 4**. **Figures 4A–C** shows that the width and depth of hydride blister increase with the increase of stress under the application of different radial stress. **Figure 4D** shows the contour comparison diagram of hydride blister under t = 1,500 s applied stress and no applied stress. The results in **Figure 4** confirm that applying radial stress will change the morphology and dynamic evolution of blisters, promote the growth of blisters and enhance the process of pitting corrosion.

Figure 5A shows the change of corrosion depth of the hydride blister with time. It can be seen intuitively that the growth of hydrogenated blister is affected by different radial stresses, and the corrosion depth of hydride blister will increase with the increase of time and radial outward stress. **Figure 5B** shows the changes of the area of hydride blister and the average corrosion rate along the pitting depth under different radial stresses. It can be found that the greater the applied radial stress is, the more the corrosion area will be increased, which also shows that the radial stress will increase the influence of pitting corrosion. The corrosion rate changed from fast to slow, which may be due to the continuous consumption of hydrogen in the surrounding environment during the evolution process. The reduction of hydrogen content has become one of the key factors restricting its growth. After the stress is applied, the initial growth speed becomes larger, and the larger the value is, the more obvious the speed increase is, and then it will tend to be consistent. The matrix has a compressive effect on the expansion and growth of hydride blisters. The expansion state of the hydride blister in the simulation area is realized by the bending of the grid (Sheng et al., 2022). After the external stress is applied, the external stress will affect the overall stress state of the blister, and then affect its growth morphology. The growth of hydride bubbles is controlled by these three effects. **Figure 5C,D** show the distribution of displacement u_x, u_y and η along the red arrow line after applying different radial stresses at t = 1,500 s. On

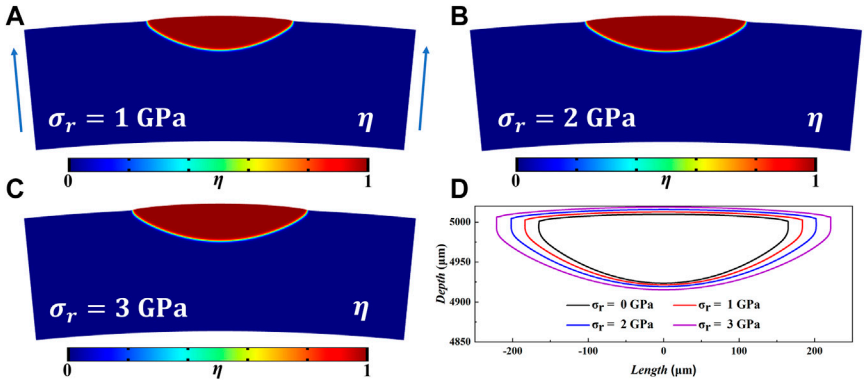

FIGURE 4 | At t = 1,500 s, **(A–C)** are the growth morphologies of hydride blisters under 1, 2, 3 GPa radial stress, respectively (The direction of stress application is indicated by blue arrows). **(D)** is the contours of hydride blisters.

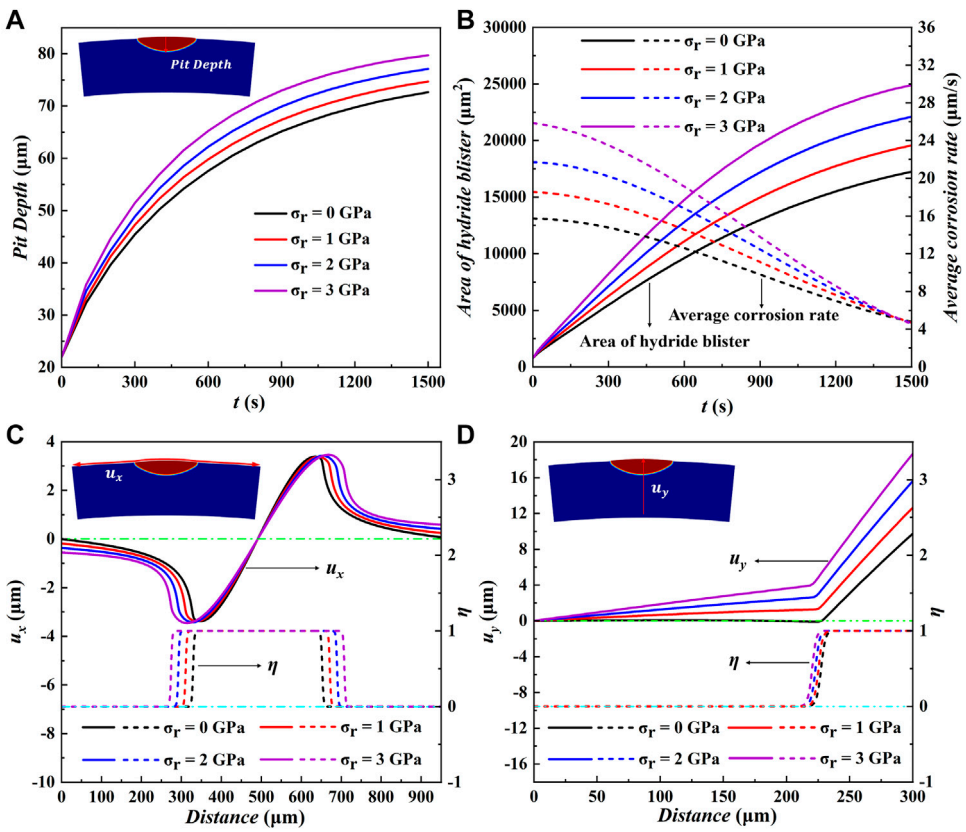

FIGURE 5 | (A) The corrosion pit depth, **(B)** the average corrosion rate and the area of hydride blister as a function of time under different radial stresses. Variation of **(C)** displacement component u_x (solid line) and order parameter η (dotted line), **(D)** displacement component u_y (solid line) and order parameter η (dotted line) along the red arrow in the diagram under different radial stresses at t = 1,500 s (The displacement of the green dotted line and the order parameter of the light blue dotted line are zero).

both sides of the hydride blister, u_x has the same size and changes in the opposite direction. The application of stress will change the initial distribution of displacement, but will not affect its change trend. Combined with the change of order parameters, it can be found that the displacement changes rapidly at the matrix-blister interface and reaches the maximum at the tip of the blister. The application of stress will promote the movement of the interface, thus changing the change of displacement at the same grid point,

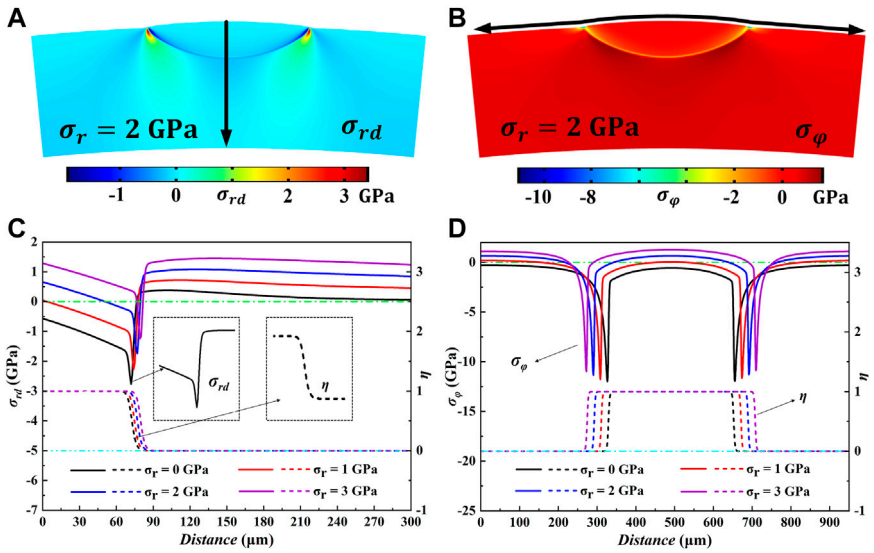

FIGURE 6 | The distribution of **(A)** σ_{rd} **(**Radial stress**)** and **(B)** σ_φ (Circumferential stress) under 2 GPa radial stress at t = 1,500 s. Variation of **(C)** σ_{rd} and η, **(D)** σ_φ and η along the black arrow in the figure under different radial stresses at t = 1,500 s.

showing a larger expansion trend on both sides. In the depth direction of the hydride blister, when no stress is applied, as shown in the black line in the figure, the displacement u_y first starts from zero (Due to the displacement of the lower surface u_y is constrained) and then the value starts to increase near the phase interface, which means that this part of the matrix point moves along the z-axis and reaches a maximum at the upper free surface. The protrusion of hydride blister can also be realized by this part. This part can realize the bulge of hydride blister, which is the reason for the bulge in **Figure 3**. When the radial stress is applied, the stress distribution of the hydride blister and the matrix changes, and the displacement will change from the fixed bottom along the direction of the red arrow. The positive displacement changes after the stress are applied. A general trend is a form of "check", and the inflection points appear at the interface.

As mentioned above, applying different of radial outward stress to the whole simulation area will have a great impact on the growth of the hydride blister. **Figure 6A** and **Figure 6B** are t = 1,500 s respectively, under the application of 2 GPa radial stress σ_{rd} and σ_φ stress distribution. **Figure 6C** and **Figure 6D** are t = 1,500 s respectively under different stress conditions σ_{rd}, σ_φ and η with the change of the black arrow in the diagram. Combined with the evolution process of order parameters, it can be found that when hydride blisters grow normally, the matrix bears compressive stress. The stress value changes rapidly at the interface and reaches the maximum, and there is a stress concentration area around the blister. The radial stress σ_{rd} reverses at the interface, and part of the matrix bears tensile stress. The tensile effect caused by tensile stress is very weak, which can not prevent the expansion and compression of hydride. The circumferential stress σ_φ has a large stress concentration at the tip of the blister, which may lead to the cracking of the blister. It can be found from the change of the displacement u_y in **Figure 5D**. When we apply stress and change the initial stress distribution, the overall stress of blister and matrix will change from compression to tension. No matter how the applied force changes, there will be stress concentration areas at the tip and interface of the hydride blister. The side of the upper surface of the blister close to the oxide layer will bear outward and upward stresses, accelerating the cracking of the upper surface. The growth process of zirconium hydride blisters is the result of the combined effect of chemical energy driving force and elastic energy driving force (Simon et al., 2021). The applied stress affects the growth of hydride blisters by affecting the elastic driving force, and the radial stress reduces the effect of the elastic driving force hindering the growth of hydrides. This leads to the difference in the morphology of hydride blisters under different stress states.

CONCLUSION

In this work, the anisotropic elastic properties are introduced into Zr-Hydride blister system, and the growth and evolution dynamics of zirconium hydride blister are studied by using phase-field model. The simulation results show that the natural growth morphology of hydride blister tends to be semi-ellipsoidal and in a compressed state, while the matrix near the interface is in a tensile state. There is a stress concentration area on the outer contour of the blister, and the maximum value appears at the end points on both sides of the hydride. The external stress affects the growth morphology of zirconium hydride blister by affecting the elastic stress

distribution. Applying radial outward stress will promote the growth of blister, and its corrosion width and depth will increase. The greater the applied stress, the more obvious the promotion effect and the faster the growth rate. This model also has certain application value in other fields of pitting corrosion.

DATA AVAILABILITY STATEMENT

The original contributions presented in the study are included in the article/Supplementary Material, further inquiries can be directed to the corresponding authors.

AUTHOR CONTRIBUTIONS

HH and YL conceived and guided the work. SW conducted simulation and data integration. The results were analyzed and discussed by all authors. JS gave guidance in the theoretical part. SW, JS, HH and YL jointly wrote the manuscript, with contributions from all the authors.

FUNDING

This work was supported by the Science Challenge Project (Grant No. TZZT2019-D1-03) and the Foundation of LCP.

ACKNOWLEDGMENTS

Authors would like to thank Changqing Guo, Yuechao Wang and Guomin Han for their help on the model and basic knowledge in this work.

REFERENCES

Allen, S. M., and Cahn, J. W. (1979). A Microscopic Theory for Antiphase Boundary Motion and its Application to Antiphase Domain Coarsening. *Acta Metall.* 27 (6), 1085–1095. doi:10.1016/0001-6160(79)90196-2

Bair, J., and Zaeem, M. A. (2017). Effects of Applied Strain on Formation, Shape Evolution, and Reorientation of Multiphase Zirconium Hydrides: A Multiphase Field Modeling Study. *arXiv e-prints*. 2017. doi:10.1016/j.commatsci.2021.110367

Bair, J., Zaeem, M. A., and Tonks, M. (2016). A Phase-Field Model to Study the Effects of Temperature Change on Shape Evolution Ofγ-Hydrides in Zirconium. *J. Phys. D Appl. Phys.* 49 (40). 405302. doi:10.1088/0022-3727/49/40/405302

Bair, J., Asle Zaeem, M., and Schwen, D. (2017). Formation Path of δ Hydrides in Zirconium by Multiphase Field Modeling. *Acta Mater.* 123, 235–244. doi:10.1016/j.actamat.2016.10.056

Bair, J., Asle Zaeem, M., and Tonks, M. (2015). A Review on Hydride Precipitation in Zirconium Alloys. *J. Nucl. Mater.* 466, 12–20. doi:10.1016/j.jnucmat.2015.07.014

Cheong, Y. M., Gong, U. S., and Chooea, K. N. (2001). Formation and Growth of Hydride Blisters in Zr-2.5Nb Pressure Tubes. *Nucl. Eng. Technol.* 33 (2), 192–200.

Domizzi, G., Enrique, R. A., Ovejero-García, J., and Buscaglia, G. C. (1996). Blister Growth in Zirconium Alloys: Experimentation and Modeling. *J. Nucl. Mater.* 229, 36–47. doi:10.1016/0022-3115(95)00204-9

Gao, R., Shi, X., Wang, J., and Huang, H. (2022). Understanding Electrocaloric Cooling of Ferroelectrics Guided by Phase-field Modeling. *Journal of the American Ceramic Society.* 105 (6). 3689–3714. doi:10.1111/jace.18370

Gao, R., Shi, X., Wang, J., Zhang, G., and Huang, H. (2021). Designed Giant Room-Temperature Electrocaloric Effects in Metal-Free Organic Perovskite $[MDABCO](NH_4)I_3$ by Phase-Field Simulations. *Adv. Funct. Mat.* 31 (38), 2104393. doi:10.1002/adfm.202104393

Ghosal, S. K., Palit, G. C., and De, P. K. (2002). Corrosion of Zirconium Alloys in Nuclear Applications – A Review. *Mineral Process. Extr. Metallurgy Rev.* 22 (4-6), 519–546. doi:10.1080/08827500208547428

Han, G. M., Zhao, Y. F., Zhou, C. B., Lin, D.-Y., Zhu, X. Y., Zhang, J., et al. (2019). Phase-Field Modeling of Stacking Structure Formation and Transition of δ-hydride Precipitates in Zirconium. *Acta Mater.* 165, 528–546. doi:10.1016/j.actamat.2018.12.009

Hellouin de Menibus, A., Auzoux, Q., Dieye, O., Berger, P., Bosonnet, S., Foy, E., et al. (2014). Formation and Characterization of Hydride Blisters in Zircaloy-4 Cladding Tubes. *J. Nucl. Mater.* 449 (1-3), 132–147. doi:10.1016/j.jnucmat.2014.03.006

Hong, S. I., Lee, K. W., and Kim, K. T. (2002). Effect of the Circumferential Hydrides on the Deformation and Fracture of Zircaloy Cladding Tubes. *J. Nucl. Mater.* 303 (2-3), 169–176. doi:10.1016/s0022-3115(02)00814-0

Kammenzind, B. F., Berquist, B. M., Bajaj, R., Kreyns, P. H., and Franklin, D. G., R. B. (2000). The Long-Range Migration of Hydrogen through Zircaloy in Response to Tensile and Compressive Stress Gradients. *Zirconium Nucl. Industry Twelfth Int. Symposium*, 196–233. doi:10.1520/stp14301s

Kim, H.-J., Han, J.-H., Kaiser, R., Oh, K. H., and Vlassak, J. J. (2008). High-throughput Analysis of Thin-Film Stresses Using Arrays of Micromachined Cantilever Beams. *Rev. Sci. Instrum.* 79 (4), 045112. doi:10.1063/1.2912826

Kim, S.-D., Kim, J.-S., and Yoon, J. (2018). Phase Analysis of Hydride Blister in Zirconium Alloy. *J. Alloys Compd.* 735, 2007–2011. doi:10.1016/j.jallcom.2017.11.359

Kim, S. G., Kim, W. T., and Suzuki, T. (1999). Phase-field Model for Binary Alloys. *Phys. Rev. E* 60 (6), 7186–7197. doi:10.1103/physreve.60.7186

Kim, Y. S., Ahn, S. B., and Cheong, Y. M. (2007). Precipitation of Crack Tip Hydrides in Zirconium Alloys. *J. Alloys Compd.* 429 (1-2), 221–226. doi:10.1016/j.jallcom.2006.09.034

Krishnan, R., and Asundi, M. K. (1981). Zirconium Alloys in Nuclear Technology. *Proc. Indian Acad. Sci. Engg. Sci.)* 4 (1), 41–56. doi:10.1007/bf02843474

Lin, J.-l., Han, X., Heuser, B. J., and Almer, J. D. (2016). Study of the Mechanical Behavior of the Hydride Blister/rim Structure in Zircaloy-4 Using *In-Situ* Synchrotron X-Ray Diffraction. *J. Nucl. Mater.* 471, 299–307. doi:10.1016/j.jnucmat.2015.12.048

Liu, D., Wang, J., Jafri, H. M., Wang, X., Shi, X., Liang, D., et al. (2022). Phase-field Simulations of Vortex Chirality Manipulation in Ferroelectric Thin Films. *npj Quantum Materials* 7, 1–8. doi:10.1038/s41535-022-00444-8

Long, F., Kerr, D., Domizzi, G., Wang, Q., and Daymond, M. R. (2017). Microstructure Characterization of a Hydride Blister in Zircaloy-4 by EBSD and TEM. *Acta Mater.* 129, 450–461. doi:10.1016/j.actamat.2017.03.016

McRae, G. A., Coleman, C. E., and Leitch, B. W. (2010). The First Step for Delayed Hydride Cracking in Zirconium Alloys. *J. Nucl. Mater.* 396 (1), 130–143. doi:10.1016/j.jnucmat.2009.08.019

Motta, A. T., Capolungo, L., Chen, L.-Q., Cinbiz, M. N., Daymond, M. R., Koss, D. A., et al. (2019). Hydrogen in Zirconium Alloys: A Review. *J. Nucl. Mater.* 518, 440–460. doi:10.1016/j.jnucmat.2019.02.042

Motta, A. T., and Chen, L.-Q. (2012). Hydride Formation in Zirconium Alloys. *Jom* 64 (12), 1403–1408. doi:10.1007/s11837-012-0479-x

Motta, A. T., Couet, A., and Comstock, R. J. (2015). Corrosion of Zirconium Alloys Used for Nuclear Fuel Cladding. *Annu. Rev. Mat. Res.* 45 (1), 311–343. doi:10.1146/annurev-matsci-070214-020951

Puls, M. P. (2009). Review of the Thermodynamic Basis for Models of Delayed Hydride Cracking Rate in Zirconium Alloys. *J. Nucl. Mater.* 393 (2), 350–367. doi:10.1016/j.jnucmat.2009.06.022

Reheman, W., and Ståhle, P. (2018). Self-inflicted Fracture of Expanding Surface Precipitates. *Fatigue Fract. Eng. Mater Struct.* 41 (12), 2614–2628. doi:10.1111/ffe.12872

Rozhnov, A. B., Belov, V. A., Nikulin, S. A., and Khanzhin, V. G. (2011). Stress Corrosion Cracking of Zirconium Cladding Tubes: I. Proximate Local SCC Testing Method. *Russ. Metall.* 2010 (10), 979–983. doi:10.1134/s0036029510100186

Santisteban, J. R. S. A., and Domizzi, G. (2009). Determination of Residual Stresses Around Blisters in Zr-2.5% Nb Pressure Tubes. *Powder Diffr.* 24 (S1), S72–S76. doi:10.1154/1.3139056

Sheng, J., Wang, Y. C., Liu, Y., Wu, S., Xu, K., Chen, Z. H., et al. (2022). A Phase-Field Model for Simulating Hydrogen-Induced Pitting Corrosion with Solid-Solid Phase Transformation in the Metal. doi:10.48550/arXiv.2203.07289

Shi, X., Wang, J., Cheng, X., and Huang, H. (2021). Ultrafast Ferroelectric Domain Switching Induced by Nano-Second Strain-Pulse, *Advanced Theory and Simulations.* 5 (3). 2100345. doi:10.1002/adts.202100345

Shi, X., Wang, J., Cheng, X., and Huang, H. (2022). Phase Diagram of Sub-GHz Electric-Field-Induced Polarization Oscillation. *Phys. Rapid Res. Ltrs* 16, 2100416. doi:10.1002/pssr.202100416

Simon, P. C. A., Aagesen, L. K., Jokisaari, A. M., Chen, L-Q., Daymond, M. R., Motta, A. T., et al. (2021). Investigation of δ Zirconium Hydride Morphology in a Single Crystal Using Quantitative Phase Field Simulations Supported by Experiments. *J. Nucl. Mater.* 557. 153303. doi:10.1016/j.jnucmat.2021.153303

Singh, R. N., Kishore, R., and Sinha, T. K.. ea. (2002). Hydride Blister Formation in Zr–2.5wt%Nb Pressure Tube Alloy. *J. Nucl. Mater.* 301 (2-3), 153–164. doi:10.1016/s0022-3115(02)00708-0

Singh, R. N., Ståhle, P., Massih, A. R., and Shmakov, A. A. (2007). Temperature Dependence of Misfit Strains of δ-hydrides of Zirconium. *J. Alloys Compd.* 436 (1-2), 150–154. doi:10.1016/j.jallcom.2006.07.049

Toghraee, A., Bair, J., and Asle Zaeem, M. (2021). Effects of Applied Load on Formation and Reorientation of Zirconium Hydrides: A Multiphase Field Modeling Study. *Comput. Mater. Sci.* 192. 110367. doi:10.1016/j.commatsci.2021.110367

Tummala, H., Capolungo, L., and Tomé, C. N. (2018). Quantifying the Stress State in the Vicinity of a δ-hydride in α-zirconium. *J. Nucl. Mater.* 511, 406–416. doi:10.1016/j.jnucmat.2018.08.050

Une, K., Ishimoto, S., Etoh, Y., Ito, K., Ogata, K., Baba, T., et al. (2009). The Terminal Solid Solubility of Hydrogen in Irradiated Zircaloy-2 and Microscopic Modeling of Hydride Behavior. *J. Nucl. Mater.* 389 (1), 127–136. doi:10.1016/j.jnucmat.2009.01.017

Vicente Alvarez, M. A., Santisteban, J. R., Domizzi, G., and Almer, J. (2011). Phase and Texture Analysis of a Hydride Blister in a Zr–2.5%Nb Tube by Synchrotron X-Ray Diffraction. *Acta Mater.* 59 (5), 2210–2220. doi:10.1016/j.actamat.2010.12.024

Xu, S., Shi, X., Pan, H., Gao, R., Wang, J., Lin, Y., et al. (2022). Strain Engineering of Energy Storage Performance in Relaxor Ferroelectric Thin Film Capacitors. *Advcd Theory Sims*, 2100324. doi:10.1002/adts.202100324

Yang, C., Wang, X., Wang, J., and Huang, H. (2020). Multiphase-field Approach with Parabolic Approximation Scheme. *Comput. Mater. Sci.* 172. 109322, doi:10.1016/j.commatsci.2019.109322

Yang, C., Liu, Y., Huang, H., Wu, S., Sheng, J., Shi, X., et al. (2021). Hydride Corrosion Kinetics on Metallic Surface: a Multiphase-Field Modeling. *Mat. Res. Express* 8 (10), 106518. doi:10.1088/2053-1591/ac1c32

Yu, Q., Reyes, M., Shah, N., and Marian, J. (2020). Kinetic Model of Incipient Hydride Formation in Zr Clad under Dynamic Oxide Growth Conditions. *Mater. (Basel)* 13 (5). 1088. doi:10.3390/ma13051088

Conflict of Interest: The authors declare that the research was conducted in the absence of any commercial or financial relationships that could be construed as a potential conflict of interest.

Publisher's Note: All claims expressed in this article are solely those of the authors and do not necessarily represent those of their affiliated organizations, or those of the publisher, the editors, and the reviewers. Any product that may be evaluated in this article, or claim that may be made by its manufacturer, is not guaranteed or endorsed by the publisher.

frontiers | Frontiers in Materials

ORIGINAL RESEARCH
published: 13 June 2022
doi: 10.3389/fmats.2022.924294

High-Throughput Screening of Optimal Process Parameters for PVD TiN Coatings With Best Properties Through a Combination of 3-D Quantitative Phase-Field Simulation and Hierarchical Multi-Objective Optimization Strategy

Rao Dai[1], *Shenglan Yang*[1], *Tongdi Zhang*[1], *Jing Zhong*[1]*, *Li Chen*[1], *Chunming Deng*[2] *and Lijun Zhang*[1]*

[1]State Key Laboratory of Powder Metallurgy, Powder Metallurgy Research Institute, Central South University, Changsha, China, [2]National Engineering Laboratory for Modern Materials Surface Engineering Technology, The Key Lab of Guangdong for Modern Surface Engineering Technology, Institute of New Materials, Guangdong Academy of Sciences, Guangzhou, China

Physical vapor deposition (PVD) is one of the most important techniques for coating fabrication. With the traditional trial-and-error approach, it is labor-intensive and challenging to determine the optimal process parameters for PVD coatings with best properties. A combination of three-dimensional (3-D) quantitative phase–field simulation and a hierarchical multi-objective optimization strategy was, therefore, developed to perform high-throughput screening of the optimal process parameters for PVD coatings and successfully applied to technically important TiN coatings. Large amounts of 3-D phase-field simulations of TiN coating growth during the PVD process were first carried out to acquire the parametric relation among the model parameters, microstructures, and various coating properties. Experimental data were then used to validate the numerical simulation results and reveal the correlation between model parameters and process parameters. After that, a hierarchical multi-objective method was proposed for the design of multiple coating properties based on the quantitative phase–field simulations and key experimental data. Marginal utility was subsequently examined based on the identification of the Pareto fronts in terms of various combinations of objectives. The windows for the best TiN coating properties were, therefore, filtered with respect to the model/process parameters in a hierarchical manner. Finally, the consistent optimal design result was found against the experimental results.

Keywords: physical vapor deposition, TiN coating, phase-field simulation, microstructure, multi-objective optimization

OPEN ACCESS

Edited by:
Yu-Hong Zhao,
North University of China, China

Reviewed by:
Zhonghui Shen,
Wuhan University of Technology, China
Houbing Huang,
Beijing Institute of Technology, China

***Correspondence:**
Jing Zhong
zhongjingjogy@csu.edu.cn
Lijun Zhang
lijun.zhang@csu.edu.cn

Specialty section:
This article was submitted to Computational Materials Science, a section of the journal Frontiers in Materials

Received: *20 April 2022*
Accepted: *06 May 2022*
Published: *13 June 2022*

Citation:
Dai R, Yang S, Zhang T, Zhong J, Chen L, Deng C and Zhang L (2022) High-Throughput Screening of Optimal Process Parameters for PVD TiN Coatings With Best Properties Through a Combination of 3-D Quantitative Phase-Field Simulation and Hierarchical Multi-Objective Optimization Strategy. Front. Mater. 9:924294. doi: 10.3389/fmats.2022.924294

1 INTRODUCTION

Due to its low process temperature and environmental friendliness, the physical vapor deposition (PVD) technique has been widely used to fabricate various industrial coatings in terms of controllable composition and structure, promising compressive strength, and desired surface performance (Deng et al., 2020). For the past decades, different PVD techniques have been developed, such as the cathodic arc evaporation (CAE) (Zhou et al., 2019) or arc ion plating (AIP) (Zhang et al., 2018), direct current magnetron sputtering (DCMS) (Barshilia et al., 2004), and high-power impulse magnetron sputtering (HiPIMS) (Alami et al., 2014; Kuo et al., 2019) and even their hybrid techniques (Bobzin et al., 2019). For the PVD coatings, the concerned properties in the industry include hardness, corrosion resistance, wear resistance, and adhesion strength. Until now, substantial experimental investigations have been conducted to improve the PVD coating properties, majorly focusing on the modification of process parameters, that is, target power (Tai et al., 1990; Bhaduri et al., 2010), N_2 partial pressure (Lousa et al., 2007; Mayrhofer et al., 2009), bias voltage (Hernández et al., 2011; Ma et al., 2017), magnetic field strength (Mayrhofer et al., 2002; Wu et al., 2017), substrate temperature (Mayrhofer et al., 2009), etc. However, the process parameters are not directly related to the properties of PVD coatings, and it is, thus, very challenging to determine the optimal process parameters for PVD coatings with best properties through the traditional time-/labor-consuming trial-and-error approach.

In fact, the microstructure forming during the preparation process directly determines the properties of PVD coatings. Hence, the quantitative description of the microstructure evolution during preparation can help establish the quantitative relation "process-microstructure" of PVD coatings. Nowadays, the phase-field method has become a powerful approach for quantitative simulation of microstructure evolution in PVD coatings. Starting from the continuum model by Lichter and Chen (Lichter and Chen 1986), Keblinski et al. (Keblinski et al., 1996) developed a phase–field model for the growth of interfaces and applied the model to simulate solid-film growth during PVD with different incident vapor fluxes. Coupling the interface growth phase–field model by Keblinski et al. (Keblinski et al., 1996) with the phase–field model for solidification of polycrystalline materials by Warren et al. (Warren et al., 2003), Stewart and Spearot (Stewart and Spearot 2016; Stewart and Spearot 2017) further developed a phase–field model for the evolution of single-phase polycrystalline thin films and utilized the model to investigate the influence of model parameters on grain size and porosity and grain orientation. Very recently, Yang et al. (Yang et al., 2019) conducted a parametric study on the PVD process of metal thin films based on the phase–field model by Keblinski et al. (Keblinski et al., 1996). Based on more than 200 three-dimensional (3-D) phase–field simulations, the quantitative relation between the deposition rate and model parameters was established, and the effect of the deposition rate on the surface roughness and microstructure of the PVD metal thin film was investigated. However, the correlation between processing parameters and model parameters and deposition rate, which was essential for establishing a quantitative relation "process-microstructure" of PVD coatings, was not completely examined by Yang et al. (Yang et al., 2019).

In addition to the quantitative relation "process-microstructure" from the quantitative phase–field simulations, the qualitative or quantitative relation "microstructure-properties" is also needed to determine the optimal process parameters for PVD coatings with best properties. That is, the properties of PVD coatings are dominantly determined by the microstructures, for example, porosity, surface roughness, and average grain size. For many industrial applications, the coatings, that are nonporous and with finer grain and smoother surface, are usually desirable. Despite the properties, the coating production efficiency is yet another major concern. A higher deposition rate may generally increase the production efficiency but probably result in porosity and a surface of severe roughness. Consequently, decision-making toward the design of processing parameters and coating properties is a complex multi-objective optimization problem, and a hierarchical multi-objective decision-making strategy is, thus, on demand.

Consequently, the major objectives of the present work are as follows: 1) to pave the way for a parametric relation between the process parameters and coating properties by utilizing a large number of phase–field simulations of PVD coatings together with limited experimental results available in the literature; 2) to develop a multi-objective decision-making strategy suitable for PVD coatings, considering metrics including both the deposition rate for production efficiency and essential microstructure properties (i.e., grain size, porosity, and surface roughness) for coating properties/performance; 3) to design the optimal process parameters for PVD coatings with best comprehensive properties by combining the 3D quantitative phase–field simulations and a hierarchical multi-objective optimization approach and compare with the experimental results. Here, the PVD TiN coatings of technical importance were chosen as the target of the present work because Wang et al. (Wang et al., 2015) performed an intensive experimental investigation on the effect of bias voltage on the microstructures and properties of PVD TiN coatings, which can serve as the experimental validation of the present phase–field simulation and coating design strategy.

2 METHODOLOGY

2.1 Phase-Field Model for the Physical Vapor Deposition Process

The phase–field model for the growth of interfaces proposed by Keblinski et al. (Keblinski et al., 1996) allows for a description of the dynamics of depositing vapor and nonlinear morphology of a growing solid film during PVD. This model can capture crucial physical processes during PVD such as 1) arbitrary surface morphology formation, 2) surface tension and vapor diffusion, and 3) non-local shadowing effects. To model PVD processing within the phase-field framework, two field variables are introduced: $\phi(\boldsymbol{r}, t)$ and $g(\boldsymbol{r}, t)$. The field variable $\phi(\boldsymbol{r}, t)$ describes the evolution of a growing thin film solid, where $\phi(\boldsymbol{r},$

$t) \approx 1$ defines a solid region, $\phi(\boldsymbol{r}, t) \approx -1$ defines a vacuum region, and $\phi(\boldsymbol{r}, t) \approx 0$ defines the solid–vapor interface. The field variable $g(\boldsymbol{r}, t)$ describes the local density of the incident vapor; therefore, $g(\boldsymbol{r}, t)$ is always larger than or equal to 0 (i.e., $g(\boldsymbol{r}, t) \geq 0$), where $g(\boldsymbol{r}, t) \approx 0$ describes a region of no vapor. Considering that the field variable $g(\boldsymbol{r}, t)$ does not contribute to the free energy of the system, the free energy functional is constructed based on the field variable $\phi(\boldsymbol{r}, t)$ and its gradient,

$$F = \int_{\Omega} \left\{ -\frac{1}{2}\phi(\boldsymbol{r},t)^2 + \frac{1}{4}\phi(\boldsymbol{r},t)^4 + \alpha\left(\nabla\phi(\boldsymbol{r},t)\right)^2 \right\}, \quad (1)$$

The first two terms in **Eq. 1** provide a double-well energy barrier between the bulk solid and vapor phases. The third term accounts for energy contribution according to the presence of the solid–vapor interface, where α is the interfacial gradient coefficient.

Given the vapor dynamics and shadowing effects, the evolution equations of the solid phase field, that is, $\phi(\boldsymbol{r}, t)$, and vapor phase field, that is, $g(\boldsymbol{r}, t)$, can be determined to incorporate the underlying physics of PVD. The interface growth mechanism for PVD processing is based on the assumption that the growth of the solid phase, that is, $\phi(\boldsymbol{r}, t)$ occurs at the expense of the incoming vapor phase, that is, $g(\boldsymbol{r}, t)$, as mathematically expressed in the following equations,

$$\dot{\phi} = \nabla^2\frac{\delta F}{\delta \phi} + B\left(\nabla\phi\right)^2 g + C\sqrt{\left(\nabla\phi\right)^2 g}\eta, \quad (2)$$

$$\dot{g} = \nabla\left[D\nabla g - \boldsymbol{A}g\right] - B\left(\nabla\phi\right)^2 g, \quad (3)$$

Eq. 2 describes the evolution of the growing thin film solid. In **Eq. 2**, the first term is the Cahn–Hilliard dynamics expression, which allows for arbitrary surface formation and surface diffusion effects. The second term serves as a source term that couples **Eq. 2** with **Eq. 3** and captures aspects relevant to the growth of the solid phase at the expense of the incident vapor phase. The last term provides surface fluctuations through a Gaussian noise distribution, $\eta(\boldsymbol{r}, t)$. **Eq. 3** describes the transport of the incident vapor. In **Eq. 3**, the first term is the diffusion equation modified by the presence of an external force, $\boldsymbol{A}$. The second term is the coupling term that is the negative of the second term in **Eq. 2** and acts as a sink for the diffusive vapor phase due to its transition into a solid phase. The parameter B controls the rate of conversion from the vapor phase to solid phase, C controls the overall noise strength, D is the diffusion coefficient, and $\boldsymbol{A}$ provides the strength and direction to the incoming vapor flux.

2.2 Material and Numerical Parameters for Phase-Field Simulation

The parametric study was conducted to overcome the drawbacks of using nondimensional parameters in our previous work (Yang et al., 2019). The interfacial gradient coefficient, α (J m^{-1}), allows for the contribution of surface energy from the solid–vapor interface. The parameter B (m^2 s^{-1}) controls the conversion of the g field into the ϕ field in the interfacial region and thus can be quantified as the generated interface area per unit time, named the vapor–solid transition velocity. The noise amplitude coefficient, C (J m^{-1}), provides sufficient noise at the thin film surface to allow the formation of surface variations and features. The parameter D (m^2 s^{-1}) is the diffusion coefficient controlling vapor diffusion in the near-surface region. The parameter $\boldsymbol{A}$ is the incident vapor vector including the incident vapor rate A (m s^{-1}) and angle (i.e., $\boldsymbol{A} = A\boldsymbol{r}$). The direction of the incident vapor in the present simulation is perpendicular to the substrate (i.e., $\boldsymbol{A} = A\,\hat{\boldsymbol{z}}$). The parameters that are constant during the entire simulations in the present work are summarized in **Table 1**, while the parameters that are varied to investigate include the vapor–solid transition velocity B and diffusion coefficient D.

TABLE 1 | List of numerical/material parameters used in the present phase-field simulations.

Parameters	Symbols	Values
Grid spacing	Δx	1.0 nm
Interfacial gradient coefficient	α	0.3 J nm^{-1} Yang et al. (2019)
Incident vapor rate	A	0.136 nm s^{-1}
Noise amplitude	C	2.5 J nm^{-1} Yang et al. (2019)
Gaussian noise factor	η	0.5 Yang et al. (2019)
Supplied incident vapor	g_0	1.0 Yang et al. (2019)

In order to perform the 3D phase-field simulation of the PVD process, an initially flat substrate is constructed in the present work along the entire x-y plane in the z direction, with a thickness less than 1/10 of the grid points of the z axis, where $\phi(\boldsymbol{r}, 0) = 1$ and $g(\boldsymbol{r}, 0) = 0$. The region above the substrate is placed in vacuum, where $\phi(\boldsymbol{r}, 0) = -1$ and $g(\boldsymbol{r}, 0) = g_0$. The equations of motion described in **Eqs (2)**, **(3)** are discretized and solved on a uniform three-dimensional mesh. For these equations, the periodic condition is applied in the direction parallel to the substrate (i.e., x and y axes), while the no-flux and fixed conditions are applied at the lower and upper boundaries of the direction perpendicular to the substrate, respectively (i.e., z axis). During the simulation, the $g = g_0$ condition is maintained at the upper boundary of the z direction providing a constant downward flux Ag during PVD.

3 RESULTS AND DISCUSSIONS

3.1 Parametric Relation Between Model Parameters and Processing Parameters

A series of phase-field simulations are performed to reproduce the growth of TiN coatings during the PVD process and investigate the effect of deposition time and rate on the resulting microstructure. The microstructure evolution of TiN coatings deposited with different deposition rates corresponding to different vapor–solid transition velocities and diffusion coefficients due to 3-D phase-field simulations is shown in **Figure 1**. In the early growth stage, the coatings exhibit featureless topography, which is mainly formed by small islands tending to display a denser structure with a smoother surface. As the deposition time increases, the columnar structure starts to form, and the pores are induced in the growing coatings. The observed growth mechanism of thin films prepared by the

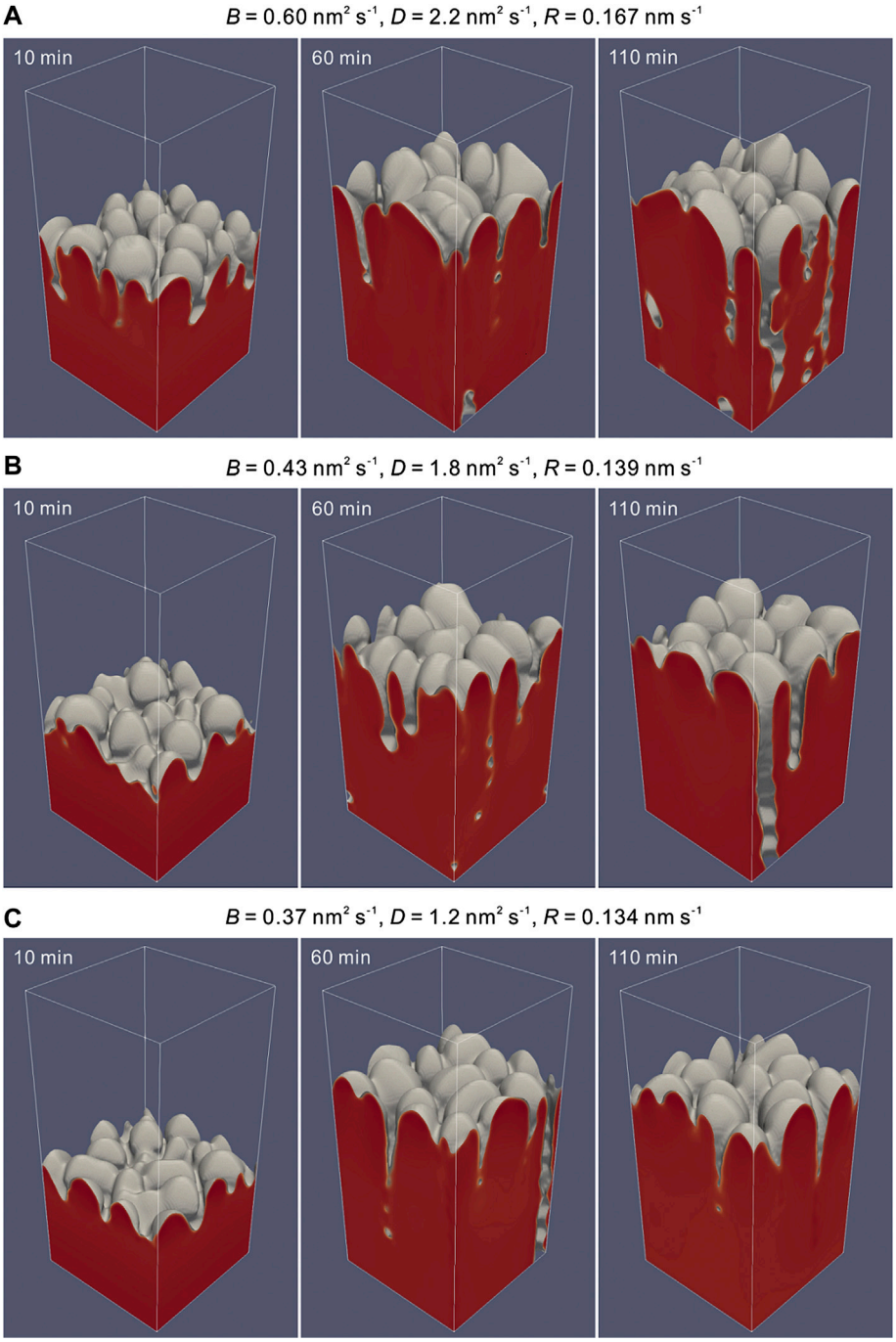

FIGURE 1 | Microstructure evolution of PVD TiN coatings due to 3D phase-field simulations with different deposition rates (i.e., *R*) corresponding to various sets of the vapor–solid transition velocity (i.e., *B*) and diffusion coefficient (i.e., *D*): **(A)** B = 0.60 nm^2 s^{-1}, D = 2.2 nm^2 s^{-1}, R = 0.167 nm s^{-1}. **(B)** B = 0.43 nm^2 s^{-1}, D = 1.8 nm^2 s^{-1}, R = 0.139 nm s^{-1}. **(C)** B = 0.37 nm^2 s^{-1}, D = 1.2 nm^2 s^{-1}, R = 0.134 nm s^{-1}. Simulation domain: 100 × 100 × 200 nm^3.

PVD method coincides with the reported phenomena in the literature (Fu and Shen 2008; Rosa et al., 2012; Aqil et al., 2017). Typical temporal surface morphologies of the corresponding simulated results are also examined as illustrated in **Figure 2** by means of heat maps of the surface height, which are comparable to the atomic force microscopy (AFM) images.

Beyond the microstructure simulation results, related coating properties can also be extracted in **Figure 3** and **Supplementary Figures S1–S3**. Currently, coating properties related to the coating performance and production efficiency are concerned. Here, the deposition rate which directly determines the production efficiency is presented in **Figure 3**, while the

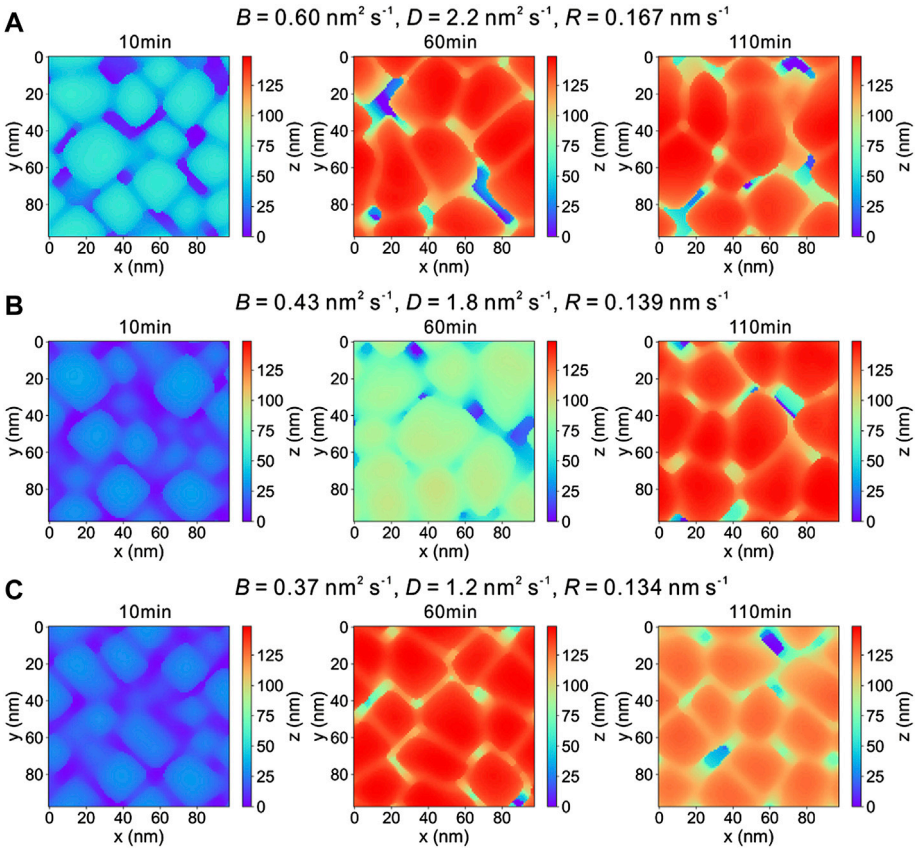

FIGURE 2 | Temporal surface morphologies of TiN coatings with various deposition rates (i.e., *R*) corresponding to different vapor–solid transition velocities (i.e., *B*) and diffusion coefficient (i.e., *D*) during the 3D phase-field simulation for PVD: **(A)** B = 0.60 nm^2 s^{-1}, D = 2.2 nm^2 s^{-1}, R = 0.167 nm s^{-1}. **(B)** B = 0.43 nm^2 s^{-1}, D = 1.8 nm^2 s^{-1}, R = 0.139 nm s^{-1}. **(C)** B = 0.37 nm^2 s^{-1}, D = 1.2 nm^2 s^{-1}, R = 0.134 nm s^{-1}.

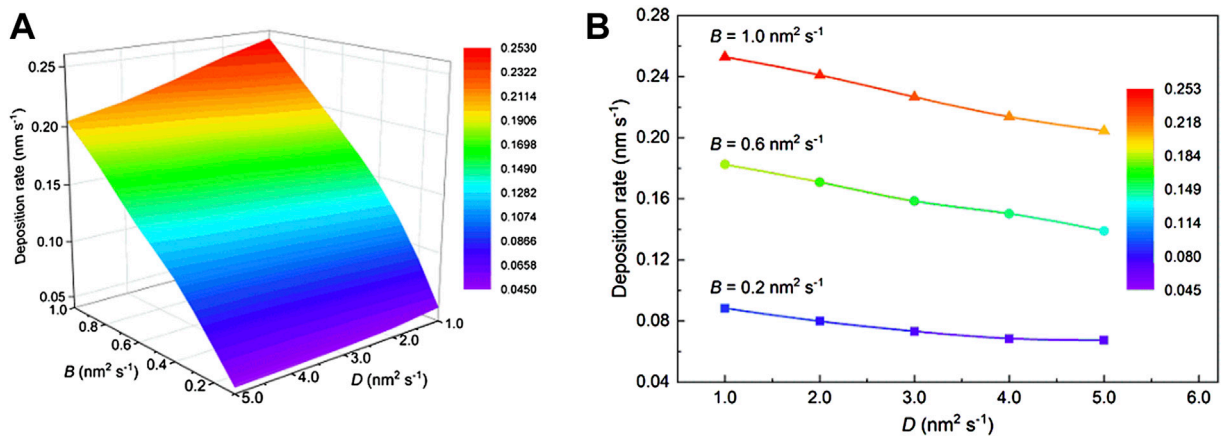

FIGURE 3 | Calculated deposition rate of TiN coatings according to the phase-field simulation results as a function of the vapor–solid transition velocity (i.e., *B*) and diffusion coefficient (i.e., *D*): **(A)** 3D surface graph and **(B)** section profiles at the vapor–solid transition velocity (i.e., *B*) of 0.2, 0.6, and 1.0 nm^2 s^{-1} from the subgraph *A*.

porosity, surface roughness, and average grain size that are related to coating performance are shown in **Supplementary Figures S1–S3**. As shown in **Figure 3B**, a quantitative relation between model parameters and deposition rate can be established, that is, by means of regression or fitting, based on the large amount of phase-field simulation results. Such relations between model

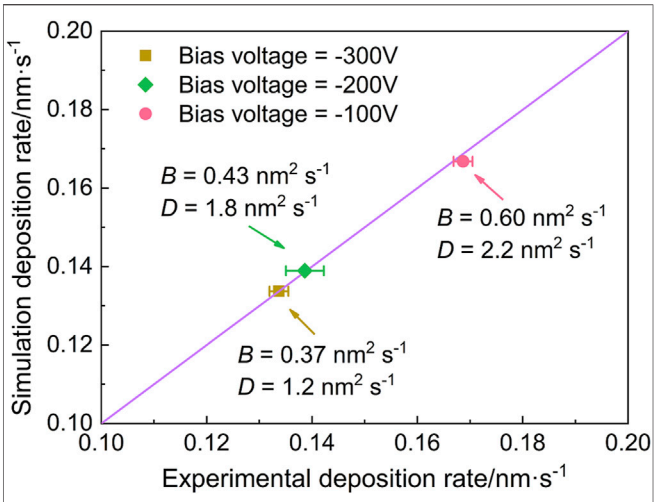

FIGURE 4 | Comparison of the deposition rate of TiN coatings between the phase-field simulation results during PVD growth applying different vapor–solid transition velocities (i.e., *B*) and diffusion coefficients (i.e., *D*) and the experimental data with various bias voltage (Wang et al., 2015).

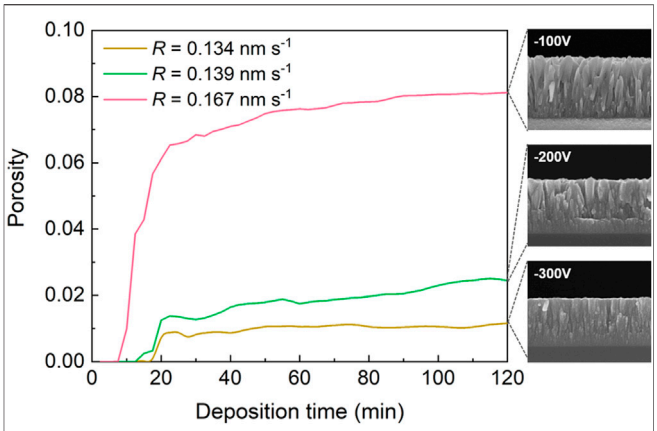

FIGURE 5 | Comparison between the temporal porosity of TiN coatings deposited with different deposition rates (i.e., *R*) according to the phase-field simulation for PVD applying different vapor–solid transition velocities (i.e., *B*) and diffusion coefficient (i.e., *D*) and the experimental cross-section images of TiN coatings for qualitative porosity analysis with various bias voltages (Wang et al., 2015). (The images of experimental results are reproduced and presented with premission from Elsevier).

parameters and coating properties can also be attained as shown in **Supplementary Figures S1–S3** of Supplementary Materials, therefore, serve as the supporting information for decision-making problems about PVD coatings, in case that the parametric relation between the process parameters and model parameters is established.

To achieve the correspondence between the model parameters and process parameters, the experimental observations by Wang et al. (Wang et al., 2015) are carefully correlated with the simulated results considering the physical essence of model parameters according to the practical process parameters of the PVD process, that is, HiPIMS. On the basis of relating the deposition rate of simulation and experiment, together with the comprehensive consideration that other coating properties (i.e., porosity, surface roughness, and average grain size) should be consistent with the trends or data reported by Wang et al. (Wang et al., 2015), the unique relation between the model parameters and process parameters can be established, as shown in **Figure 4**.

Comparison of the deposition rate of TiN coatings between the phase-field simulation results and experimental data is shown in **Figure 4**. The simulated deposition rate is dominated by the vapor–solid transition velocity and diffusion coefficient, while the experimental deposition rate varies with the substrate bias voltage (Wang et al., 2015). When the vapor–solid transition velocity and diffusion coefficient increase, the simulated deposition rate of TiN coatings increases from $0.134\ \mathrm{nm\ s^{-1}}$ to $0.167\ \mathrm{nm\ s^{-1}}$, in quantitative agreement with the experimental deposition rate, which increases as the substrate bias voltage decreases. Due to the high sputtering ionization ratio in HiPIMS, the bias voltage plays an important role in energetic ion bombardment behavior, leading to a significant influence on the vapor–solid transition velocity and diffusion coefficient. With an increase in the substrate bias voltage, the incident ion energy increases and consequently, the deposited material can be re-sputtered by heavy ion bombardment. The vapor–solid transition velocity is supposed to decrease with increasing bias voltage because of the re-sputtering effect. The diffusion coefficient (i.e., *D*) in this case indicates the ion diffusion in plasma, and is given as (Yiğit 2017).

$$D = \frac{2kT}{m\nu}, \tag{4}$$

where k is the Boltzmann constant; T is the plasma temperature; m is the ion mass; and ν is the ion-particle collision frequency. It is observed that the diffusion coefficient for incident ions is governed by the collision frequency of the ion to particle in the plasma atmosphere. Since the energetic ions at a higher bias voltage favor heavy collision with other particles in the plasma, the diffusion coefficient is reduced. When the vapor–solid transition velocity increases, the deposition rate increases as a larger number of incident ions are captured to form a solid coating per unit time. However, the increase of the diffusion coefficient prefers tangential growth to normal growth for coatings during deposition, leading to the decrease of the deposition rate measured by the growth rate in a normal direction. Generally, the deposition rate change with different bias voltages can be explained by the fact that the deposition rate is finally determined by the combined effects of the vapor–solid transition velocity and diffusion coefficient, which are directly affected by the bias voltage. Moreover, the good agreement of the deposition rate between the simulation and experiment first provides a bridge for quantified study.

Figure 5 shows the temporal porosity of PVD TiN coatings deposited with different deposition rates according to the phase-field simulations by applying different vapor–solid transition velocities and diffusion coefficients. There are no specific experimental data on the porosity of TiN coatings prepared by HiPIMS available in the literature, but the cross-sectional scanning electron microscopy (SEM) images of TiN coatings

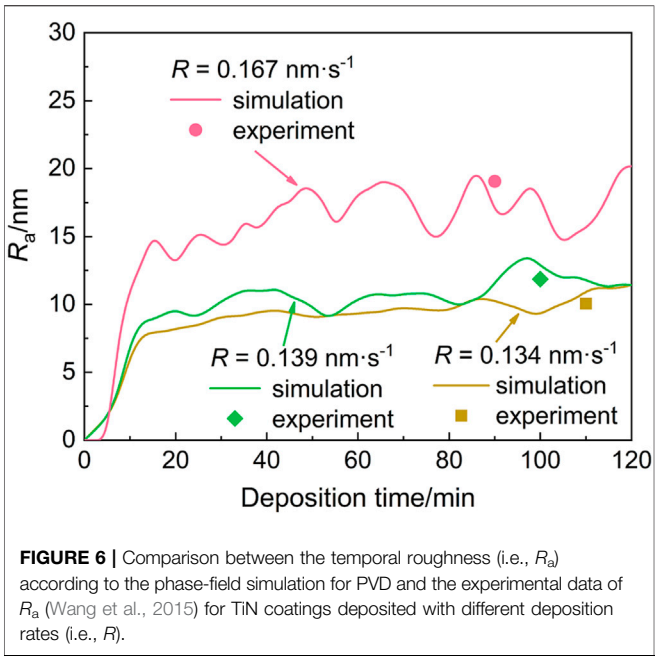

FIGURE 6 | Comparison between the temporal roughness (i.e., R_a) according to the phase-field simulation for PVD and the experimental data of R_a (Wang et al., 2015) for TiN coatings deposited with different deposition rates (i.e., R).

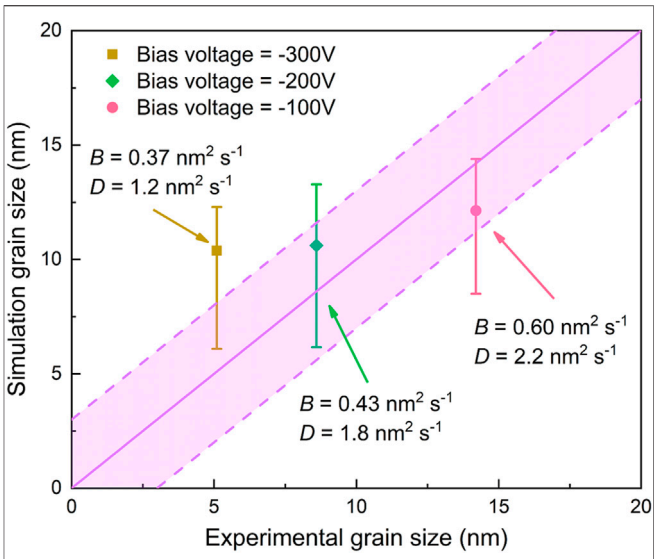

FIGURE 7 | Comparison of the grain size of TiN coatings between the phase-field simulation results during PVD growth applying different vapor-solid transition velocities (i.e., B) and diffusion coefficients (i.e., D) and the experimental data with various bias voltage (Wang et al., 2015).

from the study by Wang et al., (2015) enable a qualitative analysis of porosity or density as a function of the bias voltage. It is observed in **Figure 5** that the simulated porosity of TiN coatings sharply increases within about 20 min and then slightly increases as the deposition continues. Pores appear earlier and tend to increase faster with a higher deposition rate due to a larger vapor–solid transition velocity and diffusion coefficient. At the same deposition time as that of the experiment, the simulated porosity decreases from 8.02 to 1.05%, with the decrease of the deposition rate intrinsically attributed to the decrease of the vapor–solid transition velocity and diffusion coefficient. Experimentally, the TiN coatings exhibit a trend of densification as the bias voltage increases, that is, as the deposition rate decreases. Even if there are no quantitative experimental data for comparison, a consistent evolution of porosity along the deposition rate between the phase-field simulations and the experimental data can be observed. Based on the relationship between bias voltage and the vapor–solid transition velocity and diffusion coefficient mentioned previously, the increase of bias voltage leads to the decrease of the vapor–solid transition velocity and diffusion coefficient. It is understood that a lower vapor–solid transition velocity contributes to the decrease of coating porosity, but a lower diffusion coefficient results in the increase of porosity fraction. Therefore, the coating porosity variation with different bias voltage is intrinsically determined by a combination product of the vapor–solid transition velocity and diffusion coefficient. Furthermore, a consistent evolution of porosity along the deposition rate between the phase-field simulations and the experimental data proves the quantitative phase-field simulation in the present work.

Figure 6 displays the temporal surface roughness of PVD TiN coatings deposited with different deposition rates according to the phase-field simulations, compared with the experimental data, which was evaluated using a scanning probe microscope (SPM) by Wang et al. (Wang et al., 2015). It can be seen in the figure that the simulated surface roughness of TiN coatings increases rapidly at the early deposition stage and then reaches a state where the surface roughness fluctuates within a certain range as the deposition continues. As the deposition rate increases, the surface roughness increases faster at the early deposition stage, and the fluctuation range increases. The simulated surface roughness decreases from 19.41 to 10.98 nm with a decrease in the deposition rate from 0.167 nm s^{-1} to 0.134 nm s^{-1}. With the deposition rate serving as an intermediary, the simulated roughness based on different vapor–solid transition velocities and diffusion coefficients is comparable with the experimental roughness as a function of bias voltage, and a good agreement between the simulation results and experimental data can be found. Based on the analysis mentioned previously, the evolution of surface roughness with bias voltage is related to the variation of the vapor–solid transition velocity and diffusion coefficient. The increase of bias voltage results in the decrease of the vapor–solid transition velocity and diffusion coefficient. However, there is an opposite effect of the simultaneous decrease of the vapor–solid transition velocity and diffusion coefficient on the surface roughness. In detail, the decrease of the vapor–solid transition velocity leads to the elimination of the shadowing effect and reduction of surface roughness, while the decrease of the diffusion coefficient leads to the increase of surface roughness. The surface roughness is finally attributed to the combined effect of the vapor–solid transition velocity and diffusion coefficient. Again, the good agreement between the simulated surface roughness and the experimental data also substantiates the present quantitative phase-field simulation. Moreover, the surface roughness is

evaluated in an area with 3 μm × 3 μm for experimental results, while the simulated surface roughness is calculated within 100 nm × 100 nm due to the limitation of computing power, which might lead to some discrepancies in simulation and experimental results.

In **Figure 7**, a comparison between the phase-field-simulated grain size of PVD TiN coatings and the experimental data (Wang et al., 2015) is given. The statistical grain size is acquired according to the phase-field simulations at different vapor–solid transition velocities and diffusion coefficients. As the strategy of the moving frame is adopted in the simulation process, the mean size of the columnar structure is considered by averaging the radius of the columnar structure at different thicknesses according to the historical simulation snapshots. As for the experimental grain size, it is affected by the bias voltage and is estimated from X-ray diffraction (XRD) analysis (Wang et al., 2015). When the vapor–solid transition velocity and diffusion coefficient increase from 0.37 $nm^2 s^{-1}$ to 1.2 $nm^2 s^{-1}$ to 0.60 $nm^2 s^{-1}$ and 2.2 $nm^2 s^{-1}$, the simulated average grain size of TiN coatings slightly increases from 10.38 to 10.61 nm and then to 12.13 nm, which is in approximate agreement with the experimental data, considering the uncertainty induced by the shape factor of grains. The average grain size due to experimental mensuration exhibits a significant increase as the bias voltage decreases. The influence of bias voltage on grain size can be explained from the phase-field simulations. The increase of bias voltage is expected to lead to the decrease of both vapor–solid transition velocity and diffusion coefficient. The decrease of vapor–solid transition velocity contributes to the increase of grain size as species in vapors is likely to diffuse along the surface of the solidified parts, and epitaxial growth perpendicular to the development direction is to be enhanced. Similarly, the decrease of the diffusion coefficient has an effect on the decrease of grain size due to insufficient mass supply. Thus, the average grain size of PVD TiN coatings is determined by the combined effect of vapor–solid transition velocity and diffusion coefficient. The reason for the deviation between simulated grain size and experimental results is that the longitudinal sections of coatings are subjected to XRD in the experimental study, while the calculated grain size is analyzed from each transverse layer between tips and bottom of the simulated columnar structure.

3.2 Multi-Objective Decision-Making Strategy

For industrial applications, multiple coating property metrics are considered during the processing and service periods. Deposition rate is one of the dominant factors intimately correlating with the production efficiency and cost. In addition, the deposition rate also concerns with successive coating property metrics, that is, grain size, porosity, and surface roughness. For PVD TiN coatings for cutting tools, a finer gain size results in higher hardness and mechanical strength, but meanwhile, the porosity and unexpected surface roughness might be avoided. However, a higher deposition rate is prone to resulting in coatings with porosity, and the level of surface roughness might be high where in-sequence post-processing processes are, therefore, desired for satisfactory surface quality. Considering the marginal effect between the processing parameters and different coating property metrics, the decision-making problem toward the coatings with optimal process parameters for best properties turns to be complicated as multiple objectives are to be resolved.

In terms of the multi-objective decision-making problem, two important aspects should be addressed. The first concerns with supporting information for making the decision. Phase-field simulation has come to such a stage, where microstructures of related PVD processes can be retrieved according to the model parameters and assumed environment conditions. Practical experiments, which are generally expensive with respect to either time consumption or experiment cost, can serve as validation evidence for numerical simulations. Beyond validation, linking between the model parameters and real process parameters is likely to be formed, where either a qualitative or quantitative relation can be retained. With numerical simulation results, snapshots for microstructures during different processing periods are provided, where analysis over the corresponding coating property metrics can be conducted. Experimental data can again substantiate the validation of the related phase-field simulation results. The overall correlation between processing parameters and coating property metrics is subsequently established.

Once the supporting information is acquired, decision-making can therefore be carried out only if the specific procedures can be followed. For single-objective problem, either a convex or non-convex optimization algorithm is feasible for resolving the optimal decision vector with or without constraints. However, complex marginal effects are to be encountered even if more than one objective is being examined. One common strategy is to reasonably transform the multi-objective problem into a single-objective one by means of weighting the individual objective with suitable weights. Typically, weight is expertise-based knowledge information, which is extremely useful when the problem being examined is reaching the state of art. In case of an unexplored terrain, expertise-based information is generally absent, when decision-making processes toward the optimal design are likely to be impeded.

As multi-objective problems are one of the most well-studied problems by mathematics, feasible specification is, therefore, enabled by learning from related methods, that is, Pareto front and hierarchical analysis. Pareto front is one of the most insightful tools for measuring the marginal effects when multiple objectives are being concerned. Pareto front is the collection of feasible solutions, of which each is non-dominated by others when no performance deterioration is expected. In other words, each solution of the Pareto front is one of the decision-making suggestions, where the marginal effects of different objectives are subject to specific faith or evaluation criterion. Generally, the Pareto front is identified among the collection of many feasible solutions, which might be one or tens of times about the number of solutions located in the frontier. Acceleration is generally indispensable when the sampling procedures are time-consuming (Gao et al., 2022). Effective sampling strategies, that is, non-dominated sorting

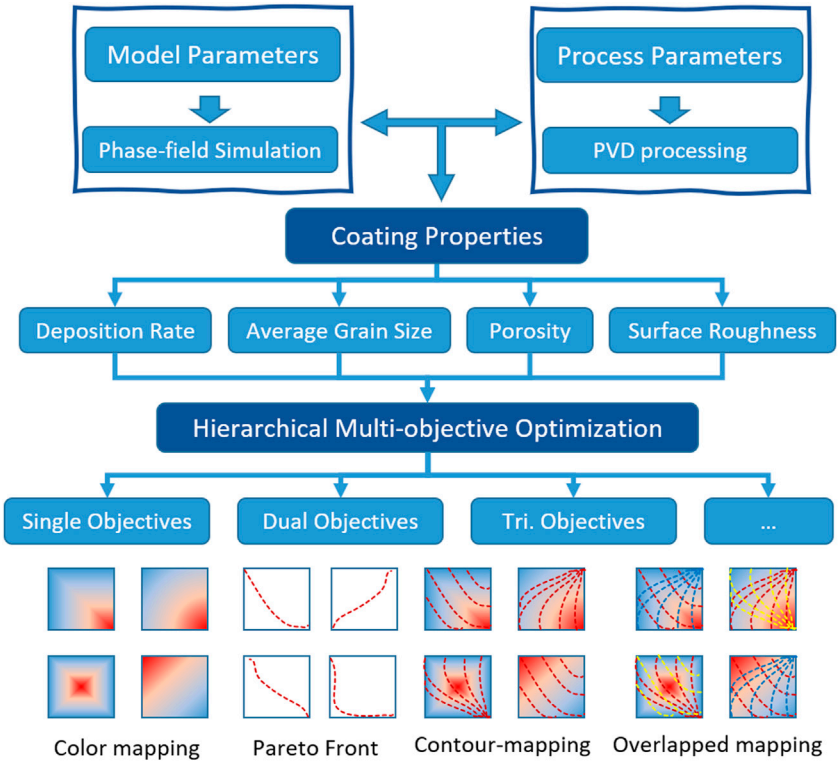

FIGURE 8 | Hierarchical multi-objective decision-making strategy for coatings by PVD processing.

genetic algorithm and multi-objective tree-structured Parzen estimator would also be desired when the evaluation processes of sampling are of high experimental or numerical computing cost.

Usually, the multi-objective problem can be reduced to a single-objective problem when multiple objectives are properly penalized. However, when expertise experience is absent, bias and subjective influence seem inevitable. To obtain the comprehensive overview toward multiple objectives, hierarchical analyses are generally adopted. The analytic hierarchy process is usually a problem-dependent method, where nebulous prior knowledge toward the importance of objectives in practical applications is required. Therefore, objectives can be classified, ranked, and selected from the overall feasible solutions, that is, the Pareto frontier.

The framework for the present hierarchical multi-objective optimization is displayed in **Figure 8**. Phase-field simulations are used for acquiring sufficient supporting information for decision-making. Metrics toward different coating properties are, therefore, evaluated based on the numerous simulation results. Experimental data from the practical PVD processing processes serve as validation evidence, which enables the linking between the processing parameters and model parameters. As a result, the correlation between the processing parameters and different objective metrics is established. In this work, the hierarchical multi-objective optimization involves two stages: intuitive visualization and analytic hierarchy process. Intuitive understanding toward the correlation between processing parameters and coating properties can be first acquired by proper visualization. Dual objectives are then examined where the Pareto frontier should be identified. Mapping with an overlapped contour could serve as an alternative approach when the number of variable factors is limited and therefore visualization is enabled. As the number of objectives increases, overlapped mapping might be the most suitable method for the analytic hierarchy process. Here, we focus on the TiN-based coatings, especially for cutting tools, and up to four objectives (i.e., deposition rate, porosity, surface roughness, and grain size) are concerned.

3.3 Screening of Optimal Model Parameters for Best Coating Properties

In terms of industrial applications, the fabricated coatings should possess the best properties with respect to specific practical requirements. For instance, PVD coatings with appropriate amount of porosity are desired for filter materials and catalytic materials, while the latter would also have special requirement on the roughness of the surface. As for cutting tools, PVD coatings are responsible for providing extremely high toughness, and thus the coatings with porosity are anticipated to be avoided as vibration during cutting processes will likely damage the coating structure. Roughness of the coatings is related to subsequential manufacturing processes and is largely

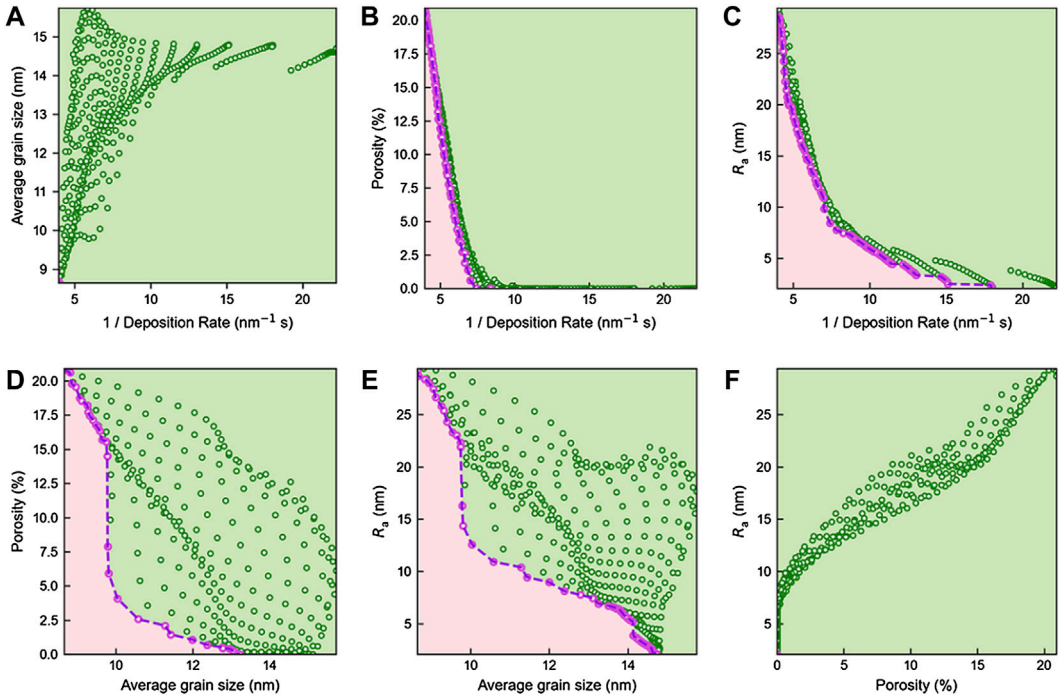

FIGURE 9 | Mathematical optimal solutions (Pareto frontier) for simultaneous optimization of multiple objectives: **(A)** deposition rate and grain size, **(B)** deposition rate and porosity, **(C)** deposition rate and surface roughness, **(D)** grain size and porosity, **(E)** grain size and surface roughness, and **(F)** porosity and surface roughness.

influential on the friction and wear properties. Furthermore, grain size plays an important role in mechanical performances such as the strength and hardness of the coatings for cutting tools. Another key point in industrial production lies in the productivity, which is closely tied to the deposition rate of coatings during PVD processing. Considering both production efficiency and coating properties, ideal factors such as high deposition rate, low porosity ratio, flattened surface morphology, and small grain size are desired in PVD coatings for cutting tools. Therefore, multiple objectives are to be considered for the present design of PVD TiN coatings.

Specifically, objective 1, which denotes the deposition rate, is to be maximized; while objectives 2–4, respectively, denoting the porosity, surface roughness and grain size, are all to be minimized. To simplify the process of optimization, the inverse of the deposition rate is applied. Then, all four objectives should be minimized, aiming at screening the optimal process parameters for PVD TiN coatings with best properties. The set of mathematical optimal solutions generally indicated as the Pareto frontier of objective space is shown in **Figure 9**. **Figure 9** illustrates the correlation between pairwise objectives from concerned properties of the imitated coatings, and all feasible choices over the objective space are denoted as green dots. By applying the Pareto search algorithm on the dataset, the Pareto frontiers are then determined, that is, the circles highlighted in purple. The Pareto frontier can be used to identify the ideal combination of pairwise coating performance. In **Figure 9**, it is observed that there are two types of relations based on a comprehensive analysis of various objective spaces. One is that the two objectives are not in conflict, as shown in **Figures 9A,F**, where the two objectives are approximately positively correlated, that is, when the value of one objective decreases, the other objective can also take a smaller value. In this case, a single solution exists that simultaneously minimizes each objective, while the other type is that the two objectives are conflicting, as shown in **Figures 9B–E**. **Figures 9B,C** exhibit more obvious negative correlation than **Figures 9D,E**. Therefore, the set of Pareto optimal solutions is found to satisfy the different objectives. For example, when the average grain size is expected to be 12 nm, the least related roughness is about 9 nm.

In order to further correlate the coating properties and model parameters, the predicted cases with respect to a combination of different objectives on the Pareto frontier are further investigated. Particularly, different objectives, that is, grain size, porosity, and surface roughness against the deposition rate are examined, as shown in **Figure 10**. The heatmap is used to visualize the deposition rate against the model parameters, while the other objectives (i.e., grain size, porosity, and surface roughness) are being imposed in the form of a contour, as shown in **Figures 10A–C**. For grain size, a similar tendency is observed with respect to the varying deposition rate. The lowest level of grain size is reached when the deposition rate is of high level. For porosity, a consistent tendency is observed considering the varying deposition rate, where a critical region is found at the region of the lower deposition rate. Moreover, a critical point can be further determined to be $B = 0.39$ nm^2 s and $D = 2.9$ nm^2 s. As for surface roughness, the potential levels of roughness are diverse and can be controlled according to the model parameters. For the

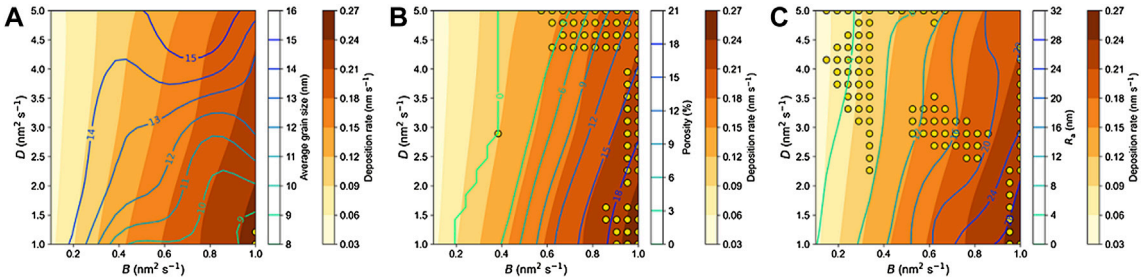

FIGURE 10 | Screening window of the model parameters for best coating property combination of: **(A)** deposition rate and grain size, **(B)** deposition rate and porosity, and **(C)** deposition rate and surface roughness.

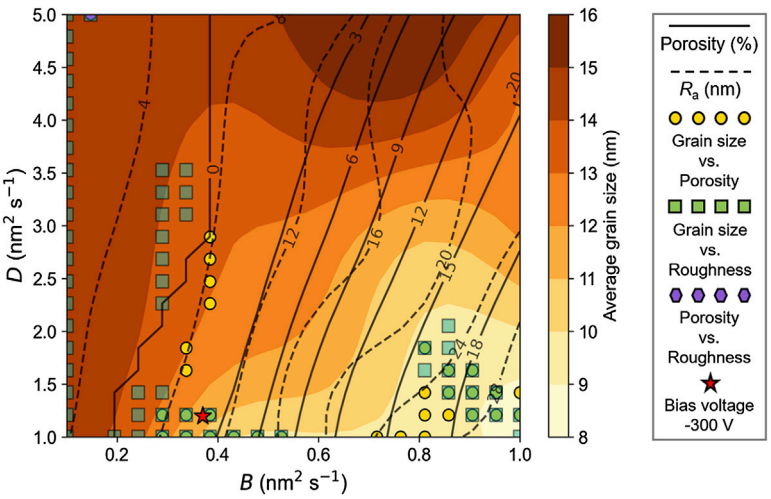

FIGURE 11 | Screening window of the model parameters for best coating property combinations of grain size, porosity, and surface roughness, compared with the best experimental result (Wang et al., 2015).

smooth surface, the processes with lower deposition rates are beneficial, while higher deposition rates lead to coatings with rough surfaces.

For a multi-objective decision-making problem, consideration of dual objectives seems to be still incomplete. Therefore, the objectives including grain size, porosity, and surface roughness are further synthesized, as shown in **Figure 11**. In the figure, the grain size against the model parameters is plotted as the heatmap, and the contour of the solid lines demonstrates the porosity, while the contour of the dash lines indicates the level of roughness. Furthermore, the optimal points for dual objectives are also recommended by Pareto front calculation. Overlapping regions are found among the Pareto front related to grain size against the porosity and surface roughness, where the surface diffusion coefficient D is of a lower level. Two distinct regions are suggested, that is, the one with B from 0.3 nm^2 s to 0.5 nm^2 s, and the other, from 0.85 nm^2 s to 1.0 nm^2 s. For the region with B of smaller magnitude, the grain size is prone to change along with the vapor–solid transition velocity. As for the region with B of larger magnitude, the deposition rate is higher than that of the others. Recalling the experimental results with relatively better coating properties reported by Wang et al., (2015), it is found that the corresponding result (marked as star symbol in **Figure 11**) exactly lies in one of the previously recommended regions, which clearly proves the reliability of the present strategy of screening the optimal model/process parameters for best coating properties. Furthermore, based on **Figure 11**, another potential processing window with a higher deposition rate is also suggested for industrial production, though the corresponding porosity and surface roughness are of a less promising level. As shown in **Figure 11**, the quantitative relation between the model parameters and coating properties (i.e., porosity, surface roughness, and grain size) has been established, which means that once the optimal model parameters are acquired, different coating properties can be quantitatively predicted, or when the coating properties are determined according to practical needs, the optimal combination of model parameters is expected to be inferred. Then, on the basis of the parametric relation between the model parameters and process parameters established in the work of **Section 3.1**, the process parameters (such as the bias voltage here) can be reversely traced, as shown in **Figure 4**. Coordinating the

research results of **Section 3.1** and this section, the quantitative relation of "process-microstructure-properties" can be established.

4 CONCLUSION

- The growth processes of TiN coatings prepared by PVD (specifically HiPIMS) under different process parameters were reproduced by phase-field simulations with different sets of model parameters. The parametric relation among the process parameters (i.e., bias voltage), model parameters, and different coating properties was then successfully established by correlating between the phase-field simulation results and the limited experimental data.
- A hierarchical multi-objective optimization-based approach for a comprehensive design of the best coating properties and the corresponding optimal process windows was proposed and successfully applied in PVD TiN coatings based on the quantitative phase-field simulations. The screened windows for PVD TiN coatings were validated to be consistent with the optimal experimental results.
- It is anticipated that a combination of 3-D quantitative phase-field simulation and hierarchical multi-objective optimization strategy should be feasible for the high-throughput screening of optimal process parameters for different PVD coatings with best properties.

DATA AVAILABILITY STATEMENT

The raw data supporting the conclusions of this article will be made available by the authors, without undue reservation.

AUTHOR CONTRIBUTIONS

LZ conceived the idea, RD conducted the phase-field simulations, RD and JZ performed the multi-objective optimization, and SY and TZ helped check grammar problems concerning tenses and syntax errors. All authors analyzed the results and contributed to writing the manuscript.

FUNDING

The financial support from the Youth Fund of the National Natural Science Foundation of China (Grant No. 52101028), China Postdoctoral Science Foundation (Grant No. 2021M703628), the Guangdong Provincial Natural Science Foundation Project (Grant No. 2020A1515010948), the Special fund project of Guangdong Academy of Sciences (Grant No. 2020GDASYL-20200104028), and Guangzhou Major Projects of Industry-University-Research (IUR) Collaborative Innovation "Surface Treatment and Repair for Key Components of Industrial Gas Turbine (IGT)" is acknowledged. RD acknowledged the financial support by the Fundamental Research Funds for the Central Universities of Central South University (Grant No. 2021zzts0582) and the financial support by the Postgraduate Scientific Research Innovation Project of Hunan Province (Grant No. CX20210195).

SUPPLEMENTARY MATERIAL

The Supplementary Material for this article can be found online at: https://www.frontiersin.org/articles/10.3389/fmats.2022.924294/full#supplementary-material

REFERENCES

Alami, J., Maric, Z., Busch, H., Klein, F., Grabowy, U., and Kopnarski, M. (2014). Enhanced Ionization Sputtering: A Concept for Superior Industrial Coatings. *Surf. Coat. Technol.* 255, 43–51. doi:10.1016/j.surfcoat.2013.11.040

Aqil, M. M., Azam, M. A., Aziz, M. F., and Latif, R. (2017). Deposition and Characterization of Molybdenum Thin Film Using Direct Current Magnetron and Atomic Force Microscopy. *J. Nanotechnol.* 2017, 1–10. doi:10.1155/2017/4862087

Barshilia, H. C., Surya Prakash, M., Poojari, A., and Rajam, K. S. (2004). Corrosion Behavior of Nanolayered TiN/NbN Multilayer Coatings Prepared by Reactive Direct Current Magnetron Sputtering Process. *Thin Solid Films* 460 (1), 133–142. doi:10.1016/j.tsf.2004.01.096

Bhaduri, D., Ghosh, A., Gangopadhyay, S., and Paul, S. (2010). Effect of Target Frequency, Bias Voltage and Bias Frequency on Microstructure and Mechanical Properties of Pulsed DC CFUBM Sputtered TiN Coating. *Surf. Coat. Technol.* 204 (21), 3684–3697. doi:10.1016/j.surfcoat.2010.04.047

Bobzin, K., Brögelmann, T., Kruppe, N. C., and Engels, M. (2019). Influence of HPPMS on Hybrid dcMS/HPPMS (Cr,Al)N Processes. *Surf. Coat. Technol.* 358, 57–66. doi:10.1016/j.surfcoat.2018.11.032

Deng, Y., Chen, W., Li, B., Wang, C., Kuang, T., and Li, Y. (2020). Physical Vapor Deposition Technology for Coated Cutting Tools: A Review. *Ceram. Int.* 46 (11), 18373–18390. doi:10.1016/j.ceramint.2020.04.168

Fu, T., and Shen, Y. (2008). Surface Growth and Anomalous Scaling of Sputter-Deposited Al Films. *Phys. B Condens. Matter* 403 (13-16), 2306–2311. doi:10.1016/j.physb.2007.12.010

Gao, J., Zhong, J., Liu, G., Yang, S., Song, B., Zhang, L., et al. (2022). A Machine Learning Accelerated Distributed Task Management System (Malac-Distmas) and its Application in High-Throughput CALPHAD Computation Aiming at Efficient Alloy Design. *Adv. Powder Mater.* 1 (1), 100005. doi:10.1016/j.apmate.2021.09.005

Hernández, L. C., Ponce, L., Fundora, A., López, E., and Pérez, E. (2011). Nanohardness and Residual Stress in TiN Coatings. *Materials* 4 (5), 929–940. doi:10.3390/ma4050929

Keblinski, P., Maritan, A., Toigo, F., Messier, R., and Banavar, J. R. (1996). Continuum Model for the Growth of Interfaces. *Phys. Rev. E* 53 (1), 759–778. doi:10.1103/physreve.53.759

Kuo, C.-C., Lin, Y.-T., Chan, A., and Chang, J.-T. (2019). High Temperature Wear Behavior of Titanium Nitride Coating Deposited Using High Power Impulse Magnetron Sputtering. *Coatings* 9 (9), 555. doi:10.3390/coatings9090555

Lichter, S., and Chen, J. (1986). Model for Columnar Microstructure of Thin Solid Films. *Phys. Rev. Lett.* 56 (13), 1396–1399. doi:10.1103/physrevlett.56.1396

Lousa, A., Esteve, J., Mejia, J. P., and Devia, A. (2007). Influence of Deposition Pressure on the Structural Mechanical and Decorative Properties of TiN Thin Films Deposited by Cathodic Arc Evaporation. *Vacuum* 81 (11), 1507–1510. doi:10.1016/j.vacuum.2007.04.017

Ma, Q., Li, L., Xu, Y., Gu, J., Wang, L., and Xu, Y. (2017). Effect of Bias Voltage on TiAlSiN Nanocomposite Coatings Deposited by HiPIMS. *Appl. Surf. Sci.* 392, 826–833. doi:10.1016/j.apsusc.2016.09.028

Mayrhofer, P. H., Geier, M., Löcker, C., and Chen, L. (2009). Influence of Deposition Conditions on Texture Development and Mechanical Properties of TiN Coatings. *Int. J. Mater. Res.* 100 (8), 1052–1058. doi:10.3139/146.110159

Mayrhofer, P. H., Kunc, F., Musil, J., and Mitterer, C. (2002). A Comparative Study on Reactive and Non-reactive Unbalanced Magnetron Sputter Deposition of TiN Coatings. *Thin Solid Films* 415 (1), 151–159. doi:10.1016/S0040-6090(02)00511-4

Rosa, A., Da Silva, E., Amorim, E., Chaves, M., Catto, A., Lisboa-Filho, P. N., et al. (2012). Growth Evolution of ZnO Thin Films Deposited by RF Magnetron Sputtering. *J. Phys. Conf. Ser.* 370, 012020. IOP Publishing. doi:10.1088/1742-6596/370/1/012020

Stewart, J. A., and Spearot, D. E. (2016). Phase-field Models for Simulating Physical Vapor Deposition and Grain Evolution of Isotropic Single-phase Polycrystalline Thin Films. *Comput. Mater. Sci.* 123, 111–120. doi:10.1016/j.commatsci.2016.06.021

Stewart, J. A., and Spearot, D. E. (2017). Phase-Field Simulations of Microstructure Evolution during Physical Vapor Deposition of Single-phase Thin Films. *Comput. Mater. Sci.* 131, 170–177. doi:10.1016/j.commatsci.2017.01.034

Tai, C. N., Koh, E. S., and Akari, K. (1990). Macroparticles on TiN Films Prepared by the Arc Ion Plating Process. *Surf. Coat. Technol.* 43-44, 324–335. doi:10.1016/0257-8972(90)90085-Q

Wang, Z., Zhang, D., Ke, P., Liu, X., and Wang, A. (2015). Influence of Substrate Negative Bias on Structure and Properties of TiN Coatings Prepared by Hybrid HIPIMS Method. *J. Mater. Sci. Technol.* 31 (1), 37–42. doi:10.1016/j.jmst.2014.06.002

Warren, J. A., Kobayashi, R., Lobkovsky, A. E., and Craig Carter, W. (2003). Extending Phase Field Models of Solidification to Polycrystalline Materials. *Acta Mater.* 51 (20), 6035–6058. doi:10.1016/S1359-6454(03)00388-4

Wu, J., Wu, B. H., Ma, D. L., Xie, D., Wu, Y. P., Chen, C. Z., et al. (2017). Effects of Magnetic Field Strength and Deposition Pressure on the Properties of TiN Films Produced by High Power Pulsed Magnetron Sputtering (HPPMS). *Surf. Coat. Technol.* 315, 258–267. doi:10.1016/j.surfcoat.2017.02.051

Yang, S., Zhong, J., Chen, M., and Zhang, L. (2019). A Parametric Three-Dimensional Phase-Field Study of the Physical Vapor Deposition Process of Metal Thin Films Aiming at Quantitative Simulations. *Coatings* 9 (10), 607. doi:10.3390/coatings9100607

Yiğit, E. (2017). *Atmospheric and Space Sciences: Ionospheres and Plasma Environments*, 2. Cham, Switzerland: Springer.

Zhang, Q., Xu, Y., Zhang, T., Wu, Z., and Wang, Q. (2018). Tribological Properties, Oxidation Resistance and Turning Performance of AlTiN/AlCrSiN Multilayer Coatings by Arc Ion Plating. *Surf. Coat. Technol.* 356, 1–10. doi:10.1016/j.surfcoat.2018.09.027

Zhou, S., Kuang, T., Qiu, Z., Zeng, D., and Zhou, K. (2019). Microstructural Origins of High Hardness and Toughness in Cathodic Arc Evaporated Cr-Al-N Coatings. *Appl. Surf. Sci.* 493, 1067–1073. doi:10.1016/j.apsusc.2019.07.051

Conflict of Interest: The authors declare that the research was conducted in the absence of any commercial or financial relationships that could be construed as a potential conflict of interest.

frontiers | Frontiers in Materials

ORIGINAL RESEARCH
published: 28 June 2022
doi: 10.3389/fmats.2022.875519

Arrangement and Decomposition of Grain Boundary Dislocations: Two-Mode Phase-Field Crystal Simulation

Huanqing Li[1†], *Xiaona Wang*[1†], *Haibin Zhang*[1†], *Xiaolin Tian*[1], *Hua Hou*[2] *and Yuhong Zhao*[1,3]*

[1]College of Materials Science and Engineering, North University of China, Taiyuan, China, [2]College of Materials Science and Engineering, Taiyuan University of Science and Technology, Taiyuan, China, [3]Beijing Advanced Innovation Center for Materials Genome Engineering, University of Science and Technology Beijing, Beijing, China

The grain-boundary dislocation arrangement and decomposition during constant-volume deformation of a nanoscale bi-crystal system in fcc-structured materials were studied by using the two-mode phase-field crystal (2PFC) method. The effects of different grain boundary misorientations (GBMs) and tensile deformation directions on the dislocation arrangement and decomposition are analyzed. In three different symmetrical tilt grain boundaries evaluated by PFC, the atomic density profile of grain boundaries changed periodically at equilibrium. The initial grain boundary dislocation arrangement of the three samples is almost the same when tensile deformation is applied to the samples in the *x*- or *y*- direction, and all are symmetrically arranged in a “bowknot ”structure. The stress at the grain boundary is concentrated with the increase of strain, and dislocation decomposition can effectively reduce the stress concentration. The time steps of dislocation decomposition at grain boundaries decreases with increasing strain rate. This work facilitates the application of PFC in the analysis of grain-boundary mechanics in an extended range of materials.

Keywords: phase-field crystal method, grain-boundary dislocation, grain-boundary misorientation, dislocation arrangement, dislocation decomposition, deformation

OPEN ACCESS

Edited by:
Zhenyu Li,
University of Science and Technology of China, China

Reviewed by:
Qing Wang,
Dalian University of Technology, China
Jichen Dong,
Institute of Chemistry (CAS), China

***Correspondence:**
Yuhong Zhao
zhaoyuhong@nuc.edu.cn

[†]These authors have contributed equally to this work

Specialty section:
This article was submitted to Computational Materials Science, a section of the journal Frontiers in Materials

Received: *14 February 2022*
Accepted: *28 April 2022*
Published: *28 June 2022*

Citation:
Li H, Wang X, Zhang H, Tian X, Hou H and Zhao Y (2022) Arrangement and Decomposition of Grain Boundary Dislocations: Two-Mode Phase-Field Crystal Simulation. Front. Mater. 9:875519. doi: 10.3389/fmats.2022.875519

INTRODUCTION

The mechanical behavior of materials is affected by defects such as dislocations and grain boundaries, which are related to atomic structure (Hirouchi et al., 2010). The study of the grain-boundary structure and dislocation movement mechanism is conducive to understanding the evolution law of material microstructure and can provide some theoretical support for optimizing processes and improving material properties to a certain extent (Kumar et al., 2003; Hou et al., 2020; Park et al., 2021; Roy et al., 2022).

The study of material properties has become more and more thorough with the progress of experimental technology. The tensile deformation behaviors under different conditions were studied by experiments. For example, tensile response and fracture behavior (Mahabadi et al., 2014), dislocation configuration near the tensile fracture (Liu et al., 2012), the change of grain orientation before and after tensile deformation, and the yield strength of the alloy can be observed by using a scanning electron microscope (SEM), orientation imaging microscopy (OIM), transmission electron microscope (TEM), and electron backscattered diffraction (EBSD) (Suh et al., 2017; Xia et al., 2019; Li et al., 2020; Yan et al.,

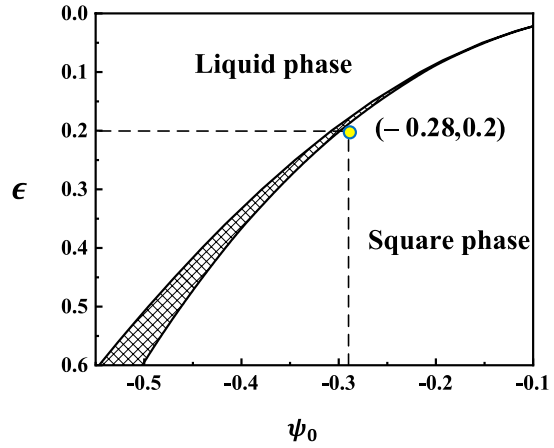

FIGURE 1 | Two-dimensional phase diagram of two-mode approximate calculation.

2021). The high-resolution transmission electron microscope (HRTEM) (Bian et al., 2017) was used to observe the microstructure on a smaller scale (Yang et al., 2020; Volnistem et al., 2021; Guo et al., 2021). However, experimental inquiry alone is not enough in scientific research. Because the process of material microstructure formation and its performance characteristics are essentially multi-scale coupling. So far, the experimental study of the microstructure of materials has some limitations. Atomic simulation can supplement it, especially in the study of scale (Xin et al., 2021; Kuang et al., 2018; Zhao et al., 2018; Guo et al., 2019). With the rapid development of computer simulation, such as the phase-field method (PF) (Peng et al., 2021), molecular dynamics (MD) (Song et al., 2014), and phase-field crystal method (PFC) (Zhao et al., 2014). The evolution morphology of multi-scale material microstructure is vividly given (Zhang et al., 2018; Zhao et al., 2019). Combined with EBSD (Nielsen et al., 2020; Zhao et al., 2021) and HRTEM (Zhang et al., 2019; Shuai et al., 2021) technology, the research efficiency is greatly improved. It is worth mentioning that the phase-field crystal method is more suitable for studying the microstructure defects of crystals. Because the PF method generally studies mesoscopic scale, it is difficult to provide atomic-scale information, and the time scale ($10^{-14} \sim 10^{-12}$s) in MD simulations is much smaller than the diffusion scale (10^{-6}s) of the microcosmic defects.

Elder et al. (2002) proposed the PFC method which closely a coupled model between atom and microscale according to Ginzburg Landau's theory. The evolution of crystal patterns simulated (Qi et al., 2020; Chen and Zhao, 2021), which can quantitatively reproduce some key characteristics affecting the evolution of microstructure (Tian et al., 2021), and clearly describe the dislocation structure of grain boundary (Qi et al., 2019). The model is expressed in terms of experimentally measurable physical quantities such as liquid structure factors (Hu et al., 2020). Now it has successfully simulated dislocation movement, grain-boundary pre-melting, growth of crystals. The model cannot describe the dislocation motion in a two-dimensional square lattice. Therefore, Wu et al. (2010) and Asadi and Zaeem (2015) modified the free energy function and proposed the 2PFC model. The study of phase diagrams makes the experiment and simulation more closely combined (Greenwood et al., 2010; Can et al., 2013). The 2PFC model studies the deformation and morphology of small-angle asymmetric grain boundaries (Zhang et al., 2014), the migration and dislocation reaction of grain boundaries under deviatoric deformation (Hu et al., 2016a), and the solidification law (Yang et al., 2014) of square phase grains under low, medium, and high driving force during phase transformation. These simulation studies reveal the microstructure phenomena under different conditions on a smaller atomic scale.

In this work, we focus on the dislocation decomposition and dislocation arrangement of low-angle symmetrically tilt grain boundaries under different tensile deformation directions. In the following, we will first describe the model and method in **Section 2**. The tensile response of grain boundary at x and y tensile deformation directions are presented in **Section 3**, followed by strain rate, deformation direction, and misorientation angle that affect the critical strain value for grainboundary dislocation decomposition discussed in **Section 4**. The final conclusion is presented in **Section 5**.

MODELS AND METHODS

Two-Mode Phase-Field Crystal Model

The two-mode PFC model (Wu et al., 2010) simulates the crystal structure and the free energy of a system is as

$$\mathcal{F} = \int \left\{ \frac{\phi}{2} \left[a + \lambda \left(\nabla^2 + q_0^2 \right)^2 \right] \left[\left(\nabla^2 + q_1^2 \right)^2 + r_1 \right] \phi + g \frac{\phi^4}{4} \right\} d\boldsymbol{x}, \quad (1)$$

where a is the lattice parameter. r_1 is related to the relative amplitude of density wave, q_0 and q_1 represents the wavelengths of the first and second density waves. λ and g are phenomenological parameters to fit the properties of the material (Blixt et al., 2022).

TABLE 1 | Parameters for sample preparation.

Sample	Tensile strain direction	Temperature	Initial density	Strain rate	Grain orientation angle		Misorientation angle
		ϵ	ψ_0	$\dot{\varepsilon}$	θ_1	θ_2	θ
A	*x*	0.2	–0.28	6e-6	3°	–3°	6°
B	*x*	//	//	//	3.5°	–3.5°	7°
C	*y*	//	//	//	//	//	7°

//The same parameter value as in the previous line.

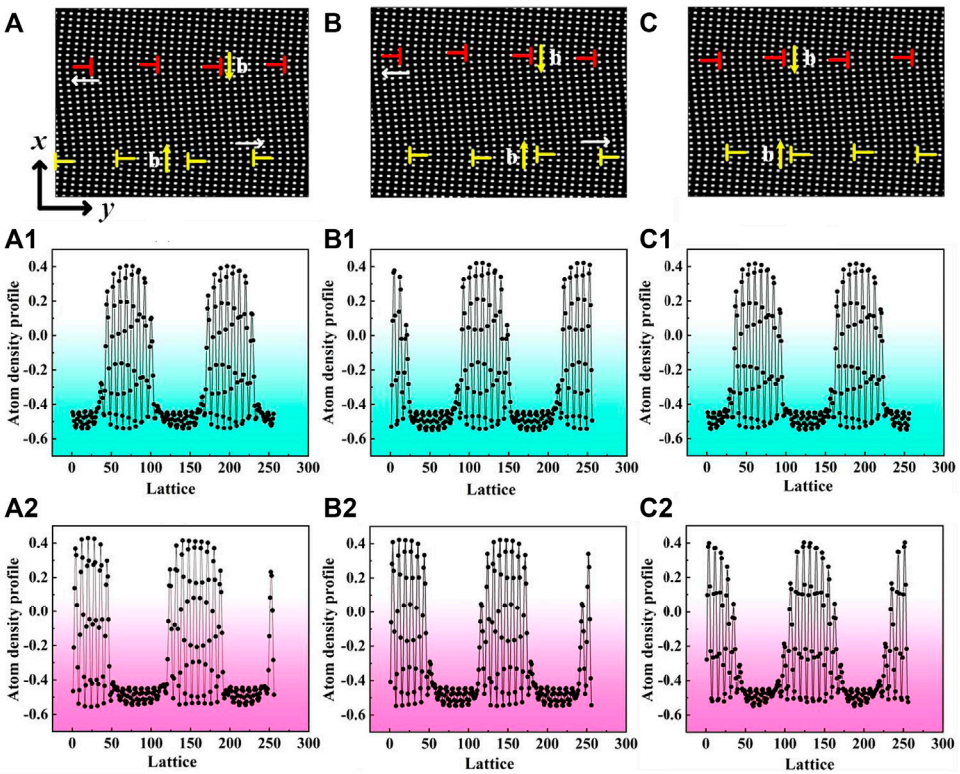

FIGURE 2 | (A), **(B)** Bi-crystal structure with grain boundary misorientation angles of 6° and 7° under *x*-direction tensile strain, and the time steps is 5,000. **(C)** The bi-crystal structure with grain boundary misorientation angles of 7° under *y*-direction tensile strain, and the time steps is 5,000. **(A1–C1)** The atomic density profile of the upper grain boundary corresponding to the misorientation angle, respectively. **(A2–C2)** The atomic density profile of the down grain boundary corresponding to the misorientation angle. The white arrow indicates the climbing direction of the edge dislocation. The yellow arrow indicates the direction of Burgers vector of the edge dislocation.

To minimize the number of parameters, we define the dimensionless parameters

$$\epsilon = -\frac{a}{\lambda q_0^8}, \quad R_1 = \frac{r_1}{q_0^4}, \quad Q_1 = \frac{q_1}{q_0}, \quad \psi = \sqrt{\frac{g}{\lambda q_0^8}}\phi, \quad F = \frac{g}{\lambda^2 q_0^{13}}\mathcal{F}, \quad \boldsymbol{r} = q_0\boldsymbol{x}. \tag{2}$$

substituting the abovementioned definitions into **Eq. 1** yields the dimensionless form

$$F = \int \left\{ \frac{\psi}{2}\left[-\epsilon + \left(\nabla^2 + 1\right)^2 \left[\left(\nabla^2 + Q_1^2\right)^2 + R_1 \right]\psi + \frac{\psi^4}{4} \right] \right\} d\boldsymbol{r}, \tag{3}$$

where ϵ controls the size of the solid-liquid coexistence regions as a function of density. Q_1 is determined by the selection of crystal structure. R_1 controls the relative stability of mode structures. In this word, $Q_1 = \sqrt{2}$, $R_1 = 0$.

The Fourier amplitudes of the first and second reciprocal lattice vectors (RLV) denote by A_i and B_i. It is assumed that all density waves in solid-state have the same amplitudes, $|A_i| = A_s$, $|B_i| = B_s$. The solid-state density field of FCC crystal is as follows

$$\psi_s = \psi_0 + 2A_s\left[\cos\left(q_s x\right) + \cos\left(q_s y\right)\right] + 4B_s \cos\left(q_s x\right)\cos\left(q_s y\right), \tag{4}$$

where $q_s = 1$.

The free energy density in the solid-state is

$$f_s = 2\left(-\epsilon + 3\psi_0^2\right)A_s^2 + 2\left(-\epsilon + 3\psi_0^2\right)B_s^2 + 24\psi_0 A_s^2 B_s + 36A_s^2 B_s^2 + 9A_s^4 + 9B_s^4 - \frac{\epsilon}{2}\psi_0^2 + 2\psi_0^2 + \frac{1}{4}\psi_0^4, \tag{5}$$

where

$$A_s = \frac{1}{9M}[\epsilon^2 + 75\psi_0^4 - 2\psi_0 N + 4\epsilon\psi_0^2 + (5\epsilon - 31\psi_0^2)M^2 + M^4 - 10\psi_0^3 - 2\epsilon\psi_0 M]^{\frac{1}{2}} + \frac{1}{9M}[\sqrt{3}\left(\epsilon^2 + 75\psi_0^4 - 2\psi_0 N + 4\epsilon\psi_0^2 - M^4 + 10\psi_0^3 M + 2\epsilon\psi_0 \mathrm{M}\right)i]^{\frac{1}{2}}, \tag{6}$$

$$B_s = -\frac{1}{18M}\left[\epsilon + 5\psi_0^2 + 8\psi_0 M + M^2 + \sqrt{3}\left(M^2 - 5\psi_0^2 - \epsilon\right)i\right], \tag{7}$$

$$M = \left(3\epsilon\psi_0 + \sqrt{-\epsilon^3 - 6\epsilon^2\psi_0^2 - 225\epsilon\psi_0^4 + 500\psi_0^6} - 25\psi_0^3\right)^{\frac{1}{3}}, \tag{8}$$

$$N = -\epsilon^3 - 6\epsilon^2\psi_0^2 - 225\epsilon\psi_0^4 + 500\psi_0^6. \tag{9}$$

The phase diagram is derived by taking the derivative of free energy for the density field of the square phase and liquid phase respectively and using the common tangent rule, as shown in **Figure 1**.

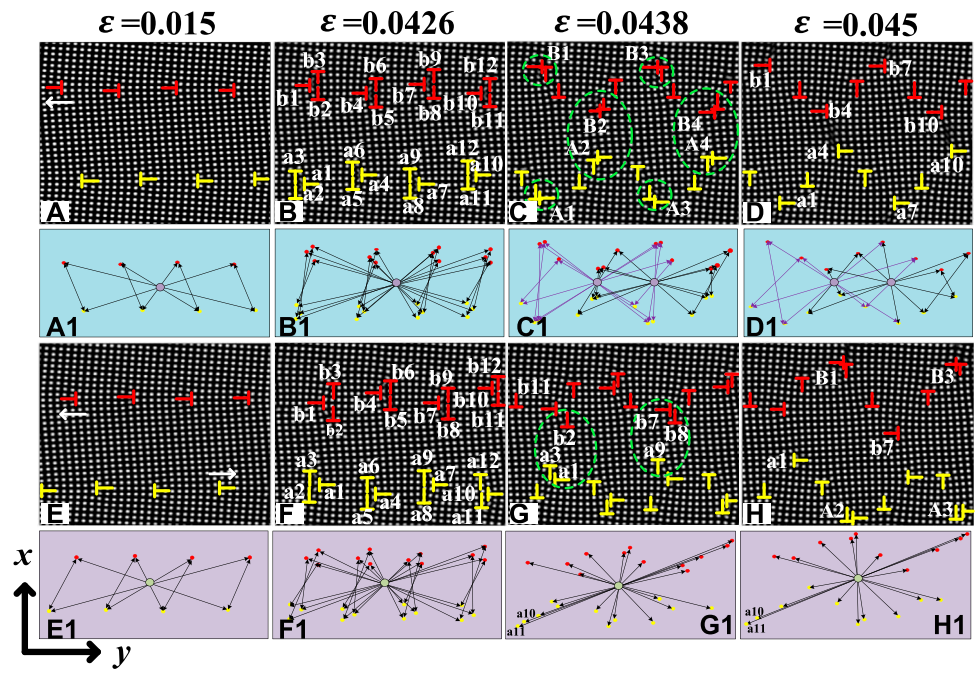

FIGURE 3 | (A–D), (A1-D1) The evolution and arrangement of grain boundary dislocations when the GBM are 7°, respectively. **(E–H), (E1–H1)** The evolution and symmetry arrangement of grain boundary dislocations when the GBM are 6°, respectively. The strain ε is 0.015, 0.0426, 0.0438, and 0.045.

Application of Applied Stress

First, we apply tensile stress along the x-direction to the system. We employ the isovolumetric numerical scheme (Hirouchi et al., 2009; Berry et al., 2015) during the deformation process:

$$S = \Delta x_0 \Delta y_0 = \Delta x \Delta y\,. \tag{10}$$

The grid sizes after n time steps are shown as follows:

$$\Delta x = \Delta x_0 \left(1 + n\dot{\varepsilon}\Delta t\right). \tag{11}$$

$$\Delta y = \frac{\Delta y_0}{1 + n\dot{\varepsilon}\Delta t}. \tag{12}$$

similarly, when tensile stress along the y-direction to the system, we have

$$\Delta x = \frac{\Delta x_0}{1 + n\dot{\varepsilon}\Delta t}, \tag{13}$$

$$\Delta y = \Delta y_0 \left(1 + n\dot{\varepsilon}\Delta t\right), \tag{14}$$

where Δx_0 and Δy_0 are initial grid sizes; Δx and Δy are grid sizes after deformation.

Numerical Calculation Method and Parameter Setting

Since the atomic density field is a conserved value, the dimensionless time evolution equation ψ can be expressed by the following Cahn-Hilliard equation (Wu et al., 2010):

$$\frac{\partial \psi}{\partial t} = \nabla^2 \frac{\delta F}{\delta \psi} = \nabla^2 \left\{ \left[-\epsilon + \left(\nabla^2 + 1\right)^2 + \left(\nabla^2 + 2\right)^2 \right] \psi + \psi^3 \right\}. \tag{15}$$

By transforming the partial differential equation into a sequence of ordinary differential equations in Fourier space, we apply a Fourier-spectral approximation to **Equation 10**, we have

$$\psi_{\boldsymbol{k},t+\Delta t} = \frac{\psi_{\boldsymbol{k},t} - k^2 \Delta t \psi_{\boldsymbol{k},t}^3}{1 + k^2 \Delta t \left[(4 - r) - 12k^2 + 13k^4 - 6k^6 + k^8 \right]}, \tag{16}$$

Where $\psi_{\boldsymbol{k},t}$ and $\psi_{\boldsymbol{k},t+\Delta t}$ represents the atomic density at a time t and $t + \Delta t$ in Fourier space, respectively. $k^2 = |k^2|$ represents the wave vector in Fourier space.

The parameters of the simulation system in this work are set as follows: the simulation region of periodic boundary conditions in all directions is $L_x \times L_y = 256\Delta x \times 256\Delta y$. The time step and space step are $\Delta t = 0.5$ and $\Delta x = \Delta y = \pi/4$, respectively. We set a sandwich simulation structure, $0 < x < L_x/4$, $L_x/4 < x < 3L_x/4$, and $3L_x/4 < x < L_x$. Grain orientation angle is set respectively θ_1, θ_2 , and θ_1 The misorientation angle $\theta = \theta_1 - \theta_2$, which is the angle between two adjacent grains. The selection of other simulation parameters is shown in **Table 1**. The reason for choosing the atomic density parameter is that it is located in the coexistence region of a liquid phase and square phase, so the solid and liquid phases can coexist stably without phase transition (Hu et al., 2016b).

We let the system relax for a period of 10^4 time steps to acquire structure equilibrium. The bi-crystal structure with GBM of 6° and 7° under x-direction tensile strain is applied, as shown in **Figure 2**. There are two symmetric tilt GBs and every GB consists of four edge dislocations arranged symmetrically. The grain orientation angle $\theta_1 = b/2D_1$, where

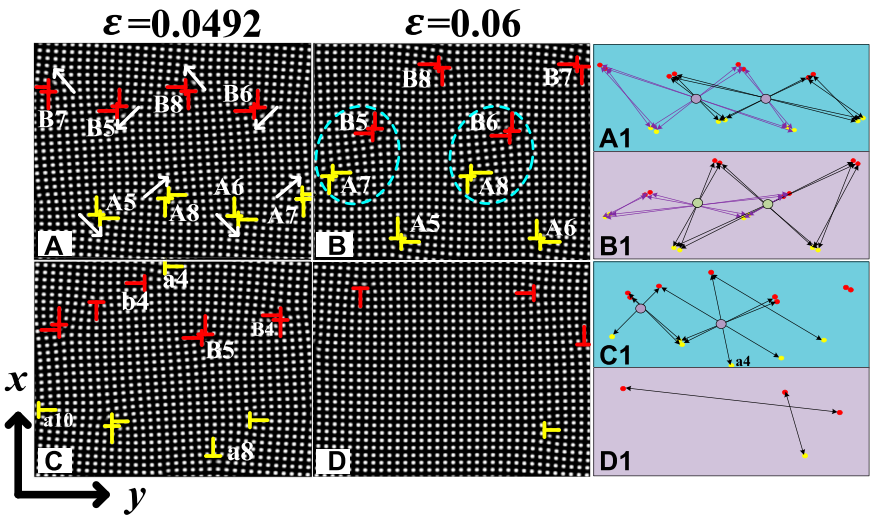

FIGURE 4 | (A–D) The dislocation evolution of 7° and 6° and the corresponding strains are both 0.0492 and 0.06. **(A1, B1), (C1, D1)** The arrangement of 7° and 6° with strains are both 0.0492 and 0.06.

b is the amount of Burgers vector and D_1 is the spacing of the arrangement of the edge dislocation (Gao et al., 2020). Because the difference in grain orientation angle is very small, the number of edge dislocations in the equilibrium structure of the two systems is the same. At the same time, we find that the atomic density distribution curves of the upper and lower grain boundaries of the two systems change periodically.

RESULTS AND ANALYSIS

The Arrangement and Movement of Edge Dislocations Under *X*-Direction Tensile Strain

The detailed arrangement and movement process of GBDs under x-direction tensile strain is illustrated in **Figures 3**, **4**. The free energy curve of the system during the deformation process is illustrated in **Figure 5**.

As shown in **Figures 3A–H**, all-grain boundary dislocations are arranged in symmetrical structure from ε = 0.015 and ε = 0.0426. The grain-boundary dislocations are completely decomposed when the strain reaches the critical value of dislocation decomposition. This process consumes energy and the free energy is reduced, (b~c) in **Figure 5**. With the increase of deformation, the dislocation movement and the symmetry are changed due to different misorientation angles and different resolved shear stresses. When ε = 0.0438 there are dislocation pairs formed in **Figures 3C, G**. For example, a4, and a6 in **Figure 3B** will form dislocation pair A2. We found that the dislocation arrangement and reaction forms 6° and 7°

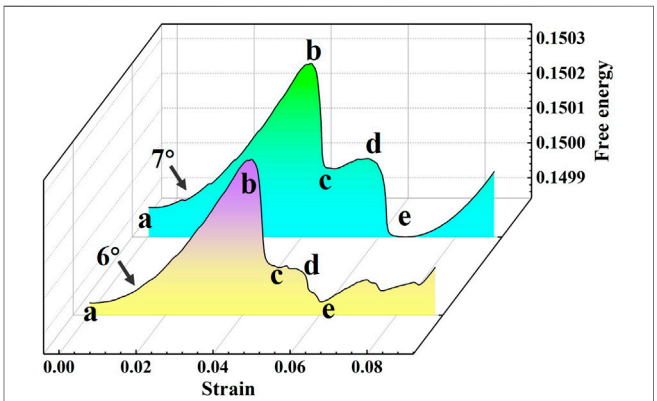

FIGURE 5 | The free energy curve of 6° and 7° grain boundary dislocation evolution process during the x-direction tensile deformation.

are different after the formation of dislocation pairs. From **Figures 3C,D**, dislocation pairs react with dislocation pairs and the dislocations arrangement structure presents a "double bowknot". From **Figures 3G,H**, dislocation reacts with the dislocation pair and a single edge dislocation and the dislocations arrangement structure is "fireworks".

At ε = 0.0492, it is observed that the system with the GBMs 7° is all dislocation pairs as shown in **Figure 4A**. At this time, the dislocation pairs arrangement is highly symmetrical showing a "double bowknot" structure. The energy consumed by dislocation pairs on the slip is less than that increased by system deformation. Thus, the energy curve rises again corresponding to the rising part in **Figures 5C,D**. When the

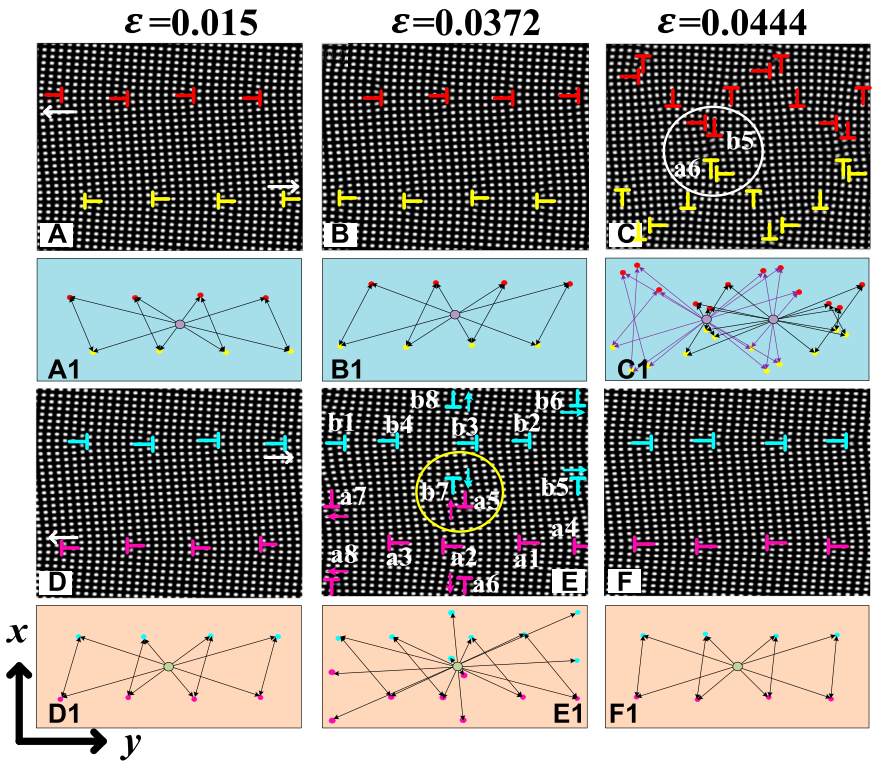

FIGURE 6 | (A–C), (D–F) The evolution process of grain boundary dislocations under tensile deformation in *x*-direction and *y*-direction with 7°, respectively, and the corresponding tensile strain ε is 0.015, 0.0372, and 0.0444. **(A1–F1)** The arrangement of grain boundary dislocations corresponding to the dislocation evolution diagram, respectively.

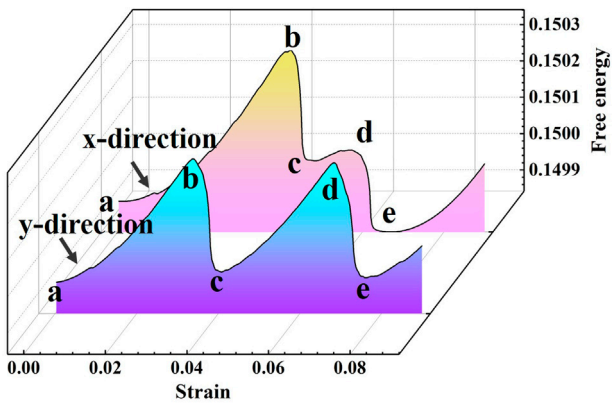

FIGURE 7 | Free energy curve of misorientation angle of 7° under *x*-and *y*-direction tensile deformation.

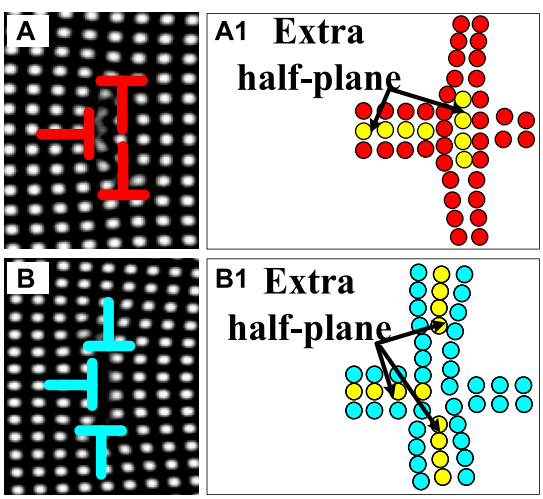

FIGURE 8 | (A), **(A1)** Dislocation decomposition under *x*-direction tensile strain and its atomic structure diagram. **(B)**, **(B1)** Dislocation decomposition under *y*-direction tensile strain and its atomic structure diagram.

GBMs of 6°, both dislocation pairs and single edge dislocations exist and the dislocations arrangement is chaotic, as shown in **Figure 4C1**. Four sub-grain boundaries appear in **Figure 4B** when the strain increases to 0.06. The existence of dislocation pairs reduces the lattice distortion energy and makes the sub-grain boundaries more stable. The dislocations are arranged in a "double bowknot" structure. Subsequently, annihilation occurs concurrently between all dislocation pairs such as A7 and B5 (blue dotted circle in **Figure 4B**), and finally, the lattice distortion disappears completely into a single crystal.

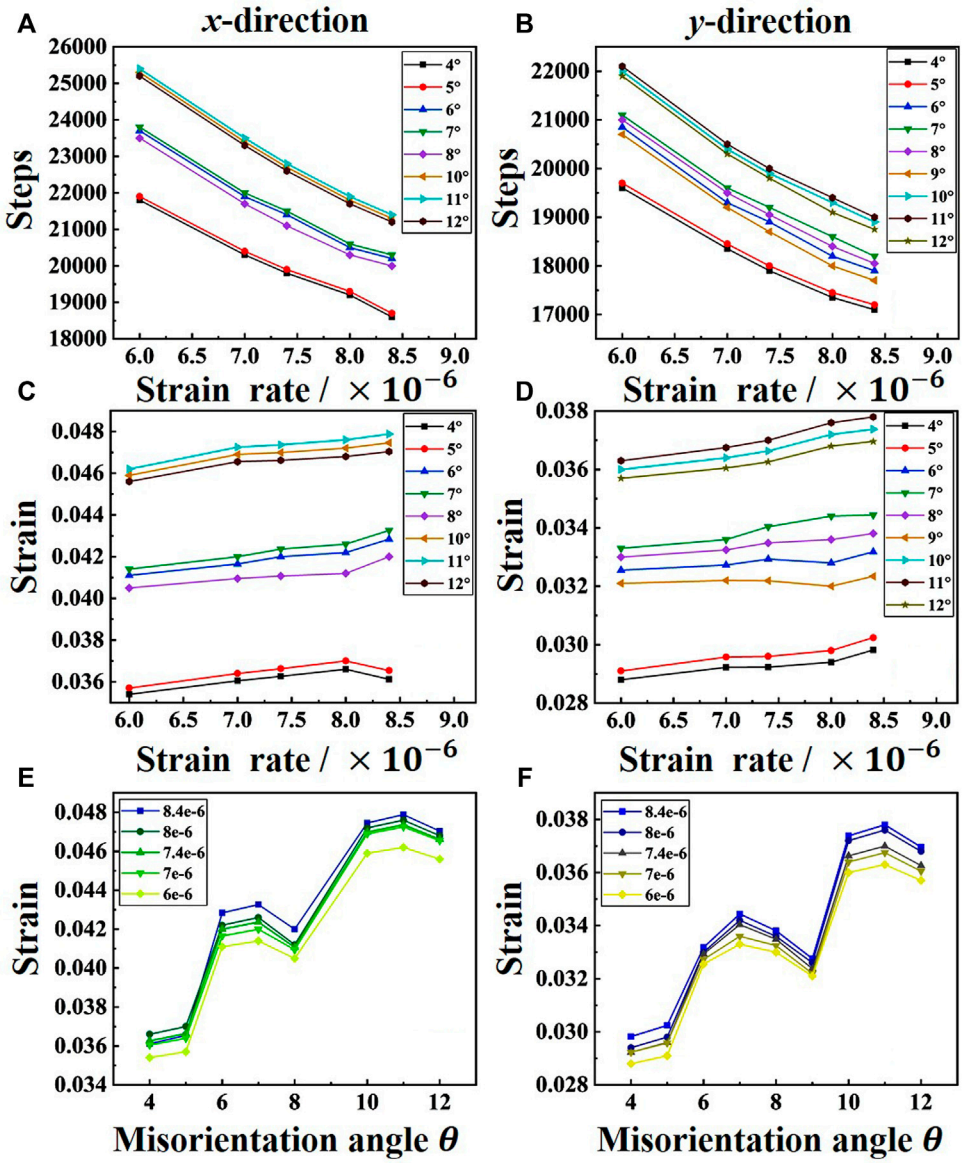

FIGURE 9 | Critical strain distribution of dislocations decomposition under different strain rates and GBMs conditions. **(A)**, **(C)**, **(E)** The critical strain distribution of tensile deformation in the *x*-direction; **(B)** **(D)**, **(F)** the critical strain distribution of tensile deformation in the *y*-direction.

However, we find that there are single edge dislocations and the dislocation arrangement is asymmetric in **Figure 4D**.

In **Figure 5**, we found that the energy trend of **Figures 5A–C** stage in the evolution of the two systems from bi-crystal to single crystal is the same, and the peak value with large GBMs is higher. From **Figures 5C,D**, the energy curve of the GBMs 7° is relatively smooth while there is two small-amplitude torsions (black box) which are caused by dislocation annihilation and dislocation pair formation. The lattice distortion completely disappears in the system with the GBMs 7° after point d. If the deformation continues to increase, the system energy increases again. Meanwhile, there are still dislocations in the system with the GBMs 6°, the remaining single edge dislocations annihilate one after another. Therefore, there are two torsions in **Figure 5D,E** stage, the lattice distortion of point e disappears completely, and the system energy increases with deformation.

Relationship Between the Direction of Tensile Strain and the Symmetry of Dislocations Arrangement

Different tensile deformation directions of samples affect the dislocation movement direction and dislocation arrangement symmetry in the system. The *y*-direction tensile strain is applied to sample B. The evolution and symmetrical distribution of grain boundary dislocations of the same strain

are shown in **Figure 6**, and the corresponding change of free energy is shown in **Figure 7**.

In the system of grain-boundary misorientation 7°, the number of grain-boundary dislocations doesn't change but the climbing direction of grain-boundary dislocations is opposite, as shown in **Figures 6A,D**. In the meantime, the grain-boundary dislocations arrangement is a highly symmetrical "bowknot" structure, as shown in **Figures 6A1,D1**. At $\varepsilon = 0.0372$, some dislocations in the *y*-direction tensile strain system decomposition first, as shown in **Figure 6E**. The GBDs arrangement is still symmetrical **Figure 6E1**, but the structure is not completely the same as that in **Figure 6D1**. While in the system with the tensile deformation direction of *x*, there is no dislocations decomposition, as shown in **Figure 6B**. At this time, all edge dislocations climb and the arrangement of grain boundary dislocations is still a "bowknot" structure. Different tensile deformation directions can affect the new dislocations climbing direction after edge dislocations decomposition, the detailed schematic diagram is shown in **Figure 8**. We know that the free energy of the system with the tensile deformation direction of the *y*-direction will reach the maximum first by observing the energy **Figure 7**.

With the increase of strain, there is no formation of dislocation pairs in the *y*-direction tensile strain system and the dislocation reactions are between single edge dislocations. In the *x*-direction tensile strain system, there are the formations and reactions of dislocation pairs and the annihilations of dislocations reduce the system energy, corresponding to the stage (b~c) in **Figure 7**. Two-grain boundaries are re-observed in **Figure 6F** when $\varepsilon = 0.0444$. The GBDs arrangement is exactly the same as in **Figure 6D1** and the system energy reaches the peak again at point d in **Figure 7**. Concurrently, the grain boundary is not obvious, all of which are single edge dislocations arranged in a "double bowknot" symmetrical structure **Figure 6C1**.

DISCUSSION

The effect of different strain rates $\dot{\varepsilon}$, grain boundary misorientations θ, and tensile deformation direction on the critical strain value of dislocations decomposition analyzed, as shown in **Figure 9**. It should be pointed out that the grain boundary with misorientation angle 9° does not emerge dislocations decomposition under *x*-direction tensile deformation. Therefore, there isno corresponding critical strain values of dislocations decomposition in **Figure 9**. But there are dislocation movement, dislocation reaction, and dislocation annihilation in the process of grain boundary evolution.

Through **Figure 9A,B**, we can find that when the grain boundary misorientations remain unchanged, the critical time steps of dislocation decomposition decrease with the increase of strain rate. This is because the critical strain required for dislocation decomposition in the same system is fixed. It can be seen from the formula $\varepsilon = n\dot{\varepsilon}\Delta t$ that when $\dot{\varepsilon}$ increases, *n* decreases. In addition, the critical time steps of dislocations decomposition under *y*-direction tensile deformation is smaller than *x*-direction. This requires a larger strain since all-grain boundary dislocations decomposes simultaneously under *x*-direction tensile deformation while grain boundary dislocations do not decomposes simultaneously when tensile deformation is applied in the *y*-direction.

In **Figure 9C**, we found that the critical strain value of grain boundary dislocation decomposition increases with the increase of grain boundary misorientations. This is because grain boundary dislocations increase with the grain boundary misorientations increase, thus the required critical strain value is larger. What we need to pay attention to is that 8° and 12° do not strictly follow this law. Similarly, we can analyze **Figure 9D**. It can be clearly observed that 8°, 9°, and 12° are special when applying y-direction tensile deformation. In order to better study the grain boundary misorientations and critical strain, we can analyze **Figures 9E,F**. It is obvious that no matter which direction of tensile strain is applied, 8° , 9°, and 12° are special angles. In addition, the critical strain value becomes larger with the increase of GBMs when the strain rate remains the same. This result is consistent with **Figures 9A,B**.

In summary, the critical strain ε increases with the increase of GBMs except for the special angle. Otherwise, decreasing the critical time steps of dislocations decomposition can be achieved by increasing the strain rate.

CONCLUSION

In this study, the phase-field crystal model of two modes is used to study the symmetry of grain boundary dislocation arrangement and the critical strain of grain boundary dislocation decomposition under different grain boundary misorientations and tensile strain directions. The results show that:

1) The *x*-direction tensile deformation is applied to the simulated samples with GBMs 6° and 7°. The grain boundary dislocations arrangement of the two systems is very similar from the equilibrium state to the complete decomposition, which shows a "bowknot" symmetrical structure. The dislocation arrangement in the two systems differs as the strain increases. Sub-grain boundaries appear in the larger GBM system, and the dislocation arrangement always shows asymmetrical structure of " bowknot " or "double bowknot." However, no sub-grain boundary is formed in the smaller GBM system under the same strain and the dislocation arrangement is no longer symmetrical.
2) The *y*-direction tensile deformation is applied to the 7°. The easiest to observe is the climbing direction of edge dislocations is opposite to *x*-direction tensile deformation. The initial grain boundary dislocations arrangement is basically the same and arranged symmetrically in a "bowknot" under *x*- and *y*-direction tensile deformation. With the increase of strain and under the same tensile strain, some grain boundary dislocations in the system with *y*-direction tensile strain will decomposition first and the dislocations arrangement is "like bowknot" symmetrical structure, while the dislocations under *x*-direction tensile strain do not decomposition and the arrangement unchanged.

3) The critical strains of dislocations decomposition are related to strain rate and GBM. The critical strain can be reached preferentially by increasing the strain rate appropriately or reducing the GBM.

DATA AVAILABILITY STATEMENT

The original contributions presented in the study are included in the article/**Supplementary Material**; further inquiries can be directed to the corresponding author.

AUTHOR CONTRIBUTIONS

HL: writing—original draft and editing. XW: writing—original draft, and formal analysis. HZ: writing—original draft, and formal analysis. XT: methodology and visualization. HH: conceptualization and formal analysis. YZ: editing, supervision, and project administration.

FUNDING

This work was supported by the National Natural Science Foundation of China (No. 52074246).

SUPPLEMENTARY MATERIAL

The Supplementary Material for this article can be found online at: https://www.frontiersin.org/articles/10.3389/fmats.2022.875519/full#supplementary-material

REFERENCES

Asadi, E., and Zaeem, M. A. (2015). A Modified Two-Mode Phase-Field Crystal Model Applied to Face-Centered Cubic and Body-Centered Cubic Orderings. *Comput. Mater. Sci.* 105, 110–113. doi:10.1016/j.commatsci.2015.04.004

Berry, J., Rottler, J., Sinclair, C. W., and Provatas, N. (2015). Atomistic Study of Diffusion-Mediated Plasticity and Creep Using Phase Field Crystal Methods. *Phys. Rev. B* 92, 134103. doi:10.1103/physrevb.92.134103

Bian, M. Z., Sasaki, T. T., Suh, B. C., Nakata, T., Kamado, S., and Hono, K. (2017). A Heat-Treatable Mg-Al-Ca-Mn-Zn Sheet Alloy with Good Room Temperature Formability. *Scr. Mater.* 138, 151–155. doi:10.1016/j.scriptamat.2017.05.034

Blixt, K. H., and Hallberg, H. (2022). Evaluation of Grain Boundary Energy, Structure and Stiffness from Phase Field Crystal Simulations. *Model. Simul. Mat. Sci. Eng.* 30, 014002. doi:10.1088/1361-651x/ac3ca1

Can, G., Zhi-Jun, W., Jin-Cheng, W., Yao-Lin, G., and Sai, T. (2013). Effect of the Direct Correlation Function on Phase Diagram of the Two-Mode Phase Field Crystal Model. *Acta Phys. Sin.* 62, 108104. doi:10.7498/aps.62.108104

Chen, L., and Zhao, Y. (2021). From Classical Thermodynamics to Phase-Field Method. *Prog. Mat. Sci.* 122, 100868. doi:10.1016/j.pmatsci.2021.100868

Elder, K. R., Katakowski, M., Haataja, M., and Grant, M. (2002). Modeling Elasticity in Crystal Growth. *Phys. Rev. Lett.* 88, 245701. doi:10.1103/physrevlett.88.245701

Gao, Y.-J., Deng, Q.-Q., Liu, Z.-y., Huang, Z.-J., Li, Y.-X., and Luo, Z.-R. (2020). Modes of Grain Growth and Mechanism of Dislocation Reaction under Applied Biaxial Strain: Atomistic and Continuum Modeling. *J. Mater. Sci. Technol.* 49, 236–250. doi:10.1016/j.jmst.2020.01.030

Greenwood, M., Provatas, N., and Rottler, J. (2010). Free Energy Functionals for Efficient Phase Field Crystal Modeling of Structural Phase Transformations. *Phys. Rev. Lett.* 105 (4), 045702. doi:10.1103/PhysRevLett.105.045702

Guo, H., Zhao, Y., Sun, Y., Tian, J., Hou, H., Qi, K., et al. (2019). Phase Field Crystal Study of Grain Boundary Structure and Annihilation Mechanism in Low-Angle Grain Boundary. *Superlattices Microstruct.* 129, 163–175. doi:10.1016/j.spmi.2019.03.020

Guo, S., Chen, H., and Wang, M. (2021). Research on the Dislocation Differences of CoCrFeMnNi with Different Local Chemical Orders during Room Temperature Tensile Test. *J. Alloys Compd.* 868, 159215. doi:10.1016/j.jallcom.2021.159215

Hirouchi, T., Takaki, T., and Tomita, Y. (2009). Development of Numerical Scheme for Phase Field Crystal Deformation Simulation. *Comput. Mater. Sci.* 44, 1192–1197. doi:10.1016/j.commatsci.2008.08.001

Hirouchi, T., Takaki, T., and Tomita, Y. (2010). Effects of Temperature and Grain Size on Phase-Field-Crystal Deformation Simulation. *Int. J. Mech. Sci.* 52, 309–319. doi:10.1016/j.ijmecsci.2009.09.036

Hou, X.-W., Tang, X.-Z., Zu, Q., and Guo, Y.-F. (2020). Plastic Deformation Mechanisms of Hierarchical Double Contraction Nanotwins in Mg. *J. Mat. Sci.* 55, 11701–11713. doi:10.1007/s10853-020-04789-y

Hu, S., Chen, Z., Peng, Y.-Y., Liu, Y.-J., and Guo, L.-Y. (2016b). Modeling and Simulation of Microcrack Propagation Behavior under Shear Stress Using Phase-Field-Crystal. *Comput. Mater. Sci.* 121, 143–150. doi:10.1016/j.commatsci.2016.04.035

Hu, S., Chen, Z., Yu, G.-G., Xi, W., and Peng, Y.-Y. (2016a). Phase-field-crystal Study on the Reaction Mechanisms of Opposite Sign Edge Dislocations Appearing in the Deformation Processes of Asymmetric Tilt Sub-grain Boundary System. *Comput. Mater. Sci.* 124, 195–203. doi:10.1016/j.commatsci.2016.07.030

Hu, S., Fan, J., Liu, Q., Li, J., and Wang, J. (2020). Phase-field-crystal Study on Shear-Induced Coupled Evolution of Intragranular Crack and Grain Boundary in Nanoscale Bicrystal System. *Eur. Phys. J. B* 93 (11), 212. doi:10.1140/epjb/e2020-10349-1

Kuang, W., Wang, H., Li, X., Zhang, J., Zhou, Q., and Zhao, Y. (2018). Application of the Thermodynamic Extremal Principle to Diffusion-Controlled Phase Transformations in Fe-C-X Alloys: Modeling and Applications. *Acta Mater.* 159, 16–30. doi:10.1016/j.actamat.2018.08.008

Kumar, K. S., Van Swygenhoven, H., and Suresh, S. (2003). Mechanical Behavior of Nanocrystalline Metals and alloys11The Golden Jubilee Issue-Selected Topics in Materials Science and Engineering: Past, Present and Future, Edited by S. Suresh. *Acta Mater.* 51, 5743–5774. doi:10.1016/j.actamat.2003.08.032

Li, X., Sha, A., Chen, B., and Chu, J. (2020). Effect of Microstructure on Tensile Deformation Behavior of Ti-3Al-4.5V-5Mo Titanium Alloy. *J. Aeronaut. Mater* 40, 45–52. doi:10.11868/j.issn.1005-5053.2020.000111

Liu, Y., Wang, L., He, S., Eng, F., Lv, X., and Zhang, B. (2012). Effect of Long-Term Aging on Dynamic Tensile Deformation Behavior of GH4169 Alloy. *Acta Metall. Sin.* 48, 49–55. doi:10.3724/sp.j.1037.2011.00435

Mahabadi, O. K., Tatone, B. S. A., and Grasselli, G. (2014). Influence of Microscale Heterogeneity and Microstructure on the Tensile Behavior of Crystalline Rocks. *J. Geophys. Res. Solid Earth* 119, 5324–5341. doi:10.1002/2014jb011064

Nielsen, B. F., Linga, G., Christensen, A., and Mathiesen, J. (2020). Substrate Curvature Governs Texture Orientation in Thin Films of Smectic Block Copolymers. *Soft Matter* 16, 3395–3406. doi:10.1039/c9sm02389e

Park, J. M., Yang, D. C., Kim, H.-J., Kim, D. G., Lee, S., Kim, H. S., et al. (2021). Ultra-strong and Strain-Hardenable Ultrafine-Grained Medium-Entropy Alloy via Enhanced Grain-Boundary Strengthening. *Mater. Res. Lett.* 9, 315–321. doi:10.1080/21663831.2021.1913768

Peng, F., Huang, W., Zhang, Z. Q., Guo, T. F., Ma, Y. E., and Zhang, Y. (2021). Conservational Integrals of the Fourth-Order Phase Field Model for Brittle Fracture via Noether Theorem. *Eng. Fract. Mech.* 245, 107590. doi:10.1016/j.engfracmech.2021.107590

Qi, K., Zhao, Y., Guo, H., Tian, X., and Hua, H. (2019). Phase Field Crystal Simulation of the Effect of Temperature on Low-Angle Symmetric Tilt Grain Boundary Dislocation Motion. *Acta Phys. Sin-Ch Ed.* 68, 80–89. doi:10.7498/aps.68.20190051

Qi, K., Zhao, Y., Tian, X., Peng, D., Sun, Y., and Hua, H. (2020). Phase Field Crystal Simulation of Effect of Misorientation Angle on Low-Angle Asymmetric Tilt Grain Boundary Dislocation Motion. *Acta Phys. Sin-Ch Ed.* 69, 69–78. doi:10.7498/aps.69.20200133

Roy, A., Devanathan, R., Johnson, D. D., and Balasubramanian, G. (2022). Grain-size Effects on the Deformation in Nanocrystalline Multi-Principal Element Alloy. *Mater. Chem. Phys.* 277, 125546. doi:10.1016/j.matchemphys.2021.125546

Shuai, X., Wang, Z. J., Mao, H., Tang, S., Kong, Y., and Du, Y. (2021). Atomic-scale Study of Compositional and Structural Evolution of Early-Stage Grain Boundary Precipitation in Al-Cu Alloys through Phase-Field Crystal Simulation. *J. Mat. Sci.* 56, 12700–12715. doi:10.1007/s10853-021-06064-0

Song, H. Y., Li, Y. L., and An, M. R. (2014). Atomic Simulations of the Effect of Twist Grain Boundaries on Deformation Behavior of Nanocrystalline Copper. *Comput. Mater. Sci.* 84, 40–44. doi:10.1016/j.commatsci.2013.11.052

Suh, B.-C., Kim, J. H., Bae, J. H., Hwang, J. H., Shim, M.-S., and Kim, N. J. (2017). Effect of Sn Addition on the Microstructure and Deformation Behavior of Mg-3Al Alloy. *Acta Mater.* 124, 268–279. doi:10.1016/j.actamat.2016.11.020

Tian, X.-l., Zhao, Y.-h., Peng, D.-w., Guo, Q.-w., Guo, Z., and Hou, H. (2021). Phase-field Crystal Simulation of Evolution of Liquid Pools in Grain Boundary Pre-melting Regions. *Trans. Nonferrous Metals Soc. China* 31, 1175–1188. doi:10.1016/s1003-6326(21)65570-x

Volnistem, E. A., Macková, L., Muniz, R. F., Estrada, F. R., de Nóbrega, S. M., Dias, G. S., et al. (2021). On the Effects of Dislocations on the Magnetism of BiFeO3 Nanoparticles. *J. Alloys Compd.* 887, 161421. doi:10.1016/j.jallcom.2021.161421

Wu, K. A., Adland, A., and Karma, A. (2010). Phase-field-crystal Model for Fcc Ordering. *Phys. Rev. E Stat. Nonlin Soft Matter Phys.* 81, 061601. doi:10.1103/PhysRevE.81.061601

Xia, Q., Liang, Y., Yang, C., Zhang, S., and Ou, M. (2019). Tensile Deformation Behavior of TC4 Titanium Alloy. *RATE Met.* 43, 765–773. doi:10.13373/j.cnki.cjrm.xy18040023

Xin, T., Zhao, Y., Mahjoub, R., Jiang, J., Yadav, A., Nomoto, K., et al. (2021). Ultrahigh Specific Strength in a Magnesium Alloy Strengthened by Spinodal Decomposition. *Sci. Adv.* 7, 1–9. doi:10.1126/sciadv.abf3039

Yan, M., Yuan, F., and Wu, X. (2021). Dynamic Shear Behaviors and Microstructural Deformation Mechanisms in FeNiAlC Dual-phase High Strength Alloy. *Explos. Shock Waves* 41 (1), 34–45. doi:10.11883/bzycj-2020-0224

Yang, T., Zhang, J., Long, J., Long, Q.-H., and Chen, Z. (2014). Phase Field Crystal Study of the Crystallization Modes within the Two-phase Region. *Chin. Phys. B* 23, 088109. doi:10.1088/1674-1056/23/8/088109

Yang, Y., Zhao, Y., Tian, X., and Hou, H. (2020). Microscopic Phase-Field Simulation for Precipitation Process of $Ni_{60}Al_{20}V_{20}$ Medium Entropy Alloy. *Acta Phys. Sin-Ch Ed.* 69, 29–38. doi:10.7498/aps.69.20200154

Zhang, J., Wang, H., Kuang, W., Zhang, Y., Li, S., Zhao, Y., et al. (2018). Rapid Solidification of Non-stoichiometric Intermetallic Compounds: Modeling and Experimental Verification. *Acta Mater.* 148, 86–99. doi:10.1016/j.actamat.2018.01.040

Zhang, S., Chen, Z., and Yang, Y. (2014). Simulation of Structure and Deformation of Asymmetrical Tilt Grain Boundaries with Small Misorientation Angles by Two-Mode Phase Field Crystal Method. *Rare Metal. Mat. Eng.* 43, 610–614. 1002-185X(2014)03-0610-05.

Zhang, X., Huang, L. K., Zhang, B., Chen, Y. Z., Duan, S. Y., Liu, G., et al. (2019). Enhanced Strength and Ductility of A356 Alloy Due to Composite Effect of Near-Rapid Solidification and Thermo-Mechanical Treatment. *Mater. Sci. Eng. A* 753, 168–178. doi:10.1016/j.msea.2019.03.039

Zhao, Y.-H., Tian, X.-L., Zhao, B., Sun, Y., Guo, H., Dong, M., et al. (2018). Precipitation Sequence of Middle Al Concentration Alloy Using the Inversion Algorithm and Microscopic Phase Field Model. *Sci. Adv. Mater* 10, 1793–1804. doi:10.1166/sam.2018.3430

Zhao, Y., Chen, Z., Long, J., and Yang, T. (2014). Influence of Temperature on the Inverse Hall-Petch Effect in Nanocrystalline Materials: Phase Field Crystal Simulation. *Acta Metall. Sin. Engl. Lett.)* 27, 81–86. doi:10.1007/s40195-014-0027-5

Zhao, Y., Jing, J., Chen, L., Xu, F., and Hou, H. (2021). Current Research Status of Interface of Ceramic-Metal Laminated Composite Material for Armor Protection. *Acta Metall. Sin.* 57, 1107–1125. doi:10.11900/0412.1961.2021.00051

Zhao, Y., Zhang, B., Hou, H., Chen, W., and Wang, M. (2019). Phase-field Simulation for the Evolution of Solid/Liquid Interface Front in Directional Solidification Process. *J. Mater. Sci. Technol.* 35, 1044–1052. doi:10.1016/j.jmst.2018.12.009

Conflict of Interest: The authors declare that the research was conducted in the absence of any commercial or financial relationships that could be construed as a potential conflict of interest.

Publisher's Note: All claims expressed in this article are solely those of the authors and do not necessarily represent those of their affiliated organizations, or those of the publisher, the editors, and the reviewers. Any product that may be evaluated in this article, or claim that may be made by its manufacturer, is not guaranteed or endorsed by the publisher.

frontiers | Frontiers in Materials

ORIGINAL RESEARCH
published: 30 June 2022
doi: 10.3389/fmats.2022.935129

The Effective Diffusion Coefficient of Hydrogen in Tungsten: Effects of Microstructures From Phase-Field Simulations

Bingchen Li[1,2], *Bowen Xue*[1,2], *Jiannan Hao*[1,2], *Shuo Jin*[1,2], *Hong-Bo Zhou*[1,2], *Linyun Liang*[1,2]* *and Guang-Hong Lu*[1,2]*

[1]School of Physics, Beihang University, Beijing, China, [2]Beijing Key Laboratory of Advanced Nuclear Materials and Physics, Beihang University, Beijing, China

In this work, we propose an efficient numerical method to study the effects of microstructures on the effective diffusion coefficient of the diffusion component in materials. We take the diffusion of hydrogen (H) atoms in porous polycrystalline tungsten (W) as an example. The grain structures and irradiated void microstructures are generated by using the phase-field model. The effective diffusion coefficients of H in these microstructures are obtained by solving the steady-state diffusion equation, using a spectral iterative algorithm. We first validate our simulation code for calculating the effective diffusion coefficient by using three simple examples. We then investigate the effects of the grain morphology and porosity on the effective diffusion coefficient of H in W. Regardless of whether the grain boundary is beneficial to the diffusion of H or not, it is found that the effective diffusion coefficient of H along the elongated grain direction in columnar crystals is always greater than that in isometric crystals. The increase of the porosity can significantly decrease the effective diffusion coefficient of H from the simulations of the porous W. A correlation of converting the two-dimensional (2D) effective diffusion coefficient into three-dimensional (3D) in the porous and polycrystalline W is fitted by using our simulation data, respectively. Two fitted correlations can be used to predict the synergistic effect of the porosity and grain boundary on the effective diffusion coefficient of H in W. Consequently, our simulation results provide a good reference for understanding the influence of the complex microstructures on H diffusion, and may help to design W-based materials for the fusion reactor.

Keywords: phase-field, microstructure evolution, effective diffusion coefficient, hydrogen, tungsten

OPEN ACCESS

Edited by:
Yu-Hong Zhao,
North University of China, China

Reviewed by:
Yongxin Wang,
Northwestern Polytechnical University, China
Chunguang Yang,
Institute of Metal Research (CAS), China
Yong Ni,
University of Science and Technology of China, China

***Correspondence:**
Linyun Liang
lyliang@buaa.edu.cn
Guang-Hong Lu
lgh@buaa.edu.cn

Specialty section:
This article was submitted to Computational Materials Science, a section of the journal Frontiers in Materials

Received: *03 May 2022*
Accepted: *30 May 2022*
Published: *30 June 2022*

Citation:
Li B, Xue B, Hao J, Jin S, Zhou H-B, Liang L and Lu G-H (2022) The Effective Diffusion Coefficient of Hydrogen in Tungsten: Effects of Microstructures From Phase-Field Simulations. Front. Mater. 9:935129. doi: 10.3389/fmats.2022.935129

1 INTRODUCTION

Due to the energy crisis caused by the exploitation of the limited fossil energy, nuclear fusion energy with many potential advantages such as abundant raw materials, pollution-free products, and high energy efficiency, has been constantly studied. The Tokamak, a magnetically confined fusion device, is considered to be the most likely future fusion device (Artsimovich, 1972). In the nuclear fusion reactor environment, tungsten (W) has been considered as one of the most promising candidate materials for plasma-facing materials (PFMs), owing to its advantages of high melting point, good thermal conductivities, as well as low sputtering rate (Bolt et al., 2004; Cottrell, 2004). However,

PFMs will be irradiated by high energy neutron (14 MeV) in combination with the high temperature ($300 < T < 2000$ K) (Li et al., 2017), which will inevitably induce microstructure changes such as grain boundary migration (Stepper, 1972; Vaidya and Ehrlich, 1983; Mannheim et al., 2018), and second-phase formation (voids/dislocations caused by clustering of point defects (Hasegawa et al., 2014; Hu et al., 2016), precipitates formed by the precipitation of the transmutation elements (Hasegawa et al., 2016)), etc. Besides, hydrogen (H) and its isotope escaped from the plasma can penetrate through the W surfaces and diffuse inside the bulk under plasma irradiation (El-Kharbachi et al., 2014; Hodille et al., 2014; Grisolia et al., 2015). The interaction between H and the defect microstructures may result in a set of safety issues of W such as surface blistering (Zhou H. et al., 2019), embrittlement (Louthan et al., 1972), and cracking (Ueda et al., 2005), which can notably degrade the mechanical and thermal properties of W and thus reduce its service lifetime. In addition, H and its isotope are very expensive reactants, finding a way to recycle them can greatly reduce the cost. The diffusion process of H and its isotope in such complex microstructures is extremely important. Therefore, understanding the effect of the microstructure on the diffusion of H is critical to improving the irradiation properties and reducing the cost of fuels.

Recently, numerous simulations and experimental studies have been conducted on the H diffusion in the bulk (Frauenfelder, 1969; Heinola et al., 2010a; Yang and Oyeniyi., 2017) and on the surface of W (Heinola and Ahlgren, 2010b; Xue and Hassanein, 2014; Yang and Wirth, 2019), as well as the effect of irradiated defects such as vacancies (Eleveld and Veen, 1994; Liu et al., 2009; Johnson and Carter, 2010), dislocations (Taketomi et al., 2008; Kimizuka and Ogata, 2011; Wang et al., 2019), and grain boundaries (Oudriss et al., 2012; Yu et al., 2014; González et al., 2015; Fu et al., 2021) on the H diffusion. The thermal desorption experimental results show that the H diffusion is influenced by various factors such as defect type (Jin et al., 2017), distribution (Fujita et al., 2017), temperature (Rieth et al., 2019), and annealing time (Sakurada et al., 2017). In addition, it is found that the desorption temperature of H from vacancies or voids does not exceed 800 K (Eleveld and Veen, 1994), and from grain boundaries is about 400–500 K (Hodille et al., 2017). And the molecular dynamics studies indicate that the H diffusion largely depends on the type of grain boundaries, i.e., certain types of grain boundaries (e.g., $\sum 5(310)[001]$) can promote the H diffusion (Yu et al., 2014), while others (e.g., $\sum 25(430)[100]$) can inhibit it (Zhou X. et al., 2019) compared to it in the bulk. Vacancies always hinder the H diffusion in W, the diffusion coefficient of H can be reduced by two orders of magnitude in the single crystalline W when the mono-vacancy concentration is only 0.5% at 1800 K and this effect becomes more obvious with the increase of the vacancy concentration (Wang et al., 2019). Results also show that the materials with mono-vacancies have a stronger inhibition effect on H diffusion than that containing vacancy clusters with the same porosity, due to mono-vacancies can provide more H capture sites (Wang et al., 2019). Despite atomistic simulations can give the microscopic mechanism of H interacting with defects, they are hard to predict the effective diffusion coefficient at the microstructural scale due to the limited spatial and time scales. Several analytical models have been developed to estimate the effective diffusion coefficient of the diffusion component in microstructures (Maxwell, 1881; Hart, 1957; Bakker et al., 1995; Chen and Schuh, 2007; Moradi, 2015; Jiang et al., 2021). Maxwell-Garnett et al. (Maxwell, 1881; Moradi, 2015) developed a model to predict the effect of the volume fraction of the second phase on the effective diffusion coefficient in a two-phase system. Hashin-Shtrikman et al. developed a model (Chen and Schuh, 2007) to calculate the effective diffusion coefficient in isometric polycrystalline materials, etc. However, these analytical models have difficulties in giving the inhomogeneous concentration distribution of the diffusion component intuitively, and more importantly, they are far from enough to investigate the effect of the complex microstructural features (e.g., arrangement and morphology) on the effective diffusion coefficient of the diffusion component in materials.

In this work, we demonstrate an efficient numerical method to study the effect of the microstructure on the H effective diffusion coefficient in W at relevant high temperatures. Grain structures and irradiated voids are considered as the main defect microstructures generated by using phase-field simulations, although other defect microstructures such as dislocations, precipitates, and gas bubbles can also be easily incorporated in the model. A spectral iterative algorithm (Wang et al., 2016; Li et al., 2022) is used to solve the stationary diffusion equation based on the phase-field microstructures to obtain the effective diffusion coefficient. The current method is only applied at high temperature or there is no interaction between the diffusion component and microstructure, where H atoms can be eventually desorbed from grain boundaries and voids consisting with the thermal desorption experimental observations (Eleveld and Veen, 1994; Hodille et al., 2014). Using this method, the effects of grain boundaries, voids, and their synergistic effect on the effective diffusion coefficient of H are systematically investigated in W. Two sets of correlations that can be used to transfer the two-dimensional (2D) into three-dimensional (3D) effective diffusion coefficient are fitted based on our simulation results, which can be used to predict the effective diffusion coefficient of H in the porous polycrystalline W. We believe that this method provides a good reference for understanding the influence of the microstructure on the H diffusion in W, and offers an efficient way to study the effect of the complex microstructure on the effective diffusion coefficient in other similar systems.

2 COMPUTATIONAL DETAILS

2.1 Phase-Field Model of Microstructure Evolutions

Controlling the grain size is a common way to tune the thermal and mechanical properties of the polycrystalline W. Within the phase-field model, a set of continuous non-conservative phase variables η_i ($i = 1, \ldots, n$) are used to represent the different grain orientations, in which n is the total number of the grain orientations. Following the free energy of describing the grain

growth developed by Chen et al. (Fan and Chen, 1997; Krill and Chen, 2002), the total free energy of the system can be written as,

$$F_{total}^{poly} = \int \left[m f_0(\eta_1(r), \eta_2(\boldsymbol{r}), \ldots, \eta_n(r)) + f_{grad}^{poly}(\eta_1(r), \eta_2(r), \ldots, \eta_n(r)) \right] dV, \tag{1}$$

where f_0 is a local microstructural energy density, and f_{grad}^{poly} is the gradient energy density contributed by the grain boundary. $\boldsymbol{r} = \{x, y, z\}$ is the spatial coordinate, m is a positive constant associated with the grain boundary width and energy, and V is the volume of the simulated system. Boldface characters (e.g., $\boldsymbol{r}$) denote vectors in this work.

The local microstructural free energy density can be formulated as (Fan and Chen, 1997; Krill and Chen, 2002)

$$f_0(\eta_1, \eta_2, \ldots, \eta_n) = \sum_i^n \left[-\frac{1}{2}\eta_i^2 + \frac{1}{4}\eta_i^4 + \frac{1}{4} \right] + \gamma \sum_i^n \eta_i^2 \sum_{j(j>i)}^n \eta_j^2, \tag{2}$$

where the first term describes a multi-well potential with a minimal value zero located at $\eta_i = 1$ and $\eta_j = 0$, ($j \neq i$). The second term represents an energy penalty term among adjacent grains, and γ is a positive constant that equals 1.5 (Moelans et al., 2008).

The gradient energy terms contributed by the grain boundaries are written as

$$f_{grad}^{poly} = \frac{k_\eta}{2} \sum_i |\nabla \eta_i|^2, \tag{3}$$

where k_η is the gradient coefficient.

The evolution of the grain parameters is controlled by the Allen-Cahn equation (Allen and Cahn, 1972; Allen and Cahn, 1973),

$$\frac{\partial \eta_i}{\partial t} = -L_{GB} \frac{\delta F_{total}^{poly}}{\delta \eta_i}, i = 1, 2, 3, \ldots, n, \tag{4}$$

where $L_{GB} = L_0 e^{-\frac{E_a}{k_B T}}$ is a temperature-dependent kinetic coefficient related to the migration of grain boundaries, L_0 is a constant, E_a is the activation energy of the grain boundary migration, k_B is the Boltzmann's constant, and T is the annealing temperature. By solving the above equation, we can get the polycrystalline structure with designed grain size of W. We then fix the grain structure to further simulate the void formation in W by using a phase-field model.

A high density of point defects will be produced in W due to the high-energy neutron irradiation (Eleveld and Veen, 1994; Hasegawa et al., 2014; Hasegawa et al., 2016; Hu et al., 2016). Although the interstitial atoms and vacancies are always generated in pairs, we only consider the evolution of vacancies based on the fact that the diffusion coefficient of the interstitial atom is at least 10^3 magnitudes larger than that of the vacancy in W at $300 < T < 2000$ K (Hao et al., 2020). Therefore, the diffusion of vacancies is the rate-controlling process in the formation of voids and the interstitial atoms can be always considered at the equilibrium state. This scenario was also used in previous work to study the effect of the void evolution on effective thermal conductivities in W (Wang et al., 2018). And it will not affect our main conclusions since the objective of this work is to investigate the effects of the porosity and void size on the effective diffusion coefficient of H in W.

In the phase-field model, a conservative phase variable $C_v(r, t)$ is used to describe the vacancy concentration and a non-conservative phase variable $\varphi(r, t)$ is used to distinguish the matrix phase and void phase. $\varphi(r, t)$ equals 1.0 in the void phase and zero in the matrix phase, and continuously changes from 1.0 to zero across the void-matrix interface. Following the Kim-Kim-Suzuki (KKS) model (Kim et al., 1999; Kim, 2007), the free energy density employed for the void evolution is described as

$$F_{total}^{void} = \int \left[h(\varphi) f^v + (1 - h(\varphi)) f^m + w g(\varphi) + f_{grad}^{void}(\varphi) \right] dV, \tag{5}$$

$$f^m = \frac{k_B T}{\Omega} \left(C_m^v \ln C_m^v / C_{eq}^v + (1 - C_m^v) \ln (1 - C_m^v) \right), \tag{6}$$

$$f^v = \frac{k_B T}{\Omega} (C_v^v - 1.0)^2, \tag{7}$$

where f^m and f^v is the free energy of the matrix and void phase, respectively. $\Omega = 1.5 \times 10^{-29}$ m^3 is the atomic volume of W. C_m^v and C_v^v is the vacancy concentration in the matrix and void phase, respectively, and C_{eq}^v is the thermodynamic equilibrium concentration of the vacancy in the matrix phase. $h(\varphi) = \varphi^3(6\varphi^2 - 15\varphi + 10)$ is a monotonous interpolation function satisfying $h(0) = 0$ and $h(1) = 1$, w is a constant, and $g(\varphi) = \varphi^2(1 - \varphi^2)$ is a double-well potential function.

The gradient energy term contributed by the void-matrix interface is written as

$$f_{grad}^{void} = \frac{k_\varphi}{2} |\nabla^2 \varphi|, \tag{8}$$

where k_φ is the gradient coefficient.

The temporal and spatial evolution equations of the phase variable and concentration can be described by the Allen-Cahn (Allen and Cahn, 1972; Allen and Cahn, 1973) and Cahn-Hilliard equations (Cahn and Hilliard, 1958; Cahn and Hilliard, 1958) as

$$\frac{\partial \varphi}{\partial t} = -L_v \frac{\delta F_{total}^{void}}{\delta \varphi} + \xi_\varphi(r, t) + P_v, \tag{9}$$

$$\frac{\partial C_v}{\partial t} = \nabla . M_v \nabla \frac{\delta F_{total}^{void}}{\delta C_v} + \xi_{C_v}(r, t) + P_v - S(1 - \Phi) C_v, \tag{10}$$

where $M_v = \frac{D_V \Omega}{k_B T}$ is the mobility of a vacancy, D_V is the diffusion coefficient of a vacancy, and L_v is the kinetic coefficient. $\xi(r, t)$ is a stochastic function. The last term in **Eq. 10** represents the annihilation of vacancies by grain boundaries (Millett et al., 2009), and S is the interaction intensity set as 1.0 to meet the experimental observation of no cavity nucleation on grain boundaries (Klimenkov et al., 2016). The term $\Phi = \eta_i^2$ is employed to ensure that the interaction is only valid at grain boundaries instead of within grains (Chen and Yang 1994). P_v is the source term of vacancies generated by cascade collisions caused by neutron irradiation, which can be described as (Millett et al., 2009),

$$P_v(\boldsymbol{r}, t) = \begin{cases} 0 & \varphi \gg 0.8 \text{ or } R_1 > P_{casc} \\ R_2 V_G & \varphi < 0.8 \text{ and } R_1 < P_{casc} \end{cases}, \tag{11}$$

where P_{casc} is the probability of cascade collisions at each grid point for each time step, which is related to the neutron irradiation, and V_G is the maximum net increase in vacancy concentration from cascade events. R_1 and R_2 are random numbers between zero and 1.0.

According to the assumption of the KKS model that the total concentration is a mixture of two phases and the chemical potential is the same at every position in the system (Kim et al., 1999; Kim, 2007), the concentrations satisfy the following two equations,

$$C_v = h(\varphi)C_v^v + (1 - h(\varphi))C_m^v, \tag{12}$$

$$\frac{\partial f^v}{\partial C_v^v} = \frac{\partial f^m}{\partial C_m^v}. \tag{13}$$

To sum up, the evolution **Eqs. 9**, **10** can be rewritten as

$$\frac{\partial \varphi_i}{\partial t} = -L_v\left\{h'(\varphi)\left[(f^v - f^m) + \frac{\partial f^v}{\partial C_v^v}(C_m^v - C_v^v)\right] - k_\varphi \nabla^2 \varphi_i + w g'(\varphi)\right\} + \xi_\varphi(r,t), \tag{14}$$

$$\frac{\partial C_v}{\partial t} = M_v \nabla^2\left(\frac{\partial f^v}{\partial C_v^v}\right) + \xi_{C_v}(r,t) - S(1-\Phi)C_v, \tag{15}$$

The semi-implicit FFTW numerical method is used to solve the **Eqs. 4**, **14**, **15** (Chen and Shen, 1998). A Newton's method is adopted to solve the nonlinear **Eqs. 12**, **13** for each time step.

2.2 Effective Diffusion Coefficient of H

Once we have the phase-field simulated grain structures and voids in W, we can investigate the effects of these microstructure evolutions on the effective diffusion coefficient of H. To do so, we solve the steady-state diffusion equation,

$$\frac{\partial}{\partial r_i}\left(D_{ij}(\boldsymbol{r})\frac{\partial C(\boldsymbol{r})}{\partial r_j}\right) = 0, \tag{16}$$

where $D_{ij}(\boldsymbol{r})$ is the microstructure-dependent diffusion coefficient tensor, which has different values in the bulk, grain boundary, and void in W and can be written as follows,

$$D_{ij} = \begin{cases} D_{ij}^m & (\eta > 0.9 \text{ and } \varphi < 0.5) \\ D_{ij}^{GB} & (\eta \le 0.9) \\ D_{ij}^{void} & (\varphi \ge 0.5) \end{cases}, \tag{17}$$

where D_{ij}^m, D_{ij}^{GB}, and D_{ij}^{void} is the H diffusion coefficient in the bulk, grain boundary, and void phase, respectively. In this inhomogeneous system, we can separate the diffusion coefficient into the homogeneous part D_{ij}^0 independent of the position and the inhomogeneous part $\Delta D_{ij}(\boldsymbol{r})$ dependent on the position. Thus, the H diffusion coefficient $D_{ij}(\boldsymbol{r})$ can be written as

$$D_{ij}(\boldsymbol{r}) = D_{ij}^0 + \Delta D_{ij}(\boldsymbol{r}), \tag{18}$$

Accordingly, the stationary distribution of the H concentration can be separated into linear and nonlinear parts, which corresponds to the homogeneous and inhomogeneous diffusion coefficient, respectively, i.e.,

$$C(\boldsymbol{r}) = C^{linear}(\boldsymbol{r}) + C^{non-linear}(\boldsymbol{r}), \tag{19}$$

where $C^{linear}(\boldsymbol{r})$ is the linear part of the concentrate, and $C^{non-linear}(\boldsymbol{r})$ is the nonlinear part that comes from the inhomogeneous distribution of the concentrate.

Based on the Fick's first law, the flux of the H concentration along the j-direction is expressed as

$$J_i = -D_{ij}(\boldsymbol{r})\partial C \big/ \partial r_j, \tag{20}$$

where $\partial C/\partial r_j$ is the gradient of the concentration along the j-direction.

Finally, the effective diffusion coefficient tensor D_{ij}^{eff} of the system caused by the inhomogeneous microstructure can be determined by solving

$$D_{ij}^{eff} = -\langle J_i \rangle \big/ \langle \partial C \big/ \partial r_j \rangle, \tag{21}$$

where J_i is the averaged flux along the i-direction, and $\partial C/\partial r_j$ represents the averaged concentration gradient along the j-direction.

To solve the steady-state diffusion equation shown in **Eq. 16**, a spectral iterative method is adopted, which has been used to solve the heat conduction equation in previous work (Wang et al., 2016; Li et al., 2022). In order to facilitate the reader's understanding, we present the details of the solution process here. Firstly, combining the **Eqs 18**, **19**, the **Eq. 16** can be rewritten as,

$$\frac{\partial}{\partial r_i}\left[\left(D_{ij}^0 + \Delta D_{ij}(\boldsymbol{r})\right)\left(\frac{\partial C^{linear}(\boldsymbol{r})}{\partial r_j} + \frac{\partial C^{non-linear}(\boldsymbol{r})}{\partial r_j}\right)\right] = 0, \tag{22}$$

Then rearranging the **Eq. 22**, we get

$$D_{ij}^0 \frac{\partial^2 C^{non-linear}(\boldsymbol{r})}{\partial r_i \partial r_j} = -\frac{\partial}{\partial r_i}\left[\Delta D_{ij}(\boldsymbol{r})\left(\frac{\partial C^{linear}(\boldsymbol{r})}{\partial r_j} + \frac{\partial C^{non-linear}(\boldsymbol{r})}{\partial r_j}\right)\right]. \tag{23}$$

After that, by taking the Fourier transform on both sides of **Eq. 23**, we have,

$$-D_{ij}^0 \xi_i \xi_j C^{non-linear}(\xi) = -\xi_i\left[\Delta D_{ij}(r)\left(\frac{\partial C(r)}{\partial r_j}\right)\right]_\xi, \tag{24}$$

where $C^{non-linear}(\xi)$ and $[\Delta D_{ij}(r)(\frac{\partial C(r)}{\partial r_j})]_\xi$ is the Fourier transform of $C^{non-linear}(r)$ and $\Delta D_{ij}(r)(\frac{\partial C(r)}{\partial r_j})$, respectively.

Thus, we can get

$$C^{non-linear}(\xi) = IG(\boldsymbol{\xi})\xi_i\left[\Delta D_{ij}(\boldsymbol{r})\left(\frac{\partial C(\boldsymbol{r})}{\partial r_j}\right)\right]_\xi, \tag{25}$$

where $G(\xi)^{-1} = k_{ij}^0 \xi_i \xi_j$, and I is the imaginary unit. At last, by taking the inverse Fourier transforms on both sides of **Eq. 25**, the nonlinear part concentration distribution can be written as,

$$C^{non-linear}(\boldsymbol{r}) = \int \frac{d^3\xi}{(2\pi)^3} C^{non-linear}(\boldsymbol{\xi}) e^{I\xi \cdot r}, \tag{26}$$

To sum up, the total concentration distribution $C(r)$ shown in **Eq. 19** can be calculated as,

$$C(\boldsymbol{r}) = C^{non-linear}(r) + \int \frac{\partial C^{linear}(r)}{\partial r_j} dr_j, \tag{27}$$

Once we have the total concentration $C(r)$, $\partial C/\partial r_j$ and the flux can be calculated based on **Eq. 20**. Thus, the effective diffusion coefficient D_{ij}^{eff} can be obtained by using **Eq. 21**.

2.3 Simulation Details and Parameters

To simulate the grain growth and void microstructure evolutions, the phase-field **Eqs. 4**, **14**, **15** are numerically solved with periodic boundary conditions. The time step for the grain growth is set at 2.4 s, and the grid spacing is $\Delta x = \Delta y = \Delta z = 1.0$ nm. A model sizes of 256.0 nm × 256.0 nm in 2D and 96.0 nm × 96.0 nm × 96.0 nm in 3D are used. According to Moelans et al. (Moelans et al., 2008), the gradient coefficient k_η and potential height m can be obtained by $\sigma_{gb} = \sqrt{2mk_\eta}/3$ and $l_{gb} = \sqrt{8k_\eta/m}$ once the grain boundary energy σ_{gb} and length l_{gb} were given. In this work, $\sigma_{gb} = 2.32\,\mathrm{J}\,m^{-2}$ is determined by averaging the grain boundary energies of 408 grain boundaries of W (Ratanaphan et al., 2017), and l_{gb} is assumed to be 4.0 nm to ensure there are sufficient grid points across the diffused interface. The grain boundary migration energy E_a is 0.6 eV based on the annealing experiment of the grain growth in W (Guo et al., 2018), and L_0 is $8.33 \times 10^{-6} m^3\,\mathrm{J}^{-1}\,\mathrm{s}^{-1}$ obtained by fitting the annealing experimental results of the grain growth (Guo et al., 2018; Li et al., 2022).

The input parameters for simulating the void evolutions under irradiation are set as follows. The sizes of the simulation domain are set as 256 Δx × 256 Δy in 2D and 64 Δx × 64Δy × 64 Δz in 3D. The time scale is set as 10^{-9} s. According to the previous work, the gradient coefficient k_φ and the potential height w can be obtained by $\sigma_{void} = \frac{\sqrt{\omega k_\eta}}{3\sqrt{2}}$ and $l_{width} = 2.2\sqrt{\frac{2k_\eta}{\omega}}$ (Aagesen et al., 2021), where the surface energy σ_{void} is set as $1.0\,\mathrm{J\,m}^{-2}$ (Briant and Walter, 1988), and interface width $l_{width} = 4.0$ nm. Following the Arrhenius formula, $D_V = D_0 \times e^{\frac{E_a^v}{K_B T}}$, in which D_0 is the pre-exponential factor and E_a^v *is* the activation energy of the vacancy diffusion. They are equal to $4.0 \times 10^{-6}\,\mathrm{m}^2\,\mathrm{s}^{-1}$ and 1.8 eV based on the experimental measurements (Rasch and Schultz 1980).

The diffusion coefficients of H in the bulk, grain boundary, and void are required to calculate the effective diffusion coefficient of H in W. Previous atomistic simulations have listed the diffusion coefficient of H in the bulk is $5.13 \times 10^{-8}\, e^{0.21\ \mathrm{eV}/k_B T}\,\mathrm{m}^2\,\mathrm{s}^{-1}$ at the temperature range of 200–3000 K (Liu et al., 2014). The effect of the grain boundary on the H diffusion largely depends on the type of the grain boundary (Yu et al., 2014; Zhou et al., 2019B). Thus, we systematically study the effect of the grain boundary on the effective diffusion coefficient of H by using various diffusion coefficients. The diffusion coefficient of H in the void is set to be zero due to the strong inhibition of the vacancy/void on H diffusion (Wang et al., 2019). It should be noted that we assume our model is an ideal phase-field model with ignoring the effect of the faster diffusion of H along the inner surface of the irradiated voids on the effective diffusion coefficient to simplify the calculation. To ensure there is a flow of the H concentration along its diffusion direction, the concentrates on the two boundaries perpendicular to the H diffusion orientations are fixed at 0.4 and 0.1. These boundary values do not affect our main calculation results. The H concentration on other boundaries is fixed at 0.4.

3 RESULTS AND DISCUSSIONS

We first use three simple structures having analytical solutions of the effective diffusion coefficient to validate our simulation code. We then quantitively calculate the effective diffusion coefficient of H in the polycrystalline and porous W. A correlation of converting the 2D effective diffusion coefficient into 3D in the porous polycrystalline W is fitted by using our simulation data, respectively. The effects of the grain morphology, porosity, and their synergistic effect on the effective diffusion coefficient of H are systematically investigated.

3.1 Simulation Code Validation

Three simple structures are used to fully validate our simulation code for calculating the effective diffusion coefficient of the diffusion component, including a two-phase structure consisting of two different arrangements of slabs (parallel and perpendicular to each other), a spherical structure embedded in a cubic box, and a 3D isometric crystalline structure. The calculated effective diffusion coefficients are compared with the analytical solutions to verify our simulation code.

3.1.1 Two Slab Structures for Validation

We first use a two-phase system with a simple slab structure to validate the code since it has an analytical solution. Two different configurations of the two-phase system are constructed. One is that these two slabs are parallel to each other (**Figure 1A**), while the other one is that they are perpendicular to each other (**Figure 1B**). For the first structure shown in **Figure 1A**, the effective diffusion coefficient along the X and Y direction can be described analytically as (Hart, 1957; Jiang et al., 2021)

$$D_x^{eff} = D_b + \frac{2w_{slab}}{L_x}(D_{slab} - D_b), \tag{28}$$

$$D_y^{eff} = \frac{D_b D_{slab}}{\left(1 - \frac{2w_{slab}}{L_x}\right) D_{slab} + \frac{2w_{slab}}{L_x} D_b}, \tag{29}$$

where D_b and D_{slab} is the diffusion coefficient in the matrix and slab phase, respectively. w_{slab} and L_x is the width of the slab phase and the side length of the simulation domain.

For the other configuration of the slab structure shown in **Figure 1B**, the effective diffusion coefficients along the X and Y

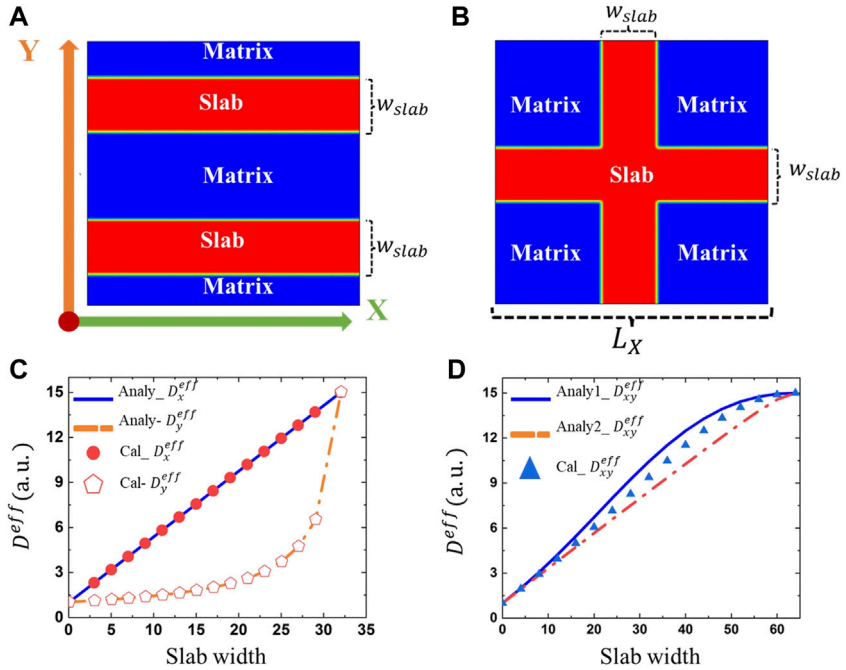

FIGURE 1 | A two-phase system with a simple slab structure **(A)** parallel with each other, and **(B)** intersect with each other. **(C)** Comparison between the calculated and theoretical effective diffusion coefficients as a function of the slab width for structure **(A)**, and **(D)** for structure **(B)**. The diffusion coefficient in the matrix and slab phase is set as 15.0 and 1.0 in the same unit, respectively.

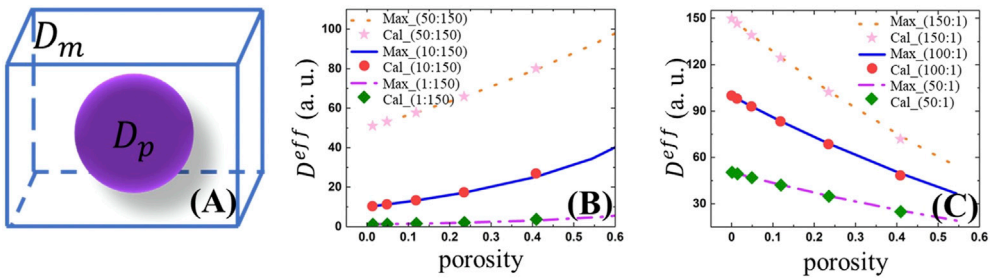

FIGURE 2 | (A) A spherical phase is embedded in a cubic box. Comparison of simulated and analytical effective diffusion coefficients as a function of the volume fraction of the spherical phase for three different diffusion coefficient ratios **(B)** D_p/D_m >1.0 and **(C)** D_p/D_m <1.0. The scatter points represent the simulation results, and the curves represent the results calculated by the Maxwell-Garnett model (Maxwell, 1881; Moradi, 2015).

direction are the same because of the symmetric structure. Two different solutions derived by Jiang et al. based on **Eqs 28**, **29** are respectively expressed as (Jiang et al., 2021)

$$D_1^{eff} = \left(1 - \frac{w_{slab}}{L_x}\right)\left(\frac{D_b D_{slab}}{\left(1 - \frac{w_{slab}}{L_x}\right)D_{slab} + \frac{w_{slab}}{L_x}D_{slab}}\right) + \frac{D_{slab}}{L_x}D_b, \tag{30}$$

$$D_2^{eff} = D_{slab}L_x \frac{D_b L_x - D_b w_{slab} + D_{slab} w_{slab}}{D_b L_x w_{slab} - D_b w_{slab}^2 + D_{slab} L_x^2 - D_{slab} L_x w_{slab} + D_{slab} w_{slab}^2} \tag{31}$$

It is believed that the true solution of this configuration should be somewhere in between these two solutions. We then calculate the effective diffusion coefficient in these two-phase structures by solving **Eq. 16**, where D_b is set to 15.0 and D_{slab} is set to 1.0. The simulation and analytical results as a function of the width of the slab phase are compared as shown in **Figures 1C, D**. Cal_D_x^{eff} and Cal_D_x^{eff} are numerical results. Analy_D_x^{eff} and Analy_D_y^{eff} represent the analytical results along the X and Y orientations based on **Eqs 28**, **29**. From **Figure 1C**, it can be seen that the numerical and analytical solutions are almost identical for the first slab structure in **Figure 1A**. For the second configuration as shown in **Figure 1B**, our simulation results shown in **Figure 1D** are within those predicted by two different analytical formulas as expected. Thus, these results can preliminarily validate our simulation code.

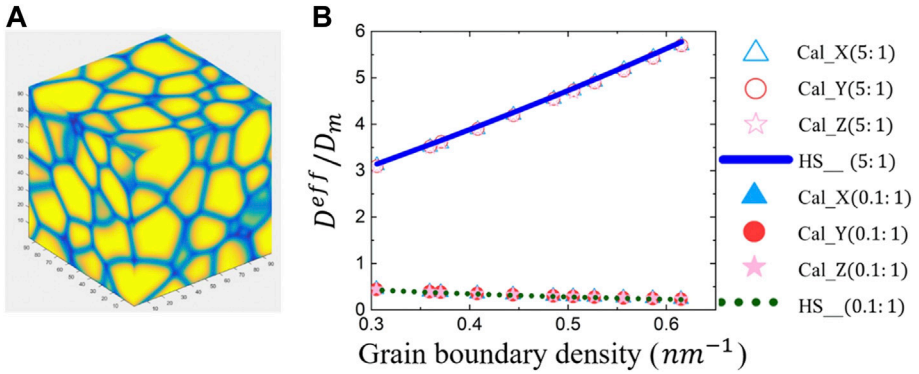

FIGURE 3 | (A) The simulated isometric polycrystalline microstructure. Blue lines are grain boundaries and the yellow parts are grains. **(B)** Comparison between the simulated and analytical effective diffusion coefficients as a function of the grain boundary density alone three different directions with diffusion coefficient ratios of H in the grain boundary to that in matrix phase are 0.1:1.0 and 5.0:1.0.

3.1.2 Sphere Embedded in a Cubic Box for Validation

We then construct a spherical structure inside a cubic box as shown in **Figure 2A**, in which the purple part refers to the spherical phase and the blank part is the matrix phase. The effective diffusion coefficient can be expressed analytically by the Maxwell-Garnett model (Maxwell, 1881; Moradi, 2015),

$$D_{eff} = D_m \frac{2D_m + D_p + 2f_p\left(D_p - D_m\right)}{2D_m + D_p - f_p\left(D_p - D_m\right)}, \tag{32}$$

where D_p and f_p is the diffusion coefficient in the spherical structure and the volume fraction of the spherical structure, respectively. We assume these two phases have different diffusion coefficients. We test two different cases to compare with the analytical solutions, one is the ratio D_p/D_m greater than 1.0 and the other one is less than 1.0. In each case, three different ratios of the diffusion coefficient are selected. The calculated results as well as the analytical solutions of the effective diffusion coefficient as a function of the volume fraction of the sphere are shown in **Figures 2B,C**, in which the scatter points represent the simulation results and the curves represent the analytical results derived by the Maxwell-Garnett model (Maxwell, 1881; Moradi, 2015). It can be seen that our simulation results agree well with the analytical solutions, which further validate our simulation code.

3.1.3 Isotropic Polycrystalline Structure for Validation

To further verify our code of solving the stationary diffusion equation with inhomogeneous diffusion coefficient distribution, we compare our results with the Hashin-Shtrikman (HS) model of a 3D isometric crystalline structure (Chen and Schuh, 2007). In the previous work, Hashin-Shtrikman derived an analytical solution that can be used to estimate the effective diffusion coefficient of H in isometric crystals as a function of the grain boundary density (Chen and Schuh, 2007),

$$D_{eff} = D_{GB} + \frac{f_m}{(D_m - D_{GB})^{-1} + 1/3f_{GB}D_{GB}^{-1}}, \tag{33}$$

where D_{eff}, D_{GB}, and D_m is the effective diffusion coefficient, the diffusion coefficient in the grain boundary, and the diffusion coefficient in the matrix phase, respectively. f_m and f_{GB} is the volume fraction of the matrix phase and grain boundary, respectively.

We first generate a 3D isometric crystalline microstructure by using the phase-field simulation as shown in **Figure 3A**, where the yellow parts represent the bulk phase and the blue lines stand for grain boundaries. After that, we consider two different diffusion coefficient ratios between grain boundary and matrix phase for comparison, i.e., promoting the diffusion (5:1) and inhibiting diffusion (0.1:1). As shown in **Figure 3B**, the effective diffusion coefficients in three directions are all in good agreement with those predicted by the HS model, which further proves that our code is suitable for the calculation of the effective diffusion coefficients of the polycrystalline materials.

Based on the above three testing examples, we validate our simulation code for calculating the effective diffusion coefficients in different structures.

3.2 Effective Diffusion Coefficient of H in Polycrystalline W

Based on our validated simulation code, we first study the effective diffusion coefficient of H in the polycrystalline W. The polycrystalline structures are generated using the phase-field model by solving **Eqs 1–4**. Three different polycrystalline structures including an isotropic grain structure and two columnar grain structures with different grain sizes are constructed as shown in **Figures 4A–C**. Then the effective diffusion coefficients of H in these three different polycrystalline structures can be obtained by solving **Eq. 16**.

The diffusion coefficient D_{ij} of H in the grain boundaries and grains can be defined as

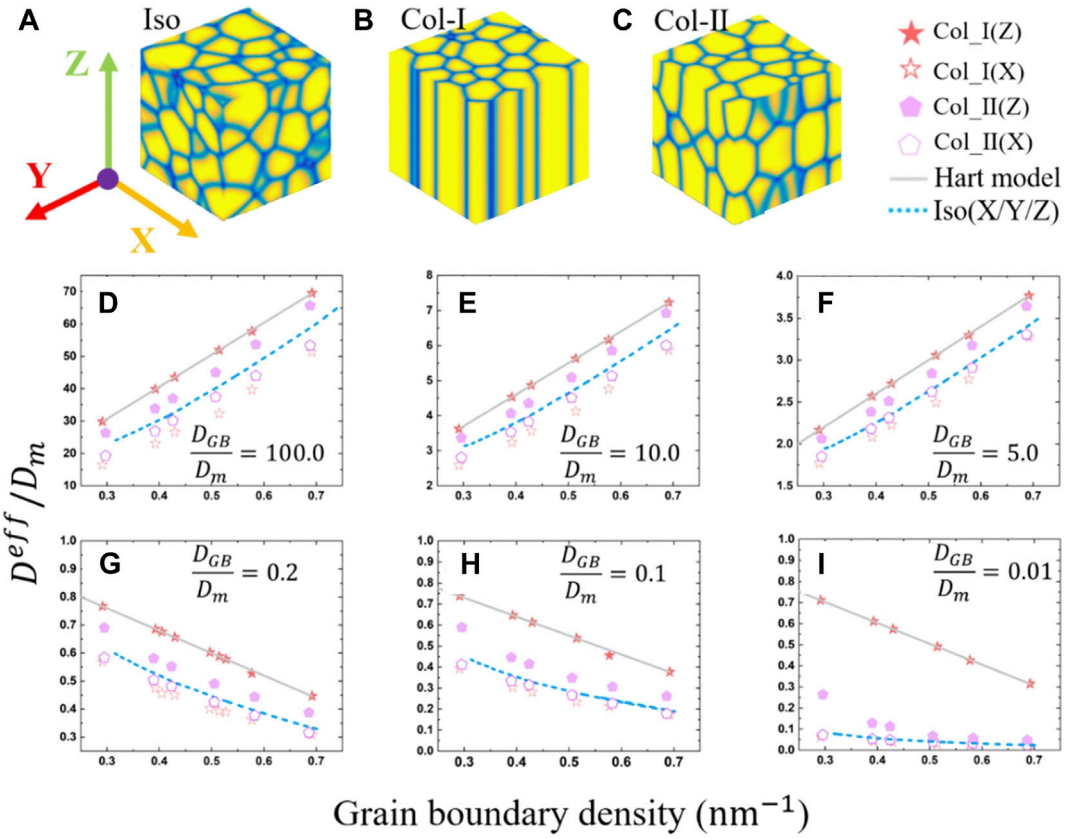

FIGURE 4 | Polycrystalline structure of the **(A)** isometric crystal, **(B)** columnar-I crystal, and **(C)** columnar-II crystal. The calculated effective diffusion coefficients for three different polycrystalline structures with three diffusion coefficient ratios D_{GB}/D_m of H are greater than 1.0 **(D–F)** and less than 1.0 **(G–I)**. The solid and hollow scatter points represent the effective diffusion coefficient parallel and perpendicular to the direction of the elongated grains of the columnar crystals. The gray solid lines represent the predicted effective diffusion coefficient as a function of the grain boundary density along the elongated orientations of structure Col-I by Hart's model and the blue dotted lines represent that predicted by the HS's model for the isometric crystal.

$$D_{ij} = \begin{cases} D_{GB} & (\eta \le 0.9) \\ D_m & (\eta > 0.9) \end{cases}. \tag{34}$$

According to previous atomic simulation results, the H diffusivity in the grain boundary can be either larger or smaller than that in the bulk, depending on the grain boundary type (Yu et al., 2014; Zhou et al., 2019B). To systematically investigate the effect of the grain boundary on the H diffusion in the polycrystalline W, six different ratios D_{GB}/D_m of the H diffusion coefficient in grain boundaries with respect to that in grains are considered in this work, i.e., three with $D_{GB}/D_m > 1.0$ and three with $D_{GB}/D_m < 1.0$ are selected for isometric and columnar grain structures.

Figure 4 shows the comparison of the numerically simulated and analytically calculated effective diffusion coefficients as a function of the grain boundary density in three polycrystalline structures. **Figures 4D–F** are for the case of $D_{GB}/D_m > 1.0$, while **Figures 4G–I** for the case of $D_{GB}/D_m < 1.0$. It can be seen that the effective diffusion coefficient increases with the increase of the grain boundary density when D_{GB}/D_m is greater than 1.0, while it decreases with the increase of the grain boundary density when the ratio D_{GB}/D_m is less than 1.0 as expected. Interestingly, the effective diffusion coefficient of H is greater in columnar crystals than that in isometric crystals along the Z direction, regardless of whether the H diffusivity in the grain boundary is larger or smaller than that in the bulk. And the effective diffusion coefficient of H in a simple columnar crystal containing parallel grain boundaries plotted in **Figure 4B** can be described by Hart's model (Hart, 1957), as shown in **Eq. 28**. It can be seen that our calculation results agree well with those results predicted by Hart's model. For the columnar-II crystal, the grains elongate along the Z-direction and grain boundaries have high density along this direction. The effective diffusion coefficient is believed to be larger than that for the isotropic crystal but smaller than that for the columnar-I crystal along the Z-direction. Both Hart's model and HS's model are hard to fit the simulation results in this case, which suggests that the numerical model without having the complex morphology of the microstructure can only predict the effective diffusion coefficient for simple grain structures.

2D simulations can save lots of computational resources compared to 3D simulations. We also calculate the effective

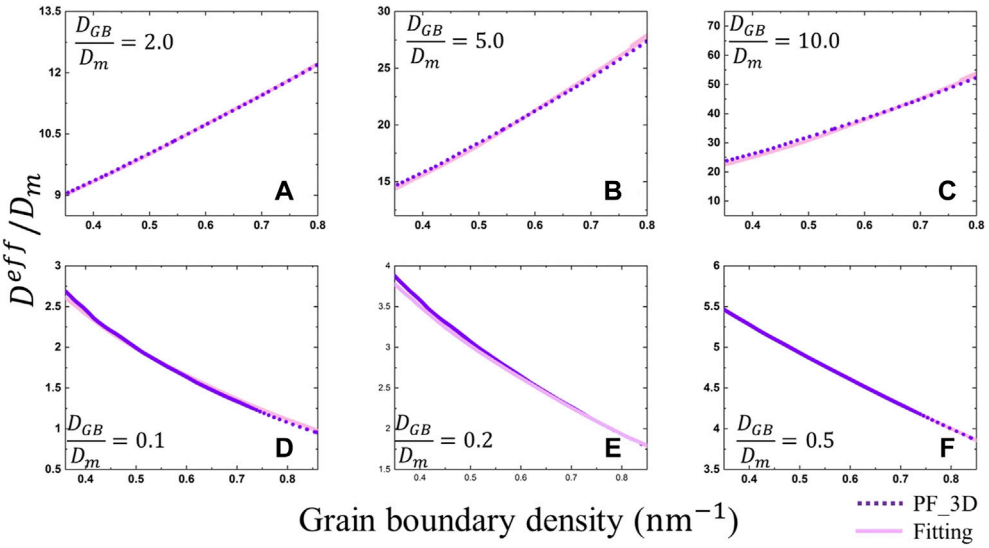

FIGURE 5 | The comparison between the simulated and fitted effective diffusion coefficients of H in 3D polycrystalline W with three diffusion coefficient ratios D_{GB}/D_m of H are greater than 1.0 **(A-C)** and less than 1.0 **(D-F)**. The fitted 3D data is calculated from the 2D results by using **Eqs 30**, **31**. The purple dotted curves represent the simulated results and the pink solid curves represent the results predicted by the fitting formula.

diffusion coefficient of H in isometric structures in 2D. At the same grain boundary density, the effective diffusion coefficients in 2D are usually smaller than that in 3D. Next, we derive a correlation that transfers the 2D effective diffusion coefficient into 3D based on Bakker et al.'s derivations, in which two formulas depending on the ratio of the diffusivity in the grain boundary and bulk that can transfer the 2D thermal conductivity into 3D were given (Bakker et al., 1995). When the H diffusion coefficient D_{GB} in the grain boundary is greater than the H diffusion coefficient D_m inside the grains, the correlation is given by

$$\frac{D_{3D}^{eff} - b}{D_{2D}^{eff} - b} = C_1 + \frac{1}{\frac{D_{GB}}{D_m} + C_2} \quad (D_{GB} > D_m), \tag{35}$$

$$b = \frac{D_{GB} D_m}{f_{GB} D_m + D_{GB} - f_{GB} D_{GB}}, \tag{36}$$

where D_{2D}^{eff} and D_{3D}^{eff} is the effective diffusion coefficient of H in the 2D and 3D simulations, respectively. C_1 and C_2 are fitting constants. We calculate the effective diffusion coefficients in 2D and 3D in order to fit the constants C_1 and C_2. By using three sets of the calculated effective diffusion coefficient from both 2D and 3D simulations, the fitted constants C_1 and C_2 are determined to be 1.13 and 3.8, respectively. The effective diffusion coefficients and the fitted results using **Eq. 35** are shown in **Figure 5A–C**, in which the purple dotted and pink solid lines represent the simulation results and fitted results by **Eq. 35**. It can be seen that the **Eq. 35** can fit well with the simulated data in all three cases.

For the H diffusion coefficient D_{GB} smaller than the H diffusion coefficient D_m, a correlation for transferring the 2D effective diffusion coefficients of H into 3D is (Bakker et al., 1995),

$$\frac{1 - \left(1 - \frac{D_{GB}}{D_m}\right) f_{GB} - \frac{D_{2D}^{eff}}{D_m}}{1 - \left(1 - \frac{D_{GB}}{D_m}\right) f_{GB} - \frac{D_{3D}^{eff}}{D_m}} = C_3 + \frac{1}{\frac{D_m}{D_{GB}} + C_4} \quad (D_{GB} < D_m), \tag{37}$$

where D_{2D}^{eff} and D_{3D}^{eff} is the effective diffusion coefficient in the 2D and 3D simulations, respectively. We use our simulated 2D and 3D effective diffusion coefficients to fit this correlation, and the fitted constants are determined as $C_3 = 1.07$ and $C_4 = 1.03$. The simulated and fitted effective diffusion coefficients of H in the 3D polycrystalline W are shown in **Figures 5D–F**, in which the purple dotted curves represent the simulated results and the pink solid curves represent the results predicted by the fitting formula **Eq. 37**. It can be seen that the fitting results are consistent with the simulation results for all three cases.

3.3 Effective Diffusion Coefficient of H in Porous Single Crystalline W

In addition to grain boundaries, irradiation-induced vacancies and their clusters can also affect the diffusion of H atoms (Wang et al., 2019). The porous structures formed by clustering of vacancies are generated by phase-field simulations through solving **Eqs 5–15**. Based on the phase-field simulated porous single crystalline W microstructures, we then study the effect of the porosity on the effective diffusion coefficient of H.

The diffusion tensor in the void and the matrix can be expressed as

$$D_{ij} = \begin{cases} D_{void} & (\varphi \geq 0.5) \\ D_m & (\varphi < 0.5) \end{cases}, \tag{38}$$

where D_{void} and D_m represents the diffusion coefficient of H in the void and matrix phase, respectively. We assume that the

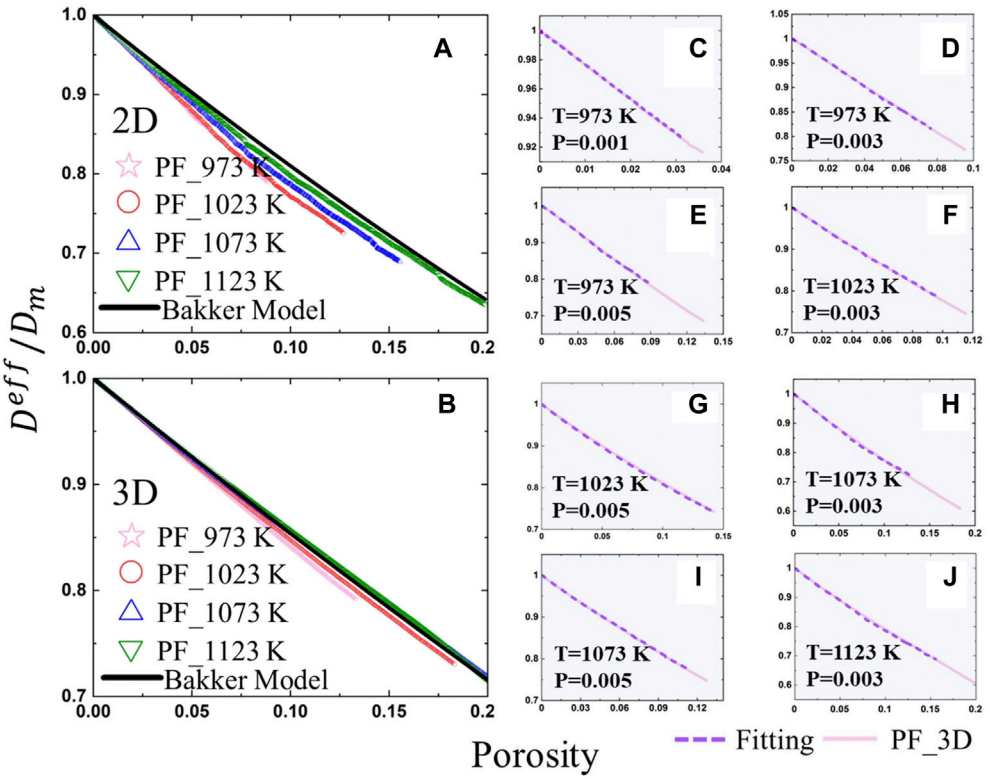

FIGURE 6 | The simulated and analytical effective diffusion coefficients as a function of the porosity for four different temperatures in 2D **(A)** and 3D **(B)**. **(C)–(J)** Comparison between the simulated and fitted effective diffusion coefficients of H in 3D porous W as a function of the temperature and porosity, in which the pink solid curves represent the simulation results and the purple dotted curves represent the results predicted by **Eq. 39** based on 2D results.

diffusion coefficient D_{void} is equal to zero based on the molecular dynamics results that the vacancy-type defects can greatly inhibit the H diffusion (Wang et al., 2019). Simulated and analytical effective diffusion coefficients as a function of the temperature and porosity in 2D and 3D porous W are plotted in **Figures 6A, B**. The colored scatter points represent the simulation results, and the solid black lines represent values of the effective diffusion coefficients predicted based on the Bakker's model (Bakker et al., 1995), i.e., $D^{eff} = D_m(1-p)^{2.0}$ in 2D and $D^{eff} = D_m(1-p)^{1.5}$ in 3D. It can be seen that the effective diffusion coefficient significantly decreases with the increase of the porosity, and values D^{eff}/D_m are basically consistent with those predicted by Bakker's model, especially in the 3D simulations. Compared with the results of 2D and 3D simulation, it can be seen that the effective diffusion coefficient of 3D simulations is higher than that of the 2D simulations under the same annealing temperature and porosity. This is because the 3D diffusion flux has one more degree of freedom than that in the 2D simulations (Bakker et al., 1995). Interestingly, the higher the temperature, the greater value D^{eff}/D_m is obtained at the same porosity. And the difference of D^{eff}/D_m between the high and low temperature increases with the increase of the porosity, which is attributed to the rapid increase in size of the void at high temperature. With the increase of the temperature, larger voids are formed due to the faster diffusion of the vacancies, which is consistent with previous results (Li et al., 2011). This also shows the advantage of our model, which can take the spatial morphology of the voids into account rather than the volume fraction in the analytical model.

Both the 2D and 3D effective diffusion coefficients of H as a function of the temperature and porosity in the porous single crystalline W are calculated. To obtain a general correlation that can transfer the 2D effective diffusion coefficient into the 3D in porous materials, we use the 2D and 3D calculated results to fit the parameter A by using the **Eq. 39** proposed by Bakker et al. (Bakker et al., 1995),

$$\frac{1-p-\dfrac{D_{2D}^{eff}}{D_m}}{1-p-\dfrac{D_{3D}^{eff}}{D_m}} = A, \tag{39}$$

where p, D_{2D}^{eff}, and D_{3D}^{eff} is the porosity, the effective diffusion coefficient in 2D, and 3D, respectively. A is a fitting constant. The fitted effective diffusion coefficient of H as well as the simulated 3D data in the porous W are plotted in **Figures 6C–J**, in which the pink solid curves represent the simulation results and the purple dotted curves represent the results predicted by **Eq. 39**. And the fitted parameter A is determined to be 2.4. We can see that the fitted results agree well with the simulated effective diffusion coefficients. Therefore, this fitted correlation can be used to

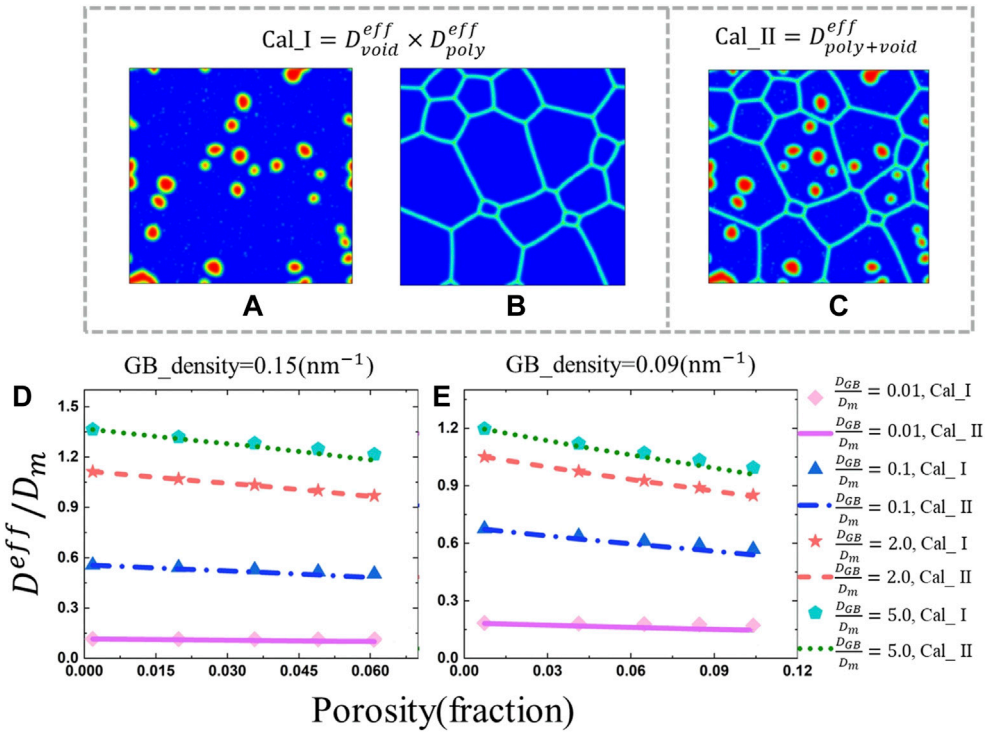

FIGURE 7 | Microstructure used for the first method **(A, B)** and second method **(C)** for calculating the effective diffusion coefficient. Comparison of the value D^{eff}/D_m calculated by two different methods as a function of the porosity under two different grain boundary densities of 0.15 nm^{-1} **(D)** and 0.09 nm^{-1} **(E)**, in which the scatter points denote D^{eff}/D_m obtained by the first method, and the curves represent that obtained by the second method.

predict the 3D effective diffusion coefficient based on the 2D data to save computational resources.

3.4 Effective Diffusion Coefficient of H in Porous Polycrystalline W

We study the effective diffusion coefficient of H during the formation of voids in two different polycrystalline W as a function of the porosity. We take a particular temperature of 1073 K for an example. The polycrystalline microstructures are generated using phase-field simulations by solving **Eqs 1–4**. The nucleation and growth of voids are simulated by solving **Eqs 5–15**. It is simply assumed that the grain structures don't evolve with the time during the formation of voids, and the same scenario was used in other relevant work (Wang et al., 2018). The simulated microstructures of the porous polycrystalline W at 0.001 s are shown in **Figure 7C**, where the solid lines represent the grain boundaries and the solid red round areas represent the voids. We assume the grain boundary is a perfect sink for vacancies, which is consistent with the experimental observations (Klimenkov et al., 2016).

The simulated microstructure is divided into three separate phases including the matrix, grain boundary, and void phases. We use two different methods to calculate the effective diffusion coefficient of H in this three-phase system. Firstly, we calculate the effective diffusion coefficient of H in the polycrystalline structure and porous structure separately as shown in **Figures 7A,B**. For the polycrystalline structure part, the solution process is the same as that in **section 3.2**, while for the effect of the porosity on the diffusion of H, the solution process is the same as that in **section 3.3**. The overall effective diffusion coefficient of H in the three-phase structure is assumed to be a product of the effective diffusion coefficient of the polycrystalline system D^{eff}_{poly} and that of the porous system D^{eff}_{void}, which can be described as,

$$D^{eff}/D_m = \left(D^{eff}_{void}/D_m\right) \times \left(D^{eff}_{poly}/D_m\right). \tag{40}$$

Secondly, the effective diffusion coefficients of H can be calculated directly from the three-phase structure by solving **Eq. 16** as shown in **Figure 7C**. The diffusion coefficient in each phase can be described in section as **Eq. 17**.

Figures 7D, E show the effective diffusion coefficients as a function of the porosity for different diffusion coefficient ratios obtained by above two different means, in which the scatter points represent the results obtained by the first approach that are calculated by multiplying the results of two separate systems as shown in **Eq. 40**, and the curves represent the results derived from the second method that are directly calculated according to the three-phase system. Two different grain boundary densities of 0.15 nm^{-1} and 0.09 nm^{-1} are considered. Results show that the effective diffusion coefficient decreases with the increase of the porosity. In the case of $D_{GB} < D_m$, it also decreases with the

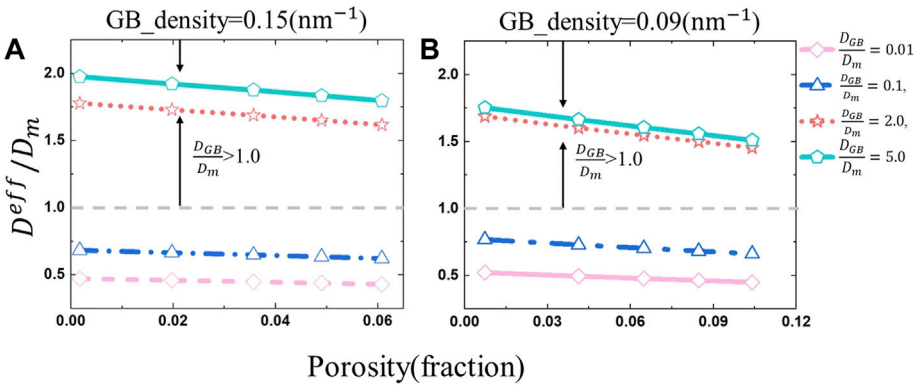

FIGURE 8 | Predicted values of D^{eff}/D_m for 3D porous polycrystalline W at 1073 K calculated by **Eqs 35**, **37**, **39** based on 2D simulation results (as shown by the scatter data in **Figures 7D, E**) as a function of the porosity under two different grain boundary densities of 0.15 nm^{-1} **(A)** and 0.09 nm^{-1} **(B)**.

increase of the grain boundary density, but it increases with the increase of the grain boundary density for the case of $D_{GB} > D_m$. More importantly, it can be seen that results obtained by these two different means agree well with each other, which verifies our above guess and also provides an important reference for estimating the effective diffusion coefficient of H in complex microstructures.

Based on the above 2D results, the effective diffusion coefficient of H in a 3D porous polycrystalline W can be predicted by using **Eqs. 35**, **37**, **39**. The predicted effective diffusion coefficients of H in the 3D porous polycrystalline W as a function of the porosity are shown in **Figure 8**. Results show that the effective diffusion coefficient decreases with the increase of the porosity, which has the same trend as that in 2D. The effective diffusion coefficient decreases with the increase of the grain boundary density for the case of $D_{GB} < D_m$, but it increases with the increase of the grain boundary density for the case of $D_{GB} > D_m$ in 3D microstructures. These results show that the grain size and grain morphology can largely affect the effective diffusion coefficient of H in W. However, by comparing the calculation results in 3D porous polycrystalline W with that in 2D plotted in **Figures 7A, B**, it is found that the effective diffusion coefficient of H in the 3D microstructure is always larger than that in 2D. This is reasonable because the effective diffusivities of H both in 3D polycrystalline or porous W are greater than that in their corresponding 2D microstructures.

4 CONCLUSION

We propose a numerical method to systemically study the effective diffusion coefficients of hydrogen (H) atoms in the porous polycrystalline tungsten (W). We assume the H atoms can be eventually desorbed from the grain boundaries and voids once they were trapped, which is based on thermal desorption experimental results (Eleveld and Veen, 1994; Hodille et al., 2017). The grain structure and irradiated voids are generated by using phase-field simulations. The effective diffusion coefficient in such an inhomogeneous system is obtained by solving the steady-state diffusion equation with a spectral iterative algorithm. The effects of the grain morphology, porosity, and their synergistic effect on the effective diffusion coefficient of H in W are systemically investigated. Our main research findings from the above simulations can be summarized as follows.

1) Using a spectral iterative algorithm, the calculated effective diffusion coefficients of three simple microstructures agree well with those predicted by previous analytical models, which fully validates our simulation code.
2) In the polycrystalline W, when the grain boundary density is a constant, the effective diffusion coefficient of H is always greater in columnar crystals than that in isometric crystals along the elongated grain direction, regardless of whether the diffusion coefficient in the grain boundary is larger or smaller than that in the bulk.
3) For the porous W, the effective diffusion coefficient of H significantly decreases with the increase of the porosity. When the porosity is a constant, our simulation results show that the effective diffusion coefficient increases with the increase of the average size of voids.
4) Based on our simulated effective diffusion coefficients in polycrystalline and porous W, two correlations that can transfer the two-dimensional (2D) effective diffusion coefficient into three-dimensional (3D) are fitted. Using these fitted correlations, we predict the effective diffusion coefficient of H in the 3D porous polycrystalline W based on 2D results, which can greatly save computational resources. It is found that the effective diffusion coefficient of H in a heterogeneous system is equal to the product of the effective diffusion coefficient of H in each phase.

The present study can help to better understand the influence of the grain boundary and void evolutions on the H diffusion in W. Other defect structures such as gas bubbles, dislocations, and precipitates influence the H diffusion can also be easily included

in the model. It is also worthy to point out that the experimental observations can be used as input microstructures instead of the phase-field simulated microstructures to calculate the effective diffusion coefficient of H. We expect that our findings can provide some references on how to control the H and its isotope retention and for the design of W-based materials fusion devices in the future. The current method can also be used in other systems that the diffusion component is not trapped by the microstructures.

DATA AVAILABILITY STATEMENT

The original contributions presented in this study are included in the article. The raw/processed data required to reproduce these findings cannot be shared at this time as the data also forms part of an ongoing study.

AUTHOR CONTRIBUTIONS

BL performed the numerical simulations, produced the figures, conducted analysis, and wrote the draft of the manuscript. JH, BX, SJ, H-BZ, and LL made substantial contributions to the analysis of the simulation results. LL and G-HL proposed the idea, revised it critically for important intellectual content, and approved the final version to be published. All authors contributed to the article and approved the submitted version.

FUNDING

This research is supported by the National Natural Science Foundation of China with Grant Nos 12075021, 12075023, and 51720105006, and the National MCF Energy R&D Program of China with Grant No. 2018YFE0308103.

REFERENCES

Aagesen, L. K., Biswas, S., Jiang, W., Andersson, D., Cooper, M. W. D., and Matthews, C. (2021). Phase-field Simulations of Fission Gas Bubbles in High Burnup UO2 during Steady-State and LOCA Transient Conditions. *J. Nucl. Mater.* 557, 153267. doi:10.1016/j.jnucmat.2021.153267

Allen, S. M., and Cahn, J. W. (1973). A Correction to the Ground State of Fcc Binary Ordered Alloys with First and Second Neighbor Pairwise Interactions. *Scr. Metall.* 7, 1261–1264. doi:10.1016/0036-9748(73)90073-2

Allen, S. M., and Cahn, J. W. (1972). Ground State Structures in Ordered Binary Alloys with Second Neighbor Interactions. *Acta Metall.* 20, 423–433. doi:10.1016/0001-6160(72)90037-5

Artsimovich, L. A. (1972). Tokamak Devices. *Nucl. Fusion* 12, 215–252. doi:10.1088/0029-5515/12/2/012

Bakker, K., Kwast, H., and Cordfunke, E. H. P. (1995). Determination of a Porosity Correction Factor for the Thermal Conductivity of Irradiated U02 Fuel by Means of the Finite Element Method. *J. Nucl. Mater.* 226, 128–143. doi:10.1016/0022-3115(95)00087-9

Bolt, H., Barabash, V., Krauss, W., Linke, J., Neu, R., Suzuki, S., et al. (2004). Materials for the Plasma-Facing Components of Fusion Reactors. *J. Nucl. Mater.* 329-333, 66–73. doi:10.1016/j.jnucmat.2004.04.005

Cahn, J. W., and Hilliard, J. E. (1958). Free Energy of a Nonuniform System. I. Interfacial Free Energy. *J. Chem. Phys.* 28, 258–267. doi:10.1063/1.1744102

Cahn, J. W. (1961). On Spinodal Decomposition. *Acta Metall.* 9, 795–801. doi:10.1016/0001-6160(61)90182-1

Chen, L.-Q., Yang, W., et al. (1994). Computer Simulation of the Domain Dynamics of a Quenched System with a Large Number of Nonconserved Order Parameters: The Grain-Growth Kinetics. *Phys. Rev. B* 50, 15752–15756. doi:10.1103/physrevb.50.15752

Chen, L. Q., and Shen, J. (1998). Applications of Semi-implicit Fourier-Spectral Method to Phase Field Equations. *Comput. Phys. Commun.* 108, 147–158. doi:10.1016/s0010-4655(97)00115-x

Chen, Y., and Schuh, C. A. (2007). Geometric Considerations for Diffusion in Polycrystalline Solids. *J. Appl. Phys.* 101, 063524. doi:10.1063/1.2711820

Cottrell, G. A. (2004). Sigma Phase Formation in Irradiated Tungsten, Tantalum and Molybdenum in a Fusion Power Plant. *J. Nucl. Mat.* 334, 66–68. doi:10.1016/j.jnucmat.2004.07.001

El-Kharbachi, A., Chêne, J., Garcia-Argote, S., Marchetti, L., Martin, F., Miserque, F., et al. (2014). Tritium Absorption/desorption in ITER-like Tungsten Particles. *Int. J. Hydrogen Energy* 39, 10525–10536. doi:10.1016/j.ijhydene.2014.05.023

Eleveld, H., and van Veen, A. (1994). Void Growth and Thermal Desorption of Deuterium from Voids in Tungsten. *J. Nucl. Mater.* 212-215, 1421–1425. doi:10.1016/0022-3115(94)91062-6

Fan, D., and Chen, L.-Q. (1997). Computer Simulation of Grain Growth Using a Continuum Field Model. *Acta Mater.* 45, 611–622. doi:10.1016/s1359-6454(96)00200-5

Frauenfelder, R. (1969). Solution and Diffusion of Hydrogen in Tungsten. *J. Vac. Sci. Technol.* 6, 388–397. doi:10.1116/1.1492699

Fu, B., Qiu, M., Cui, J., Wang, J., and Hou, Q. (2021). Diffusion, Trapping, and Dissociation Behaviours of Helium at the Σ5 Grain Boundary in Tungsten: A Molecular Dynamics Study. *J. Nucl. Mater.* 543, 152599. doi:10.1016/j.jnucmat.2020.152599

Fujita, H., Uemura, Y., Sakurada, S., Azuma, K., Zhou, Q., Toyama, T., et al. (2017). The Damage Depth Profile Effect on Hydrogen Isotope Retention Behavior in Heavy Ion Irradiated Tungsten. *Fusion Eng. Des.* 125, 468–472. doi:10.1016/j.fusengdes.2017.05.141

González, C., Panizo-Laiz, M., Gordillo, N., et al. (2015). H Trapping and Mobility in Nanostructured Tungsten Grain Boundaries: a Combined Experimental and Theoretical Approach Nucl. *Fusion* 55, 113009. doi:10.1088/0029-5515/55/1/113009

Grisolia, C., Hodille, E., Chene, J., Garcia-Argote, S., Pieters, G., El-Kharbachi, A., et al. (2015). Tritium Absorption and Desorption in ITER Relevant Materials: Comparative Study of Tungsten Dust and Massive Samples. *J. Nucl. Mater.* 463, 885–888. doi:10.1016/j.jnucmat.2014.10.089

Guo, W., Cheng, L., De Temmerman, G., Yuan, Y., and Lu, G.-H. (2018). Retarded Recrystallization of Helium-Exposed Tungsten. *Nucl. Fusion* 58, 106011. doi:10.1088/1741-4326/aad2b0

Hao, J., Jin, S., Lu, G.-H., and Xu, H. (2020). Migration Energy Barriers and Diffusion Anisotropy of Point Defects on Tungsten Surfaces. *Comput. Mater. Sci.* 184, 109893. doi:10.1016/j.commatsci.2020.109893

Hart, E. W. (1957). On the Role of Dislocations in Bulk Diffusion. *Acta Metall.* 5, 597–605. doi:10.1016/0001-6160(57)90127-x

Hasegawa, A., Fukuda, M., Nogami, S., and Yabuuchi, K. (2014). Neutron Irradiation Effects on Tungsten Materials. *Fusion Eng. Des.* 89, 1568–1572. doi:10.1016/j.fusengdes.2014.04.035

Hasegawa, A., Fukuda, M., Yabuuchi, K., et al. (2016). Neutron Irradiation Effects on the Microstructural Development of Tungsten and Tungsten Alloys. *J. Nucl. Mat.* 471175-183. doi:10.1016/j.jnucmat.2015.10.047

Heinola, K., and Ahlgren, T. (2010a). Diffusion of Hydrogen in Bcc Tungsten Studied with First Principle Calculations. *J. Appl. Phys.* 107, 113531. doi:10.1063/1.3386515

Heinola, K., and Ahlgren, T. (2010b). First-principles Study of H on the Reconstructed W (100) Surface. *Phys. Rev. B* 81, 073409. doi:10.1103/physrevb.81.073409

Hodille, E. A., Begrambekov, L. B., Pascal, J. Y., Saidi, O., Layet, J. M., Pégourié, B., et al. (2014). Hydrogen Trapping in Carbon Film: From Laboratories Studies to Tokamak Applications. *Int. J. Hydrogen Energy* 39, 20054–20061. doi:10.1016/j.ijhydene.2014.09.027

Hodille, E. A., Ghiorghiu, F., Addab, Y., Založnik, A., Minissale, M., Piazza, Z., et al. (2017). Retention and Release of Hydrogen Isotopes in Tungsten Plasma-Facing Components: the Role of Grain Boundaries and the Native Oxide Layer from a Joint Experiment-Simulation Integrated Approach. *Nucl. Fusion* 57, 076019. doi:10.1088/1741-4326/aa6d24

Hu, X., Koyanagi, T., Fukuda, M., Kumar, N. A. P. K., Snead, L. L., Wirth, B. D., et al. (2016). Irradiation Hardening of Pure Tungsten Exposed to Neutron Irradiation. *J. Nucl. Mater.* 480, 235–243. doi:10.1016/j.jnucmat.2016.08.024

Jiang, C., Ke, J. H., Simon, P. C. A., et al. (2021). *Atomistic and Mesoscale Simulations to Determine Effective Diffusion Coefficient of Fission Products in SiC*. Idaho National Lab. (INL), Idaho Falls, ID (United States) https://www.osti.gov/servlets/purl/1825508.

Jin, Y., Roh, K.-B., Sheen, M.-H., Kim, N.-K., Song, J., Kim, Y.-W., et al. (2017). Enhancement of Deuterium Retention in Damaged Tungsten by Plasma-Induced Defect Clustering. *Nucl. Fusion* 57, 126042. doi:10.1088/1741-4326/aa856c

Johnson, D. F., and Carter, E. A. (2010). Hydrogen in Tungsten: Absorption, Diffusion, Vacancy Trapping, and Decohesion. *J. Mat. Res.* 25, 315–327. doi:10.1557/jmr.2010.0036

Kim, S. G. (2007). A Phase-Field Model with Antitrapping Current for Multicomponent Alloys with Arbitrary Thermodynamic Properties. *Acta Mater.* 55, 4391–4399. doi:10.1016/j.actamat.2007.04.004

Kim, S. G., Kim, W. T., and Suzuki, T. (1999). Phase-field Model for Binary Alloys. *Phys. Rev. E* 60, 7186–7197. doi:10.1103/physreve.60.7186

Kimizuka, H., and Ogata, S. (2011). Slow Diffusion of Hydrogen at a Screw Dislocation Core Inα-Iron. *Phys. Rev. B* 84, 024116. doi:10.1103/physrevb.84.024116

Klimenkov, M., Jäntsch, U., Rieth, M., Schneider, H. C., Armstrong, D. E. J., Gibson, J., et al. (2016). Effect of Neutron Irradiation on the Microstructure of Tungsten. *Nucl. Mater. Energy* 9, 480–483. doi:10.1016/j.nme.2016.09.010

Krill III, C. E., Iii, and Chen, L.-Q. (2002). Computer Simulation of 3-D Grain Growth Using a Phase-Field Model. *Acta Mater.* 50, 3059–3075. doi:10.1016/s1359-6454(02)00084-8

L. Briant, C., and Walter, J. L. (1988). Void Growth in Tungsten Wire. *Acta Metall.* 36, 2503–2514. doi:10.1016/0001-6160(88)90196-4

Li, B., Jin, S., Xue, B., Liang, L., and Lu, G.-H. (2022). Phase-field Microstructure-Based Effective Thermal Conductivity Calculations in Tungsten. *Nucl. Fusion* 62, 076041. doi:10.1088/1741-4326/ac6284

Li, Y.-H., Zhou, H.-B., Jin, S., Zhang, Y., Deng, H., and Lu, G.-H. (2017). Behaviors of Transmutation Elements Re and Os and Their Effects on Energetics and Clustering of Vacancy and Self-Interstitial Atoms in W. *Nucl. Fusion* 57, 046006. doi:10.1088/1741-4326/aa5893

Li, Y., Hu, S., Sun, X., Gao, F., Henager, C. H., and Khaleel, M. (2011). Phase-field Modeling of Void Evolution and Swelling in Materials under Irradiation. *Sci. China Phys. Mech. Astron.* 54, 856–865. doi:10.1007/s11433-011-4316-y

Liu, Y.-L., Zhang, Y., Zhou, H.-B., Lu, G.-H., Liu, F., and Luo, G.-N. (2009). Vacancy Trapping Mechanism for Hydrogen Bubble Formation in Metal. *Phys. Rev. B* 79, 172103. doi:10.1103/physrevb.79.172103

Liu, Y.-N., Wu, T., Yu, Y., Li, X.-C., Shu, X., and Lu, G.-H. (2014). Hydrogen Diffusion in Tungsten: A Molecular Dynamics Study. *J. Nucl. Mater.* 455, 676–680. doi:10.1016/j.jnucmat.2014.09.003

Louthan, M. R., Jr, Caskey, G. R., Jr, Donovan, J. A., and Rawl, D. E. (1972). Hydrogen Embrittlement of Metals. *Mater. Sci. Eng.* 10, 357–368. doi:10.1016/0025-5416(72)90109-7

Mannheim, A., Van Dommelen, J. A. W., and Geers, M. G. D. (2018). Modelling Recrystallization and Grain Growth of Tungsten Induced by Neutron Displacement Defects. *Mech. Mater.* 123, 43–58. doi:10.1016/j.mechmat.2018.04.008

Maxwell, J. C. A. (1881). *Treatise on Electricity and Magnetism: Pt. III. Magnetism. Pt. IV. Electromagnetism*. Clarendon Press.

Millett, P. C., Rokkam, S., El-Azab, A., Tonks, M., and Wolf, D. (2009). Void Nucleation and Growth in Irradiated Polycrystalline Metals: a Phase-Field Model. *Model. Simul. Mat. Sci. Eng.* 17, 064003. doi:10.1088/0965-0393/17/6/064003

Moelans, N., Blanpain, B., and Wollants, P. (2008). Quantitative Analysis of Grain Boundary Properties in a Generalized Phase Field Model for Grain Growth in Anisotropic Systems. *Phys. Rev. B* 78, 024113. doi:10.1103/physrevb.78.024113

Moradi, A. (2015). Maxwell-Garnett Effective Medium Theory: Quantum Nonlocal Effects. *Phys. Plasmas* 22, 042105. doi:10.1063/1.4917252

Oudriss, A., Creus, J., Bouhattate, J., Conforto, E., Berziou, C., Savall, C., et al. (2012). Grain Size and Grain-Boundary Effects on Diffusion and Trapping of Hydrogen in Pure Nickel. *Acta Mater.* 60, 6814–6828. doi:10.1016/j.actamat.2012.09.004

Rasch, K.-D., Siegel, R. W., and Schultz, H. (1980). Quenching and Recovery Investigations of Vacancies in Tungsten. *Philos. Mag. A* 41, 91–117. doi:10.1080/01418618008241833

Ratanaphan, S., Boonkird, T., Sarochawikasit, R., Beladi, H., Barmak, K., and Rohrer, G. S. (2017). Atomistic Simulations of Grain Boundary Energies in Tungsten. *Mater. Lett.* 186, 116–118. doi:10.1016/j.matlet.2016.09.104

Rieth, M., Doerner, R., Hasegawa, A., Ueda, Y., and Wirtz, M. (2019). Behavior of Tungsten under Irradiation and Plasma Interaction. *J. Nucl. Mater.* 519, 334–368. doi:10.1016/j.jnucmat.2019.03.035

Sakurada, S., Uemura, Y., Fujita, H., Azuma, K., Toyama, T., Yoshida, N., et al. (2017). Impact of Annealing on Deuterium Retention Behavior in Damaged W. *Fusion Sci. Technol.* 72, 785–788. doi:10.1080/15361055.2017.1350480

Stepper, H.-J. (1972). Recrystallization of α Particle Irradiated Tungsten. *Mt* 3, 2293–2294. doi:10.1007/bf02643247

Taketomi, S., Matsumoto, R., and Miyazaki, N. (2008). Atomistic Study of Hydrogen Distribution and Diffusion Around a {112} Edge Dislocation in Alpha Iron. *Acta Mater.* 56, 3761–3769. doi:10.1016/j.actamat.2008.04.011

Ueda, Y., Funabiki, T., Shimada, T., Fukumoto, K., Kurishita, H., and Nishikawa, M. (2005). Hydrogen Blister Formation and Cracking Behavior for Various Tungsten Materials. *J. Nucl. Mater.* 337-339, 1010–1014. doi:10.1016/j.jnucmat.2004.10.077

Vaidya, W. V., and Ehrlich, K. (1983). Radiation-Induced Recrystallization, its Cause and Consequences in Heavy-Ion Irradiated 20% Cold-Drawn Steels of Type 1.4970. *J. Nucl. Mat.* 113, 149–162. doi:10.1016/0022-3115(83)90137-X

Wang, H., Biswas, S., Han, Y., and Tomar, V. (2018). A Phase Field Modeling Based Study of Microstructure Evolution and its Influence on Thermal Conductivity in Polycrystalline Tungsten under Irradiation. *Comput. Mater. Sci.* 150, 169–179. doi:10.1016/j.commatsci.2018.03.070

Wang, J.-J., Wang, Y., Ihlefeld, J. F., Hopkins, P. E., and Chen, L.-Q. (2016). Tunable Thermal Conductivity via Domain Structure Engineering in Ferroelectric Thin Films: A Phase-Field Simulation. *Acta Mater.* 111, 220–231. doi:10.1016/j.actamat.2016.03.069

Wang, L. F., Shu, X., Lin, D. Y., et al. (2019). Molecular Dynamics Studies of Hydrogen Diffusion in Tungsten at Elevated Temperature: Concentration Dependence and Defect Effects. *Int. J. Hydrogen Energy* 45, 822–834. doi:10.1016/j.ijhydene.2019.10.151

Xue, Y., and Hassanein, A. (2014). Kinetic Monte Carlo Simulation of Hydrogen Diffusion on Tungsten Reconstructed (0 0 1) Surface. *Fusion Eng. Des.* 89, 2545–2549. doi:10.1016/-j.fusengdes.2014.06.001

Yang, L., and Wirth, B. D. (2019). First-principles Study of Hydrogen Diffusion and Self-Clustering below Tungsten Surfaces. *J. Appl. Phys.* 125, 1651051–2165105.14. doi:10.1063/1.5092595

Yang, X., and Oyeniyi, W. O. (2017). Kinetic Monte Carlo Simulation of Hydrogen Diffusion in Tungsten. *Fusion Eng. Des.* 114, 113–117. doi:10.1016/j.fusengdes.2016.12.012

Yu, Y., Shu, X., Liu, Y.-N., and Lu, G.-H. (2014). Molecular Dynamics Simulation of Hydrogen Dissolution and Diffusion in a Tungsten Grain Boundary. *J. Nucl. Mater.* 455, 91–95. doi:10.1016/j.jnucmat.2014.04.016

Zhou, H., Yu, J., Chen, C., and Zhu, K. (2019a). Effect of Pre-damage Induced by Argon Ions on the Deuterium Blister Formation in Tungsten-Tantalum Alloys Exposed to Deuterium Plasma. *Int. J. Hydrogen Energy* 44, 23320–23329. doi:10.1016/j.ijhydene.2019.07.061

Zhou, X., Mousseau, N., and Song, J. (2019b). Is Hydrogen Diffusion along Grain Boundaries Fast or Slow? Atomistic Origin and Mechanistic Modeling. *Phys. Rev. Lett.* 122, 215501. doi:10.1103/physrevlett.122.215501

Conflict of Interest: The authors declare that the research was conducted in the absence of any commercial or financial relationships that could be construed as a potential conflict of interest.

Publisher's Note: All claims expressed in this article are solely those of the authors and do not necessarily represent those of their affiliated organizations, or those of the publisher, the editors and the reviewers. Any product that may be evaluated in this article, or claim that may be made by its manufacturer, is not guaranteed or endorsed by the publisher.

frontiers | Frontiers in Materials

TYPE Original Research
PUBLISHED 15 September 2022
DOI 10.3389/fmats.2022.950785

OPEN ACCESS

EDITED BY
Yu-Hong Zhao,
North University of China, China

REVIEWED BY
Hock Jin Quah,
University of Science Malaysia, Malaysia
Houbing Huang,
Beijing Institute of Technology, China

*CORRESPONDENCE
Wenbo Liu,
liuwenbo@xjtu.edu.cn
Di Yun,
diyun1979@xjtu.edu.cn

SPECIALTY SECTION
This article was submitted to Computational Materials Science, a section of the journal Frontiers in Materials

RECEIVED 23 May 2022
ACCEPTED 22 August 2022
PUBLISHED 15 September 2022

CITATION
Wen C, Liu W, Yun D and Qian Z (2022), A phase-field model with irradiation-enhanced diffusion for constituent redistribution in U-10wt%Zr metallic fuels.
Front. Mater. 9:950785.
doi: 10.3389/fmats.2022.950785

A phase-field model with irradiation-enhanced diffusion for constituent redistribution in U-10wt%Zr metallic fuels

Chunyang Wen[1], Wenbo Liu[1]*, Di Yun[1,2]* and Zhengyu Qian[1]

[1]School of Nuclear Science and Technology, Xi'an Jiaotong University, Xi'an, China, [2]State Key Laboratory of Multiphase Flow, Xi'an Jiaotong University, Xi'an, China

Constituent redistribution is a unique phenomenon to metal fuels that threatens the safety of such fuel forms. Therefore, it is imperative to establish models to understand the intrinsic mechanisms and predict the redistribution kinetics. In this work, we derived the conservative field equations of the phase-field model from near-equilibrium thermodynamic theory. A macroscopic constituent redistribution phase-field model was developed by introducing the effect of irradiation on the atom mobility and the effect of temperature on the interface mobility. An expression of phase boundary width, applicable to both microscopic and macroscopic scenarios was proposed. The interfacial parameters of the model and the Zr concentration distribution near the fuel surface were discussed at last. These works may help understand constituent redistribution characteristics and promote the application of the phase-field method in studying constituent redistribution in macroscopic scenarios.

KEYWORDS

U-Zr, constituent redistribution, phase-field method, irradiation-induced diffusion, interface

Introduction

Metal fuels are ideal for fast reactors due to their higher fissile and fertile densities, and they possess high thermal conductivity and inherent safety features as demonstrated by the EBR-II (Experimental Breeder Reactor II) ULOF (Unprotected Loss-Of-Flow) and ULOHS (Unprotected Loss-Of-Heat-Sink) experiments (Feldman et al., 1987; Mohr et al., 1987). However, constituent redistribution in metal fuels is a significant threat to fuels' safety. The initial uniform radial constituent distribution of metal-fuel transforms to an inhomogeneous counterpart due to the redistribution phenomenon driven by thermodynamics. Inhomogeneous distribution of ingredients and fission products significantly impacts fuels' mechanical and physical properties (Murphy et al., 1969; Kim et al., 2004; Rahn et al., 2021). Therefore, it is crucial to understand and predict the redistribution kinetics.

Murphy et al. first observed the redistribution phenomenon in irradiated U-Pu-Zr fuel rods (Murphy et al., 1969). Thereafter, constituent redistribution was observed in U-Zr alloys at elevated temperatures (Hofman et al., 1996). Researchers have been establishing thermodynamic models to describe the constituent redistribution process. One of the most popular models was a

U-10wt%Zr redistribution model (Hofman et al., 1996) based on a thermal diffusion mechanism. In addition, similar models were also established (Nam and Hwang, 1998; Kim et al., 2006) to analyze the constituent redistribution process. More innovatively, a quantitative constituent redistribution model for U-10wt%Zr alloy using the phase-field method was developed recently (Hirschhorn et al., 2019a; Hirschhorn et al., 2021). Phase-field method is good at dealing with thermodynamic problems and interface behaviour issues (Hu et al., 2009; Hu et al., 2010; Millett and Tonks, 2011a; Millett et al., 2011; Ahmed et al., 2014; Tonks et al., 2014; Liang et al., 2016; Mei et al., 2016). This method has been increasingly used for modelling and simulation in the field of nuclear materials in recent years, including U-Zr and U-Pu-Zr (Millett and Tonks, 2011b; Mohanty et al., 2011; Li et al., 2017; Tonks et al., 2018; Hirschhorn et al., 2019b; Hirschhorn et al., 2020). In all the above-described models, chemical diffusion coefficients, which control the diffusion of atoms and determine the final constituent distribution, were artificially enlarged several times by multiple a number, because the original chemical diffusion coefficients were not enough large to satisfy the simulation results. If key parameters in model cannot be theoretically and accurately determined, the subsequent prediction and design of materials in engineering will have a vital threat.

In this work, we have developed a more accurate phase field model than before. To obtain a more accurate diffusion coefficient, we introduced the irradiation-enhanced diffusion theory into the phase-field model of constituent redistribution and discussed the effects of irradiation on both chemical and thermal diffusion in U-10wt%Zr in this work. It has become an accepted fact that the additional vacancies introduced by irradiation will accelerate the diffusion of atoms, and such acceleration is particularly important at lower temperatures where thermal diffusion becomes limited. We also considered the effect of temperature on the interface mobility, which was overlooked by the previous phase-field model. This will also further improve the accuracy of the phase-field model. Besides, element concentration gradient free energy was added into the total free energy expression to make the free energy expression more comprehensive. In addition to making the model more accurate, the interfacial parameters related to phase boundary in our model were redefined and interpreted because the definition of grain boundary under microscopic conditions is unsuitable for phase boundaries under macroscopic conditions (Faulkner et al., 1996; Moelans et al., 2008). Finally, the interfacial parameters of the model and the Zr concentration distribution near the fuel surface were discussed.

Model development

The phase-field equations

Constituent redistribution is an irreversible process associated with material transport, which is essentially a near-equilibrium thermodynamic phenomenon. During U-Zr constituent redistribution, the Soret phenomenon, also called thermal diffusion, which is driven by the temperature gradient, was observed in the EBR-II X447 irradiation experiment (Hofman et al., 1996). The linear phenomenological law can derive the expression of diffusion flux caused by temperature gradient $J_i = \sum L_{ij} X_j$(Kreuzer, 1981). Where J_i is the i^{th} thermodynamic flux; the coefficient L_{ij}satisfies Onsager's reciprocal relationship $L_{ij} = L_{ji}$ and X_j is the j^{th}thermodynamic force stemming from a kind of gradient, such as temperature gradient, chemical potential gradient, etc. In the constituent redistribution of U-Zr, the thermodynamic flux refers to the Zr diffusion flux, and the thermodynamic force contains two parts. One is produced by the temperature gradient, and the other is generated by the chemical potential gradient. Thus, the term which represents the contribution of a temperature gradient to the Zr diffusion flux (Kreuzer, 1981; Mohanty et al., 2009) was added into the model based on the original phase-field model which only considered the contribution from a chemical potential gradient.

$$J_T = M_T \frac{\nabla T}{T} \tag{1}$$

J_T represents the Zr diffusion flux induced by the temperature gradient, M_T is the thermal mobility, and $T$is the temperature. The Zr diffusion flux generated by chemical potential gradient can be expressed as,

$$J_c = -M_c^I \nabla \frac{\delta F}{\delta c} \tag{2}$$

where M_c^I is the chemical mobility with the effect of irradiation; $F$is the system's free energy, and c is the Zr atomic fraction, and here we use it to represent the Zr concentration. The variation of free energy versus concentration is precisely the chemical potential. According to Fick's second law, we have,

$$\frac{\partial c}{\partial t} = -\nabla \cdot (J_T + J_c) \tag{3}$$

By substituting Eq. 1 and 2 into Eq. 3, the equation of the evolution of concentration with respect to time can be derived,

$$\frac{\partial c}{\partial t} = \nabla \cdot \left(M_c^I \nabla \frac{\delta F}{\delta c} - M_T \frac{\nabla T}{T} \right) \tag{4}$$

That is actually one part of the phase-field model.

In the previous U-Zr component redistribution models, only the pure thermodynamic models were used, and the phase distributions needed to be determined *a priori* without considering phase evolutions (Hofman et al., 1996; Nam and Hwang, 1998; Kim et al., 2006). Determining the spatial distribution of phases followed by calculating the concentration can cause great inconvenience to deal with phase boundaries. Though phase interfaces are always complicated subjects, they can be effectively dealt with by introducing the phase diffusion equation into the phase-field model. Ever since the beginning of the development of phase-field method, the method has always been proven to have

unique advantages in dealing with boundary problems (Millett et al., 2012; Ahmed et al., 2014; Biner, 2017). Another advantage of using phase-field model is that the specific distributions of each phase can be seen intuitively, which is not available in traditional thermodynamic models. Based on these considerations, the Allen-Cahn equation (Allen and Cahn, 1972; Allen and Cahn, 1973) was introduced into the phase-field model to describe the diffusion evolution of phases:

$$\frac{\partial \gamma}{\partial t} = -L\frac{\delta F}{\delta \gamma} \tag{5}$$

Where, $\gamma$is the phase fraction of γ phase, and can be seen as the order parameter, ranging from 0 to 1. $L$is the kinetic coefficient of phase boundary mobility led by the evolution of the multi-phase region. Though L can be seen as a constant under isothermal conditions, the effect of temperature on L should be explicitly considered if temperature plays a vital role in the system. It has been verified that temperature significantly impacts grain-boundary mobility in previous studies (Tonks et al., 2014). Consequently, in this case, the Arrhenius formula should be taken into account (Wen et al., 2006; Mei et al., 2016),

$$L = L_0 e^{-\frac{Q_\gamma}{RT}} \tag{6}$$

Where, L_0 is a constant. $Q_\gamma$is the activation energy of phase boundary diffusion (Wang et al., 2009; Mei et al., 2016). Since the essence of phase boundary diffusion is the atomic diffusion, it is suggested that Q_γ can take the value of activation energy of the diffusion of Zr, namely$Q_\gamma = 128000 - 107000c_\gamma + 174000\,(c_\gamma)^2$ (Kim et al., 2006); $R$is the gas constant.

The constituent redistribution of U-Zr mainly involves three single phases, γ, a and β. We inherited the idea of Hirschhorn et al. (Hirschhorn et al., 2019a) for the co-evolution of three phases. One order parameter γ was used to simplify the three-phase model to a two-phase counterpart because phase-field can easily handle two-phase problems while it encounters a lot more difficulties dealing with three-phase issues. Due to the unique distribution of the three phases in the U-Zr phase diagram, the a and β phases can be reasonably regarded as one phase (α-β phase) independent of the γ phase. Then they can be distinguished through the phase transition temperature $T_{\alpha\beta} = 935$K of a phase and β phase. Here, we introduce the interpolation functions:

$$h_{\alpha\beta} = \frac{1}{2} + \frac{1}{2}\tanh\left(\frac{T_{\alpha\beta} - T}{2}\right) \tag{7}$$

$$\begin{aligned} \alpha &= \left(1 - h_{\alpha\beta}\right)(1 - \gamma) \\ \beta &= h_{\alpha\beta}\,(1 - \gamma) \end{aligned} \tag{8}$$

Where, α is the phase fraction of the a phase, and β is the phase fraction of the β phase. In the non-γ phase area where the temperature is higher than $T_{\alpha\beta}$, β phase is present; and where the temperature is lower than $T_{\alpha\beta}$, a phase is present.

Free energy

The selection and discussion of free energy and migration coefficient are manifested below. In the phase-field model, total free energy generally contains volume free energy and gradient free energy (Kim et al., 1999; Chen et al., 2017). The volume free energy is composed of γ phase, a phase, and β phase, and the gradient free energy is composed of the concentration gradient and phase fraction gradient. The expression is as follows:

$$\begin{aligned} F = \int_V \Bigg\{ &\frac{1}{V_m}\left[(1 - h(\gamma))f_{\alpha\beta} + h(\gamma)f_\gamma\right] + \omega g + \frac{1}{2}\kappa_c\,(\nabla c)^2 \\ &+ \frac{1}{2}\kappa_\gamma\,(\nabla\gamma)^2 \Bigg\} dV \end{aligned} \tag{9}$$

Where, $f_{\alpha\beta}$ represents the bulk free energy in a-β phase; $f_\gamma$is the free energy of the γ phase, $h(\gamma)$is an interpolation function of γ, $h(\gamma) = \gamma^3(6\gamma^2 - 15\gamma + 10)$, V_m is defined as the fractional volume $V_m = N_A a^3/2$, $N_A$is the Avogadro's constant, and a is the lattice parameter of U-10wt%Zr, which is 0.3462; $g$is a barrier function, expressed as $g = \gamma^2(1 - \gamma)^2$; ω is the height of the double potential well function; κ_c is the concentration gradient energy coefficient, and it needs to be in the 10^{-9} order of magnitude; $\kappa_\gamma$is the energy coefficient of the phase fraction gradient; ω and κ_γ determine the shape and width of the phase diffusion interface, which will be discussed in the following. The expression of the thermodynamic free energy of a-β phase and γ phase comes from references (Dinsdale, 1991; Quaini et al., 2018; Hirschhorn et al., 2019a) and is given by:

$$\begin{aligned} f_{\alpha\beta} = &\left(1 - c_{\alpha\beta}\right)G_0^{\gamma-U} + c_{\alpha\beta}\left(38000 + G_0^{\alpha-Zr}\right) \\ &+ RT\left[\left(1 - c_{\alpha\beta}\right)\ln\left(1 - c_{\alpha\beta}\right) + c_{\alpha\beta}\ln c_{\alpha\beta}\right] \\ &+ \left(1 - c_{\alpha\beta}\right)c_{\alpha\beta}\,(-7000) - 23500.0 + 24.0T \end{aligned} \tag{10}$$

$$\begin{aligned} f_\gamma = &\left(1 - c_\gamma\right)G_0^{\gamma-U} + c_\gamma G_0^{\beta-Zr} + R988.4\left[\left(1 - c_\gamma\right)\ln\left(1 - c_\gamma\right)\right. \\ &\left. + c_\gamma \ln c_\gamma\right] + \left(1 - c_\gamma\right)c_\gamma\left\{28369.0639 - 14.741714{*}998.4\right. \\ &\left. + 4992.02639\left(1 - 2c_\gamma\right) + 2609.10711\left(1 - 2c_\gamma\right)^2\right\} \end{aligned} \tag{11}$$

Where $c_{\alpha\beta}$ is the equilibrium atomic fraction of Zr in the a-β phase; $c_\gamma$is the equilibrium atomic fraction of Zr in the γ phase; $G_0^{\alpha-U}$, $G_0^{\alpha-Zr}$, $G_0^{\gamma-U}$, $G_0^{\beta-Zr}$are the intrinsic free energy, and all of them can be found in the SGTE database (Scientific Group Thermodata Europe) (Dinsdale, 1991), corresponding to each component described therein, respectively. The KKS (Kim-Kim-Suzuki) model (Kim et al., 1999) was adopted to deal with phase boundaries in pursuit of accuracy. According to the KKS model, there should be a mutually restrictive relationship between Zr concentration, phase, and equilibrium concentration, as shown below:

$$c = (1 - h)c_{\alpha\beta} + hc_\gamma \tag{12}$$

$$\frac{\partial f_{\alpha\beta}}{\partial c_{\alpha\beta}} = \frac{\partial f_{\gamma}}{\partial c_{\gamma}} \tag{13}$$

It should be noted that it is required that not only the above equations be satisfied near the interface, but also the equilibrium relationship be satisfied at each location point in the system. $c_{\alpha\beta}$ and c_{γ} are not compositions of the phase interface, but compositions of different phases, respectively, at a certain infinitesimal point which is assumed to be a mixture of a phase, β phase, and γ phase. Thus, Eq. 13 does not imply a constant chemical potential throughout the interfacial region. It is consistent across the interface only at a thermodynamic equilibrium state. The chemical potential can vary across the moving interface from the γ phase side to the a-β phase side, which results in the solute trapping effect (Aziz, 1982; Aziz and Kaplan, 1988; Aziz, 1996). Eq. 12 and 13 are a transcendental system of equations and have no analytical solution, so the equations were discretized using the explicit finite difference method. Then Newton's method was used to solve the discrete equations. We set the accuracy as 10^{-15} to ensure enough iterations to obtain a satisfactory numerical solution.

Migration coefficient accelerated by radiation

The diffusion coefficient of atoms in a crystal matrix $D_i$can be given by (Shewmon, 1989),

$$D_i = \theta w p_v \tag{14}$$

Where θ is a constant determined by material, w is the probability that an atom jumps into a vacant nearest-neighbour lattice site, and p_v is the probability that any given nearest-neighbour lattice site is vacant and it is approximately equal to the vacancy concentration C_v. w can be obtained from

$$w = \nu \exp\left(-\frac{G_m}{kT}\right) \tag{15}$$

Where ν is the vibrational frequency of the atoms, $G_m$is the free energy required for an atom to migrate from an equilibrium position to the nearest neighbour site and is a function of absolute temperature T, and k is the Boltzmann constant. By substituting Eq. 15 into Eq. 14, the diffusion coefficient of atoms can be rewritten as

$$D_i = \theta \nu \exp\left(-\frac{G_m}{kT}\right) C_v \tag{16}$$

Where we define $\delta(T) = \theta\nu \exp\left(-\frac{G_m}{kT}\right)$, which is not influenced by irradiation. Under irradiation condition, the vacancy concentration is the sum of the thermal equilibrium vacancy concentration C_v^e and the remaining free vacancy concentration created by irradiation C_v^r

$$C_v = C_v^e + C_v^r \tag{17}$$

Then the irradiation-enhanced diffusion coefficient can be rewritten as

$$D_i^* = \delta(T)\left(C_v^e + C_v^r\right) \tag{18}$$

D_i^* is equal to the intrinsic diffusion coefficient D_i^0, in the absence of irradiation. According to Eq. 16, $\delta(T)$ is given by

$$\delta(T) = D_i^0 / C_v^e \tag{19}$$

Thus, the irradiation-enhanced solute diffusion coefficient D_i^*can be obtained as,

$$D_i^* = \xi D_i^0 \tag{20}$$

where,

$$\xi = \left(\frac{C_v^e + C_v^r}{C_v^e}\right) \tag{21}$$

and

$$D_i^0 = D_{oi} \exp\left(-\frac{E_i}{kT}\right) \tag{22}$$

$$C_v^e = A_v \exp\left(-\frac{E_f^v}{kT}\right) \tag{23}$$

Where E_i is the activation energy and D_{oi} is the pre-exponential constant for solute diffusion in the matrix; A_v is a constant correlating with the vibrational entropy of atoms around the vacancy; the value can be taken as 1. $E_f^v$is the vacancy formation energy, and it is 1.20eV in U-10Zr (Vizoso and Deo, 2021).

By introducing the relationship of intrinsic diffusion and irradiation-enhanced diffusion, as shown in Eq. 20, into the phase-field model of constituent redistribution, we can get the diffusion mobility enhanced by irradiation,

$$M_c^I = M_c \xi \tag{24}$$

Where M_c is the chemical diffusion coefficient caused by the chemical potential gradient. According to the research of R. G. Faulkner (Faulkner et al., 1997), after 350 °C, the radiation enhanced diffusion coefficient is equal to the thermal diffusion coefficient in the a-Fe matrix, thermal diffusion starts to become significant and dominate at higher temperatures. Therefore, the value of ξ here should be as small as possible though we do not know the exact value without experimental data. Thermal equilibrium vacancy concentration can be obtained easily using Eq. 23. In contrast, the value of the vacancy concentration in an irradiated material is more challenging to calculate as it is a function of the radiation flux, the vacancy formation energy, the dislocation density, etc. Here, rate theory (Olander, 1976) was used to get an approximate reference value of vacancy concentration (7.04×10^{-7}) in the condition that the power was 30 kW/m and the temperature was about 1000K (Hofman et al., 1996). The vacancy concentration was derived from the vacancy created minus the vacancy

TABLE 1 Parameters required in calculating the diffusion coefficients.

Parameters	D_0^{α} (Hofman et al., 1996; Hirschhorn et al., 2019a)	D_0^{β} (Hofman et al., 1996; Hirschhorn et al., 2019a)	Q_{α} (Hofman et al., 1996)	Q_{β} (Hofman et al., 1996)	H_U (Mohanty et al., 2011)	H_{Zr} (Mohanty et al., 2011)	Q_{α}^{*} (Mohanty et al., 2011)	Q_{β}^{*} (Galloway et al., 2015)	Q_U^{*} (Hofman et al., 1996)	Q_{Zr}^{*}(Hofman et al., 1996)
Values	0.02	5.7	1.7	1.8	1.28	1.95	2.0	4.5	1.1	1.05
Units	$10^{-5}m^2/s$		10^5J/mol							

absorbed, as calculated by a computer program developed based on the rate theory model of J. Rest (Rest, 1993). The other relevant parameters needed in this calculation can be found in the reference (Rest, 1993).

$M_c$is expressed by the three-phase chemical diffusion coefficient (Mohanty et al., 2009),

$$M_c = \left(1 - h_{\alpha\beta}\right)(1-h)M_c^{\alpha} + h_{\alpha\beta}(1-h)M_c^{\beta} + hM_c^{\gamma} \tag{25}$$

Where $M_c^{\alpha}$is the chemical diffusion coefficient in the *a* phase, and M_c^{β} is the chemical diffusion coefficient in the β phase. The specific expressions of $M_c^i$are given below. The chemical diffusion coefficient in the *a*-β phase is:

$$M_c^i = \frac{D_0^i V_m}{RT}\exp\left(\frac{-Q_i}{RT}\right),\ (i = \alpha, \beta) \tag{26}$$

The chemical diffusion coefficient in the γ phase (Mohanty et al., 2011) is,

$$M_c^{\gamma} = V_m c_{\gamma}\left(1 - c_{\gamma}\right)\left[c_{\gamma}\beta_U + \left(1 - c_{\gamma}\right)\beta_{Zr}\right] \tag{27}$$

Where,

$$\beta_i = \beta_0 \exp\left(\frac{-H_i}{RT}\right) \tag{28}$$

Where $D_0^i$is the pre-exponential factor of the diffusion coefficient, and Q_i is the activation energy of the mutual migration of U and Zr in the i phase (i stands for α, β, and γ); β_U and β_{Zr} are the atomic mobility of U and Zr in the γ phase, H_i is the activation energy for the migration of U and Zr in the *i* phase, and β_0 is the pre-exponential factor of the diffusion coefficient.

M_T is similarly composed of the three parts, and it is expressed as follows:

$$M_T = \left(1 - h_{\alpha\beta}\right)(1-h)M_T^{\alpha} + h_{\alpha\beta}(1-h)M_T^{\beta} + hM_T^{\gamma} \tag{29}$$

The thermal migration coefficient in the *a*-β phase is:

$$M_T^i = \frac{D_0^i Q_i^*}{RT}\exp\left(\frac{-Q_i}{RT}\right) \tag{30}$$

The thermal migration coefficient in the γ phase is:

$$M_T^{\gamma} = c_{\gamma}\left(1 - c_{\gamma}\right)\left(Q_U^*\beta_U + Q_{Zr}^*\beta_{Zr}\right) \tag{31}$$

Where Q_i^* is an experimentally determined parameter describing the heat transport effect. Its sign determines whether the material migrates to the high-temperature region or the low-temperature region, and its value determines the amount of migration. In Table 1, the values of all the required parameters used above are summarized.

Simulation methods

The thermodynamic parameters used in our simulation were all inherited from the DP-81 fuel. The DP-81 fuel element was

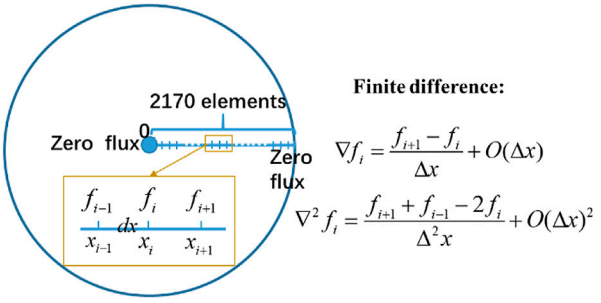

FIGURE 1
Schematic diagram of finite difference method simulation.

irradiated at the EBR-II reactor by Argonne National Laboratory. The experimental data of the DP-81 pin provided a typical example for verification of this work because there exists not only the temperature profile but also measured data which indicates significant migration of zirconium. The experimental data about Zr concentration we used here were from Figure 7 of Hofman et al.'s article (Hofman et al., 1996). The fuel surface temperature was 900K, while the central temperature was about 988K, and the temperature distribution profile used here was from A. M. Yacout et al. (Yacout et al., 1996). All the simulations were conducted using the explicit finite difference method on the Matlab platform in this work. 1D simulations with 2170 μm long axisymmetric domain discretized into 2,170 elements were used in the current work to represent the DP-81 fuel, as shown in Figure 1. The left side of the 1-D linear segment represents the centerline, and the right side represents the outer surface of the fuel. Zero-flux boundary conditions were applied to all the centerline and the external surface variables. The time step was chosen to be 1s, and a total time length of 1.3×10^5 s was conducted in all simulations.

Simulation results

As described before, the driving forces acting on the Zr migration can be divided into two parts, i.e., heat transport term due to the temperature gradient and chemical potential gradient term which tends to equalize the concentration distribution. The diffusion coefficient controls the amount of Zr relocated, and heat transport and chemical potential gradient control the direction and the trend of the redistribution. To highlight the importance of radiation-accelerated diffusion in constituent redistribution models, we compared the simulation results between redistribution without the effect of irradiation and redistribution with the effect of irradiation, as shown inFigure 2, 3. Figure 2 shows the simulation results without considering the accelerated diffusion of irradiation. It can be seen that although Zr still tends to move to the high-temperature region due to the existence of the temperature gradient, there is almost no constituent redistribution. While the simulation results of Figure 3 are much in good agreement with the experimental data.

A noticeable feature of the Zr redistribution in Figure 3 is that a "Zr well" formed in the middle radial region of the fuel slug. Zr atoms migrate towards the fuel centre at high temperatures, causing the Zr concentration in the fuel centre to increase and U concentration to decline correspondingly. Consequently, the concentration of Zr in the middle radial region is relatively low. Phase distribution is also in line with the experimental results. The red line is the γ phase fraction, and the γ phase is mainly located in the central region of the fuel, coexisting with the β phase in the middle radial region, and coexisting with the a phase near the outer fuel surface.

The comparison of the Zr concentration redistribution simulated by different models, including the model in this work, are shown in Figure 4. It is found that the introduction of the radiation-enhanced diffusion coefficient into the existing phase-field model seems to be able to replace reasonably the artificial increase of the diffusion coefficient. And by improving the rationality of some parameters of the phase-field model, such as the influence of temperature on the interface mobility, the accuracy of the simulation is significantly improved.

Discussion

Discussion of interfacial parameters

The interface energy and the interface width occupy extraordinary significance in the phase-field model. The model parameters are often phenomenological and don't possess the essence of natural physical properties (Moelans et al., 2008). Therefore, it is necessary to analyze the parameters and their effects on the simulation results. In this section, we first discussed the interface energy and then discussed the interface width by defining the macro phase boundary width.

For the KKS model, the chemical energy is decoupled from the interfacial energy, and the interfacial energy is only provided by the potential well term and the gradient term (Aagesen et al., 2018). It should be noted that the interface energy is not a specific phase boundary energy but rather a homogenized parameter describing all the phase boundaries in the two-phase region. The interface energy of phase boundaries in the two-phase areas in the discrete system model can thus be written as:

$$\sigma_{pb} = \sum_x \left[\omega g(\gamma) + \frac{\kappa_\gamma}{2} \left(\left| \frac{d\gamma}{dx} \right| \right)^2 \right] \tag{32}$$

Where x is the axial coordinate of the phase boundaries in the two-phase regions. ω is the height of the double potential well

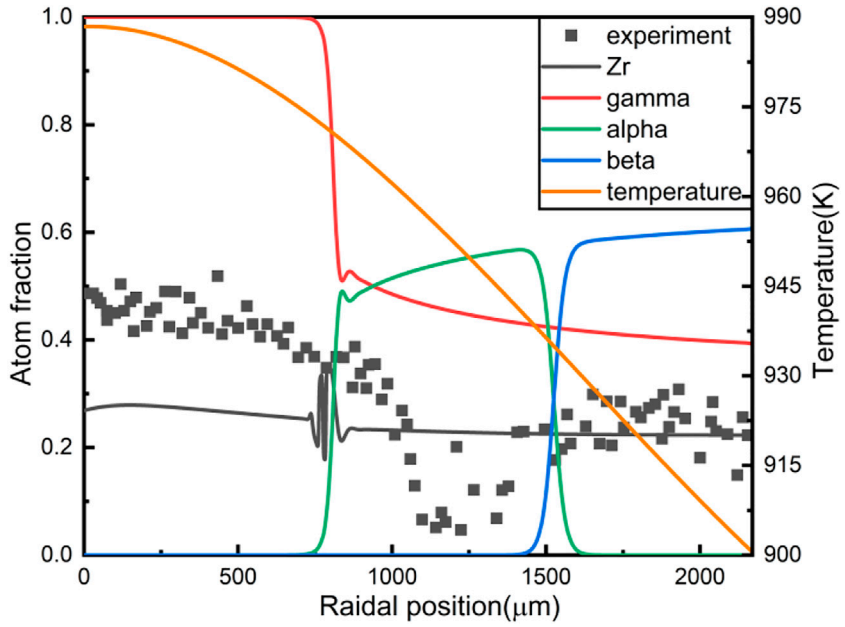

FIGURE 2
The results of U-10wt%Zr constituent redistribution without the effect of irradiation.

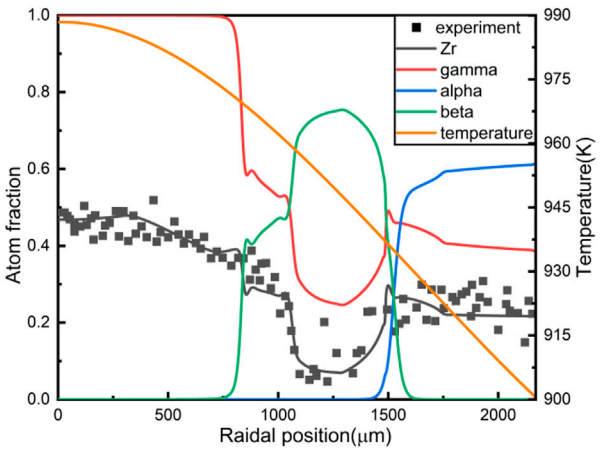

FIGURE 3
The results of U-10wt%Zr constituent redistribution with introducing the radiation-enhanced diffusion.

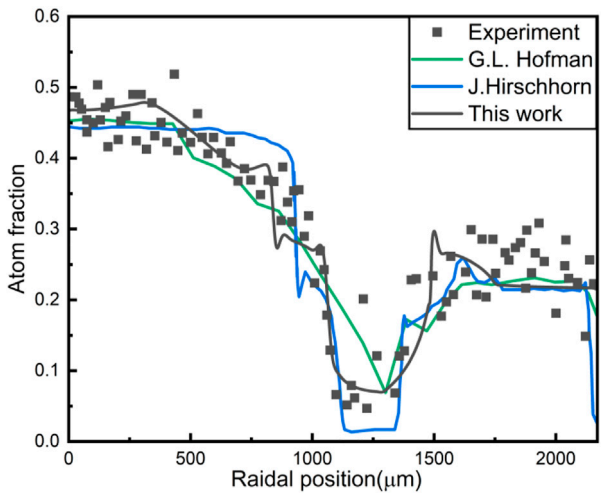

FIGURE 4
The U-10%Zr constituent redistribution obtained by different models.

function and κ_γ is the energy coefficient of the phase fraction gradient in Eq. 9.

It is well known that the interfacial width is chosen mainly based on computational consideration in interface growth models. The phase boundary, which refers to the boundary between different phases, will be discussed in the following, referencing the definition of the grain boundary. Strictly speaking, there are many possibilities to define a measure for the boundary once the diffusion surface thickness reaches infinity. For example, Moelans et al. (Faulkner et al., 1996; Moelans et al., 2008) described the grain boundary based on the absolute value of the gradient.

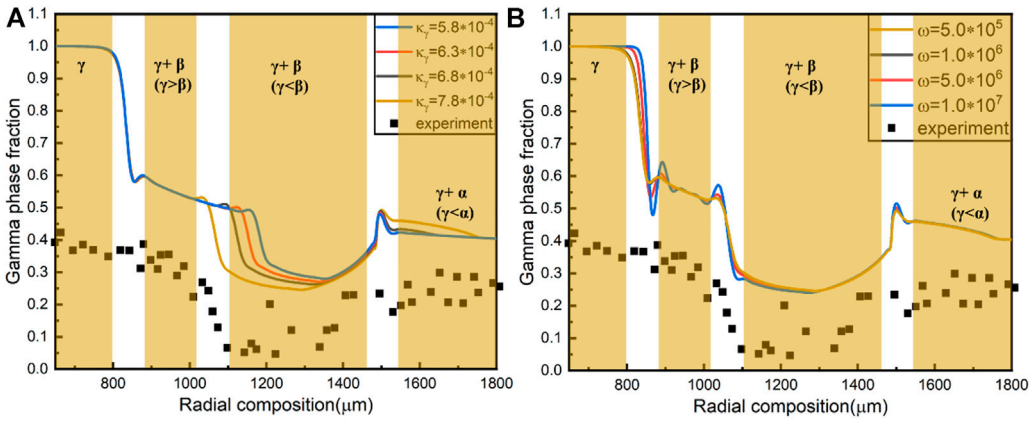

FIGURE 5
(A) γ Phase fraction as a function of κ_γ, with $\omega = 5.0 \times 10^5 J/m^3$; **(B)** The curve of γ phase fraction concerning the ω at the interface, with$\kappa_\gamma = 7.8 \times 10^{-4} J/m$. Rectangular areas are different phase areas divided according to the yellow curves.

$$l_{gb} = \frac{1}{\left|(d\gamma(x)/dx)_{x=x_{inter}}\right|} \tag{33}$$

Where x_{inter} is the position where the interface gradient is the greatest. The gradient term is expressed using the finite difference method,

$$\frac{d\gamma(x)}{dx} = \frac{\gamma(x_2) - \gamma(x_1)}{x_2 - x_1} \tag{34}$$

Since the profiles are steepest at the middle of the diffuse boundary region, a grain boundary width defined in this way can be used as numerical criteria for stability and accuracy. However, the description of the boundary in the microscopic situation does not apply to the situation of the macroscopic edge. Here, we proposed a new definition of boundary width based on Moelans et al., as shown in Eq. 35.

$$l_{pb} = \frac{\left|d\gamma(x)\right|_{x=x_{inter}}}{\left|(d\gamma(x)/dx)_{x=x_{inter}}\right|} \propto \sqrt{\frac{\kappa_\gamma}{\omega}} \tag{35}$$

This equation is an extension of Eq. 34. In phase-field method, it can be used to express the phase boundaries and make the boundaries describable and discussible in macroscopic scenarios. For example, in a microscopic system with grain boundaries, two crystal grains can be distinguished by $\eta = 0$ and $\eta = 1$, and the value of $d\eta$ at the grain boundary always equals 1. Under this circumstance, Eq. 33 is applicable. However, in a macroscopic system, it is not enough to distinguish different phase regions based on whether the value of γ is 0 or 1. For example, in the γ phase area, γ is equal to 1, while in the γ+β phase area, γ is not equal to 0, but the γ phase area and the γ+β phase area are two-phase regions, which are also needed to be distinguished. Similarly, γ+β phase area and γ+α phase area are also two different phases, as shown by the yellow rectangles in Figure 5. One boundary between two-phase areas is shown as the white areas in Figure 5. The values of $d\gamma$ at boundaries between two-phase areas are also not equal to 1, and in most cases, they are not fixed values. Therefore, we flexibly defined the area where the phase fraction γ has obvious saltation as the phase boundary. Its width is the interface width, which can describe the actual situation more accurately.

To get the values of interface energy σ_{pb} and interface width l_{pb}, κ_γ and ω should be first determined. By comparing the Zr concentration, obtained with different values of κ_γ and ω with the experimental data, we locked the order of magnitude of the two parameters and then continuously refined and finally determined the values. In Figure 5, the evolution of γ at a flat boundary is shown for different values of the parameters κ_γ and ω. The variation of the phase fraction is concentrated in the 700–1300 μm region along the radial direction. Comparisons among these profiles were helpful to analyze the effects of ω and κ_γ. In Figure 5A, the value of ω was fixed to observe the impact of κ_γ. It can be found that the role of κ_γ is primarily reflected by the size of the "Zr well". The larger the value of κ_γ, the deeper and broader the well becomes. By comparing the experimental data (Zr concentration) with the simulation results and regarding the "Zr well" as an apparent reference, it is found that the yellow curve is mostly in good agreement. Either too large or too small values of κ_γ can distort the simulation results. In Figure 5B, the predicted γ profiles show that the value of ω can vary across two orders of magnitude. Within this range, variations of ω produce minor local variations in the predicted γ profiles. With the increase of ω, the interface width decreases gradually, and the interfaces between different phase regions are getting sharper, which can also degrade the computational efficiency.

The interfacial energy σ_{pb} and the interfacial width l_{pb} can be calculated by numerical computation from Eq. 32 and 35. Their

TABLE 2 Different κ_γ and ω corresponding to different interfacial energy and interface width. σ_1 is the interfacial energy between γ phase and γ+ β (γ>ß) phase.

$\kappa_\gamma(10^{-4}\mathrm{J/m})$	$\omega(10^5\mathrm{J/m^3})$	$\sigma_1(10^6\mathrm{J})$	$l_{pb}(\mu\mathrm{m})$
5.8	5.0	0.7243	34.059
6.3	5.0	1.3421	35.496
6.8	5.0	1.3438	36.878
7.8	5.0	1.3465	39.497
7.8	10.0	2.6270	27.928
7.8	50.0	10.768	12.490
7.8	100.0	16.660	8.8318

values are shown in Table 2, corresponding to the different interfacial parameter values. The values in the grey background line are found to be the most appropriate values for the model by trial-and-error type of calculations.

Discussion of the results near the fuel surface

Obviously, there is a distinct difference between the simulation results and the experimental data near the fuel surface among all constituent redistribution models, shown as Figure 4. Some Zr atoms migrate to the region between 1700 and 2000μm, making the Zr concentration higher than the initial concentration (0.225). Under normal circumstances, there is hardly Zr migration due to the small atom diffusion coefficient in the *a*-U phase. The specific reason is unknown, but it shall not be interpreted to be caused by temperature because the heat of transport parameter Q^* analysis by G. L. Hofman (Hofman et al., 1996) has shown that Zr concentration at this position has nothing to do with Q^*. According to Thaddeus et al. (Rahn et al., 2021), it seems that the Zr rind can form during fabrication. But we cannot rule out that the increased atom diffusion coefficient due to irradiation effects made Zr gather locally in a long time-scale. Another possibility is that the structural change causes the free energy of the initial *a*-U phase to no longer apply. If so, the high fuel consumption effect cannot be ruled out. These will need to be clarified with further research.

Conclusion

Combined with traditional thermodynamics, the phase-field model coupling the radiation-enhanced diffusion model was constructed in this work. Firstly, the results of Zr redistribution simulated by the phase-field model were given and compared with the results of the model without the effect of radiation, which demonstrated the importance and necessity of introducing the radiation-enhanced diffusion model. Secondly, the influence of temperature on the kinetic coefficients was also imported to improve the rigour of the model. The computational results of the improved model appear to be in better agreement with the experimental data, compared to the previous models. Thirdly, an expression of boundary width applied to the macroscopic scenario was proposed to analyse the phase distribution. Through the analysis of phase interfacial parameters, the magnitude of the potential barrier played an essential role in forming a sharp interface and the energy coefficients had few effects on the redistribution results. This model may further help extend the application of phase-field in the constituent redistribution.

Data availability statement

The original contributions presented in the study are included in the article/supplementary material, further inquiries can be directed to the corresponding authors.

Author contributions

CW: The realization of the phase-field model; Manuscript writing WL: Study conception and design; Model modification idea DY: Study conception and design; The manuscript revised ZQ: Calculation of rate theory.

Funding

This work was supported by the NSAF Joint Fund (No. U2130105), the National Natural Science Foundation of China (No. 11675126) and the Innovative Scientific Program of CNNC.

Conflict of interest

The authors declare that the research was conducted in the absence of any commercial or financial relationships that could be construed as a potential conflict of interest.

Publisher's note

References

Aagesen, L. K., Gao, Y., Schwen, D., and Ahmed, K. (2018). Grand-potential-based phase-field model for multiple phases, grains, and chemical components. *Phys. Rev. E* 98 (2), 023309. doi:10.1103/physreve.98.023309

Ahmed, K., Pakarinen, J., Allen, T., and El-Azab, A. (2014). Phase field simulation of grain growth in porous uranium dioxide. *J. Nucl. Mater.* 446 (1-3), 90–99. doi:10.1016/j.jnucmat.2013.11.036

Allen, S. M., and Cahn, J. W. (1973). A correction to the ground state of FCC binary ordered alloys with first and second neighbor pairwise interactions. *Scr. Metall.* 7 (12), 1261–1264. doi:10.1016/0036-9748(73)90073-2

Allen, S. M., and Cahn, J. W. (1972). Ground state structures in ordered binary alloys with second neighbor interactions. *Acta Metall.* 20 (3), 423–433. doi:10.1016/0001-6160(72)90037-5

Aziz, M. J. (1996). Interface attachment kinetics in alloy solidification. *Metallurgical Mater. Trans. A* 27 (3), 671–686. doi:10.1007/bf02648954

Aziz, M. J., and Kaplan, T. (1988). Continuous growth model for interface motion during alloy solidification. *Acta Metall.* 36 (8), 2335–2347. doi:10.1016/0001-6160(88)90333-1

Aziz, M. J. (1982). Model for solute redistribution during rapid solidification. *J. Appl. Phys.* 53 (2), 1158–1168. doi:10.1063/1.329867

Biner, S. B. (2017). *An overview of the phase-field method and its formalisms*. Cham, Switzerland: Springer International Publishing, 1–7. Programming Phase-Field Modeling.

Chen, W., Peng, Y., Li, X. A., Chen, K., Ma, J., Wei, L., et al. (2017). Phase-field study on geometry-dependent migration behavior of voids under temperature gradient in UO_2 crystal matrix. *J. Appl. Phys.* 122 (15), 154102. doi:10.1063/1.4996692

Dinsdale, A. (1991). SGTE data for pure elements. *Calphad* 15 (4), 317–425. doi:10.1016/0364-5916(91)90030-n

Faulkner, R. G., Song, S., and Flewitt, P. E. J. (1996). A model describing neutron irradiation-induced segregation to grain boundaries in dilute alloys. *Metallurgical Mater. Trans. A* 27 (11), 3381–3390. doi:10.1007/bf02595431

Faulkner, R. G., Song, S., Flewitt, P. E. J., and Fisher, S. B. (1997). Irradiation-enhanced solute diffusion in alloys. *J. Mat. Sci. Lett.* 16 (14), 1191–1194. doi:10.1007/bf02765407

Feldman, E. E., Mohr, D., Chang, L. K., Planchon, H., Dean, E., and Betten, P. (1987). EBR-II unprotected loss-of-heat-sink predictions and preliminary test results. *Nucl. Eng. Des.* 101 (1), 57–66. doi:10.1016/0029-5493(87)90150-6

Galloway, J., Unal, C., Carlson, N., Porter, D., and Hayes, S. (2015). Modeling constituent redistribution in U-Pu-Zr metallic fuel using the advanced fuel performance code BISON. *Nucl. Eng. Des.* 286, 1–17. doi:10.1016/j.nucengdes.2015.01.014

Hirschhorn, J., Aitkaliyeva, A., Adkins, C., and Tonks, M. (2019). The microstructure and thermodynamic behavior of as-cast U-24Pu-15Zr: Unexpected results and recommendations for U-Pu-Zr fuel research methodology. *J. Nucl. Mater.* 518, 80–94. doi:10.1016/j.jnucmat.2019.02.039

Hirschhorn, J., Tonks, M., Aitkaliyeva, A., and Adkins, C. (2020). Reexamination of a U-Zr diffusion couple experiment using quantitative phase-field modeling and sensitivity analysis. *J. Nucl. Mater.* 529, 151929. doi:10.1016/j.jnucmat.2019.151929

Hirschhorn, J., Tonks, M., and Matthews, C. (2021). A CALPHAD-informed approach to modeling constituent redistribution in Zr-based metallic fuels using BISON. *J. Nucl. Mater.* 544, 152657. doi:10.1016/j.jnucmat.2020.152657

Hirschhorn, J., Tonks, M. R., Aitkaliyeva, A., and Adkins, C. (2019). A study of constituent redistribution in U-Zr fuels using quantitative phase-field modeling and sensitivity analysis. *J. Nucl. Mater.* 523, 143–156. doi:10.1016/j.jnucmat.2019.05.053

Hofman, G. L., Hayes, S. L., and Petri, M. C. (1996). Temperature gradient driven constituent redistribution in U- Zr alloys. *J. Nucl. Mater.* 227 (3), 277–286. doi:10.1016/0022-3115(95)00129-8

Hu, S., Henager, C. H., Heinisch, H. L., Stan, M., Baskes, M. I., and Valone, S. M. (2009). Phase-field modeling of gas bubbles and thermal conductivity evolution in nuclear fuels. *J. Nucl. Mater.* 392, 292–300. doi:10.1016/j.jnucmat.2009.03.017

Hu, S., Li, Y., Sun, X., Gao, F., Devanathan, R., Henager, C. H., et al. (2010). Application of the phase-field method in predicting gas bubble microstructure evolution in nuclear fuels. *Int. J. Mater. Res.* 101, 515–522. doi:10.3139/146.110304

Kim, S. G., Kim, W. T., and Suzuki, T. (1999). Phase-field model for binary alloys. *Phys. Rev. E* 60 (6), 7186–7197. doi:10.1103/physreve.60.7186

Kim, Y. S., Hayes, S. L., Hofman, G. L., and Yacout, A. (2006). Modeling of constituent redistribution in U-Pu-Zr metallic fuel. *J. Nucl. Mater.* 359 (1-2), 17–28. doi:10.1016/j.jnucmat.2006.07.013

Kim, Y. S., Hofman, G. L., Hayes, S. L., and Sohn, Y. (2004). Constituent redistribution in U-Pu-Zr fuel during irradiation. *J. Nucl. Mater.* 327 (1), 27–36. doi:10.1016/j.jnucmat.2004.01.012

Kreuzer, H. J. (1981). *Nonequilibrium thermodynamics and its statistical foundations*. London, United Kingdom: Clarendon Press, 438.

Li, Y., Hu, S., Sun, X., and Stan, M. (2017). A review: Applications of the phase field method in predicting microstructure and property evolution of irradiated nuclear materials. *NPJ Comput. Mat.* 3 (1), 16–17. doi:10.1038/s41524-017-0018-y

Liang, L., Mei, Z. G., Kim, Y. S., Ye, B., Hofman, G., Anitescu, M., et al. (2016). Mesoscale model for fission-induced recrystallization in U-7Mo alloy. *Comput. Mater. Sci.* 124, 228–237. doi:10.1016/j.commatsci.2016.07.033

Mei, Z. G., Liang, L., Kim, Y. S., Wiencek, T., O'Hare, E., Yacout, A. M., et al. (2016). Grain growth in U-7Mo alloy: A combined first-principles and phase field study. *J. Nucl. Mater.* 473, 300–308. doi:10.1016/j.jnucmat.2016.01.027

Millett, P. C., El-Azab, A., and Wolf, D. (2011). Phase-field simulation of irradiated metals Part II: Gas bubble kinetics. *Comput. Mater. Sci.* 50, 960–970. doi:10.1016/j.commatsci.2010.10.032

Millett, P. C., and Tonks, M. (2011). Application of phase-field modeling to irradiation effects in materials. *Curr. Opin. Solid State Mater. Sci.* 15 (3), 125–133. doi:10.1016/j.cossms.2010.10.002

Millett, P. C., and Tonks, M. (2011). Phase-field simulations of gas density within bubbles in metals under irradiation. *Comput. Mater. Sci.* 50, 2044–2050. doi:10.1016/j.commatsci.2011.02.006

Millett, P. C., Tonks, M. R., Biner, S. B., Zhang, L., Chockalingam, K., and Zhang, Y. (2012). Phase-field simulation of intergranular bubble growth and percolation in bicrystals. *J. Nucl. Mater.* 425 (1-3), 130–135. doi:10.1016/j.jnucmat.2011.07.034

Moelans, N., Blanpain, B., and Wollants, P. (2008). Quantitative analysis of grain boundary properties in a generalized phase field model for grain growth in anisotropic systems. *Phys. Rev. B* 78 (2), 024113. doi:10.1103/physrevb.78.024113

Mohanty, R. R., Bush, J., Okuniewski, M. A., and Sohn, Y. (2011). Thermotransport in γ (bcc) U-Zr alloys: A phase-field model study. *J. Nucl. Mater.* 414 (2), 211–216. doi:10.1016/j.jnucmat.2011.03.028

Mohanty, R. R., Guyer, J. E., and Sohn, Y. H. (2009). Diffusion under temperature gradient: A phase-field model study. *J. Appl. Phys.* 106 (3), 034912. doi:10.1063/1.3190607

Mohr, D., Chang, L. K., Feldman, E. E., Betten, P., and Planchon, H. (1987). Loss-of-primary-flow-without-scram tests: Pretest predictions and preliminary results. *Nucl. Eng. Des.* 101 (1), 45–56. doi:10.1016/0029-5493(87)90149-x

Murphy, W. F., Beck, W. N., Brown, F. L., Koprowski, B. J., and Neimark, L. A. (1969). *Postirradiation examination of U-Pu-Zr fuel elements irradiated in EBR-II to 4.5 atomic percent Burnup*. Illinois, United States: Argonne National Laboratory.

Nam, C., and Hwang, W. (1998). A calculation model for fuel constituent redistribution and temperature distribution on metallic U-10Zr fuel slug of liquid metal reactors. *Nucl. Eng. Technol.* 30 (6), 507–517.

Olander, D. R. (1976). *Fundamental aspects of nuclear reactor fuel elements. TID-26711-P1*. Berkeley (USA): California University.

Quaini, A., Guéneau, C., Gossé, S., Dupin, N., Sundman, B., Brackx, E., et al. (2018). Contribution to the thermodynamic description of the corium-the U-Zr-O system. *J. Nucl. Mater.* 501, 104–131. doi:10.1016/j.jnucmat.2018.01.023

Rahn, T., Capriotti, L., Di Lemma, F., Trowbridge, T. L., Harp, J. M., and Aitkaliyeva, A. (2021). Investigation of constituent redistribution in U-Pu-Zr fuels and its dependence on varying Zr content. *J. Nucl. Mater.* 557, 153301. doi:10.1016/j.jnucmat.2021.153301

Rest, J. (1993). Kinetics of fission-gas-bubble-nucleated void swelling of the alpha-uranium phase of irradiated U-Zr and U-Pu-Zr fuel. *J. Nucl. Mater.* 207, 192–204. doi:10.1016/0022-3115(93)90261-v

Shewmon, P. (1989). *Diffusion in solids. The minerals, Metals & Materials Series* (Cham, Switzerland: Springer), 53–130.

Tonks, M. R., Cheniour, A., and Aagesen, L. (2018). How to apply the phase field method to model radiation damage. *Comput. Mater. Sci.* 147, 353–362. doi:10.1016/j.commatsci.2018.02.007

Tonks, M. R., Zhang, Y., Bai, X., and Millett, P. C. (2014). Demonstrating the temperature gradient impact on grain growth in UO_2 using the phase field method. *Mater. Res. Lett.* 2, 23–28. doi:10.1080/21663831.2013.849300

Vizoso, D., and Deo, C. (2021). Determination of vacancy formation energies in binary UZr alloys using special quasirandom structure methods. *Front. Mat.* 8, 243. doi:10.3389/fmats.2021.692660

Wang, M., Zong, B., and Wang, G. (2009). Grain growth in AZ31 Mg alloy during recrystallization at different temperatures by phase field simulation. *Comput. Mater. Sci.* 45, 217–222. doi:10.1016/j.commatsci.2008.09.010

Wen, Y. H., Wang, B., Simmons, J. P., and Wang, Y. (2006). A phase-field model for heat treatment applications in ni-based alloys. *Acta Mater.* 54, 2087–2099. doi:10.1016/j.actamat.2006.01.001

Yacout, A. M., Yang, W. S., Hofman, G. L., and Orechwa, Y. (1996). Average irradiation temperature for the analysis of in-pile integral measurements. *Nucl. Technol.* 115 (1), 61–72. doi:10.13182/nt96-a35275

frontiers | Frontiers in Materials

TYPE Original Research
PUBLISHED 19 September 2022
DOI 10.3389/fmats.2022.989040

OPEN ACCESS

EDITED BY
Yu-Hong Zhao,
North University of China, China

REVIEWED BY
Houbing Huang,
Beijing Institute of Technology, China
Dongke Sun,
Southeast University, China

*CORRESPONDENCE
Ming Chen,
chenming@ustl.edu.cn

SPECIALTY SECTION
This article was submitted to Computational Materials Science, a section of the journal Frontiers in Materials

RECEIVED 08 July 2022
ACCEPTED 26 August 2022
PUBLISHED 19 September 2022

CITATION
Zeng HB, Ai XG, Chen M and Hu XD (2022), Application of phase field model coupled with convective effects in binary alloy directional solidification and roll casting processes.
Front. Mater. 9:989040.
doi: 10.3389/fmats.2022.989040

Application of phase field model coupled with convective effects in binary alloy directional solidification and roll casting processes

Hong Bo Zeng[1], Xin Gang Ai[1], Ming Chen[2]* and Xiao Dong Hu[1]

[1]School of Materials and Metallurgy, University of Science and Technology Liaoning, Anshan, China, [2]School of Mechanical Engineering and Automation, University of Science and Technology Liaoning, Anshan, China

Based on the Kim-Kim-Suzuki (KKS) phase field model coupled with the thermodynamic parameters, the transformation process from columnar dendrites to equiaxed crystals during directional solidification of aluminium alloy was simulated, and the effects of phase field parameters on the growth morphology and dendrite segregation were discussed. Furthermore, considering the effect of the microcosmic flow field, the convection influence gradient term is introduced into KKS formula near the solid-liquid interface, and the phase field model considering flow field was applied to the inherent convective environment of the actual roll casting process, also the multiple dendrites growth behavior of magnesium alloy under the action of microscopic convection was further explored. When coupling calculation of microscopic velocity field and pressure field, the staggered grid method was used to deal with the complex interface. The combined solution of Marker in Cell (MAC) algorithm and phase field discrete calculation was realized. In order to further describe the influence of convection on the solidification process, the roll casting experiments are used to verify the impact growth of multiple dendrites under convection. The results show that the dendrites undergo solute remelting and the dendrites melt into equiaxed crystals, showing the phenomenon of Columnar to Equiaxed Transition (CET).

KEYWORDS

phase field method, convection, columnar dendrites, numerical simulation, directional solidification

1 Introduction

The growth process of directionally solidified dendrites was influenced by the interplay of heat, mass and momentum transport as well as interfacial dynamics (Zhao et al. (2019); Shiga et al. (2019)), which ultimately results in a complex and variable structure (Li et al. (2021); Cui et al. (2020)). The use of numerical simulation methods with lower cost than thermal experiments to explore the growth patterns of

dendrites under different conditions, which not only provides important guidance for practical production but also helps to gain insight into the solidification characteristics of metallic materials (Lee et al. (2020); Noubary et al. (2017)). The development of computer numerical simulation technology provides a practical method for the quantitative description of complex metal solidification processes (Sinhababu and Bhattacharya, (2022)). By coupling external fields such as temperature field, solute field and flow field, the phase field method can simulate the evolution of metal microstructure in the casting process more accurately (Wei et al. (2020); Li et al. (2020)), which helps people to deeply understand the metal solidification theory and predict the microstructure of metal materials (Wang et al. (2019)), and use it as a basis to optimize the casting process. Pinomaa et al. (Pinomaa and Provatas, (2019)) quantitatively mapped the thin interface behavior of an ideal dilute binary alloy phase field model to CGM dynamics, the simulation results show that the mapping was convergent for different interface widths, and the effect of solute trapping on cell crystal growth in directional solidification was found. Novokreshchenova et al. (Novokreshchenova and Lebedev, (2017)) optimized the local nonequilibrium phase field model and accurately predicted the relationship between interfacial mobility and temperature during directional solidification of pure nickel. Steinmetz, Ghosh et al. (Steinmetz et al. (2018); Ghosh et al. (2019)) conducted a simulation study using a thermodynamically consistent phase field model, the effects of different interfacial energies, diffusivity, lamellar spacing and solidification rate on the growth of the solid phase during directional solidification were studied. The results show that all the factors have significant effects on the growth of dendrites. Lenart et al. (Lenart and Eshraghi, (2020)) used the phase field Boltzmann model (PF-LBM) to simulate the transformation process of Inconel 718 alloy from columnar dendrites to equiaxed crystal, and found that the simulation results were consistent with those obtained in the Inconel 718 solidification experiments. A lot of achievements have also been achieved in the micro simulation of directional solidification in China. Ma et al. (Ma et al. (2020)) proposed a new 3D cellular automata-lattice Boltzmann method (CA-LBM) for simulating the formation of facet and facet dendrites in directional solidification, and reasonably solved the interaction of interfacial energy anisotropy and dynamical anisotropy. Yang et al. (Yang et al. (2017)) investigated the microstructure of a nickel-based superalloy during three-dimensional solidification using the phase field method, and found that the simulated results of dendrites directional solidification were in good agreement with the experimental results. Zhang, Zhu, and Wang et al. (Zhang B. et al. (2019); Zhu et al. (2019); Wang et al. (2020)) used the phase field method to simulate the directional solidification process of Al-Si, Al-Cu, and Mg-Gd binary alloys, all the simulation results show that the increase of anisotropy, cooling rate and temperature gradient can accelerate the solidification rate of columnar dendrites. Based on the above research, in order to simulate the real dendritic growth process more closely in recent years, metallurgical researchers put emphasis on the optimization of phase-field model, but at the same time, the phase-field model becomes more and more complex, which increases the pressure of computer calculation. Therefore, it is very important to find a faster and better calculation method to promote the development of phase-field method.

It is an unquestionable fact that convection has a significant effect on the morphology of solidified dendrites (Nabavizadeh et al. (2020)). Convection can promote or hinder the growth of dendrites, and the microstructure of dendrites is completely different from that of pure diffusion (Geng et al. (2020); Xiong et al. (2022)). The research on the effect of convection on the evolution of solidification organization is relatively fast in China, but there is still scarce of foreign research in this area. Yang et al. (Yang et al. (2020)) combined the multiphase field model with Boltzmann's method to simulate the dendrites growth process of superalloys under the action of convection, the distribution of solute with the velocity of dendrites tip during solidification was obtained, and the effect of natural convection on the microsegregation and dendrites growth rate was confirmed. Yuan et al. (Yuan and Ding, (2012)) studied the growth morphology of pure nickel dendrites by using a phase field model with coupled flow fields, it was found that the melt flow significantly changes the heat transfer at the solidification front, which affects the dendrites growth. Chen and Wang et al. (Chen et al. (2011); Wang et al. (2012)) simulated the dendritic evolution of Ni-Cu alloy under non-isothermal conditions and found that the nuclei grew into asymmetric dendrites in forced convection. Later, Luo and Zhang et al. (Luo et al. (2020); Zhang A. et al. (2019)) investigated the dendrites growth behavior of Fe-C alloys under forced convection, and also found that the unsymmetrical behavior of dendrites growth was caused by forced convection. In addition, Chen et al. (Chen et al. (2016)) used KKS phase field model to simulate the microstructure evolution of AZ31 magnesium alloy dendrites in the center of roll casting molten pool. The effect of different flow rate values on dendrite evolution was discussed in detail, and it is found that the microstructure was consistent with the actual pattern observed by optical microscopy. Therefore, there is no doubt that micro convection makes the dendrites in the melt grow asymmetrically, but the above research only establishes a phase field model with convective properties and does not consider the actual metallurgical process including the flow field. Moreover, the research on the microstructure evolution of polycrystalline directional solidification with real flow field in the actual process is relatively scarce. Due to the actual

production process is complex and changeable, the simulation results should also be different. Based on this, it will be of far-reaching significance to explore the growth behavior of dendrites under actual process conditions.

In this paper, based on the KKS phase field model coupled with the thermodynamic parameters, the transformation process from columnar dendrites to equiaxed crystals during directional solidification of aluminum alloy was simulated. The effects of phase field parameters on the growth morphology and dendrites segregation were discussed. Furthermore, considering the effect of the microcosmic flow field, the convection influence gradient term is introduced into KKS formula near the solid-liquid interface, and the phase field model considering flow field was applied to the inherent convective environment of the actual roll casting process, also the multiple dendrites growth behavior of magnesium alloy under the action of microscopic convection was further explored. The combined solution of MAC algorithm and phase field discrete calculation realized. The dendrites growth behavior of magnesium alloy under the action of microscopic convection in the roll casting was further explored.

2 Phase field model

2.1 Phase field equation

The directional solidification technique can obtain a specific columnar dendrites structure, which is very significant for optimizing the axial mechanical properties of the alloy. Although the traditional experimental has the advantage of being intuitive and operable, it does not reveal the mechanism of dendrites formation. In this paper, the KKS phase field model of the system free energy changing with time was used (Kim et al. (1999)). The control equation of the KKS phase field is:

$$\frac{\partial \varphi}{\partial t} = M_{\varphi}\left(\epsilon^2 \nabla^2 \varphi - f\left(c, \varphi\right)\right) \tag{1}$$

In Eq. 1, the free energy density $f\left(c, \varphi\right)$can be expressed as:

$$f\left(c, \varphi\right) = h\left(\varphi\right) f^S\left(c_s\right) + \left(1 - h\left(\varphi\right)\right) f^L\left(c_L\right) + W g\left(\varphi\right) \tag{2}$$

where$W g\left(\varphi\right)$is a specific double potential well function, $h\left(\varphi\right)$is the potential function, $g\left(\varphi\right)$is the residual free energy function, in this paper: $h\left(\varphi\right) = \varphi^3\left(6\varphi^2 - 15\varphi + 10\right)$, $g\left(\varphi\right) = \varphi^2\left(1 - \varphi^2\right)$, $f^S\left(c_s\right)$and$f^L\left(c_L\right)$are the free energies of the solid and liquid phases, respectively.

Therefore, the phase field equation can be re-expressed as:

$$\frac{\partial \varphi}{\partial t} = M_{\varphi}\left[\epsilon^2\left(\theta\right)\nabla^2 \varphi + h\left(\varphi\right)\left(f^L\left(c_L\right) - f^S\left(c_s\right)\right) - W g\left(\varphi\right)\right] \tag{3}$$

where$M_{\phi}$is the interface migration rate, $\varepsilon$and$W$are the phase field parameters related to the interface energy and interface thickness.

2.2 Solute field equation

During the numerical simulation of directional solidification, it is also necessary to solve the solute diffusion equation at the same time. The diffusion equation is:

$$\frac{\partial c}{\partial t} = \nabla \cdot \left(\frac{D\left(\varphi\right)}{f_{cc}} \nabla f_c\right) \tag{4}$$

The effect of flow field action on solute diffusion during solidification was considered, and the microscopic flow field was coupled to the solute field equation by modifying the solute gradient term near the solid-liquid interface, it is feasible to simulate dendrite growth by considering a phase field model that incorporates the flow field (Natsume et al. (2005)). Therefore, the solute field equation under forced convection becomes:

$$\frac{\partial c}{\partial t} = \nabla \cdot \left(\frac{D\left(\varphi\right)}{f_{cc}} \nabla f_c\right) + k \nabla c \tag{5}$$

where$D\left(\phi\right)$is the solute diffusion coefficient, $D\left(\varphi\right) = D_L + h\left(\varphi\right)\left(D_S - D_L\right)$, $D_S$and$D_L$are the solute diffusion coefficients of the solid and liquid phases, respectively, $f$is the free energy density of the metal system, and the subscript$c$represents the partial derivative of$f$, $k$is a parameter related to the flow velocity.

The solute concentration$c$in the interface region is the sum of the mass fractions of the solid and liquid phases. In addition, the chemical potentials of the solid and liquid phases at any point in the interface region are equal when the solid and liquid phases are in equilibrium:

$$c = h\left(\varphi\right) c_S + \left(1 - h\left(\varphi\right)\right) c_L \tag{6}$$

$$\mu^S\left(c_S\left(x, t\right)\right) = \mu^L\left(c_L\left(x, t\right)\right) \tag{7}$$

where$c_L$and$c_S$are the solute concentrations in the liquid and solid phases, respectively, $\mu^L$and$\mu^S$are the chemical potentials of the liquid and solid phases, respectively.

2.3 Determination of thermodynamic parameters and boundary conditions

Thermodynamic parameters of the alloy were obtained by the CALPHAD method (Kim et al. (1998); Chen et al. (2016)), as shown in Table 1.

In the numerical simulation of directional solidification of aluminium alloy, the explicit difference solution method was used, and the 2D simulation interface was discretized into a grid space of 750 × 750. Grid size of 1.0×10^{-8}m($dx = dy$; $dt = dx^2/5D_L$). 50 random nucleus were set underneath the calculation area. The Neumann boundary condition was used in the simulation, and the undercooling value was set to 20 K.

For the 2D simulation interface of the phase field coupled with flow field under conditions of roll casting, three different

TABLE 1 Thermophysical data of alloys.

Property	Al-2mol%Si	Mg-3mol%Al
Interfacial energy $\sigma\,(J\cdot m^{-2})$	0.093	4.82×10^{-5}
Liquidus temperature $T_m\,(K)$	933.6	908
Equilibrium coefficientk^e	0.0807	0.4
Liquid-phase solute diffusion coefficient $D_1\,(m^2\cdot s^{-1})$	3.0×10^{-9}	1.8×10^{-9}
Solid-phase solute diffusion coefficient $D_s\,(m^2\cdot s^{-1})$	1.0×10^{-2}	1.0×10^{-12}

grid differential forms of$500\times500, 750\times750, 1000\times1000$ were used according to the actual calculation needs. Grid size of1×10^{-6}m$(dx=dy;\ \ dt=dx^2/5D_L)$. The magnitude of anisotropy is$v=0.02$and the magnitude of the noise is $\omega=0.01$. A grid size of10×10nuclei was set in the center of the simulation plane. The Neumann boundary condition was used in the simulation. Frozen temperature approximation was employed (Langer, (2007)), and the undercooling value was set to 20 K.

3 The N-S equation and pressure Poisson equation were calculated by marker in cell (MAC) algorithm

The dendrites growth behavior of roll casting magnesium alloys was affected by the external field and the structure of the molten pool, which makes the roll casting microstructure show abundant dendrites morphology than ordinary casting and die-casting (Bao et al. (2020); Zhang et al. (2020); Wu et al. (2015)). Among them, the effect of flow field has a great influence on the growth morphology of dendrites. The flow in the molten pool was expressed as turbulent flow, and solving the continuity equation of the flow field was achieved by solving the Navier-Stokes (N-S) equation. The equation is a nonlinear partial differential equation, the solution of which is very difficult and complex, and the exact solution can be obtained only for some very simple flow problems. The N-S equation and the continuity equation are as follows:

$$\frac{\partial u}{\partial t}+\frac{\partial\left(u^2\right)}{\partial x}+\frac{\partial(uv)}{\partial y}=-\frac{1}{\rho}\frac{\partial p}{\partial x}+\mu\left(\frac{\partial^2u}{\partial x^2}+\frac{\partial^2u}{\partial y^2}\right) \tag{8}$$

$$\frac{\partial v}{\partial t}+\frac{\partial\left(v^2\right)}{\partial y}+\frac{\partial(uv)}{\partial x}=-\frac{1}{\rho}\frac{\partial p}{\partial y}+\mu\left(\frac{\partial^2v}{\partial x^2}+\frac{\partial^2v}{\partial y^2}\right) \tag{9}$$

$$\frac{\partial u}{\partial x}+\frac{\partial v}{\partial y}=0 \tag{10}$$

where$u$and$v$indicate the components of the velocity vector in the horizontal and vertical directions, respectively. ρindicates the density of the fluid, and$\mu$is the viscosity coefficient.

There are many algorithms for solving the N-S system of equations, the most famous of which is the Marker in Cell (MAC) algorithm (Zhang, (2010)). Initially, the MAC algorithm was specifically designed to solve for positions with free surfaces, but the MAC algorithm has been improved and extended, and applied to various incompressible viscous flows in recent years (Liu et al. (2019)). Chen et al. (Chen et al. (2016)) used the MAC algorithm to calculate the evolution of dendrites in the center of the roll casting melt pool and found that the microstructure was very similar to that of AZ31 alloy under the microscope. Jinho et al. (Jinho et al. (2007)) used the MAC algorithm to simulate the fluid flow process during the pure metal filling process and the subsequent solidification process. The fluid flow problem with free surface motion was analyzed, making it possible to predict the defects occurring during the filling and solidification processes. The MAC algorithm is a hybrid Eulerian-Lagrangian finite-difference algorithm with pressure and velocity as the original variables. When solving the N-S equation and continuity equation, Eqs 8–10 can be expressed as follows:

$$\frac{\partial k}{\partial t}=-k\cdot\nabla k+\mu\nabla^2k-\frac{\nabla p}{\rho} \tag{11}$$

Where$p$is the pressure, $k$is a uniform representation of the velocity$u$in the horizontal direction and the velocity$v$in the vertical direction.

In order to facilitate programming, the above formula can be rewritten into discrete format:

$$k^{n+1}=k^n+\Delta t\left(-\mathrm{A}_{i,j}^n+\mathrm{D}_{i,j}^n\right)+\Delta t\nabla_hP_{i,j} \tag{12}$$

$$\nabla_h\cdot k^{n+1}=0 \tag{13}$$

Where$\mathrm{A}_{i,j}^n$and$\mathrm{D}_{i,j}^n$represent the divergence in the (i, j)grid, used to determine whether the iterations have converged, $P=p/\rho$, In the MAC algorithm difference scheme, $h=dx/L$, $L=Lx\cdot dx$, andLxrepresent grid numbers.

Solving the above equation is divided into two steps: 1. Solving fork^tfromk^n. 2. Solving$k^{n+1}$from$k^t$and satisfy$\nabla_h\cdot k^{n+1}=0$.

For the numerical calculation, a staggered grid is used, and the x, y directions are designed in a differential format based on nodes $(i+\frac{1}{2},\mathrm{j})$and $(i, j+\frac{1}{2})$, respectively. The iterative flow and simulation results of multi-crystal phase field in the center of roll casting melt pool were shown in Figure 1.

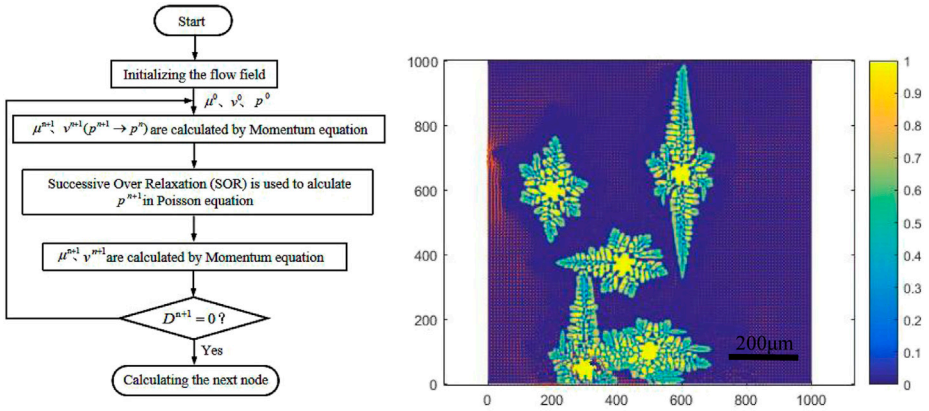

FIGURE 1
The iterative flow and simulation results of multi-crystal phase field in the center of roll casting melt pool.

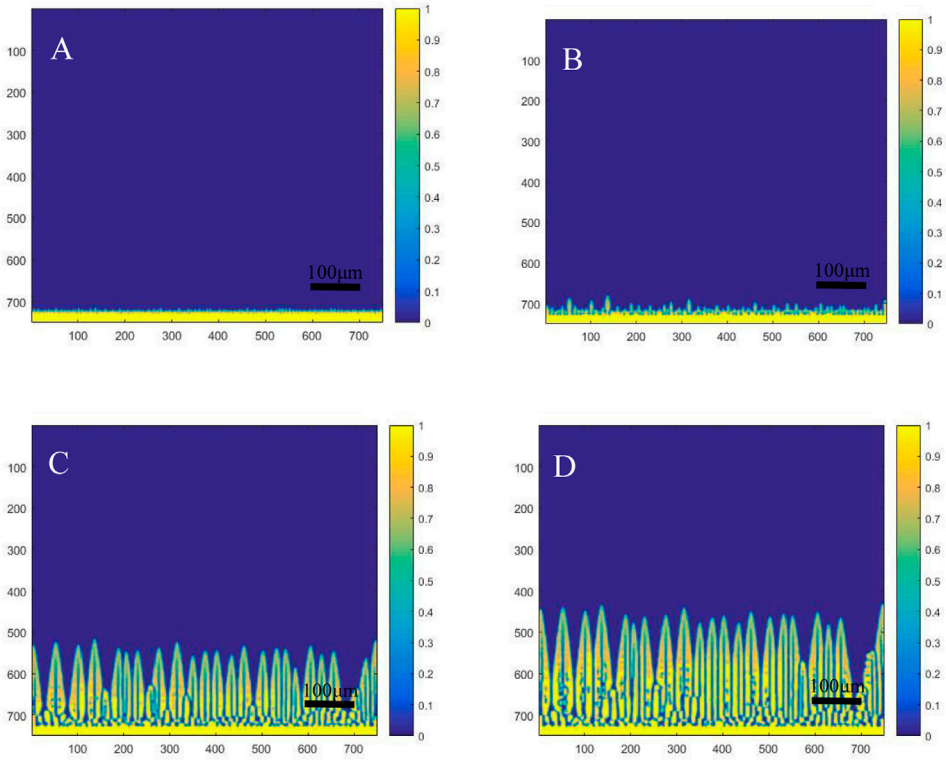

FIGURE 2
The dendrites growth of directional solidification at different stages: **(A)** 1000 dt; **(B)** 2000 dt; **(C)** 4000 dt; **(D)** 6000 dt.

4 Results and discussion

In order to better illustrate the universality of the KKS model for rare alloys, the KKS model is used to simulate the solidification process of aluminum alloys and directional solidification growth process of magnesium alloy under roll casting conditions at the edge of roll casting molten pool, respectively. In addition, in order to further describe the correctness of the influence of convection on the solidification process when the phase field KKS model is coupled with MAC algorithm, roll casting experiments are used to verify the convection effect.

4.1 Directional solidification of aluminium alloy by KKS model

4.1.1 The transformation process of aluminium alloy flat interface - Cell crystal - columnar dendrites

As shown in Figure 2, the transformation process of aluminium alloy flat interface - cell crystal - columnar dendrites was reproduced by phase field simulation. where the horizontal coordinate represents the grid scale and the different colors of the vertical coordinate describe the diffuse phase field interface. As the solidification progresses, the solutes at the front of the solid-liquid interface were enriched, which lead to the components supercooling. Therefore, the solidification flat interface unstable and evolves into a cellular morphology, resulting in the appearance of cellular crystals. The cellular crystals continue to grow under the action of supercooling, some of the cellular crystals were eliminated due to the phenomenon of competitive growth between dendrites. In addition, as solidification progresses, solutes are largely expelled due to the growth of equiaxed crystals. The solute will be enriched in the root of the main dendrites, inhibiting the growth of the root of the main dendrites. Therefore, the root position of the main dendrites appears to be necked. Overall, the growth of dendrites is consistent under the effect of supercooling degree, and only a small amount of secondary dendrites are found in Figure 2D. At a certain cooling rate, the appearance of secondary dendrite arms during the growth of primary dendrites is normal, but it can be seen from the figure that no secondary dendrites capable of hindering the growth of oriented primary dendrite arms have developed.

4.1.2 Effect of anisotropy on interface morphology

The interfacial anisotropy strength has an important effect on the dendrites growth morphology and tip velocity. In this paper, the interfacial anisotropy was introduced into the phase field using Eq 14:

$$\epsilon(\theta) = \epsilon\left[1 + 4\cos\gamma(\theta - \theta_0)\right] \tag{14}$$

Where$\gamma$is the interface anisotropy coefficient, $\theta$is the angle between the normal direction of the interface and the main arms of the dendrites, $\theta_0$is the angle between the grain preferential growth direction and the horizontal direction, in this paper: $\theta_0 = 0$.

As shown in Figure 3, the dendrites growth morphology was simulated at the same calculation step for each anisotropy coefficient of 0.04, 0.05 and 0.06, respectively. When the anisotropy coefficient is 0.04, the dendrite arms are thicker, the growth rate is slower, there are no secondary dendrites, and the dendrites show a cytosolic structure. When the anisotropy coefficient increases to 0.05, the dendrites become denser, the radius of the dendrites tip becomes significantly smaller, the dendrites competition growth phenomenon becomes more obvious, and the elimination rate further increases. The growth rate is significantly faster than when the anisotropy coefficient was 0.04. When the anisotropy coefficient increases to 0.06, the growth rate of dendrites was almost constant, but the dendrites become denser. It can also be found from Figure 3 that with the increase of the anisotropy coefficient, the equiaxed crystals at the root of the dendrites are obviously refined. When the anisotropy coefficient is 0.06, the wall of the dendrite arms were unstable and secondary dendrites appear. Because of the accelerated growth of dendrites, the latent heat of solidification cannot be fully released. Therefore, the latent heat causes thermal disturbance on the dendrites surface, which develops secondary dendrites. The research shows that the anisotropy coefficient is proportional to the density of dendrites growth, but the increase of the anisotropy coefficient is not conducive to the growth of directional primary dendrites, and there is a tendency to develop secondary dendrites.

4.1.3 Effect of interfacial energy on dendrites segregation and CET

According to the MS theory proposed by Mullins and Sekerka in the 1960s, the existence of interfacial energy has a very significant effect on dendrites growth (Mullins and Sekerka, (1985)). A large number of studies have also proved that interfacial energy can stabilize the solidification interface (Dantzig et al. (2013); Chen and Zhao, (2022)), but the research on the effect of interfacial energy on dendrites segregation and CET is still relatively scarce. In this paper, the effects of interfacial energy on dendrites solute segregation and CET transition were discussed. The relationship between the interface energy$\sigma$and the phase field parametersM_ϕ, ε, and$W$were described by using Eqs 15–17:

$$M_\varphi^{-1} = \frac{\epsilon^2}{\sigma}\left(\frac{RT}{V}\frac{1-k^e}{m^e}\beta\right) \tag{15}$$

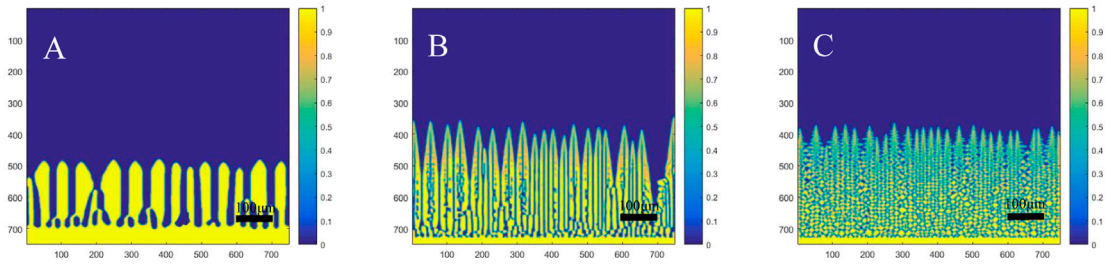

FIGURE 3
Effect on dendrites morphology by anisotropy: **(A)**$\gamma = 0.04$; **(B)**$\gamma = 0.05$; **(C)**$\gamma = 0.06$.

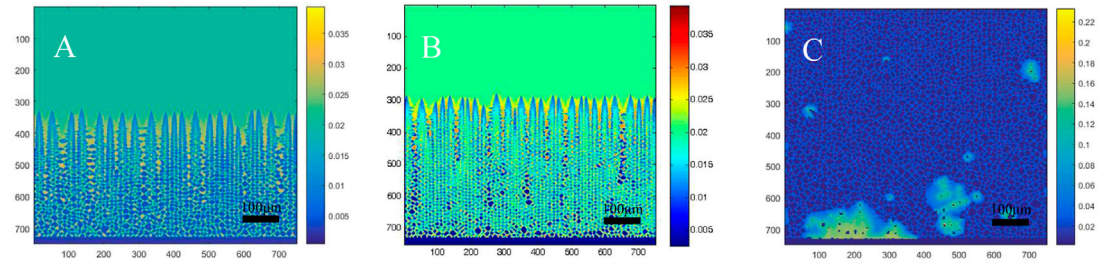

FIGURE 4
Effect on segregation by interface energy: **(A)**$\sigma = 0.06J \cdot m^{-2}$; **(B)**$\sigma = 0.08J \cdot m^{-2}$; **(C)**$\sigma = 0.09J \cdot m^{-2}$.

$$\varepsilon = \sqrt{\frac{6\lambda}{2.2}\sigma} \tag{16}$$

$$W = \frac{6.6\sigma}{\lambda} \tag{17}$$

Where$\beta$is the coefficient of interface dynamics, $R$is the gas constant, $T$is the temperature, $V_m$is molar volume, $m^e$is the equilibrium slope of the liquids, $k^e$is the equilibrium partition coefficient.

As shown in Figure 4, the solute field simulation results of directional solidification dendrites growth under the action of different interface energies are shown. When the interface energy was selected to be$0.06J \cdot m^{-2}$or$0.08J \cdot m^{-2}$, the solutes are mostly concentrated in the front of the solidification interface and between the dendrites. With the increase of the interfacial energy, the solute trapping phenomenon becomes more and more obvious. This is because the solute precipitated from the liquid phase during the growth of dendrites does not have time to diffuse, which leads to the solute interception phenomenon. In addition, with the interface energy increasing to$0.09J \cdot m^{-2}$, solute remelting can be observed. The reason is that the slope of liquidus is negative and the accumulation of solute leads to the decrease of melting point, which leads to solute remelting.

Columnar dendrites and equiaxed crystal are two main components of casting solidification microstructure. Although the columnar dendrite structure has more beneficial axial mechanical properties, However, the equiaxed crystal structure will make the material more dense and optimization segregation phenomenon. It is very important to master the mechanism of CET transformation for controlling the solidification structure and predicting the performance of castings. Figure 5 reproduces the transformation process of dendrites to equiaxed crystals. It can be seen from the figure that as the solidification progresses, the dendrites tip grow into the liquid phase under the action of the temperature gradient. However, the dendrites were gradually broken from the root to the tip and transformed into equiaxed crystals, finally, all transformed. This is because the solute was greatly enriched in the solidification dendrites front and between the dendrites during the solidification process, which leads to component supercooling. CET occurs when the solute is sufficient to dissipate the supercooling of the columnar dendrites front. This is consistent with the solute blocking mechanism proposed by Martorano et al. (Martorano et al. (2003)). Based on the above analysis, it can be concluded that the increase of interfacial energy will lead to serious solute segregation. At the same time, the CET phenomenon is easier to occur when the interface energy is larger. Therefore, the effect

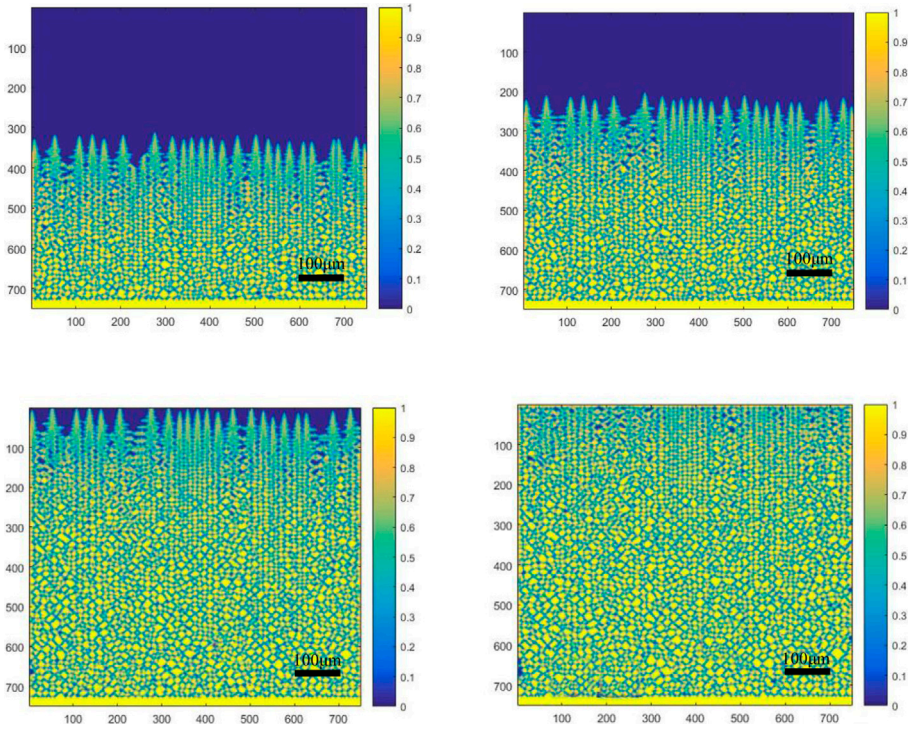

FIGURE 5
CET transformation process.

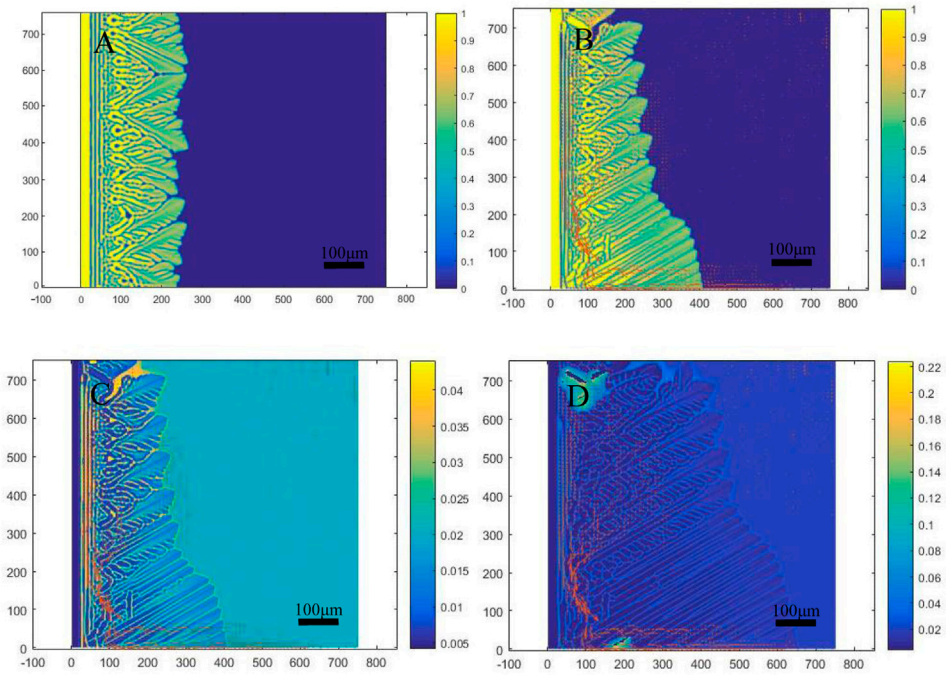

FIGURE 6
The simulation results of dendrites growth phase field and solute field of edge directional solidification under the condition of roll casting. **(A,B)** The simulation results of phase field. **(C,D)** The simulation results of solute field.

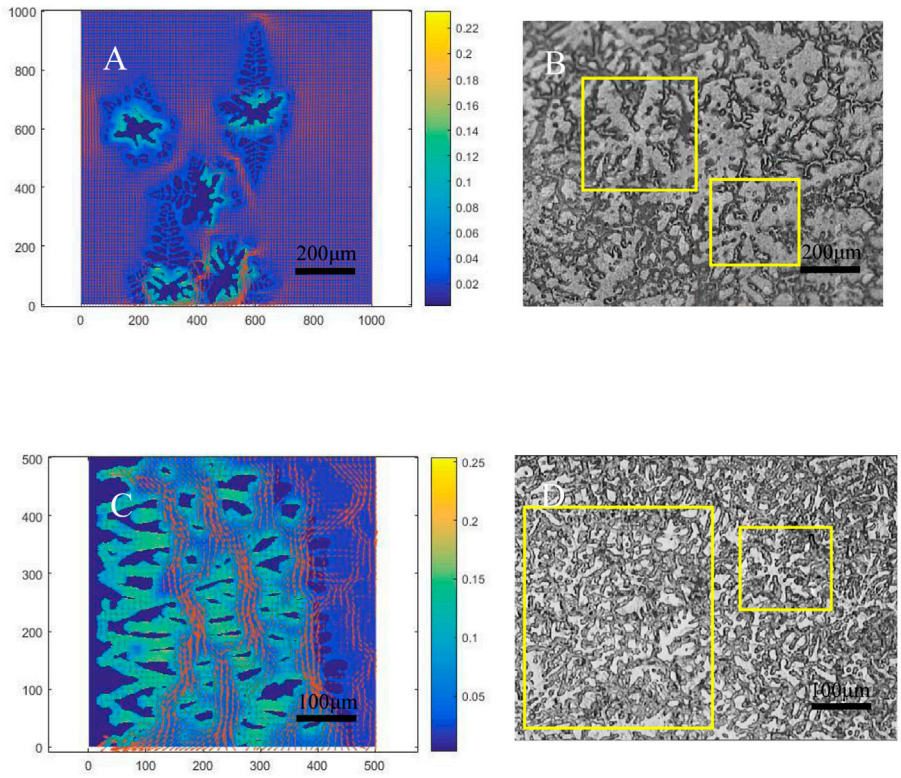

FIGURE 7
Phase field simulation results and microstructure comparison of Magnesium Alloy: **(A)** Simulation results of solute remelting of equiaxed crystals in the central area of roll casting; **(B)** Microstructure of central area of roll casting after experiment; **(C)** Simulation results of dendrites melt in directional solidification region of edge; **(D)** Microstructure of edge area of roll casting after experiment.

of interface energy on the morphology of dendrites growth should not only be considered but also the effect of interface energy on the solute segregation of dendrites should be considered in the simulation of directional solidification.

4.2 Roll casting solidification of magnesium alloy by KKS model coupled convection

4.2.1 Effect of forced convection on the segregation and growth morphology of columnar dendrites for directional solidification at the melt pool edge

There is still a paucity of reports exploring dendrite segregation and edge directional solidification dendrite growth under conditions of roll casting. Chen et al. (Chen et al. (2016)) explored the effect of flow rate on grain growth in the center of the melt pool under conditions of roll casting, but did not investigate dendrite segregation and the growth of edge-directed dendrites. Therefore, this article is inspired and started work.

Figure 6 shows the simulation results of dendrites growth phase field and solute field of edge directional solidification under the condition of roll casting. From the phase field results (Figures 6A, B), it can be seen that a large number of cytosol crystals were produced and a thick protective shell was formed driven by the supercooling degree. And continues to transform to equiaxed dendrites. The dendrite grows further into the liquid phase, and at this time the dendrite was influenced by the high flow rate in the center of the roll casting molten pool. The direction of directional dendrites growth shifts upstream and the dendrites growth become more and more dense. In addition, the solute field simulation results show that the solute distribution coincides with the dendrite growth (Figures 6C, D). The concentration of solute in dendrite center is the lowest, which is due to the curvature effect of dendrite tip during solidification. Supercooling causes the solid line to move downwards, and the diffusion rate of solute in the solid phase is slower than the growth rate of Dendrite. In addition, solute enrichment occurs at the dendrite solidification interface, which is caused by the solute redistribution effect during solidification. The solute

concentration in the solid phase is lower than the initial concentration, and the solute diffusion rate in the liquid phase is also lower than the dendrite growth rate. The solute can not fully diffuse into the liquid phase, thus enriching in the dendrite front. In the interface region surrounded by secondary dendrite arms, the solute is not easy to diffuse into the liquid phase, so the solute concentration is also relatively high.

4.2.2 Effect of forced convection on the CET transition of dendrites in the roll casting melt pool and experimental verification

Figure 7 are the phase field simulation result of magnesium alloys and the actual roll casting experiment result. It can be seen from the diagram that the countercurrent dendrite arms easily induce lateral branching under the condition of rapid cooling roll casting. The dendrites showed obvious anisotropy, and the growth rate was inconsistent in all directions, the symmetry of the dendrites morphology was broken. The dendrites growth in the countercurrent direction was faster than that in the downstream direction under the action of forced convection. In addition, the length of each dendrite arms was different, and the dendrite arms become abnormally thick (Figures 7A, B). For the directional solidification region at the edge, the dendrites undergo solute remelting because of the mutual influence of supercooling and microscopic convection. Furthermore, the dendrites melt into equiaxed crystals, showing the phenomenon of CET (Figures 7C, D. Therefore, it is further proved that the micro flow field has a significant effect on the dendrite's growth morphology. In addition, it is found by comparison that the dendrites morphology obtained from the simulation and the experiment are very similar, which reflects the accuracy of the simulation results in this paper.

5 Conclusion

In this paper, based on the KKS phase field model coupled with the thermodynamic parameters, the transformation process from columnar dendrites to equiaxed crystal during directional solidification of aluminium alloy was simulated. The effects of phase field parameters on the growth morphology and dendrites segregation were discussed. In addition, considering the inherent convective environment of the actual roll casting process, the dendrite growth behavior of magnesium alloy under the action of microscopic convection in the roll casting was further explored. The conclusion as follows:

(1) The phase field simulation of dendrites morphology and competition growth between dendrites during directional solidification of aluminium alloy was realized, and the crystal growth mode of the flat interface - cell crystal - columnar dendrites - equiaxed crystals was reproduced.
(2) When the anisotropy coefficient is 0.04, the dendrite arms are thicker, the growth rate is slower, there are no secondary dendrites. When the anisotropy coefficient increases to 0.05, the dendrites become denser, the radius of the dendrites tip becomes significantly smaller, the dendrites competition growth phenomenon becomes more obvious. When the anisotropy coefficient increases to 0.06, the growth rate of dendrites was almost constant, and secondary dendrites were developed.
(3) In the process of directional dendrites growth, the solute trapping phenomenon becomes more and more obvious with the increase of the interfacial energy. Solute remelting occurs when the interfacial energy is$0.09J \cdot m^{-2}$. In addition, by reproducing the CET phenomenon of dendrites, it is further proved that the interface energy has a large effect on the CET transition, and it is consistent with the solute blocking mechanism proposed by Martorano et al.
(4) For the multi-crystal growth of magnesium alloy in the center of roll casting molten pool, the dendrites growth behavior exhibits obvious anisotropy under the action of the microscopic flow field. The symmetry of the dendrite's morphology was destroyed, the dendrites growth in the countercurrent direction was faster than in the downstream direction, and the dendrite arms are thicker.
(5) For the directional solidification region at the edge of roll casting molten pool, directional solidification dendrites were affected by the high flow rate in the center of the roll casting melt pool during the growth process. The direction of directional dendrites growth shifts upstream, and the dendrites become denser. The dendrites undergo solute remelting because of the mutual influence of supercooling and microscopic convection. Furthermore, the dendrites melt into equiaxed crystals, showing the phenomenon of CET. And it was found by comparison that the dendrites morphology obtained from the simulation and the experiment is very similar, which reflects the accuracy of the simulation results in this paper.

Data availability statement

The original contributions presented in the study are included in the article/supplementary material further inquiries can be directed to the corresponding author.

Author contributions

HZ, XA, and MC contributed conception and design of the study. HZ organized the database and analytic result and wrote the first draft of the manuscript. HZ, MC, and XH provided the

experimental resources and conducted experimental supervision. HZ, XA, MC, and XH did the writing-review and editing.

Acknowledgments

The authors acknowledge the financial support for this work from the 14th Five-Year National Key R and D Plan (2021YFB3702005), Liaoning Provincial Department of Education Project (LJKZ0281) and General Program of National Natural Science Foundation of China (51774179), as well as Key Technology and Demonstration Application of Steel for Marine Engineering Equipment in Extreme Environment (2020JH1/10100001). And The authors wish to thank the help given by the Roll casting Research Center of Magnesium Alloy in University of Science and Technology Liaoning.

Conflict of interest

The authors declare that the research was conducted in the absence of any commercial or financial relationships that could be construed as a potential conflict of interest.

Publisher's note

References

Bao, Y. J., Li, Y., Wei, B. W., Xu, B. Y., and Xu, G. M. (2020). Effect of cast-rolling rate on microstructure of Al-9Si-0.25Mg alloy cast-rolling sheet. *Foundry Technol.* 41, 974–977+985. doi:10.16410/j.issn1000-8365.2020.10.018

Chen, L. Q., and Zhao, Y. H. (2022). From classical thermodynamics to phase-field method. *Prog. Mater. Sci.* 124, 100868–100869. doi:10.1016/j.pmatsci.2021.100868

Chen, M., Hu, X. D., Han, B., Deng, X. H., and Ju, D. Y. (2016). Study on the microstructural evolution of AZ31 magnesium alloy in a vertical twin-roll casting process. *Appl. Phys. A* 122, 91–10. doi:10.1007/s00339-016-9627-4

Chen, Z., Hao, L. M., and Chen, C. L. (2011). Simulation of faceted dendrite growth of non-isothermal alloy in forced flow by phase field method. *J. Cent. South Univ. Technol.* 18, 1780–1788. doi:10.1007/s11771-011-0902-4

Cui, C., Liu, W., Deng, L., Ang, Y. W., Su, H., Wang, S., et al. (2020). Primary dendrite arm spacing and preferential orientations of the Ni–Si hypereutectic composites at different solidification rates. *Appl. Phys. A* 126, 898–899. doi:10.1007/s00339-020-04080-6

Dantzig, J. A., Di Napoli, P., Friedli, J., and Rappaz, M. (2013). Dendritic growth morphologies in Al-Zn alloys-Part II: Phase-field computations. *Metall. Mat. Trans. A* 44A, 5532–5543. doi:10.1007/s11661-013-1911-8

Geng, S., Jiang, P., Shao, X., Guo, L., and Gao, X. (2020). Heat transfer and fluid flow and their effects on the solidification microstructure in full-penetration laser welding of aluminum sheet. *J. Mater. Sci. Technol.* 46, 50–63. doi:10.1016/j.jmst.2019.10.027

Ghosh, S., Karma, A., Plapp, M., Akamatsu, S., Bottin-Rousseau, S., and Faivre, G. (2019). Influence of morphological instability on grain boundary trajectory during directional solidification. *Acta Mater.* 175, 214–221. doi:10.1016/j.actamat.2019.04.054

Jinho, L., Jinho, M., and Hong, C. P. (2007). Straightforward numerical analysis of casting process in a rectangular mold: From filling to solidification. *Trans. Iron Steel Inst. Jpn.* 39, 1252–1261. doi:10.2355/isijinternational.39.1252

Kim, S. G., Kim, W. T., and Suzuki, T. (1998). Interfacial compositions of solid and liquid in a phase-field model with finite interface thickness for isothermal solidification in binary alloys. *Phys. Rev. E* 58, 3316–3323. doi:10.1103/physreve.58.3316

Kim, S. G., Kim, W. T., and Suzuki, T. (1999). Phase-field model for binary alloys. *Phys. Rev. E* 60, 7186–7197. doi:10.1103/PhysRevE.60.7186

Langer, J. S. (2007). Instabilities and pattern formation in crystal growth. *Rev. Mod. Phys.* 52, 1–28. doi:10.1103/RevModPhys.52.1

Lee, W., Jeong, Y., Lee, J. W., Lee, H., Kang, S. H., Kim, Y. M., et al. (2020). Numerical simulation for dendrite growth in directional solidification using LBM-CA (cellular automata) coupled method. *J. Mater. Sci. Technol.* 49, 15–24. doi:10.1016/j.jmst.2020.01.047

Lenart, R., and Eshraghi, M. (2020). Modeling columnar to equiaxed transition in directional solidification of Inconel 718 alloy. *Comput. Mater. Sci.* 172, 109374–109378. doi:10.1016/j.commatsci.2019.109374

Li, L. J., Li, W. M., Chen, M., and Zang, X. M. (2020). Application status of phase field method in metal solidification process. *J. Iron Steel Res.* 32, 847–859. doi:10.13228/j.boyuan.issn1001-0963.20200079

Li, Y., Hong, L., and Han, B. (2021). Microstructure and volume shrinkage during directional solidification of peritectic steel. *Mater. Sci. Technol.* 37, 395–404. doi:10.1080/02670836.2021.1904600

Liu, J. L., Lu, Y. Q., and Xu, B. (2019). Two dimensional debris flow numerical calculation model based on MACcormack-TVD finite difference algorithm. *Bull. Sci. Technol.* 35, 222–228.

Luo, S., Wang, P., Wang, W., and Zhu, M. (2020). PF-LBM modelling of dendritic growth and motion in an undercooled melt of Fe-C binary alloy. *Metall. Mat. Trans. B* 51, 2268–2284. doi:10.1007/s11663-020-01925-6

Ma, W., Li, R., and Chen, H. J. (2020). Three-dimensional CA-LBM model of silicon facet formation during directional solidification. *Crystals* 10, 669–710. doi:10.3390/cryst10080669

Martorano, M. A., Beckermann, C., and Gandin, C. A. (2003). A solutal interaction mechanism for the columnar-to-equiaxed transition in alloy solidification. *Metall. Mat. Trans. A* 34, 1657–1674. doi:10.1007/s11661-003-0311-x

Mullins, W. W., and Sekerka, R. F. (1985). On the thermodynamics of crystalline solids. *J. Chem. Phys.* 82, 5192–5202. doi:10.1063/1.448644

Nabavizadeh, S. A., Eshraghi, M., Felicelli, S. D., Tewari, S. N., and Grugel, R. N. (2020). The Marangoni convection effects on directional dendritic solidification. *Heat. Mass Transf.* 56, 1329–1341. doi:10.1007/s00231-019-02799-4

Natsume, Y., Ohsasa, K., and Narita, T. (2005). Investigation of the mechanism of alloy dendrite deflection due to flowing melt by Phase-Field simulation. *Mat. Trans.* 43, 2228–2234. doi:10.2320/matertrans.43.2228

Noubary, K. D., Kellner, M., Steinmetz, P., Hoetzer, J., and Nestler, B. (2017). Phase-field study on the effects of process and material parameters on the tilt angle during directional solidification of ternary eutectics. *Comput. Mater. Sci.* 138, 403–411. doi:10.1016/j.commatsci.2017.07.006

Novokreshchenova, A. A., and Lebedev, V. G. (2017). Determining the phase-field mobility of pure nickel based on molecular dynamics data. *Tech. Phys.* 62, 642–644. doi:10.1134/s1063784217040181

Pinomaa, T., and Provatas, N. (2019). Quantitative phase field modeling of solute trapping and continuous growth kinetics in quasi-rapid solidification. *Acta Mater.* 168, 167–177. doi:10.1016/j.actamat.2019.02.009

Shiga, K., Kawano, M., Maeda, K., Morito, H., and Fujiwara, K. (2019). The *in situ* observation of faceted dendrite growth during the directional solidification of GaSb. *Scr. Mater.* 168, 56–60. doi:10.1016/j.scriptamat.2019.04.022

Sinhababu, A., and Bhattacharya, A. (2022). A fixed grid based accurate phase-field method for dendritic solidification in complex geometries. *Comput. Mater. Sci.* 202, 110973–110978. doi:10.1016/j.commatsci.2021.110973

Steinmetz, P., Kellner, M., Hoetzer, J., and Nestler, B. (2018). Quantitative comparison of ternary eutectic phase-field simulations with analytical 3D jackson-hunt approaches. *Metall. Materi. Trans. B* 49, 213–224. doi:10.1007/s11663-017-1142-2

Wang, J. W., Wang, Z. P., Yang, L. U., Zhu, C. S., Feng, L., and Xiao, R. Z. (2012). Effect of forced lamina flow on microsegregation simulated by phase field method

quantitatively. *Trans. Nonferrous Metals Soc. China* 22, 391–397. doi:10.1016/S1003-6326(11)61189-8

Wang, K., Wang, Y. X., Wei, P., Lu, Y. L., Zhang, J., and Chen, Z. (2019). Microscopic phase-field model and its application for solid-state phase transformation of alloys. *Rare Metal Mater. Eng.* 48, 3770–3780.

Wang, Y. B., Wei, M. G., Liu, X. T., Chen, C., Wu, Y. J., Peng, L. M., et al. (2020). Phase-field study of the effects of the multi-controlling parameters on columnar dendrite during directional solidification in hexagonal materials. *Eur. Phys. J. E* 43, 41–49. doi:10.1140/epje/i2020-11964-9

Wei, C., Ke, C. B., Liang, S. B., Cao, S., Ma, H. T., and Zhang, X. P. (2020). An improved phase field method by using statistical learning theory-based optimization algorithm for simulation of martensitic transformation in NiTi alloy. *Comput. Mater. Sci.* 172, 109292–109298. doi:10.1016/j.commatsci.2019.109292

Wu, X. H., Zhao, H. Y., and Hu, X. D. (2015). Microstructure and mechanical properties of twin-roll casting strips of high-Al Magnesium alloy. *Special Cast. Nonferrous Alloys* 35, 533–536. doi:10.15980/j.tzzz.2015.05.023

Xiong, F., Gan, Z., Chen, J., and Lian, Y. (2022). Evaluate the effect of melt pool convection on grain structure of IN625 in laser melting process using experimentally validated process-structure modeling. *J. Mater. Process. Technol.* 303, 117538–117539. doi:10.1016/j.jmatprotec.2022.117538

Yang, C., Xu, Q., and Liu, B. (2017). GPU-accelerated three-dimensional phase-field simulation of dendrite growth in a nickel-based superalloy. *Comput. Mater. Sci.* 136, 133–143. doi:10.1016/j.commatsci.2017.04.031

Yang, C., Xu, Q. Y., and Liu, B. C. (2020). Phase-field-lattice Boltzmann simulation of dendrite growth under natural convection in multicomponent superalloy solidification. *Rare Met.* 39, 147–155. doi:10.1007/s12598-019-01292-5

Yuan, X. F., and Ding, Y. T. (2012). Study on the phase field method of pure Ni dendrite growth under forced convection. *Cast. Technol.* 33, 913–917.

Zhang, A., Du, J., Guo, Z., Wang, Q., and Xiong, S. (2019b). Phase-field lattice-Boltzmann investigation of dendritic evolution under different flow modes. *Philos. Mag.* 99, 2920–2940. doi:10.1080/14786435.2019.1646437

Zhang, B., Zhao, Y., Chen, W., Xu, Q., Wang, M., and Hou, H. (2019a). Phase field simulation of dendrite sidebranching during directional solidification of Al-Si alloy. *J. Cryst. Growth* 522, 183–190. doi:10.1016/j.jcrysgro.2019.06.027

Zhang, C., Guo, C., Zhang, S., Feng, H., Chen, Y., Kong, F., et al. (2020). The effect of rolling temperature on the microstructure and mechanical properties of 5 vol.% (TiBw + TiCp)/Ti composites. *JOM J. Minerals* 72, 1376–1383. doi:10.1007/s11837-019-03972-0

Zhang, D. L. (2010). *Computational fluid dynamics*. BeiJing: Higher Education Press.

Zhao, Y., Zhang, B., Hou, H., Chen, W., and Wang, M. (2019). Phase-field simulation for the evolution of solid/liquid interface front in directional solidification process. *J. Mater. Sci. Technol.* 35, 1044–1052. doi:10.1016/j.jmst.2018.12.009

Zhu, C. S., Xu, S., Feng, L., Han, D., and Wang, K. M. (2019). Phase-field model simulations of alloy directional solidification and seaweed-like microstructure evolution based on adaptive finite element method. *Comput. Mater. Sci.* 160, 53–61. doi:10.1016/j.commatsci.2018.12.058

frontiers | Frontiers in Materials

TYPE Original Research
PUBLISHED 21 October 2022
DOI 10.3389/fmats.2022.1007502

OPEN ACCESS

EDITED BY
Yu-Hong Zhao,
North University of China, China

REVIEWED BY
Zhiqin Wen,
Guilin University of Technology, China
Xiaofeng Niu,
Taiyuan University of Technology, China

*CORRESPONDENCE
Huiqin Chen,
chenhuiqin@tyust.edu.cn
Juan Chen,
juanchcumt@126.com

SPECIALTY SECTION
This article was submitted to Computational Materials Science, a section of the journal Frontiers in Materials

RECEIVED 30 July 2022
ACCEPTED 05 October 2022
PUBLISHED 21 October 2022

CITATION
Chen H, He S, Chen J, Chen F, Zhang S and Zhang Y (2022), Molecular dynamics simulation of nanocrack closure mechanism and interface behaviors of polycrystalline austenitic steel.
Front. Mater. 9:1007502.
doi: 10.3389/fmats.2022.1007502

Molecular dynamics simulation of nanocrack closure mechanism and interface behaviors of polycrystalline austenitic steel

Huiqin Chen*, Sizhe He, Juan Chen*, Fei Chen, Sairu Zhang and Yingfan Zhang

School of Materials Science and Engineering, Taiyuan University of Science and Technology, Taiyuan, China

Void-type defects in heavy forgings deteriorate their mechanical properties and service life. In this work, the evolutions of a pre-crack closure and the healing and mechanical properties of FeCrNi polycrystalline samples are assessed under different loading conditions using molecular dynamics simulation. The stress–strain curves show that the sample with interface exhibits higher Young's modulus and yield strength than those with cracks, despite the loading conditions. These results imply that samples under compression loading have a higher ability to resist plasticity, while the shear stress facilitates plastic flow. Crack closure and healing occur under compression stress by dislocation-dominant plastic deformation, while the crack length shrinks and the crack tips expand along grain boundaries (GBs) and the interface because of its higher stress under shear loading. Dislocation activities, including dislocation emission, slip, and interactions with cracks, grain boundaries, and dislocations, contribute to the plasticity of the specimen under compressive loading. In addition to dislocation activities, grain boundary slip, grain rotation, and twinning are potential plastic-deformation mechanisms under shear loading.

KEYWORDS

crack closure, crack healing, plastic deformation mechanism, molecular dynamics simulation, FeCrNi polycrystalline

Introduction

Void-type defects (such as shrinkage cavities, porosities, and cracks) in heavy forgings are inevitable during manufacturing and application of non-uniform solidification of the materials during casting, which can severely deteriorate the product strength and service life. In the manufacturing process, it is important to eliminate these internal voids through an appropriate molding process. In general, eliminating voids inside large ingots includes two stages: void closure and healing of closed void surfaces (Qiu et al., 2020). The void closure process is to contact the internal surface of void (Zhang et al., 2009). Crack closure and healing are mainly achieved through thermoplastic deformation (Chen and Lin, 2013;

Wang et al., 2015) and heat treatment (Qiu et al., 2020). Thermoplastic deformation has been widely used in actual production because of its feasibility and high efficiency.

A criterion for void closure in large ingots during hot forging was proposed, based on numerous numerical computations, by developing a cell model, and the effects of the Norton exponent, remote stress triaxiality, and remote effective strain were considered (Zhang et al., 2009). Evolution behaviors of an elliptic–cylindrical void were analyzed by the representative volume element model incorporated into the finite element (FE) method by considering void deformation and rotation; the results showed that deviation stress significantly influences both void radius and void orientation (Feng et al., 2017). This method was also applied to study the evolution of dilute ellipsoidal voids under triaxial loading conditions, with void radius strain rate and volume strain rate expressed as functions of void shape index, macroscopic stress, and strain rate. In the process of large compression deformation, the predicted results of this model were in good agreement with the analytical solution, experimental measurements, and numerical simulation results (Feng et al., 2016). The void closure efficiency of different cogging processes in large ingots conducted using a 3-D void evolution model suggested that compression perpendicular to the longer principal axis of the prolate void provides a higher void-closure efficiency than that aligned with this direction. Surface bonding experiments showed that void defects after void closure are favorable to eliminate under the conditions of higher pressure, temperature, and long holding time (Feng et al., 2016). Evolution mechanisms for spherical or spheroidal voids during hot working were studied by varying the initial void size, aspect ratio, and void positions by theoretical and experimental analysis (Chen and Lin, 2013). Recently, the evolution of nanocracks induced by plastic deformation in single crystals and bicrystalline copper was investigated using molecular dynamics simulations. The results showed that compressive stress induced by defects such as dislocation, 9R phases, and deformation twinning drives crack closure (Fang et al., 2017). Under shear stress, dislocation emission from the crack tip leads to crack closure through the dislocation shielding effect and atomic diffusion, and crack healing largely depends on crystallographic orientation and the direction of external loading (Li et al., 2015). Elevated temperature facilitates crack healing because atomic diffusion occurs (Wei et al., 2004; Wei et al., 2013); furthermore, compression pressure, irrespective of biaxial and uniaxial loading, promotes crack healing and leads to a more uniform distribution of defects after healing.

The evolution behaviors of voids of different sizes during the hot rolling process were investigated by FE simulation and experimental observation, which showed that their shapes change from spherical to ellipsoidal and then become irregular. The two surfaces of the void bond together after the last rolling pass (Huang et al., 2014; Wang et al., 2015). Crack healing and the recovery percentage of the impact properties of internal crack healing in SA508 steel were studied under various deformation modes and under quenching and tempering. The study addressed the fact that the recovery of impact properties by multi-pass thermal deformation is lower than that by uniaxial compression at 950°C and 1,050°C, and that a newly formed Z-type grain belt is observed in the crack healing zone, exhibiting higher resistance to dynamic load at 1,150°C (Qiu et al., 2020). Crack closure induced by laser peening (LP) and its effects on the fatigue-life extension of an Al alloy with initial fatigue crack were investigated, and the results showed that the fatigue life of treated samples is higher than for those not treated and that LP-induced plastic deformation around a pre-crack contributes to crack closure and fatigue-life extension (Hu et al., 2020). Although much effort has been made theoretically and experimentally, a full understanding of crack closure, closure healing evolution, and the mechanical behaviors of samples with cracks under different loads is still absent. Fortunately, the molecular dynamics technique can provide meaningful insights into the mechanical behaviors of FeCrNi polycrystalline samples, due to its capacity for high spatiotemporal processes and *in situ* observation.

In this work, compression and shear tests were conducted for FeCrNi polycrystals with interfaces and nanocracks using molecular dynamics simulation. A focus was placed on exploring the evolutions of crack closure and healing and the plastic-deformation behaviors of polycrystalline samples. This work may contribute to a better understanding of the plastic-deformation characteristics of nanoscale polycrystalline samples and to practical engineering processing.

Materials and methods

In this work, polycrystalline austenitic FeCrNi samples with additions of Cr wt. 18% (at. 19%) and Ni wt. 9% (at. 8.7%) were prepared using Atomsk software (Hirel, 2015). The size of the polycrystalline sample was 82 × 82 × 10 nm^3 and contained 1094283 Cr atoms, 788808 Ni atoms, and 3877596 Fe atoms with a lattice parameter of 0.35 nm, as shown in Figure 1. The Cr and Ni atoms were randomly distributed within the samples as substitutional atoms. One sample, termed an interface-containing sample, consisted of 28 grains in various crystallographic orientations, among which eight intact grains were constructed around the interface located in the middle of the sample. The other sample considered had a prefabricated crack placed in the interface, with two triangular GBs on the interface selected as the beginning and end of the prefabricated crack. By erasing atoms, a prefabricated crack with a length of 51 nm and a width (about 2.8 nm) of about six times the average width of the GBs appeared within the sample. The simulation process can was divided into two stages: relaxation and mechanical-loading stages. Before the loading, the designed

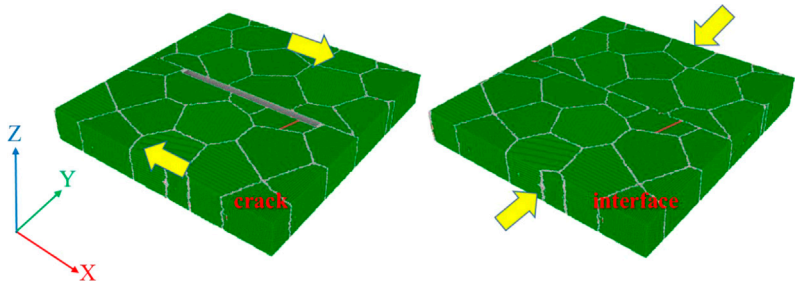

FIGURE 1
Schematic of samples with crack and interface loaded under compression and shear stress.

samples were relaxed to local minimum energy by the steepest-descent algorithm and then equilibrated with a canonical ensemble (NVT) with a Nose–Hoover thermostat for 90 ps at a constant temperature of 300 K; the constant pressure/constant temperature ensemble (NPT) was then used during compression and shear loading. Compressive force was applied parallel to the *y*-axis direction, while shear force was applied parallel to the *x*-axis direction with a strain rate of 2.8×10^8 s^{-1} and a time step of 1.0 fs. Periodic boundary conditions were applied in all three directions.

Atomic interactions in the FeCrNi samples were described by the potential function of the embedded atom method (EAM), which describes austenite's properties in a large concentration range based on the *ab initio* calculation (Bonny et al., 2011). This potential has been successfully used to describe dislocation movement (Fan et al., 2020), the relationship between solute segregation and GB state (Barr et al., 2014), and high-energy collision cascades coupled with *ab initio* calculation in FeCrNi alloys (Béland et al., 2017). In this work, the visualization and analysis of polycrystalline samples was performed using OVITO software (Polak, 2022). The simulations were performed by the Large-scale Atomic Parallel Simulator (LAMMPS) (Li et al., 2021).

Results and discussions

Austenitic FeCrNi samples have a face-centered cubic (FCC) crystal structure, with more slip systems and a greater coordinated deformation capacity. However, if the GBs interact with interfaces and cracks during loading deformation, the dislocation slip motion and propagation are easily hindered, which affects the mechanical properties and plastic-deformation behaviors of materials. Stress–strain curves, which provide useful information about the samples' responses to external force, are the most intuitive method for identifying the mechanical properties of austenitic materials during loading. Therefore, the stress–strain curves of the polycrystalline samples with interface and crack during compression and shear are shown in Figure 2. The curves illustrate that applied stress increases dramatically, and then the samples yield different yield stresses depending upon their characteristics and loading conditions; subsequently, the stress first decreases rapidly and then increases steadily under compression. The stress increases slightly after yielding under shear. In addition, the yield strength of the sample with interface

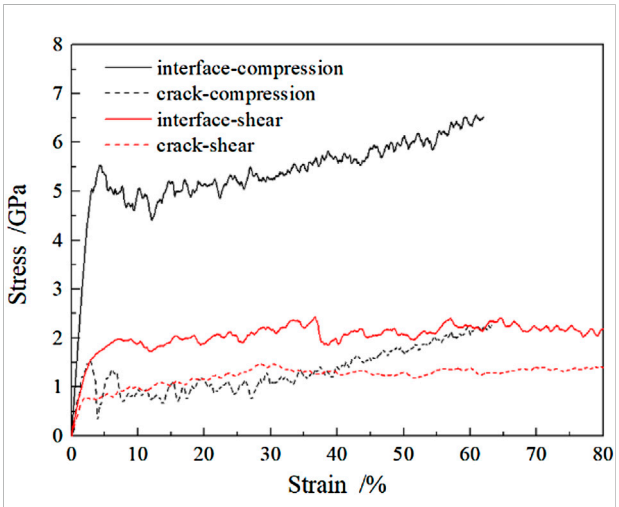

FIGURE 2
Stress–strain curves under various loading conditions.

was 5.5 GPa, which is about four times higher than that with crack under compression. A similar result was additionally seen under shear but with lower yield strength (e.g., the values of yield strength are 2.0 GPa and 0.9 GPa for samples with interface and crack, respectively). It was observed that the elastic modulus (reflected by the slope of stress–strain curves in the elastic deformation stage) for samples with interface was much higher than for those with crack under the same loading

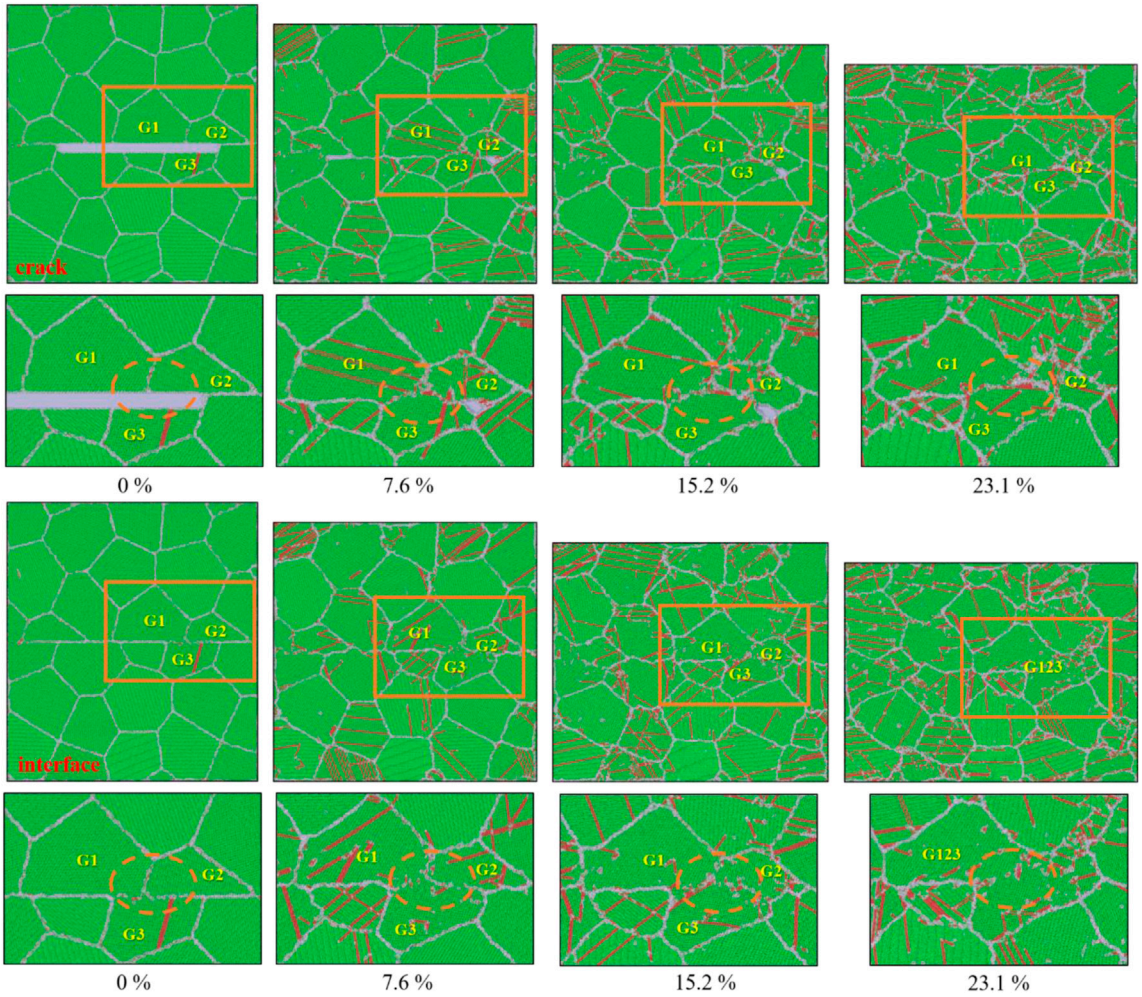

FIGURE 3
Deformation evolutions of atomic configuration under compression versus strain (atoms are colored according to the crystalline structure based on dislocation extraction analysis, DXA). Green, red, and white represent the face-centered cubic (FCC) crystal structure, hexagonal close-packed (HCP) crystal structure, grain boundaries, and other unknown structures, respectively).

conditions. These outcomes indicate that the interface-containing sample has a higher resistance to plastic deformation than that with crack.

Analysis of pre-crack closure

Cracks and other void-type defects are defects caused by the loss of a large number of atoms under the action of stress (Kardani and Montazeri, 2018) and are inevitable in the manufacture of heavy ingots. The existence of a nanocrack deteriorates the mechanical properties and leads to early failure of the final product. In this work, the crack closure process of the sample during compression was carefully explored. The evolutions of the atomic configuration of the sample during compression are shown in Figure 3, with the sample with interface considered for comparison. By comparing the atomic configuration of the two kinds of samples at the same strain rate, it was found that the upper and lower interfaces of the middle part of the crack became closed and contacted each other when the strain reached 7.6%. Voids appeared at both ends of the crack and shrank gradually, finally disappearing with increasing strain. That is to say, crack closure takes place as the compression strain increases, up to 15.2%. With the progress of compression, the relatively straight interface newly generated by crack closure becomes curved due to plastic deformation and is dominated by dislocations, implying that crack healing occurs. As for the sample with interface, the original long and straight shape varied to a sawtooth shape with the accumulation of strain, and some smaller grains on both sides of the interface continued to aggregate with the surrounding large grains, resulting in the coarsening of the grains. For example, grains G1, G2, and

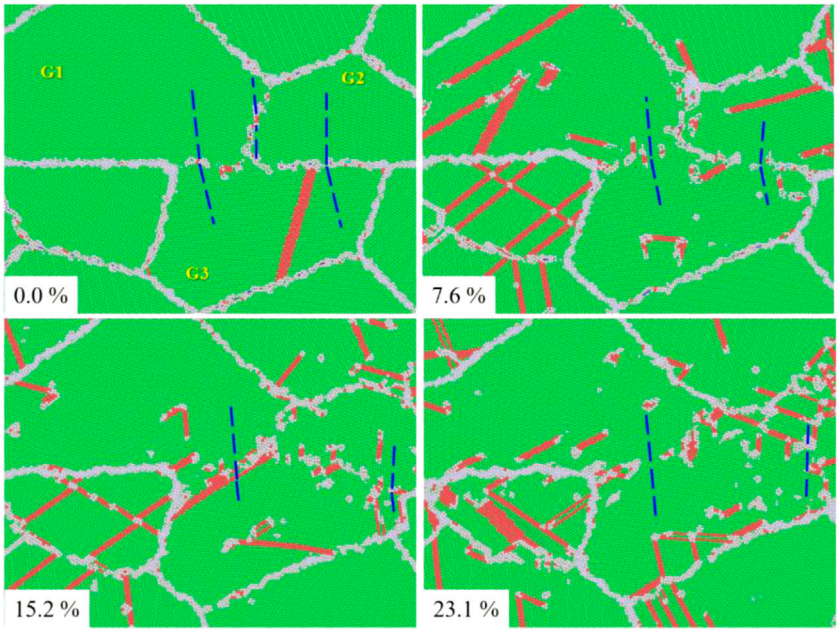

FIGURE 4
Crystallographic orientation changings of G1, G2, and G3 grains within the sample with the interface versus strain (atoms are colored similar to Figure 3, and blue dotted lines present directions of atomic arrangement).

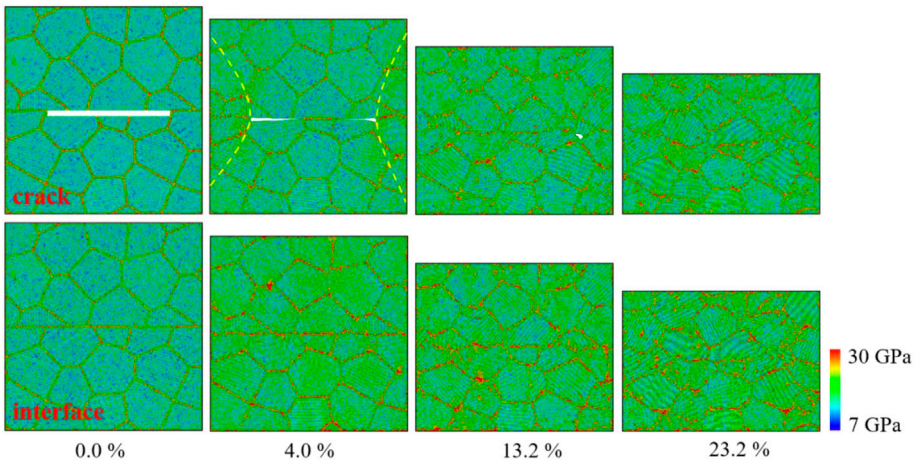

FIGURE 5
Cross-section snapshots of von Mises stress distribution at different compression strains (yellow dotted lines denote stress-concentrated areas).

G3 within the sample with interface merged into a new grain (recorded as G123) when the strain reached 23.1%, as illustrated in Figure 4. A small decrease was observed in the atomic arrangement between each other grain for G1, G2, and G3 at 0.0%, and the distinction decreases with strain and finally vanished at 23.1%, implying that slight grain rotation occurs through lattice torsion under compression loading.

To further explore the crack closure mechanism, von Mises stress analysis as a function of strain was performed in Figure 5. The value of shear stress was observed to increase with increasing compression strain for the two samples, and the stress at GBs and within the grain interior of the interface-containing sample were significantly higher than in samples with cracks because of higher

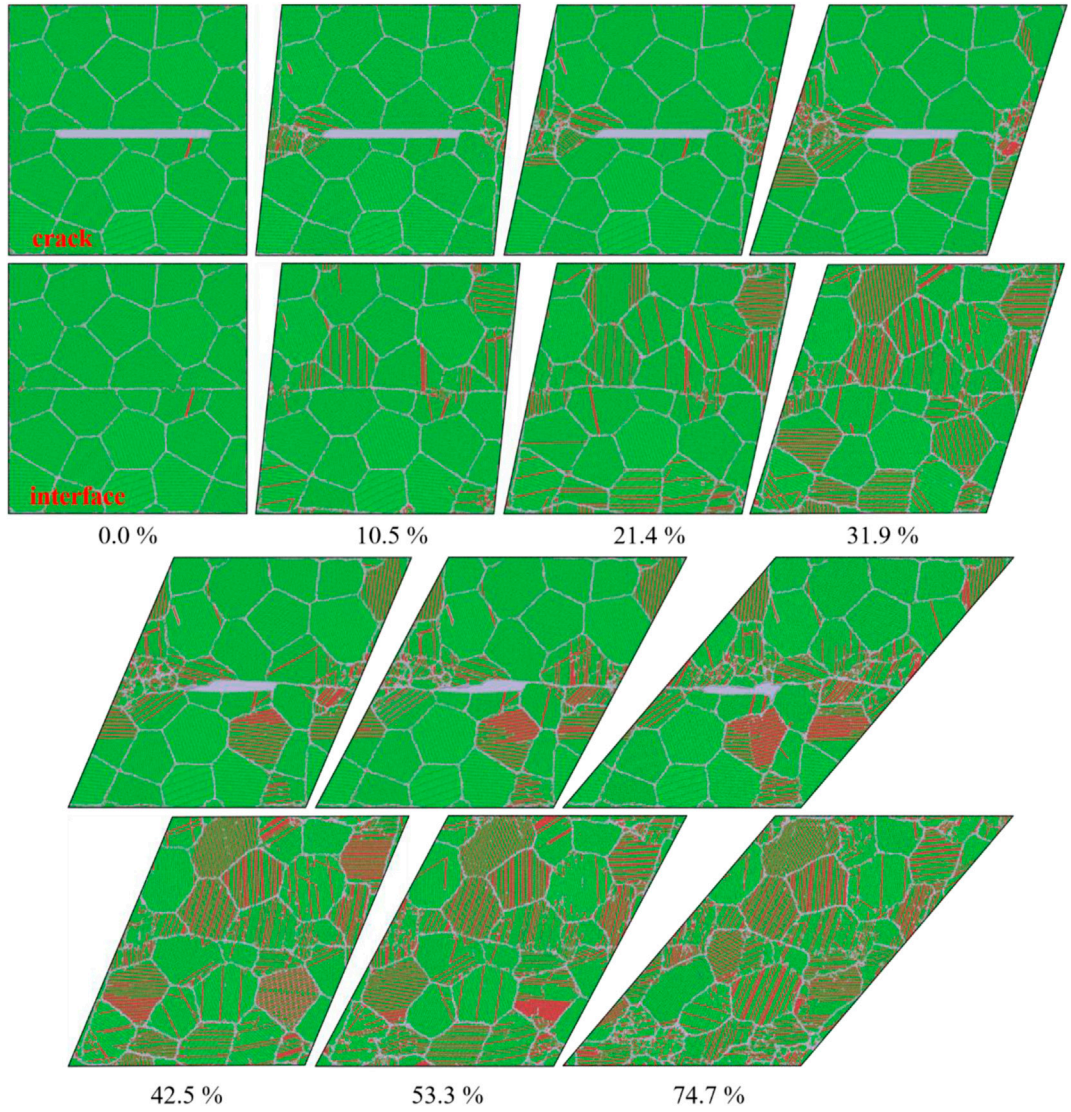

FIGURE 6
Atomic configuration of deformation evolutions under shear versus strain (atoms are colored according to the crystalline structure based on DXA method; green, red, and white represent the face-centered cubic [FCC] crystal structure, hexagonal close-packed [HCP] crystal structure, grain boundaries, and other unknown structures, respectively).

applied stress at the same strain (Figure 2). Before the crack is closed, the stress is primarily concentrated in the exterior of crack tips, especially in trigeminal GB regions, where GB migration and stress relaxation are more likely to occur. Stress distribution after crack closure is relatively homogeneous, and a similar distribution also happens within the sample with interface.

Analysis of pre-crack propagation

To investigate the load-dependent crack behaviors of polycrystalline samples, shear force was applied to both crack and interface samples, and the deformation evolutions versus shear strain are shown in Figure 6. It was found that with the increase of strain, more stacking faults (SFs, determined as HCP atoms) were present from the two crack tips and then extended heterogeneously along the crack plane. The appearance of SFs means that partial dislocation movement is activated, and its degree is enhanced with increasing shear strain. Though the total length of the crack seems to decrease as shear continues, the surfaces of the crack become curved due to interface emigration induced by interactions between dislocations and surfaces. The number of crack tips gradually extends to 4 along the surrounding GBs (upper and lower sides of the crack), instead

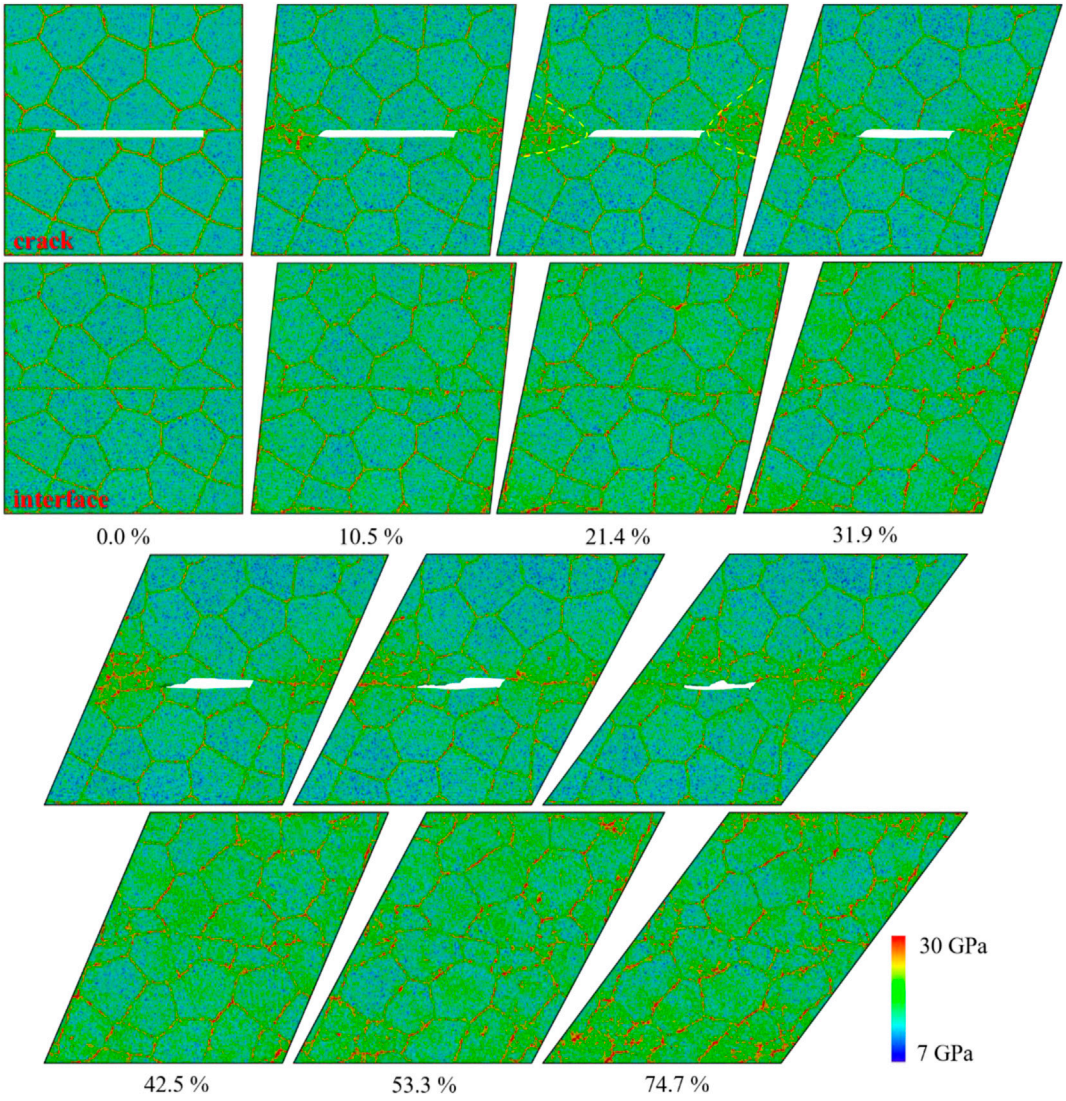

FIGURE 7
Cross-section snapshots of von Mises stress distribution at different shear strains (yellow dotted lines denote stress-concentrated areas.).

of the front of the crack tips, as the shear strain reaches 74.7%, which has also been theoretically and experimentally studied in other work (Li and Jiang, 2019; Li et al., 2021). As for the interface-containing sample, the SFs mainly appeared within the grains close to the interface at a strain of 10.5% and then expanded significantly around the entire sample; the detailed variations of SF atoms are given as follows. It is worth noting that grain rotation occurs synergistically along the direction of the shear load to the sample with interface to compensate for the increasing shear strain.

The corresponding evolution of von Mises stress distribution as a function of shear strain is illustrated in Figure 7 and indicates that variations of stress are similar and comparable to those under compression, except for the sample with crack, where shear stress is mainly concentrated near two crack tips (including GBs and interior grains), as shown by the yellow dotted line in Figure 7. This indicates again that the shear stress distribution follows changes in atomic configurations, as shown in Figure 6.

Analysis of plastic-deformation mechanisms

It is generally accepted that the dominant plastic-deformation mechanisms for crystalline metals are dislocation activities and twinning (Shi et al., 2018; Sun et al., 2019; Shi et al., 2020), which is different from those for amorphous materials (Spaepen, 1977; Argon, 1979; Chen et al., 2018a; Chen et al.,

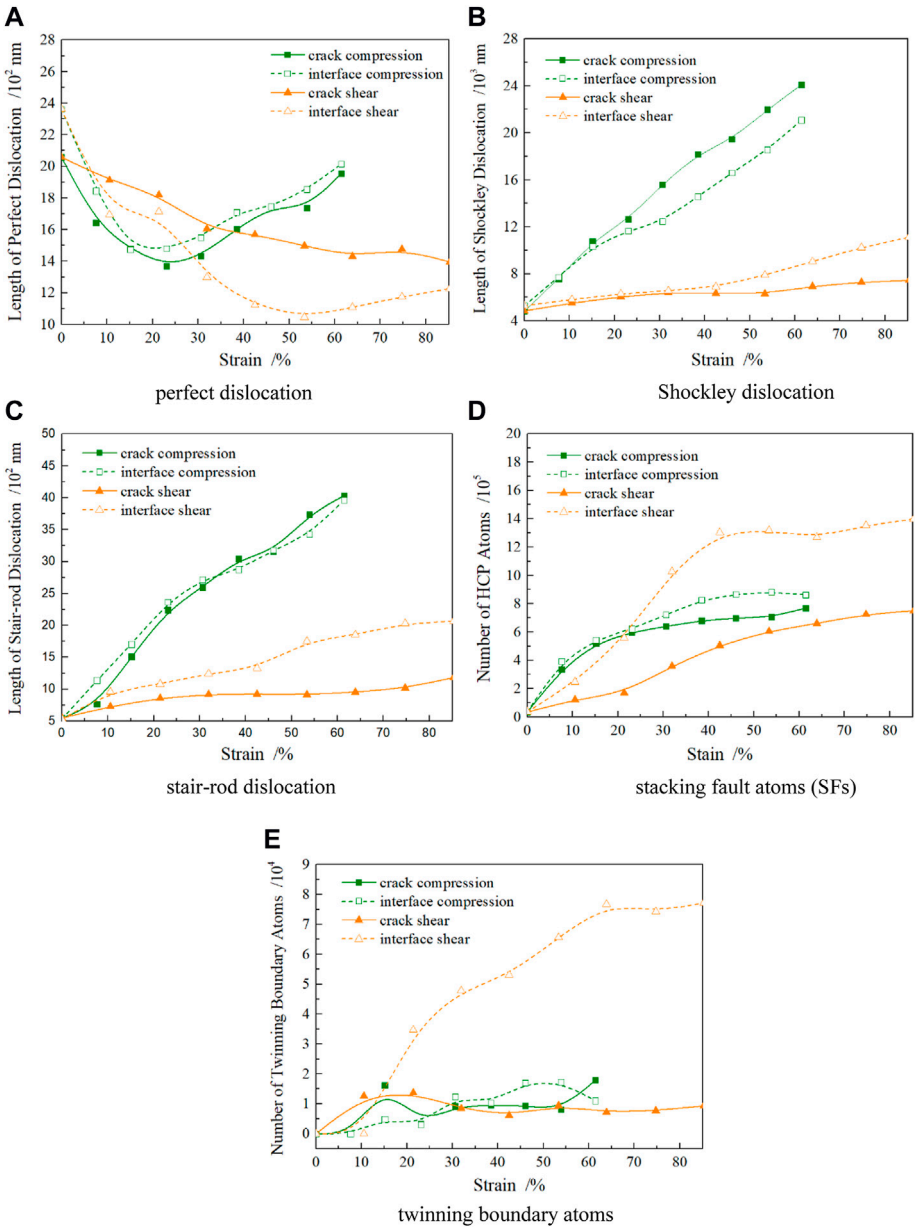

FIGURE 8
Variations of dislocation, SF atoms, and twinning boundary atoms versus strain, **(A)** perfect dislocation **(B)** Shockley dislocation, **(C)** stair-rod dislocation, **(D)** stacking fault atoms (SFs), and **(E)** twinning boundary atoms.

2018b; Chen et al., 2019; Chen et al., 2020) and semiconductors (Sun et al., 2014; Shi et al., 2017; Han et al., 2019; Sun et al., 2020). Therefore, detailed variations of dislocation length determined by the DXA analysis method and of twinning boundaries atoms obtained by coordinate number during compression and shear load are given in Figure 8. It was found that with the increase of compressive strain, the perfect dislocation lengths of the two samples decreased sharply and then increased after reaching a minimum value when the strain was about 23%. However, according to the characteristics of the sample, the corresponding value under shear decreased steadily at different rates, that is, during shear deformation, and the length of perfect dislocations in the sample with crack was longer than that in the sample with interface, as shown in Figure 8A. The amount of Shockley partial dislocation increased almost linearly with increasing strain, and its values under compression were much higher than those under shear at the same strain. It is interesting to note that the Shockley

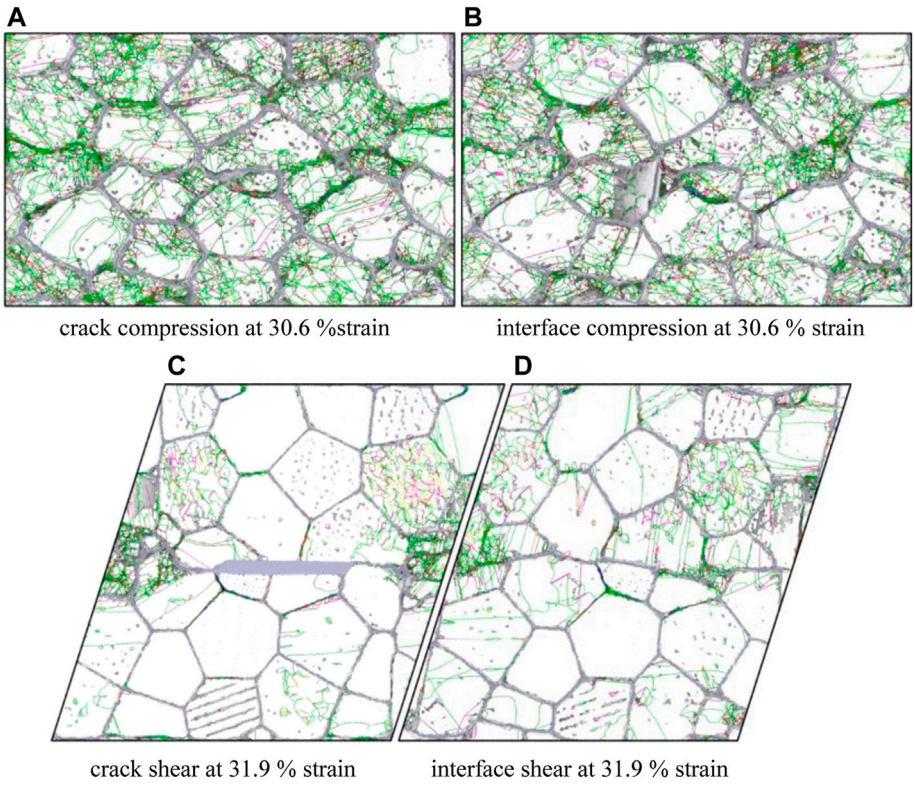

FIGURE 9
Dislocation distribution for different samples (blue lines represent perfect dislocations, green lines are partial dislocations, and pink lines are stair-rod dislocations), **(A)** crack compression at 30.6% strain, **(B)** interface compression at 30.6% strain, **(C)** crack shear at 31.9% strain, and **(D)** interface shear at 31.9% strain.

dislocation length of the sample with interface was slightly lower than the counterpart with crack under compression, which reverses the changes under shear. During deformation, two Shockley partial dislocations slipping on different (111) planes interact and generate a stair-rod dislocation, which is unmovable and prevents the further slipping of the two partial dislocations. The trends for stair-rod dislocation during loading are similar to those of Shockley dislocation but with a much higher value for the sample with interface under shear loading. The HCP atoms, as determined by OVITO visualization software, include intrinsic stacking faults and extrinsic stacking faults. The intrinsic stacking faults appear as Shockley partial dislocation glides toward the contrary side of the grain, leaving two adjacent (111) planes of HCP atoms. The extrinsic stacking faults, which are created by two Shockley partial dislocations slipping through the grain on the adjacent planes, are two (111) planes of HCP atoms separated by a (111) plane of FCC atoms (Zhang et al., 2019). Consequently, the number variations of HCP atoms during loading are analyzed and shown in Figure 8D; their amount is enhanced with increasing strain, with the values for the sample with interface higher than those with crack, especially for the sample with interface under shear loading (e.g., it is 13×10^5 and is more than twice as high as that with crack at 45% strain). The number variations of twinning boundary (TB) atoms are illustrated in Figure 8E, indicating that the atoms increase slightly with strain, except for the sample with interface under shear loading, which is the highest among the others.

Since the GB in a polycrystalline sample is often an obstacle to crack propagation, dislocation accumulation occurs easily around GBs (Li and Jiang, 2019). The dislocation distribution after loading is demonstrated in Figure 9, which shows that massive Shockley partial dislocations and perfect dislocations are generated near GBs, while stair-rod dislocations appear within grain interiors during compression loading; thus, the dislocation density of GBs is much higher than within grain interiors. This implies again that during the compression process, a large number of dislocations are emitted from GBs, interfaces, and crack tips, where the atoms do not mismatch well and have higher stress concentrations, as shown in Figures 5,7. Then, the generated dislocations slip along glide planes and finally interact with opposite sides of the grains, crack, and dislocations, leading to an enhanced dislocation density as shown in Figure 8. Dislocation emission during shear loading mainly occurs at the two crack tips as well as in some individual grains where

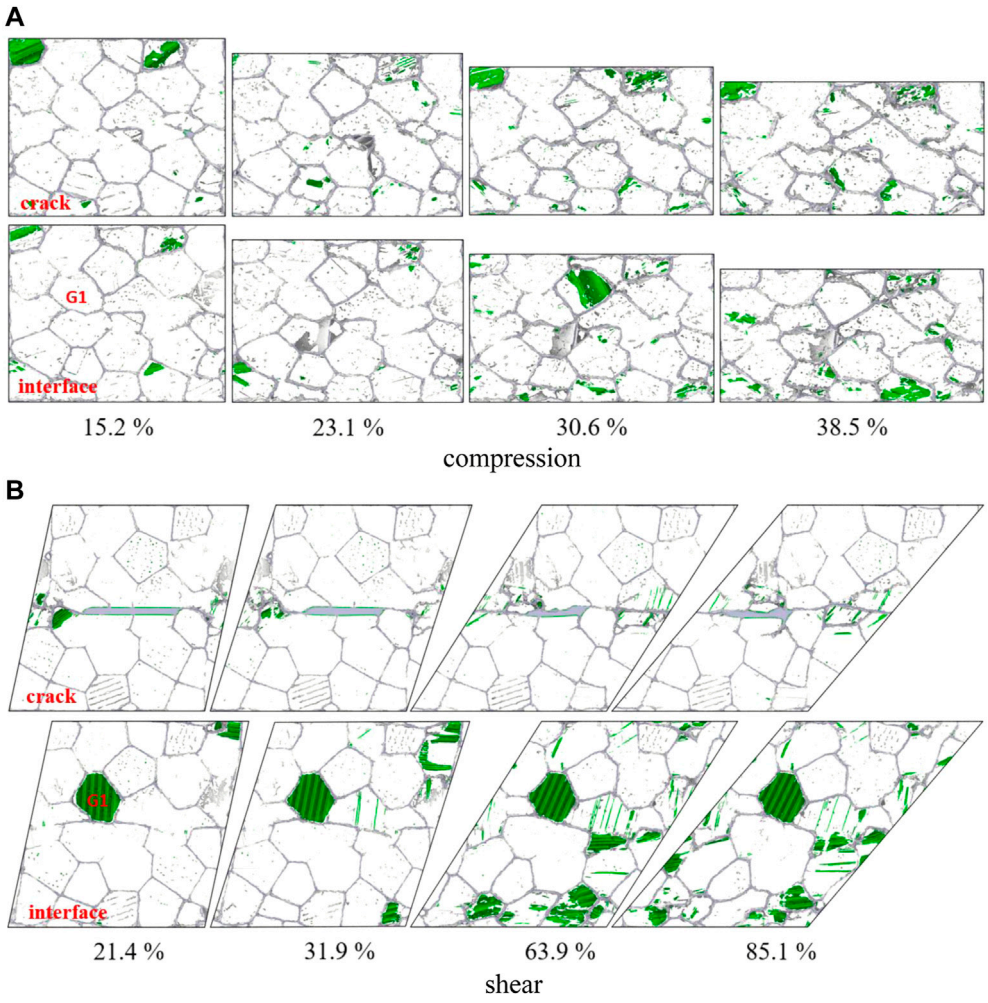

FIGURE 10
Evolutions of twinning boundary atoms as a function of strain (TB atoms are colored in green), **(A)** compression, **(B)** shear.

dislocation motion is activated earlier due to higher concentrated shear stress. Its degree of dislocation concentration is stronger for the sample with crack than for that with interface.

Considering that twinning and dislocation slip are the primary deformation mechanisms that dominate the plasticity of polycrystalline materials, the nucleation and growth of twins can not only hinder the movement of dislocation but can also increase deformation resistance and harden the materials. To more intuitively explore the quantity and distribution characteristics of twinning in samples with crack and interface under different loads, the evolutions of TB atoms were determined through coordination number analysis, as shown in Figure 10. It was found that the TB atoms appear when the strain increases to 15.2% of compressive strain and 21.4% of shear strain, respectively. TBs only take place within a small number of grains under compression, and the number of TB atoms increases slightly with growing compression strain. The TBs occur within some grains around crack tips, and the amount extends to grains along crack areas because of higher shear stress, as illustrated in Figure 7. However, a large number of micro-twins are generated at 21.4% for the sample with interface under shear loading in Figure 10B; its number, as well as twinning, grows significantly with strain, which is in accordance with the corresponding variations in Figure 8.

Based on the abovementioned analysis of deformation evolution and deformation mechanisms for samples with crack and interface, we know that perfect dislocation dissociation takes place with growing strain, resulting from increased Shockley dislocation density and declining length of perfect dislocation during the early compression process when the strain is less than 20%. The generation, movement, and interactions of massive partial dislocations hence lead to an increase in stair-rod dislocations and stacking fault atoms, as well as some twinning. Crack closure happens during dislocation-dominant plastic deformation

under lower applied stress compared with the sample with interface. As compression proceeds, an enormous number of perfect dislocations are emitted from the newly generated interface and GBs where the stress is higher than the grain interior. Then the perfect dislocations separate into partial dislocations, causing significant increases in the lengths of partial dislocations and stair-rod dislocations due to dislocation interactions with interface and dislocations. The growing stair-rod dislocations and higher dislocation density, and their hindrance of dislocation motion, enhance the applied force for further compression plastic deformation. The compression stress-induced dislocation activities play significant parts in crack healing. During the shear process, the higher lengths of perfect dislocations, lower density of partial dislocations, and lower stair-rod dislocations and stacking faults for the sample with crack together imply that dislocation activities, as well as twinning, are substantially less than for the sample with interface. With these results, combined with the evolution of atomic configuration in Figure 6, the GB emigration, GB sliding along the existing interface, and crack tip extension along GBs play significant roles in shear plastic deformation for the sample with crack, while massive dislocation activities, twinning, and grain rotation contribute to plasticity for the sample with interface.

Conclusion

In this work, crack closure, healing evolutions, and mechanical behaviors of polycrystalline FeCrNi samples with pre-crack and interface were conducted using molecular dynamics simulation under varying loading conditions. The results were as follows:

1) As compression loading proceeds, the stress increases sharply until the material yield, then decreases, and subsequently continues to increase. The stress almost saturates after yielding under shear, exhibiting a much lower yield strength for the same sample than for compression.
2) Crack closure and healing take place under compression through dislocation-dominated plastic deformation, while the length of the crack shrinks and the crack tips expand along GBs and interface due to its higher stress under shear loading.
3) Dislocation activities, including dislocation emitting, gliding, and interactions with crack, GBs, and dislocations, contribute to the plasticity of the samples under compression. In addition to dislocation activities, GB gliding, grain rotation, and twinning are the underlying plastic-deformation mechanisms under shear loading.

Data availability statement

The original contributions presented in the study are included in the article/Supplementary Material; further inquiries can be directed to the corresponding authors.

Author contributions

HC: methodology, writing (review and editing), and funding acquisition. SH: investigation, formal analysis, and conceptualization. JC: methodology, writing (review and editing), and funding acquisition. FC: writing (original draft). SZ: investigation. YZ: formal analysis.

Funding

This study is supported by the National Natural Science Foundation of China (Grant number 51575372), Shanxi Scholarship Council of China (HGKY2019084), and the Doctor Funds of Taiyuan University of Science and Technology (20202004).

Conflict of interest

The authors declare that the research was conducted in the absence of any commercial or financial relationships that could be construed as a potential conflict of interest.

Publisher's note

References

Argon, A. S. (1979). Plastic deformation in metallic glasses. *Acta Metall.* 27, 47–58. doi:10.1016/0001-6160(79)90055-5

Barr, C. M., Vetterick, G. A., Unocic, K. A., Hattar, K., Bai, X.-M., and Taheri, M. L. (2014). Anisotropic radiation-induced segregation in 316L austenitic stainless steel with grain boundary character. *Acta Mater.* 67, 145–155. doi:10.1016/j.actamat.2013.11.060

Béland, L. K., Tamm, A., Mu, S., Samolyuk, G. D., Osetsky, Y. N., Aabloo, A., et al. (2017). Accurate classical short-range forces for the study of collision

cascades in Fe–Ni–Cr. *Comput. Phys. Commun.* 219, 11–19. doi:10.1016/j.cpc.2017.05.001

Bonny, G., Terentyev, D., Pasianot, R. C., Poncé, S., and Bakaev, A. (2011). Interatomic potential to study plasticity in stainless steels: The FeNiCr model alloy. *Model. Simul. Mat. Sci. Eng.* 19, 085008. doi:10.1088/0965-0393/19/8/085008

Chen, J., Fang, L., Sun, K., and Han, J. (2020). Creep behaviors of surface-modified silicon: A molecular dynamics study. *Comput. Mater. Sci.* 176, 109494. doi:10.1016/j.commatsci.2019.109494

Chen, J., Shi, J. Q., Chen, Z., Zhang, M., Peng, W. X., Fang, L., et al. (2019). Mechanical properties and deformation behaviors of surface-modified silicon: A molecular dynamics study. *J. Mat. Sci.* 54, 3096–3110. doi:10.1007/s10853-018-3046-1

Chen, J., Shi, J., Wang, Y., Sun, J., Han, J., Sun, K., et al. (2018). Nanoindentation and deformation behaviors of silicon covered with amorphous SiO_2: A molecular dynamic study. *RSC Adv.* 8, 12597–12607. doi:10.1039/c7ra13638b

Chen, J., Shi, J., Zhang, M., Peng, W., Fang, L., Sun, K., et al. (2018). Effect of indentation speed on deformation behaviors of surface modified silicon: A molecular dynamics study. *Comput. Mater. Sci.* 155, 1–10. doi:10.1016/j.commatsci.2018.08.019

Chen, M.-S., and Lin, Y. C. (2013). Numerical simulation and experimental verification of void evolution inside large forgings during hot working. *Int. J. Plasticity* 49, 53–70. doi:10.1016/j.ijplas.2013.02.017

Fan, Y., Wang, W., Hao, Z., and Zhan, C. (2020). Work hardening mechanism based on molecular dynamics simulation in cutting Ni–Fe–Cr series of Ni-based alloy. *J. Alloys Compd.* 819, 153331. doi:10.1016/j.jallcom.2019.153331

Fang, Q., Li, J., Luo, H., Du, J., and Liu, B. (2017). Atomic scale investigation of nanocrack evolution in single-crystal and bicrystal metals under compression and shear deformation. *J. Alloys Compd.* 710, 281–291. doi:10.1016/j.jallcom.2017.03.230

Feng, C., Cui, Z., Liu, M., Shang, X., Sui, D., and Liu, J. (2016). Investigation on the void closure efficiency in cogging processes of the large ingot by using a 3-D void evolution model. *J. Mater. Process. Technol.* 237, 371–385. doi:10.1016/j.jmatprotec.2016.06.030

Feng, C., Cui, Z., Shang, X., and Liu, M. (2017). An evolution model for elliptic-cylindrical void in viscous materials considering the evolvements of void shape and orientation. *Mech. Mater.* 112, 101–113. doi:10.1016/j.mechmat.2017.06.002

Han, J., Song, Y., Tang, W., Wang, C., Fang, L., Zhu, H., et al. (2019). Reveal the deformation mechanism of (110) silicon from cryogenic temperature to elevated temperature by molecular dynamics simulation. *Nanomaterials* 9, 1632. doi:10.3390/nano9111632

Hirel, P. (2015). Atomsk: A tool for manipulating and converting atomic data files. *Comput. Phys. Commun.* 197, 212–219. doi:10.1016/j.cpc.2015.07.012

Hu, Y., Cheng, H., Yu, J., and Yao, Z. (2020). An experimental study on crack closure induced by laser peening in pre-cracked aluminum alloy 2024-T351 and fatigue life extension. *Int. J. Fatigue* 130, 105232. doi:10.1016/j.ijfatigue.2019.105232

Huang, H.-g., Liu, Y., Du, F.-s., and Chen, L. (2014). Void closure behavior in large diameter steel rod during H-V rolling process. *J. Iron Steel Res. Int.* 21, 287–294. doi:10.1016/s1006-706x(14)60044-3

Kardani, A., and Montazeri, A. (2018). MD-based characterization of plastic deformation in Cu/Ag nanocomposites via dislocation extraction analysis: Effects of nanosized surface porosities and voids. *Comput. Mater. Sci.* 152, 381–392. doi:10.1016/j.commatsci.2018.06.018

Li, J., Dong, L., Xie, H., Meng, W., Zhang, X., Zhang, J., et al. (2021). Molecular dynamics simulation of nanocrack propagation mechanism of polycrystalline titanium under tension deformation in nanoscale. *Mater. Today Commun.* 26, 101837. doi:10.1016/j.mtcomm.2020.101837

Li, J., Fang, Q. H., Liu, B., Liu, Y., Liu, Y. W., and Wen, P. H. (2015). Mechanism of crack healing at room temperature revealed by atomistic simulations. *Acta Mater.* 95, 291–301. doi:10.1016/j.actamat.2015.06.006

Li, X., and Jiang, X. (2019). Theoretical analyses of nanocrack nucleation near the main crack tip in nano and micro crystalline materials. *Eng. Fract. Mech.* 221, 106672. doi:10.1016/j.engfracmech.2019.106672

Polak, W. Z. (2022). Efficiency in identification of internal structure in simulated monoatomic clusters: Comparison between common neighbor analysis and coordination polyhedron method. *Comput. Mater. Sci.* 201, 110882. doi:10.1016/j.commatsci.2021.110882

Qiu, Y., Xin, R., Luo, J., and Ma, Q. (2020). Effect of deformation modes and heat treatment on microstructure and impact property restoration of internal crack healing in SA 508 steel. *Mater. Sci. Eng. A* 778, 139073. doi:10.1016/j.msea.2020.139073

Shi, J., Chen, J., Fang, L., Sun, K., Sun, J., and Han, J. (2018). Atomistic scale nanoscratching behavior of monocrystalline Cu influenced by water film in CMP process. *Appl. Surf. Sci.* 435, 983–992. doi:10.1016/j.apsusc.2017.11.199

Shi, J., Chen, J., Wei, X., Fang, L., Sun, K., Sun, J., et al. (2017). Influence of normal load on the three-body abrasion behaviour of monocrystalline silicon with ellipsoidal particle. *RSC Adv.* 7, 30929–30940. doi:10.1039/c7ra02148h

Shi, J., Fang, L., Sun, K., Peng, W., Ghen, J., and Zhang, M. (2020). Surface removal of a copper thin film in an ultrathin water environment by a molecular dynamics study. *Friction* 8, 323–334. doi:10.1007/s40544-019-0258-6

Spaepen, F. (1977). A microscopic mechanism for steady state inhomogeneous flow in metallic glasses. *Acta Metall.* 25, 407–415. doi:10.1016/0001-6160(77)90232-2

Sun, J., Fang, L., Han, J., Han, Y., Chen, H., and Sun, K. (2014). Phase transformations of mono-crystal silicon induced by two-body and three-body abrasion in nanoscale. *Comput. Mater. Sci.* 82, 140–150. doi:10.1016/j.commatsci.2013.09.055

Sun, J., Xu, B., Zhuo, X., Han, J., Yang, Z., Jiang, J., et al. (2020). Investigation of indenter-size-dependent nanoplasticity of silicon by molecular dynamics simulation. *ACS Appl. Electron. Mat.* 2, 3039–3047. doi:10.1021/acsaelm.0c00659

Sun, J., Yang, Z., Liu, H., Han, J., Wu, Y., Zhuo, X., et al. (2019). Tension-compression asymmetry of the AZ91 magnesium alloy with multiheterogenous microstructure. *Mater. Sci. Eng. A* 759, 703–707. doi:10.1016/j.msea.2019.05.093

Wang, B., Zhang, J., Xiao, C., Song, W., and Wang, S. (2015). Analysis of the evolution behavior of voids during the hot rolling process of medium plates. *J. Mater. Process. Technol.* 221, 121–127. doi:10.1016/j.jmatprotec.2015.02.012

Wei, D., Han, J., Tieu, K., and Jiang, Z. (2004). Simulation of crack healing in BCC Fe. *Scr. Mater.* 51, 583–587. doi:10.1016/j.scriptamat.2004.05.032

Wei, D., Jiang, Z., and Han, J. (2013). Modelling of the evolution of crack of nanoscale in iron. *Comput. Mater. Sci.* 69, 270–277. doi:10.1016/j.commatsci.2012.11.043

Zhang, M., Xu, T., Li, M., Sun, K., and Fang, L. (2019). Constructing initial nanocrystalline configurations from phase field microstructures enables rational molecular dynamics simulation. *Comput. Mater. Sci.* 163, 162–166. doi:10.1016/j.commatsci.2019.03.026

Zhang, X.-X., Cui, Z.-S., Chen, W., and Li, Y. (2009). A criterion for void closure in large ingots during hot forging. *J. Mater. Process. Technol.* 209, 1950–1959. doi:10.1016/j.jmatprotec.2008.04.051

frontiers | Frontiers in Materials

TYPE Original Research
PUBLISHED 11 November 2022
DOI 10.3389/fmats.2022.978025

OPEN ACCESS

EDITED BY
Yu-Hong Zhao,
North University of China, China

REVIEWED BY
Qing Wang,
Dalian University of Technology, China
Zhiqin Wen,
Guilin University of Technology, China

*CORRESPONDENCE
Ming Chen,
chenming@ustl.edu.cn

SPECIALTY SECTION
This article was submitted to Computational Materials Science, a section of the journal Frontiers in Materials

RECEIVED 25 June 2022
ACCEPTED 05 October 2022
PUBLISHED 11 November 2022

CITATION
Liu Q, Jiang J, Chen M, Deng X, Wang J and Ju D (2022), Study on the mechanism of carbide precipitation by surface quenching treatment on GCr15 bearing rings based on the phase-field method.
Front. Mater. 9:978025.
doi: 10.3389/fmats.2022.978025

Study on the mechanism of carbide precipitation by surface quenching treatment on GCr15 bearing rings based on the phase-field method

Qian Liu[1], Jiaxuan Jiang[2], Ming Chen[2]*, Xiaohu Deng[3], Jiangang Wang[4] and Dongying Ju[5]

[1]School of Materials and Metallurgy, University of Science and Technology Liaoning, Anshan, China, [2]School of Mechanical Engineering and Automation, University of Science and Technology Liaoning, Anshan, China, [3]National Local Joint Engineering Laboratory of Intelligent Manufacturing Oriented Automobile Die & Mold, Tianjin University of Technology and Education, Tianjin, China, [4]College of Material Science and Engineering, Hebei University of Science and Technology, Shijiazhuang, China, [5]Saitama Institute of Technology, Fukaya, Japan

In this paper, the thermodynamics database describing Gibbs free energy of *FCC* phase and $M_{23}C_6$ phase based on *Fe-Cr-C* ternary alloy was coupled into phase field simulation, and the phase field model was developed on the mesoscopic scale which simulates precipitation, growth and coarsening of $M_{23}C_6$ carbides in *FCC* austenitic matrix by considering the elastic energy. As the boundary condition of imported phase field calculation, the heat treatment COSMAP software was applied to obtain the macro numerical simulation results of quenching. The phase composition, element distribution, and the evolution including the nucleation, growth and coarsening was simulated by phase field method for the $M_{23}C_6$ carbides in quenching process of GCr15 bearing ring. By means of comparison between the calculation results of phase field simulation and the morphology, quantity and distribution of carbides observed by SEM experiment, this paper present the mechanism on precipitation of micro $M_{23}C_6$ carbides influenced by quenching process parameters, and the experiment verifies the feasibility and accuracy of phase field simulation.

KEYWORDS

phase-field method, carbide, GCr15 bearing steel, elastic properties, quenching, phase change

1 Introduction

Bearings have already been indispensable core components in many areas, such as aerospace, high-speed rail, and the automotive industry. In practical application, a bearing has been designed to withstand cyclical loads and resist external shocks. The purpose has provided an important guarantee for the high rotational accuracy and high wear resistance of many rotary machines at high speeds (Zhao-kun et al., 2016; Zou, 2021). In the manufactured process of bearing, metallurgy, and preparation of the material, the processing technology of

materials and heat treatment technology have been the main factors affecting bearing performance. The bearing ring is the main part. The quenching process of the bearing ring has been very important in determining the final strength, wear resistance, rotation accuracy, and rotation noise performance because it is close to the last process of manufacturing the bearing ring.

High-carbon–chromium bearing steel has good fatigue resistance, elasticity, and toughness. After quenching, it could have high and uniform hardness (Laing et al., 1967). The distribution and composition of carbides have an important influence on the properties of bearing steel. Research on it has been difficult at present, providing a basis for improving the bearing ring dimensional stability and optimizing the heat treatment process (Zong et al., 2020). GCr15 is high-carbon–chromium earing steel. $M_{23}C_6$ are the main carbides in GCr15. Their phase composition, element distribution, and evolution, including nucleation, growth, and coarsening, have an important influence on the dimensional stability of the bearing outer ring (Du, 2017). And $\gamma \rightarrow M_{23}C_6$, the organization and distribution of M23C6 would be influenced by the phase transformation mechanism of GCr15, so to study the phase transformation mechanism of the carbide educt be revealed from *FCC* phase of $M_{23}C_6$ is great significance. The study of the effect of quenching treatment of GCr15 steel on the $\gamma \rightarrow M_{23}C_6$ phase transformation mechanism is of practical guidance.

The phase-field method is a powerful mesoscale calculation method based on density. Based on the concept of MGI, the phase-field method simulates organizational evolution, realizes the prediction of material properties, and accelerates the material development process (Li, 2009; Ding, 2019). Xin et al. provided compelling morphological, chemical, structural, and thermodynamic evidence for the spinodal decomposition and showed that the lattice mismatch at the diffuse transition region between the spinodal zones and matrix is the dominating factor for enhancing yield strength in this class of alloy (Xin et al., 2021). Zhao et al. studied the multi-controlling factors of the dendritic growth in directional solidification through the phase-field method. The effects of the temperature gradient, propelling velocity, thermal disturbance, and growth orientation angle on the growth morphology of the dendritic growth at the solid/liquid interface were discussed (Zhao et al., 2019). Zhang et al. (2018) developed a model of rapid solidification of non-stoichiometric intermetallic compounds based on the thermodynamic extremal principle, and the *Co-xat. %Si* alloys (*x ¼ 50, 53, 55*) were undercooled to test the model. Kuang et al. (2018) considered the thermodynamic extremal principle and proposed a modified quasi-sharp-interface model that integrates trans-interface diffusion from the product phase to the interface, trans-interface diffusion from the interface to the parent phase, and interface migration and bulk diffusion of *C* and *X*. Applications to isothermal and cyclic phase transformations showed that the model allows the arbitrary setting of the initial conditions. Zhao et al. used a multi-component continuous phase-field model based on the Gibbs free energy of the sub-regular solution. The core-shell structure precipitates of *Fe-xCu-3.0Mn-1.5Ni-1.5Al* alloys under internal and external strain were investigated (Zhao et al., 2022a). Tian et al. (2022) used the phase-field-crystal method and dynamically displayed the interaction between twins and dislocations. In this study, the phase-field method was used to study the effect of the precipitation mechanism of $M_{23}C_6$ carbides during bearing ring quenching. First, COSMAP was used to simulate the GCr15 bearing ring quenched to obtain elastic field data. The heat treatment simulation results were introduced into the phase-field model to obtain the nucleation, growth, and coarsening process of $M_{23}C_6$ carbides precipitated from the *FCC* matrix phase under the influence of coupling elastic energy and describe the morphology and distribution of $M_{23}C_6$ carbides in the *FCC* matrix phase. Finally, the morphology and distribution of $M_{23}C_6$ carbides in the quenched GCr15 bearing ring were tested by SEM, and the phase-field simulation and experimental results were compared.

2 Multi-field coupling quenching process simulation

The research sample is the bearing ring, and the material is GCr15. The workflow is as follows: first, it completes model preprocessing by GID and then analyzes the material properties. These are preparations for the next numerical simulation. The main focus of the quenching process is the deformation problem for the bearing ring. The temperature field variation and deformation behavior could be analyzed. The simulation process by COSMAP is shown in Figure 1.

2.1 Geometric model

The specimen's critical dimensions are a diameter of 125 mm, a wall thickness of 7.5 mm, and a width of 11 mm. It belongs to the thin-walled part.

2.2 Building a finite element model

As shown in Figure 2, analytical model had been created 16,611 nodes and 13,328 cells. On the section of the bearing model, there are three points, called P1, P2, P3, and P1 node represent endpoint of the outer ring, P2 node represent endpoint of the middle surface and P3 node represent endpoint of the inner surface. These three nodes move along the arc and vertical direction and divided the model into hexahedral elements of similar size for the calculation units of finite element analysis. The purpose is to determine the temperature *f* variation and deformation at different positions and accurately describe the deformation behavior of the quenched bearing ring.

2.3 Quenching process

The experimental heat treatment process is heating for 15 min to 845°C, then holding for 25 min, and finally quenching in oil.

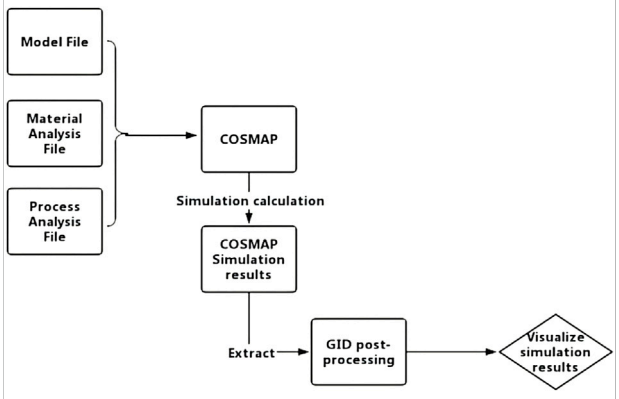

FIGURE 1
Flowchart of COSMAP simulation.

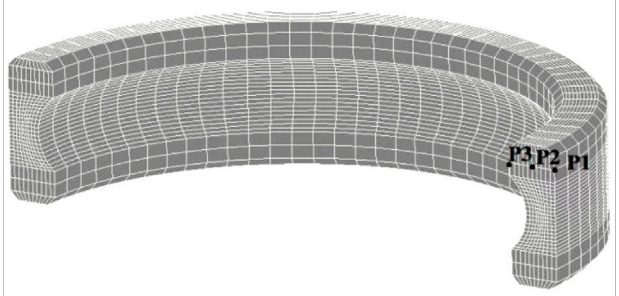

FIGURE 2
Diagram of the analysis area based on the model meshed.

According to experience, the heat transfer law of the ring has been set, and the adopted values are shown in Figure 3. The heat transfer coefficient curve could accurately reflect the temperature cooling in oil quenching, compared with the oil cooling curve (Liu et al., 2022) Table 1 shows the chemical composition of GCr15 used in the analysis.

2.4 Simulation results and analysis

Temperature variation and deformation law are listed in this study. From Figure 4, the results of temperature cooling in various regions of the ring quenched could be analyzed. Temperature cooling varies for the interior and surface of the bearing ring entity. Because the surface has direct contact with the oil, its cooling rate is faster. The heat transfer between the surface and the interior is heat conduction; there is a certain time difference, so the internal cooling rate is slow. There is no obvious temperature difference between the inner and outer surfaces for the thin-walled part. Temperature difference at different locations is likely to affect carbide formation, distribution, and coarsening. It could be verified in the subsequent phase-field simulation and test.

Studying the deformation mechanism of the quenched bearing outer ring is always difficult. Although the ovality of the outer ring can be adjusted by subsequent processing, the dimensional stability is an unresolved fundamental problem for long-term applications, which affects the performance of bearings. Therefore, how to better control the deformation of the heat treatment process is still a topic of research in the industry.

The variation trend of deformation can be obtained from Figure 5. When the cooling rate is the fastest, the deformation is reduced to the lowest. After about 6 s, a parabolic trend appears, which is affected by the latent heat of phase change. In the convective heat transfer stage, the deformation tends to be stable.

3 Phase-field simulation

The precipitation process of carbides from phases in GCr15 bearing steel was simulated by the phase-field method. The influence of elastic energy on the $\gamma \rightarrow M_{23}C_6$ phase transition mechanism is also considered.

4 Flowchart for introducing elastic energy in phase-field simulation

Figure 6 shows the analysis process of elastic strain energy introduction.

4.1 Establishment of the phase-field model

Because there are many kinds of elements in GCr15 bearing steel and our phase-field simulation program only supports the ternary alloy system, three main elements (Fe, Cr, and C) in GCr15 steel are selected. Independent component field variables $c_i(r,t)(i=1,2,3)$ and single-ordered parameter $\phi(r,t)$ have been used to describe its microstructure evolution. In the formula $c_i(r,t)(i=1,2,3)$, where it represents, respectively, instantaneous concentrations of Fe, Cr, and C atoms in specific spatial positions r at some times t. Order parameters $\phi(r,t)$ represent phase distribution in specific spatial positions, and $h(\phi)$ ranges from 0 to 1, where $h(\phi)=0$ corresponds to the *FCC* structural phase and $h(\phi)=1$ corresponds to the $M_{23}C_6$ phase. It mainly expresses the carbide phase transformation process. The phase-field model can be analyzed using Eqs. 1, 2 as follows:

$$\frac{\partial c_i(r,t)}{\partial t} = \sum_j \left(M_i \nabla^2 \frac{\delta F}{\delta c_j(r,t)} \right) + \xi_{c_i}(r,t), i = j = Cr, C, \quad (1)$$

$$\frac{\partial \phi(r,t)}{\partial t} = -L \frac{\delta F}{\delta \phi(r,t)} + \xi_{\phi}(r,t), \quad (2)$$

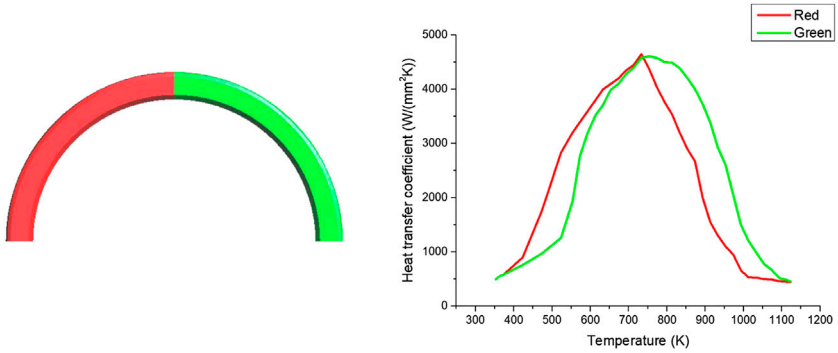

FIGURE 3
Surface heat transfer coefficient law of GCr15 steel quenched in oil.

TABLE 1 Chemical composition of GCr15 steel.

Ingredient	C	Si	P	S	Fe
Mass fraction (%)	0.95–1.05	0.15–0.35	0.25	0.25	Bal
Ingredients	Cr	Mn	Mo	Ni	Cu
Mass fraction (%)	1.40–1.65	0.25–0.45	≤ 0.1	0.30	0.25

where $\xi_{c_j}(r,t)$ and $\xi_{\phi}(r,t)$ represent the Gauss noise term from the fluctuation–dissipation theorem (Guo, 2021). They are added to the equation to cause small component fluctuations and provide initial energy for the occurrence of the phase transition process. The parameter L represents the kinetic coefficient of phase transition, which can be used to characterize the phase transition evolution between the *FCC* and $M_{23}C_6$ phases (Hu et al., 2007). It has been simplified as a constant in the analytical process. The parameter F represents the total free energy of the microstructure. Contributions of local chemical free energy, gradient energy, and elastic strain energy have been considered simultaneously. Eq. 3 is used to calculate the total free energy F of the system. M_i represents the diffusion mobility of effective components in the alloy system and is analyzed in Eq. 4 (Zhu et al., 2004; Koyama and Onodera, 2005):

$$F = \int_v f dv = \int_v \left[\frac{f_{local}(c,\phi,T)}{V_m} + f_{grad} + \frac{f_{el}}{V_m} \right] dV, \quad (3)$$

where f_{local}, f_{grad}, and f_{el} represent local chemical free energy, gradient energy (Cahn and Hilliard, 1958), and elastic strain energy, respectively. The parameter V represents the volume of the system.

$$M_i = h(\phi) \cdot M_{M_{23}C_6} + (1 - h(\phi)) M_{fcc}, \text{the i} = \text{Cr, C}, \quad (4)$$

where $M_{M_{23}C_6}$ represents the atomic diffusion mobility of the Cr and C atoms in the $M_{23}C_6$ phase and M_{fcc} represents the atomic diffusion mobility of the Cr and C atoms in the FCC phase. Eq. 5 can be used to calculate the following:

$$M_\phi = \frac{D_\phi^{self}}{RT}, \quad (5)$$

where parameter R represents the gas constant (Jiang et al., 2022), $R = 8.314472 \text{J}/(\text{mol} \cdot \text{k})$. The parameter T represents temperature. D_ϕ^{self} represents self-diffusion coefficient and has been calculated using Eq. 6:

$$D_\phi^{self} = D_0 \, exp\left(-\frac{Q}{RT}\right), \quad (6)$$

where the parameter Q represents diffusion activation energy and the parameter D_0 represents the frequency factor.

Available kinetic parameters have been referred to in Table 2.

4.2 Local chemical free energy

The Wheeler et al. (1992) (WBM) model has been applied to the analysis. Local chemical free energy can be considered by combining two single-phase free energies:

$$f_{local}(c,\phi,T) = \frac{1}{V_m}\left\{h(\phi) G_m^{M_{23}C_6} + [1 - h(\phi)] G_m^{fcc} + \omega g(\phi)\right\}. \quad (7)$$

V_m represents the molar volume of the system (Zhu et al., 2011); the value can be referred to in Table 2. c represents the mass percentage of the solute atom. The value of ϕ equals 0 in the *FCC* phase and 1 in the $M_{23}C_6$ phase. The parameter T represents temperature. ω represents the height of the potential well and has been used to analyze the resistance, which needs to be overcome for phase transformation (Koyama et al., 2006; Zhao et al., 2022b). Two continuous interpolation functions $g(\phi)$ and $h(\phi)$ have value in the range of 0–1 (Koyama et al., 2006; Zhao, 2022). The function of $h(\phi)$ has mainly reflected the smooth transition of the precipitated phase from the *FCC* phase to the $M_{23}C_6$ phase. $g(\phi)$ has been applied in the form

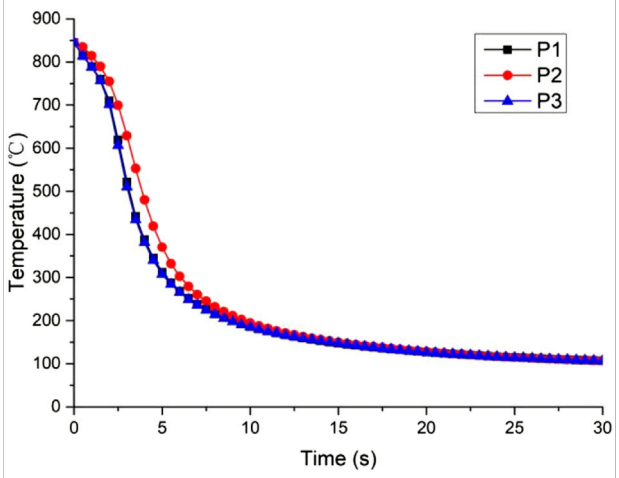

FIGURE 4
Cooling curves of different nodes during quenching of the GCr15 bearing ring.

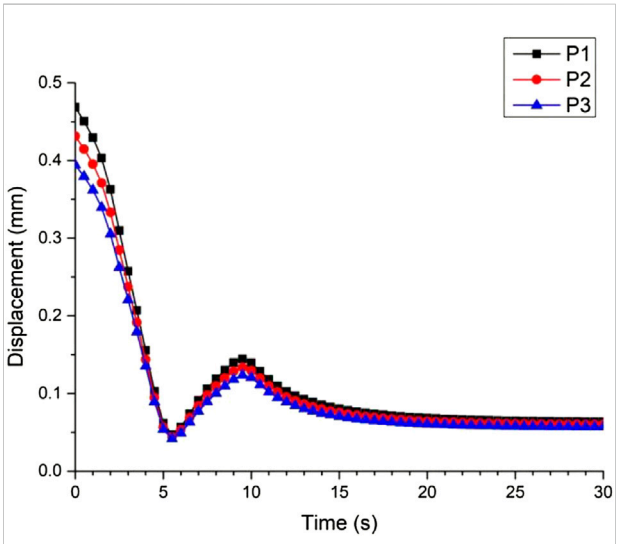

FIGURE 5
Curve of deformation in quenching.

of double-well potential and represented an energy barrier for phase transition. They can be analyzed, respectively, through Eqs. 8, 9. $G_m^{M_{23}C_6}$ and G_m^{fcc} represent the molar Gibbs free energy of the *FCC* and $M_{23}C_6$ phases, respectively:

$$g(\phi) = \phi^2(1-\phi^2), \tag{8}$$

$$h(\phi) = \phi^3(6\phi^2 - 15\phi + 10). \tag{9}$$

The relationship between them can be derived from Eq. 10 (Loginova et al., 2003):

$$\frac{dh(\phi)}{d\phi} = 30g(\phi). \tag{10}$$

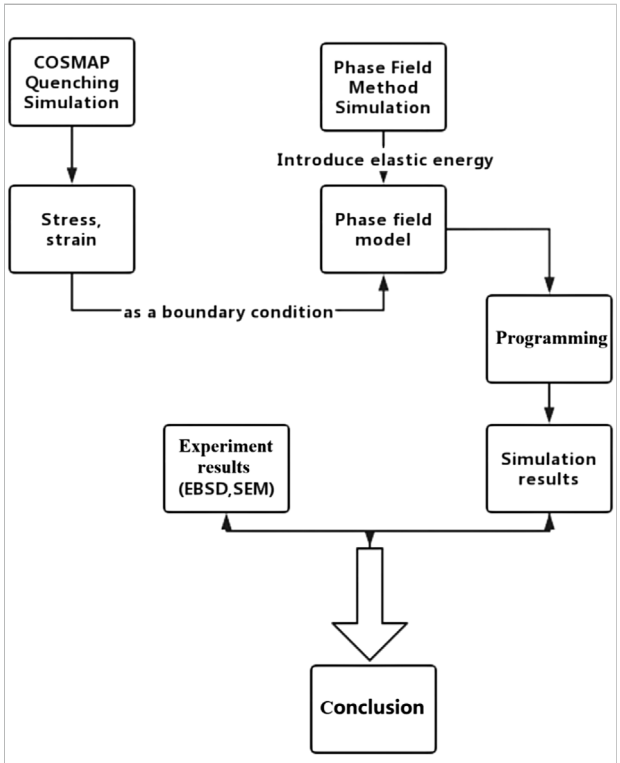

FIGURE 6
Flowchart for the introduction of elastic energy.

Based on the CALPHAD method (Saunders and Miodownik, 1992), the molar Gibbs free energy of the *FCC* matrix phase can be described through two sub-lattice models (Fe, Cr) and (C, Va). Metal elements have been mixed in the first sublattice and carbon and vacancy in the interstitial sub-lattice (Andersson, 1988; Khvan et al., 2014):

$$\begin{aligned} G_m^{fcc} = {} & y_{Fe}y_c{}^0G_{Fe,c}^{fcc} + y_{Fe}y_{va}{}^0G_{Fe,va}^{fcc} + y_{Cr}y_c{}^0G_{Cr,c}^{fcc} + y_{Cr}y_{va}{}^0G_{Cr,va}^{fcc} \\ & + RT(y_{Fe}\ln y_{Fe} + y_{Cr}\ln y_{Cr}) + RT(y_{va}\ln y_{va} + y_c\ln y_c) \\ & + {}^EG_m^{fcc}, \end{aligned} \tag{11}$$

where

$$\begin{aligned} {}^EG_m^{fcc} = {} & y_{Fe}y_{Cr}\left(y_cL_{Cr,Fe:\,c}^{fcc} + y_{va}L_{Cr,Fe:\,va}^{fcc}\right) + y_{va}y_c\left(y_{Cr}L_{Cr:\,va,c}^{fcc}\right. \\ & \left. + y_{Fe}L_{Fe:\,va,c}^{fcc}\right). \end{aligned} \tag{12}$$

y_i represents the lattice fraction of the *Ith* component between metallic and interstitial sub-lattices. The parameter L is an interaction parameter related to the concentration. ${}^0G_{i:\,va}^{fcc}$ represents the Gibbs free energy of the *Ith* pure component under the assumed non-magnetic state. ${}^0G_{i:\,c}^{fcc}$ represents the Gibbs free energy in the assumed non-magnetic state when the interstitial position has been completely filled with carbon elements. The relationship between the lattice fraction and molar fractions has been described by Eqs. 13, 14:

TABLE 2 Calculation results of kinetic parameters.

Parameter	Symbol	Value	Unit	Reference
Interface dynamics coefficient	L	1×10^{-5}	$m^3 J^{-1} s^{-1}$	Zhao et al. (2022a)
Molar volume	V_m	7.09×10^{-6}	$m^3 mol^{-1}$	Zhu et al. (2011)
Self-diffusion coefficient $D_\phi^{self} = D_0 exp(-\frac{Q}{RT})$	$D_{C\,in\,M_{23}C_6}^{self}$	$D_0 = 15 \times 10^{-7}$	$m^2 s^{-1}$	Levchenko et al. (2009)
		$Q = 1.8 \times 10^5$		
	$D_{Cr\,in\,M_{23}C_6}^{self}$	8.72×10^{-12}		Song et al. (2014)
	$D_{C\,in\,fcc}^{self}$	$D_0 = (0.146 - 0.36C(1 - 1.075Cr) + K_1 M) \times 10^{-4}$		
		$K_1 = 0$		Lee et al. (2011)
		$Q = (-144.3 - 15.0C + 0.37C^2 + K_2 M) \times 10^3$		
		$K_2 = 7.7260$		
	$D_{Cr\,in\,fcc}^{self}$	$D_0 = 5.2 \times 10^{-9}$		Kučera and Stránský (1982)
		$Q = 1.8 \times 10^5$		
Elastic constant	C_{ij}	$M_{23}C_6$ { $C_{11} = 471.6$; $C_{12} = 215.7$; $C_{44} = 135.1$ }	Gpa	Liu et al. (2015)
		FCC { $C_{11} = 204.0$; $C_{12} = 133.0$; $C_{44} = 126.0$ }		Kamel and Hafid (2013)

$$y_{Fe} = x_{Fe}/(1 - x_c),\ y_{Fe} + y_{Cr} = 1, \tag{13}$$

$$y_c = x_c/(1 - x_c),\ y_c + y_{va} = 1. \tag{14}$$

Molar free energy of the $M_{23}C_6$ carbide phase has also been treated by two sub-lattice models $(Fe.Cr)_{23}C_6$:

$$G_m^{M_{23}C_6} = y_{Fe}\,{}^0G_{Fe:c}^{M_{23}C_6} + y_{Cr}\,{}^0G_{Cr:c}^{M_{23}C_6} + 7RT(y_{Fe}\,ln\,y_{Fe} + y_{Cr}\,ln\,y_{Cr}) + y_{Fe}y_{Cr}L_{Cr,Fe:c}^{M_{23}C_6}. \tag{15}$$

In Eq. 15, ${}^0G_{i:c}^{M_{23}C_6}$ represents the Gibbs free energy of the pure binary carbide.

All thermodynamic parameters in the molar Gibbs free energy of the *FCC* and $M_{23}C_6$ phases have been calculated (Andersson, 1987; Andersson, 1988; Khvan et al., 2014). Parameter calculation is summarized in Table 3.

The distribution of the molar free energy of the *FCC* and $M_{23}C_6$ phases varying with the lattice fraction has been obtained from Figure 7. Figure 7A shows that the molar free energy of the $M_{23}C_6$ phase decreases with the increase in the sub-lattice fraction of iron and carbon elements, and the molar free energy of the $M_{23}C_6$ phase is minimum when the sub-lattice fraction of iron and carbon elements reaches an equilibrium value. Figure 7B shows that the molar free energy of the *FCC* phase is minimum when the sub-lattice fraction of iron and chromium elements reaches an equilibrium value. Meanwhile, the sub-lattice fraction of the carbon element equals to about 0.5.

4.3 Gradient energy (physics)

The uneven interface composition and difference in structural order parameters should be the main reason for the existence of gradient energy. There is a certain relationship between gradient energy and system interface energy. System interface energy could reflect gradient energy, and details can be explained using Eq. 16.

$$f_{grad} = \frac{1}{2}k_c \sum_j |\nabla c|^2 + \frac{1}{2}k_\phi |\nabla \phi|^2, \tag{16}$$

where k_c defines the gradient energy coefficient of the concentration or composition field and equals 7.05×10^{-9}j/m (Kitashima et al., 2008). k_ϕ defines the gradient energy coefficient of the phase-field or the order parameter and equals 1.4×10^{-10}j/m (Jokisaari and Thornton, 2015).

4.4 Elastic strain energy

The elastic strain energy plays an important role in the morphology, size, and orientation of precipitates and the precipitation kinetic process during the solid-state transformation of alloys. Differences in elastic constants between the new and parent phases, the lattice mismatch between elements or phases, and external stress or strain field should actuate the generation of elastic strain energy and form a stress–strain effect (Sun., 2020; Wu, 2021). For these reasons, strain energy should be added to the total free energy equation to develop the phase-field model, which would study the effect of elastic energy on the solid-state phase transformation process of alloys. Elastic energy in the phase-field model is analyzed using Eq. 17.

$$f_{el} = \frac{1}{2}\int_V \sigma_{ij}\varepsilon_{ij}^{el} dv. \tag{17}$$

In Eq 17, σ_{ij} reflects elastic stress and ε_{ij}^{el} reflects the elastic strain, which has a relation with the total strain ε_{ij} and eigenstrain ε_{ij}^0:

TABLE 3 Calculation parameters of thermodynamic parameters with the *FCC* and $M_{23}C_6$ phases (Andersson, 1987; Andersson, 1988; Khvan et al., 2014).

Phase	Thermodynamic parameter (J/mol)
$M_{23}C_6$	${}^0G_{Fe:C}^{M_{23}C_6} = GFEM23C6$
	${}^0G_{Cr:C}^{M_{23}C_6} = GCRM23C6$
	$L_{Cr:Fe:C}^{M_{23}C_6} = 10434 - 14.281T$
	$GFEM23C6\,(298.15 < T < 6000) = +7.66667GFECEM - 1.666667{}^0G_C^{graphite} + 15000$
	$GCRM23C6\,(298.15 < T < 6000) = -521.983 + 3622.24T - 620.965T\,ln(T) - 0.126431T^2$
	${}^0G_C^{graphite}\,(298.15 < T < 6000) = -17368.441 + 170.73T - 24.3T$ $ln(T) - 4.723E-04T^2 + 2562600T^{-1} - 2.643E+08T^{-2} + 1.2E+10T^{-3}$
	$GFECEM\,(163 < T < 6000) = -10195.860754 + 690.949887637T - 118.47637T\,ln(T) - 0.0007T^2 + 590527T^{-1}$
fcc	${}^0G_{Fe:C}^{fcc} = {}^0G_{Fe}^{fcc} + {}^0G_C^{graphite} + 77207 - 15.877T$
	${}^0G_{Cr:C}^{fcc} = {}^0G_{Cr}^{fcc} + {}^0G_C^{graphite} + 1200 - 1.94T$
	${}^0G_C^{graphite}\,(298.15 < T < 6000) = -17368.441 + 170.73T - 24.3T\,ln(T) - 4.723$ $E-04T^2 + 2562600T^{-1} - 2.643E+08T^{-2} + 1.2E+10T^{-3}$
	$L_{Cr:Fe,C}^{fcc} = -69534 + 3.2353T$
	${}^0L_{Cr,Fe:va}^{fcc} = 10833 - 7.477T$
	${}^1L_{Cr,Fe:va}^{fcc} = 1410$
	$L_{Fe:C,va}^{fcc} = -34671$
	$L_{Cr:va,C}^{fcc} = -29686 - 18T$
	${}^0G_{Fe}^{fcc}\,(298.15 < T < 1811) = -1462.4 + 8.282T - 1.15T\ln(T) + 6.4E-04T^2 + {}^0G_{Fe}^{bcc\_A2}$
	${}^0G_{Cr}^{fcc}\,(298.15 < T < 6000) = {}^0G_{Cr}^{bcc\_A2} + 7284 + 0.163T$
	${}^0G_{Fe}^{bcc\_A2}\,(298.15 < T < 1811) = +1225.7 + 124.134T - 23.5143T\ln(T) - 0.00439752T^2 - 5.8927E-08T^3 + 77359T^{-1}$
	${}^0G_{Cr}^{bcc\_A2}\,(298.15 < T < 2180) = -8856.94 + 157.48T - 26.908T\ln T + 0.00189435T^2 - 1.47721E-06T^3 + 139250T^{-1}$

$$\varepsilon_{ij}^{el} = \varepsilon_{ij} - \varepsilon_{ij}^{0}. \tag{18}$$

The value of the eigenstrain, which should be calculated through Eq. 19, has been affected by the concentration field:

$$\varepsilon_{ij}^{0} = \varepsilon_0^i \delta_{ij}\left(c_i - c_i^0\right), \tag{19}$$

$$\varepsilon_0^{\mathrm{i}} = \frac{1}{\mathrm{a}}\left(\frac{\mathrm{da}}{\mathrm{dc_i}}\right). \tag{20}$$

ε_0^i represents the lattice expansion coefficient of the *Ith* element to the matrix element, as described by Eq. 20. The Kronecker delta function δ_{ij} equals 1 when $i = j$. In other cases, it equals 0. c_i^0 represents the initial concentration of the *Ith* element.

The total strain ε_{ij} is described by Eq. 21.

$$\varepsilon_{ij} = \frac{1}{2}\left\{\frac{\vartheta u_i}{\vartheta r_j} + \frac{\vartheta u_j}{\vartheta r_i}\right\}, \tag{21}$$

where u represents the displacement field. The parameter r is a vector that reflects the position of the lattice space.

Assuming there is a linear elastic relation between the *FCC* and $M_{23}C_6$ phases, both follow Hook's law. Then,the following equations are derived:

$$\sigma_{ij} = C_{ijkl}\varepsilon_{kl}^{el}, \tag{22}$$

$$f_{el} = \frac{1}{2}\int_V \sigma_{ij}\varepsilon_{ij}^{el}dv = \frac{1}{2}\int_V C_{ijkl}\varepsilon_{kl}^{el}\varepsilon_{ij}^{el}dv. \tag{23}$$

The elastic modulus of the matrix phase is different from that of the precipitated phase. The elastic modulus tensor C_{ijkl} described by Eq. 24 considered the uneven effect of elasticity. The tensor of the elastic modulus depend on the concentration as the Eq. 24 can be shown. So the coefficient of the elastic modulus tensor can be derived form the formula of the concentration field of it. ε_{ij}^{el} represents the elastic strain and is described in Eq. 25.

$$C_{ijkl}(c) = C_{ijkl}^{eff} + \alpha(c)\Delta C_{ijkl}. \tag{24}$$

In Eq. 24, $\alpha(c)$ is the linear function of c, $\alpha(c) = c - c_0$, and c_0 represents the initial concentration value. C_{ijkl}^{eff} represents the average elastic modulus tensor from the elastic modulus tensor of the *FCC* phase, C_{ijkl}^{fcc}, and the $M_{23}C_6$ phase $C_{ijkl}^{M_{23}C_6}$ (Gururajan and Abinandanan, 2007). ΔC_{ijkl} represents the elastic modulus difference and is described by the difference between the elastic modulus tensor of the *FCC* phase, C_{ijkl}^{fcc}, and the $M_{23}C_6$ phase $C_{ijkl}^{M_{23}C_6}$. The uniform elastic system appears when the difference equals 0:

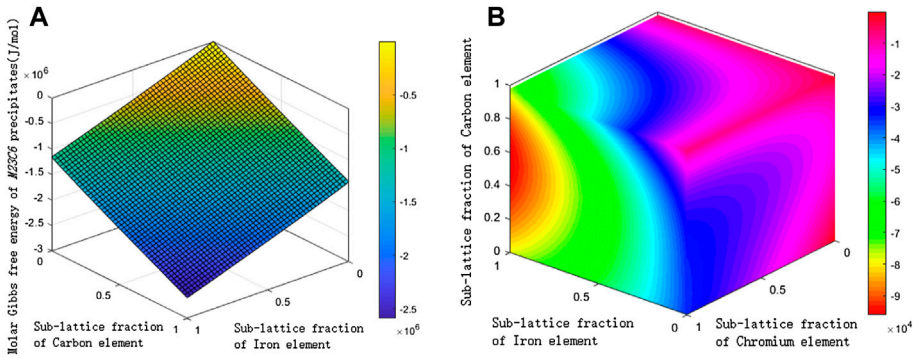

FIGURE 7
Distribution of free energy at 1,073 K. **(A)** $M_{23}C_6$ phase. **(B)** *FCC* matrix phase.

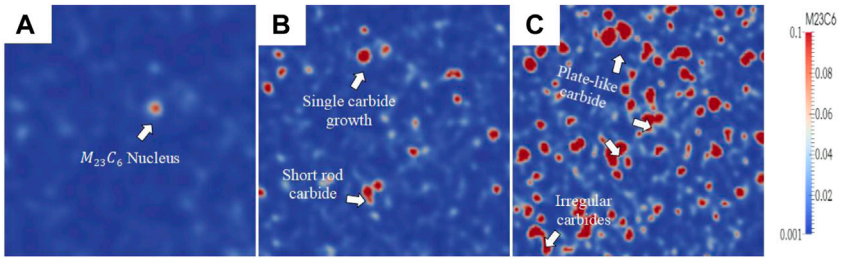

FIGURE 8
Evolution of carbide over time based on 1,123 K. **(A)** t* = 14. **(B)** t* = 15. **(C)** t* = 16.

$$\varepsilon_{ij}^{el} = \varepsilon_{ij}^{a} + \delta\varepsilon_{ij} - \varepsilon_{ij}^{0}. \tag{25}$$

In Eq. 25, ε_{ij}^{a} represents the applied strain and $\delta\varepsilon_{ij}$ represents the internal nonuniform strain. According to Eqs. 22, 24, 25 can evolve into Eq. 26.

$$\sigma_{ij} = \left[C_{ijkl}^{eff} + \alpha(c)\Delta C_{ijkl}\right]\left(\varepsilon_{ij}^{a} + \delta\varepsilon_{ij} - \varepsilon_{ij}^{0}\right). \tag{26}$$

4.5 Phase-field solution

In order to obtain the instantaneous state for the phase-field simulation of the microstructure, the dynamic equations in the phase-field model are solved. As the expression of free energy belongs to the nonlinear equation, the phase-field evolution is mostly to solve the complex nonlinear partial differential equation. At present, there are three methods for solving such complex partial differential equations: the Fourier spectrum method, the finite element method, and the finite difference method (Chen and Jie, 1998). These equations usually have no analytical solution, so an efficient solution has been used to improve the computational efficiency. The Fourier spectral algorithm could transform nonlinear partial differential equations into ordinary differential equations. The Fourier spectral algorithm has eliminated spatial dependence of field variables and realized the Fourier transform rapidly, so computational efficiency achieved improvement. By referring to the factor, the semi-implicit Fourier spectral algorithm has been applied to solving equations in the phase-field model.

Eqs. 27, 28 are obtained by deducing Eqs. 1, 2:

$$\frac{\partial\{c_i(r,t)\}_k}{\partial t} = -k^2\sum\nolimits_J M_{ij}\left\{\left\{\frac{\delta f_{local}}{\delta c_i(r,t)}\right\}_k + \left\{\frac{\delta f_{el}}{\delta c_i(r,t)}\right\}_k + k^2\kappa\{c_i(r,t)\}_k\right\} + \{\xi_{ci}(r,t)\}_k, \tag{27}$$

$$\frac{\partial\{\phi(r,t)\}_k}{\partial t} = -k^2\left\{\frac{\delta f_{local}}{\delta\phi(r,t)}\right\}_k - k^2\kappa L\{\phi(r,t)\}_k + \left\{\xi_\phi(r,t)\right\}_k. \tag{28}$$

In Eqs. 27, 28, $\{\cdot\}_k$ represents the Fourier transform. k represents the vector in the Fourier space, and k equals $\sqrt{k_x^2 + k_y^2}$ for the two-dimensional space. κ represents the gradient energy coefficient.

Eqs. 27, 28 are treated by the semi-implicit method, including implicit processing of linear and second-order items and display processing of other items. Eqs. 29, 30 result from this derivation:

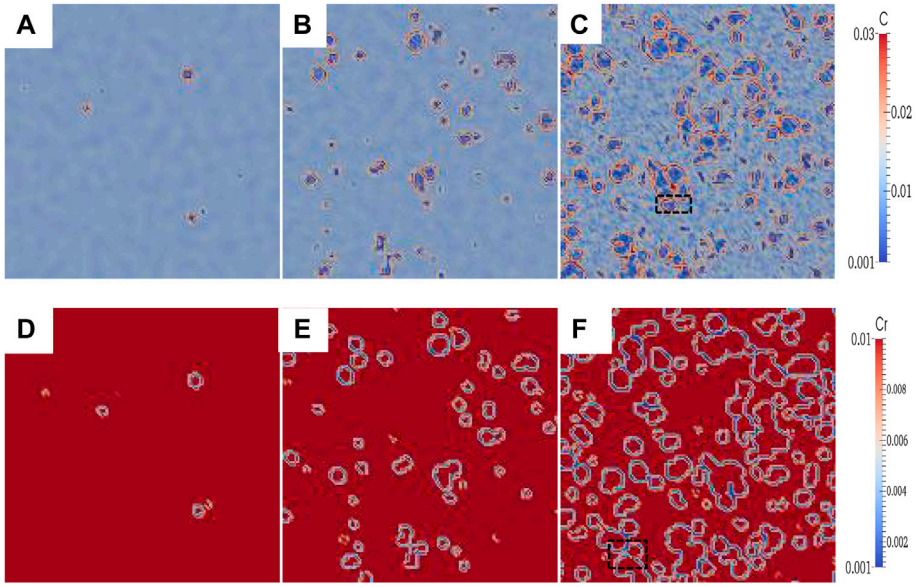

FIGURE 9
Evolution of the concentration field with time based on 1,123 K. **(A–C)** C concentration field; **(D–F)** Cr concentration field. Dimensionless time: (a, d) t* = 14; (b, e) t* = 15; (c, f) t* = 16.

$$\frac{\{c_i(r,t)\}_k^{n+1} - \{c_i(r,t)\}_k^n}{\Delta t} = -k^2 \sum_J M_{ij} \left\{ \left\{ \frac{\delta f_{local}}{\delta c_i(r,t)} \right\}_k^n + \left\{ \frac{\delta f_{el}}{\delta c_i(r,t)} \right\}_k^n + k^2 \kappa \{c_i(r,t)\}_k^{n+1} \right\} + \{\xi_{ci}(r,t)\}_k, \tag{29}$$

$$\frac{\{\phi(r,t)\}_k^{n+1} - \{\phi(r,t)\}_k^n}{\Delta t} = -k^2 \left\{ \left\{ \frac{\delta f_{local}}{\delta \phi(r,t)} \right\}_k^n \right\} - k^2 L \kappa \{\phi(r,t)\}_k^{n+1} + \left\{ \xi_\phi(r,t) \right\}_k, \tag{30}$$

where Δt represents the increment of time. In the calculation process, when the thermal fluctuations meet the Gaussian distribution, the random matrices can be randomly superimposed with the variables field, and the calculation process can be simplied. Eqs. 31, 32 have been derived. They simplify the problem of the C-H and A-C equations in the solution model to the concentration field and phase-field problems:

$$\{c_i(r,t)\}_k^{n+1} = \frac{\{c_i(r,t)\}_k^n - \Delta t k^2 \sum_j M_{ij} \left\{ \left\{ \frac{\delta f_{local}}{\delta c_i(r,t)} \right\}_k^n + \left\{ \frac{\delta f_{el}}{\delta c_i(r,t)} \right\}_k^n \right\}}{1 + \Delta t k^4 \{c_i(r,t)\}_k^{n+1}}, \tag{31}$$

$$\{\phi(r,t)\}_k^{n+1} = \frac{\{\phi(r,t)\}_k^n - \Delta t k^2 \left\{ \frac{\delta f_{local}}{\delta \phi(r,t)} \right\}_k^n}{1 + \Delta t k^2 \kappa L \{\phi(r,t)\}_k^{n+1}}. \tag{32}$$

Finally, the simulation results are saved in the VTK format, and the results are visualized to obtain the dynamic simulation of the phase transition process.

4.6 Simulation of the phase-field evolution of carbide growth

Red represents the precipitated carbide phase, and the matrix phase is represented by blue in Figure 8. Noise nucleation has been used in the simulation. When the dimensionless time equals 14, there are only a few $M_{23}C_6$ carbide cores in the *FCC* matrix, which indicates that the $M_{23}C_6$ phase begins to precipitate, and nucleation from the *FCC* phase, so the area fraction of the $M_{23}C_6$ phase is small. When the dimensionless time equals 15, the number of $M_{23}C_6$ carbide cores increases significantly and grows to form large round carbides or even two adjacent carbides, contacting to form rod carbides due to their own growth, as shown in Figure 8B. With the continuous precipitation and growth of carbides, the adjacent carbides would gradually approach until merging, and plate-like carbides and even irregular carbides would be formed, as shown in Figure 8C. It could analyze the formation mechanism of the $M_{23}C_6$ carbide from the simulation result for the mono-nuclear $M_{23}C_6$ carbide itself; carbide would grow. When two or more $M_{23}C_6$ carbide core phases contact each other, necking could occur. This argument has been verified in the following comparison with SEM images. When the two carbide phases contact each other, the total free energy of the system decreases, the contact surface

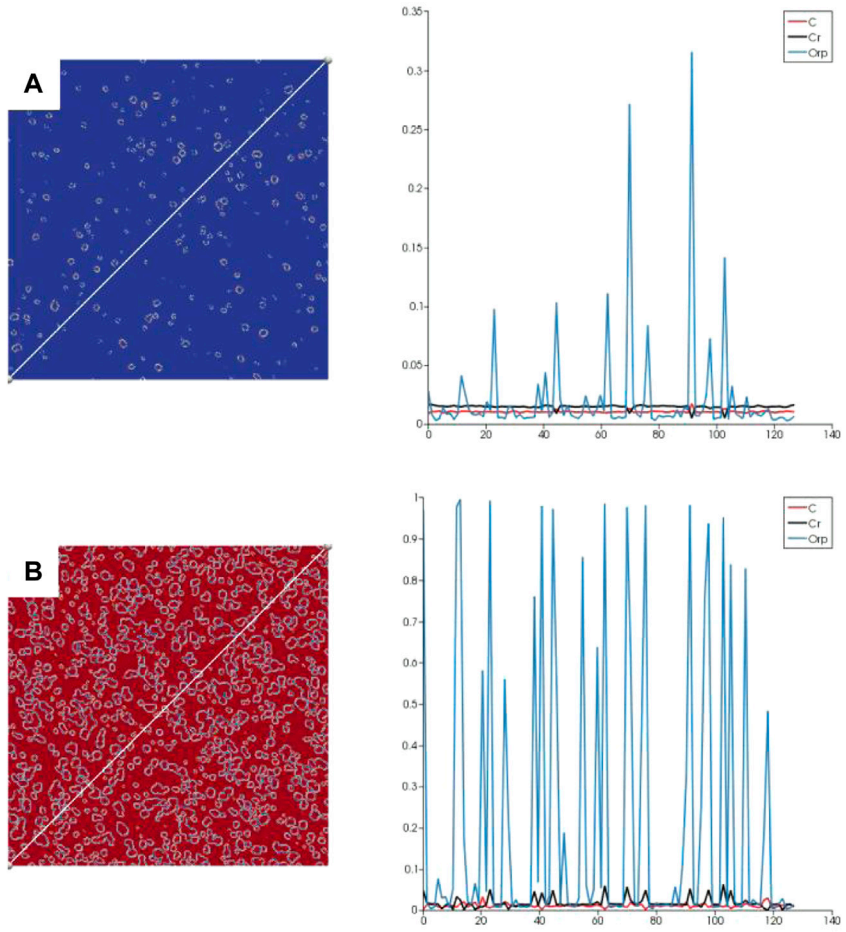

FIGURE 10
Concentration *versus* time curve along the concentration field diagonal. **(A)** Carbon concentration field. **(B)** Cr concentration field.

shrinks inward, and the specific surface area decreases, causing necking. With the continuous aging time, a series of irregular carbides could be formed.

4.7 Concentration field evolution

Figure 9 shows the change in the concentration field with time. The initial temperature equals 1,123 K, corresponding to the precipitation process of the $M_{23}C_6$ phase in Figure 8. It represents the change in the *C* concentration with time from Figures 9A–C and the change in the *Cr* concentration with time from Figures 9D–F. Dimensionless time is consistent with Figure 8. By comparing with Figure 8, it can be observed that the precipitated $M_{23}C_6$ carbides have a shell structure. Chromium is mainly concentrated in the inner layer, and the outer layer is mainly a carbon-rich area. In the process of carbide precipitation, the chemical composition in the matrix will also change accordingly. Iron, chromium, and carbon atoms could diffuse in different directions. Iron atoms could diffuse from carbide to matrix, whereas carbon and chromium atoms could diffuse from matrix to carbide (Wieczerzak et al., 2016). When multiple carbides in the matrix contact each other, there would be a carbon concentration enrichment zone and a chromium concentration depletion zone at the phase interface because carbon atoms tend to diffuse toward the interface, whereas chromium atoms diffuse in the opposite direction. Figure 10 shows the curve distribution of each phase along the diagonal of the concentration field. Orp represents M32C6 carbide phase.

5 Experimental and simulation comparison

5.1 SEM experimental study on $M_{23}C_6$ carbides

Figure 11A1 shows that many round carbides exist in the matrix for the neutral surface of the quenched part. By local amplification, it

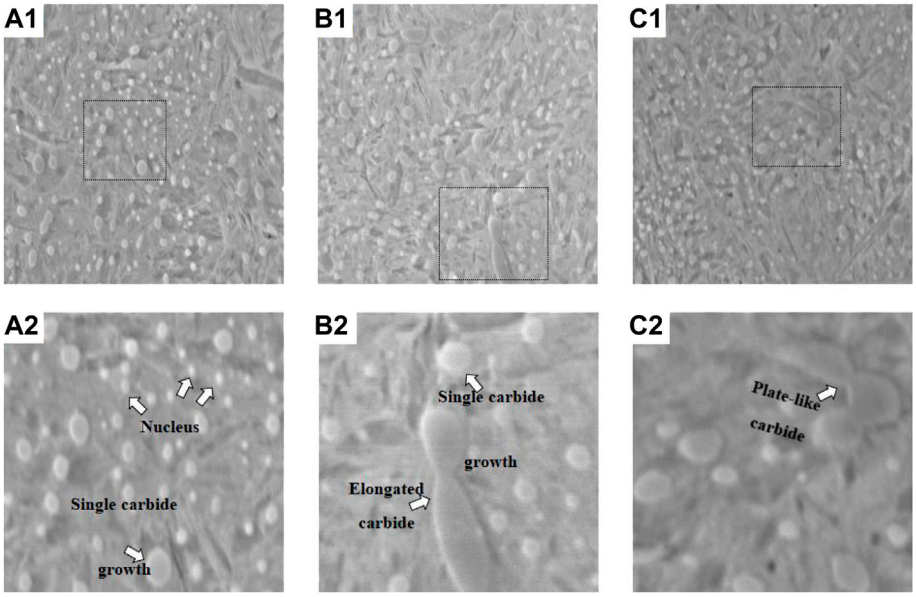

FIGURE 11
Microstructure of the GCr15 bearing outer ring quenched at different positions. **(A1)** Neutral surface of the quenched part. **(B1)** Outer surface of the quenched part. **(C1)** Inner surface of the quenched part. **(A2)** Local amplification of the neutral surface. **(B2)** Local amplification of the outer surface. **(C2)** Local amplification of the inner surface.

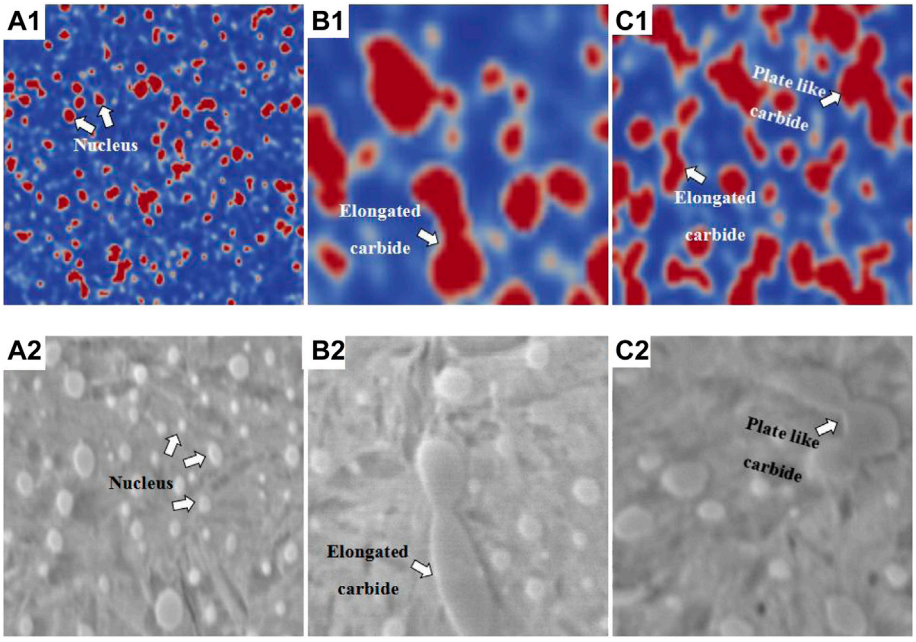

FIGURE 12
Comparison of phase-field simulation results with SEM experimental results.

could be observed that, in addition to several round carbides, there are some single coarse and short rod carbides. As a result, the $M_{23}C_6$ carbides are distributed uniformly, which is affected by the cooling rate during quenching. The heat transfer mode of the neutral surface is mainly heat conduction, without direct contact with the oil.

As shown in Figures 11B1,C1, in addition to the existence of round and short rod-like carbides, a small amount of elongated rod-like and a few irregular $M_{23}C_6$ carbides exist in the matrix for the outer and inner surfaces of the quenched part. By local amplification, it could be observed that necking occurred. The existence of a few irregular $M_{23}C_6$ carbides is due to direct contact with oil and a rapid cooling rate during quenching.

Figure 12A1 represents the phase-field simulation results of the $M_{23}C_6$ phase structure field. Figures 12B1,C1 represent the local amplification diagrams at different locations of the phase-field simulation results. The purpose is to clearly observe the $M_{23}C_6$ phases with different characteristics. Figures 12A2,B2,C2 represent the local magnification of the microstructure of the neutral, outer, and inner surfaces of the quenched part, respectively. Round, rod, plate-like, and elongated $M_{23}C_6$ carbides shown in the simulation results can be observed in the SEM results. The cooling rate could affect $M_{23}C_6$ carbide precipitation and growth, combined with experimental results. The mechanism of $M_{23}C_6$ carbide precipitation has already been verified. It indicates that the experimental results agree with the phase-field simulation results, proving the feasibility of the phase-field simulation method. Rapid cooling has accelerated the precipitation and growth of $M_{23}C_6$ carbides. The growth rate causes contact between adjacent carbides and eventually merges; rod, plate-like, elongated, and even a few nonuniform formal $M_{23}C_6$ carbides have been formed easily. Therefore, round-shaped $M_{23}C_6$ carbides have been precipitated and formed on the neutral surface of the quenched part because of the slow cooling rate, which has been caused by indirect contact with oil. However, $M_{23}C_6$ carbides show a variety of shapes in the outer and inner surfaces of the quenched part. Direct contact with oil brings more possibilities. How to control the cooling rate of quenching and contact area with oil to optimize $M_{23}C_6$ carbide precipitation and the growth state remains unexplored.

6 Conclusion

By compared the simulation results with the SEM results, we can judge the formation mechanism of carbide; for mono-nuclear carbide itself, carbide would grow. When two or more carbide core phases contact each other, necking could occur. This argument has been verified in comparison with SEM results. When the two carbide phases contact each other, the total free energy of the system decreases, the contact surface shrinks inward, and the specific surface area decreases, causing necking. With the continuous aging time, a series of irregular carbides could be formed.

The cooling rate in quenching could affect $M_{23}C_6$ carbide precipitation and growth, combined with experimental results. Rapid cooling has accelerated the precipitation and growth of $M_{23}C_6$ carbides, the growth rate causes contact between adjacent carbides, and eventually merges; rod, plate-like, elongated, and even a few nonuniform formal $M_{23}C_6$ carbides have been formed easily. How to control the cooling rate of quenching and contact area with oil to optimize $M_{23}C_6$ carbide precipitation and growth state remains unexplored.

It indicates that the experimental results agree with the phase-field simulation results, proving the feasibility of the phase-field simulation method used. Meanwhile, the difference between the parameters selected in the phase-field simulation and the true value may lead to errors in the analysis results. Further optimization of the phase-field model is the direction of future efforts.

Data availability statement

The original contributions presented in the study are included in the article/Supplementary Material; further inquiries can be directed to the corresponding author.

Author contributions

Conceptualization: MC and DJ. Methodology: QL and JJ. Software: MC and DJ. Validation: QL and JJ. Formal Analysis: JJ and QL. Experiment: QL. Investigation: MC and DJ. Resources: MC and DJ. Data curation: XD and JW. Supervision: MC and DJ. Writing—original draft preparation: JJ and QL. Writing—review and editing: QL and JJ. Project administration: DJ. All authors read and agreed to the published version of the manuscript.

Funding

This research was funded by the National Key Research and Development Project (2018YFE0207000).

Acknowledgments

The authors thank ChangZhou NRB Corporation in China and the High-Tech Research Center at the Saitama Institute of Technology in Japan for the related experiments.

Conflict of interest

The authors declare that the research was conducted in the absence of any commercial or financial relationships that could be construed as a potential conflict of interest.

Publisher's note

References

Andersson, J. O . (1988). A thermodynamic evaluation of the Fe-Cr-C system. *J.* 19 (3), 627–636. doi:10.1007/bf02649276

Andersson, J. O . (1987). Thermodynamic properties of Cr-C. *Calphad* 11, 271–276. doi:10.1016/0364-5916(87)90045-9

Cahn, J. W., and Hilliard, J. E. (1958). Free energy of a nonuniform system. I. Interfacial free energy. *J. Chem. Phys.* 28 (2), 258–267. doi:10.1063/1.1744102

Chen, L. Q., and Jie, S. (1998). Applications of semi-implicit Fourier-spectral method to phase field equations. *Comput. Phys. Commun.* 108 (2-3), 147–158. doi:10.1016/s0010-4655(97)00115-x

Ding, W (2019). *Study on the evolution of residual stress during continuous cooling and annealing process of high strength steel [D]*. China, Beijing: University of Science and Technology Beijing.

Du, G (2017). *Study on the control of carbides in bearing steel GCr15 based on electroslag remelting process [D]*. China, Beijing: University of Science and Technology Beijing.

Guo, Z (2021). *Study on precipitation mechanism of Ni—rich phase in Cu-Ni-Si-Mg alloy by phase field method [D]*. Taiyuan, China: North University of China.

Gururajan, M. P., and Abinandanan, T. A. (2007). Phase field study of precipitate rafting under a uniaxial stress. *Acta Mater.* 55 (15), 5015–5026. doi:10.1016/j.actamat.2007.05.021

Hu, S. Y., Murray, J., Weiland, H., Liu, Z., and Chen, L. (2007). Thermodynamic description and growth kinetics of stoichiometric precipitates in the phase-field approach. *Calphad* 31 (2), 303–312. doi:10.1016/j.calphad.2006.08.005

Jiang, X.-A., Zhao, Y.-H., Wen-Kui, Y., Xiao-Lin, T., and Hou, H. (2022). Mechanism of internal magnetic energy of Cu-rich phase precipitation in Fe84Cu15Mn1 alloy by phase field method [J]. *Acta Phys. Sinca* 71 (8), 080201. doi:10.7498/aps.71.20212087

Jokisaari, A. M ., and Thornton, K . (2015). General method for incorporating CALPHAD free energies of mixing into phase field models : Application to the α -zirconium/δ-hydride system. *Calphad* 51, 334–343. doi:10.1016/j.calphad.2015.10.011

Kamel, B., and Hafid, A. (2013). Elastic constants of austenitic stainless steel: Investigation by the first-principles calculations and the artificial neural network approach. *Comput. Mater. Sci.* 67 (1-2), 353–358. doi:10.1016/j.commatsci.2012.09.005

Khvan, A. V., Hallstedt, B., and Broeckmann, C. (2014). A thermodynamic evaluation of the Fe–Cr–C system. *Calphad* 46, 24–33. Pergamon Press. doi:10.1016/j.calphad.2014.01.002

Kitashima, T., Yokokawa, T., Yeh, A. C., and Harada, H. (2008). Analysis of element-content effects on equilibrium segregation at γ/γ′ interface in Ni-base superalloys using the cluster variation method. *Intermetallics* 16 (6), 779–784. doi:10.1016/j.intermet.2008.02.015

Koyama, T., Hashimoto, K., and Onodera, H. (2006). Phase-field simulation of phase transformation in Fe-Cu-Mn-Ni quaternary alloy. *Mat. Trans.* 47 (11), 2765–2772. doi:10.2320/matertrans.47.2765

Koyama, T., and Onodera, H. (2005). Computer simulation of phase decomposition in Fe–Cu–Mn–Ni quaternary alloy based on the phase-field method. *Mat. Trans.* 46 (6), 1187–1192. doi:10.2320/matertrans.46.1187

Kuang, W., Wang, H., Xin, L., Zhang, J., Zhou, Q., and Zhao, Y. (2018). Application of the thermodynamic extremal principle to diffusion-controlled phase transformations in Fe-C-X alloys: Modeling and applications. *Acta Mater.* 159, 16–30. doi:10.1016/j.actamat.2018.08.008

Kučera, J., and Stránský, K. (1982). Diffusion in iron, iron solid solutions and steels. *Mater. Sci. Eng.* 52 (1), 1–38. doi:10.1016/0025-5416(82)90067-2

Laing, P G., Ferguson, A B., Jr., and Hodge, Ph.D. E S. (1967). Tissue reaction in rabbit muscle exposed to metallic implants. *J. Biomed. Mat. Res.* 1 (1), 135–149. doi:10.1002/jbm.820010113

Lee, S. J., Matlock, D. K., and Tyne, C. J. V. (2011). An empirical model for carbon diffusion in austenite incorporating alloying element effects. *ISIJ Int.* 51 (11), 1903–1911. doi:10.2355/isijinternational.51.1903

Levchenko, E. V., Evteev, A. V., Belova, I. V., and Murch, G. (2009). Molecular dynamics simulation and theoretical analysis of carbon diffusion in cementite. *Acta Mater.* 57 (3), 846–853. doi:10.1016/j.actamat.2008.10.025

Li, F (2009). *Phase-field method research on microstructure of multicomponent alloys solidification [D]*. Lanzhou, China: Lanzhou University of Technology.

Liu, Q., Ju, D., Li, X., Ishikawa, K., Lv, R., Lian, W., et al. (2022). Verification of the non-axisymmetric deformation mechanism of bearing rings after quenched in a multi-field coupled simulation. *Coatings (Basel).* 12 (5), 676. doi:10.3390/coatings12050676

Liu, Y., Jiang, Y., Xing, J., Zhou, R., and Jing, F. (2015). Mechanical properties and electronic structures of M23C6 (M = Fe, Cr, Mn)-type multicomponent carbides. *J. Alloys Compd.* 648, 874–880. doi:10.1016/j.jallcom.2015.07.048

Loginova, I., Odqvist, J., Amberg, G., and Agren, J. (2003). The phase-field approach and solute drag modeling of the transition to massive γ → α transformation in binary Fe-C alloys. *Acta Mater.* 51 (5), 1327–1339. doi:10.1016/s1359-6454(02)00527-x

Saunders, N., and Miodownik, A. P. (1992). *Calphad (calculation of phase diagrams) A comprehensive guide[J]*. pergamon: Elsevier.

Song, W, Choi, P-P, Inden, G, Prahl, U, Raabe, D, and Bleck, W (2014). On the spheroidized carbide dissolution and elemental partitioning in high carbon bearing steel 100Cr6. *Metall. Mat. Trans. A* 45, 595–606. doi:10.1007/s11661-013-2048-5

Sun., Y. (2020). *Effects of elastic field and microelements on the precipitation of Cu-rich phase in Fe-Cu-Mn-Ni-A1 quinary alloy: A phase-field study [D]*. Taiyuan, China: North University of China.

Tian, X., Zhao, Y., Gu, T., Guo, Y., Xu, F., and Hou, H. (2022). Cooperative effect of strength and ductility processed by thermomechanical treatment for Cu–Al–Ni alloy. *Mater. Sci. Eng. A* 849, 143485. doi:10.1016/j.msea.2022.143485

Wheeler, A. A., Boettinger, W. J., and Mcfadden, G. B. (1992). Phase-field model for isothermal phase transitions in binary alloys. *Phys. Rev. A . Coll. Park.* 45 (10), 7424–7439. doi:10.1103/physreva.45.7424

Wieczerzak, K., Bala, P., Dziurka, R., Tokarski, T., Cios, G., Koziel, T., et al. (2016). The effect of temperature on the evolution of eutectic carbides and M 7 C 3 → M 23 C 6 carbides reaction in the rapidly solidified Fe-Cr-C alloy. *J. Alloys Compd.* 698, 673–684. doi:10.1016/j.jallcom.2016.12.252

Wu, M. (2021). *Hot deformation behavior, microstructure and property of super duplex stainless steel S32750 [D]*. Taiyuan, China: Taiyuan University of Technology.

Xin, T., Zhao, Y., Mahjoub, R., Jiang, J., Yadav, A., Nomoto, K., et al. (2021). Ultrahigh specific strength in a magnesium alloy strengthened by spinodal decomposition. *Sci. Adv.* 7 (23), eabf3039. doi:10.1126/sciadv.abf3039

Zhang, J. B., Wang, H. F., Kuang, W. W., Zhang, Y. H., Li, S., Zhao, Y. H., et al. (2018). Rapid solidification of non-stoichiometric intermetallic compounds: Modeling and experimental verification. *Acta Mater.* 148, 86–99. doi:10.1016/j.actamat.2018.01.040

Zhao, Y., Liu, K., Hou, H., and Chen, L-Q. (2022). Role of interfacial energy anisotropy in dendrite orientation in Al-Zn alloys: A phase field study. *Mater. Des.* 216, 110555. doi:10.1016/j.matdes.2022.110555

Zhao, Y. (2022). Stability of phase boundary between L12-Ni3Al phases: A phase field study. *Intermetallics* 144, 107528. doi:10.1016/j.intermet.2022.107528

Zhao, Y., Sun, Y., and Hou, H. (2022). Core-shell structure nanoprecipitates in Fe-xCu-3.0Mn-1.5Ni-1.5Al alloys: A phase field study. *Prog. Nat. Sci. Mater. Int.* 32 (3), 358–368. doi:10.1016/j.pnsc.2022.04.001

Zhao, Y., Zhang, B., Hou, H., Chen, W., and Wang, M. (2019). Phase-field simulation for the evolution of solid/liquid interface front in directional solidification process. *J. Mater. Sci. Technol.* 35 (6), 1044–1052. doi:10.1016/j.jmst.2018.12.009

Zhao-kun, L., Jian-zhong, L., Xu, H., Yu, F., Dong, H., and Wen-quan, C. (2016). Current status and development trend of bearing steel in China and abroad [J]. *J. Iron Steel Res.* 28 (3), 1–12. doi:10.13228/j.boyuan.issn1001-0963.20150345

Zhu, J. Z., Wang, T., Ardell, A. J., Zhou, S., Liu, Z., and Chen, L. (2004). Three-dimensional phase-field simulations of coarsening kinetics of γ′ particles in binary Ni–Al alloys. *Acta Mater.* 52 (9), 2837–2845. doi:10.1016/j.actamat.2004.02.032

Zhu, N. Q., He, Y. L., Liu, W. Q., L, L., Huang, S. G., Vleugels, J., et al. (2011). Modeling of nucleation and growth of $M_{23}C_6$ carbide in multi-component Fe-based alloy. *J. Mater. Sci. Technol.* 27 (8), 725–728. doi:10.1016/s1005-0302(11)60133-3

Zong, N., Huang, J., Liu, J., Lu, Z., and Jing, T. (2020). Present situation and prospect of Key metallurgical technologies for improving quality of bearing steel [J]. *Bearing* (12), 60–66. doi:10.19533/j.issn1000-3762.2020.12.013

Zou, W. (2021). Surface defect analysis of GCr15 bearing steel parts [J]. *Fujian Metall.* 50 (4), 37–40. doi:10.3969/j.issn.1672-7665.2021.04.010

frontiers | Frontiers in Materials

TYPE Original Research
PUBLISHED 06 December 2022
DOI 10.3389/fmats.2022.1043249

OPEN ACCESS

EDITED BY
Benjamin Klusemann,
Leuphana University Lüneburg,
Germany

REVIEWED BY
Seshadev Sahoo,
Siksha O Anusandhan University, India
Lijun Zhang,
Central South University, China

*CORRESPONDENCE
Qiang Du,
qiang.du@sintef.no
Renhai Shi,
renhai.shi.nick@gmail.com

SPECIALTY SECTION
This article was submitted to Computational Materials Science, a section of the journal Frontiers in Materials

RECEIVED 13 September 2022
ACCEPTED 28 November 2022
PUBLISHED 06 December 2022

CITATION
Chen M, Du Q, Shi R, Fu H, Liu Z and Xie J (2022), Phase field simulation of microstructure evolution and process optimization during homogenization of additively manufactured Inconel 718 alloy.
Front. Mater. 9:1043249.
doi: 10.3389/fmats.2022.1043249

Phase field simulation of microstructure evolution and process optimization during homogenization of additively manufactured Inconel 718 alloy

Miaomiao Chen[1], Qiang Du[2]*, Renhai Shi[1]*, Huadong Fu[1,3,4], Zhuangzhuang Liu[1] and Jianxin Xie[1,3,4]

[1]Beijing Advanced Innovation Center for Materials Genome Engineering, University of Science and Technology Beijing, Beijing, China, [2]SINTEF Industry, Oslo, Norway, [3]Key Laboratory for Advanced Materials Processing (MOE), Institute for Advanced Materials and Technology, University of Science and Technology Beijing, Beijing, China, [4]Beijing Laboratory of Metallic Materials and Processing for Modern Transportation, Institute for Advanced Materials and Technology, University of Science and Technology Beijing, Beijing, China

An in-depth and integral understanding of the microstructural evolution during thermomechanical process (TMP) is of great significance to optimize the manufactural process for high-quality components *via* additive manufacturing. The solidified microstructure model of Inconel 718 alloy fabricated *via* laser powder bed fusion (L-PBF) is established by multiphase field model firstly. Furthermore, the microstructural evolution during homogenization process is simulated and optimized in this study. Phase field simulation results show that the concentration gradient of Nb along the radius of the cellular substructure decreases from the initial 1.217 wt% to 0.001 wt%, and 67% area fraction of the Laves phase dissolves at the homogenization time of 0.5 h, which have achieved the homogenization purpose. The experimental results show that the average grain size decreases from 9.4 μm to 5.9 μm at the homogenization time from 1.5 h (the standard AMS 5383) to 0.5 h, which resulted in the increase of yield strength and tensile strength of the aged alloy by 14% and 6%, respectively. This research can provide guidance and reference for the microstructural control as well as the TMP parameters design of the additive manufactured alloys.

KEYWORDS

phase field, Inconel 718, laser powder bed fusion, laves phase, mechanical properties

1 Introduction

Inconel 718 alloy is a typical precipitation strengthened nickel-base superalloy with excellent strength, high fatigue resistance, and desirable structural stability at higher temperature. The alloy has been widely applied in gas turbine, ship, nuclear power plant, and aerospace sectors to make turbine disk, blade, support, pipeline, brake, seal, fastener (Reed,

2006; De Bartolomeis et al., 2021). However, it is still a challenge to machine and manufacture Inconel 718 alloy parts with complex geometry due to higher cutting temperature and serious work hardening (Paturi et al., 2021). Focusing on the above problem, Laser Powder Bed Fusion (L-PBF), an attractive laser additive manufacturing technology, has been applied successfully in improving mechanical properties and broadening the application of Inconel 718 components (Trosch et al., 2016; Hosseini and Popovich, 2019). Nevertheless, there are some problems in as-built Inconel 718 parts fabricated *via* L-PBF, such as large residual stress, solute segregation, and the precipitation of Laves phase ($(Ni, Fe, Cr)_2(Nb, Mo, Ti)$). The formation of long-chain Laves phase not only consumes the elements (Nb, Ti, Al) required for the formation of γ' (Ni3(Al, Ti, Nb)) and γ'' (Ni3Nb) strengthening phases but also promotes initiation and propagation of cracks (Sui et al., 2017; Yuan et al., 2018; Luu et al., 2022). Another issue is that there is no special heat treatment developed for AM-ed Inconel 718 alloy. So far, the heat treatments applied to Inconel 718 alloy fabricated by L-PBF are based on the standard heat treatments proposed for casting and forging alloys (Rao et al., 2003; Blackwell, 2005; Zhao et al., 2008; Zhang et al., 2015).

Microstructure modeling, an essential part of integrated computational materials engineering (ICME) approach, has proven to be useful in accelerating material design and heat treatment process parameter optimization (Sahoo and Chou, 2014; Du et al., 2017; Nandy et al., 2019; Chen et al., 2022; Chen and Zhao, 2022; Dai et al., 2022). Among various microstructure simulation methods, phase field method (PFM) has become one of the most commonly used computational modeling techniques for studying microstructure evolution and an important component in the ICME approach to materials design. PFM has been coupled with temperature field (Sahoo and Chou, 2016; Sahoo, 2022) and solute field to realize scale-crossing simulation (Kumara et al., 2020; Nabavizadeh et al., 2020) and the description of actual engineering process to guide material design and processing parameters optimization (Hu et al., 2019; Seiz and Nestler, 2021; Zeng et al., 2021). Some PFM simulation studies have been carried out on L-PBF Inconel 718 alloy. For example, the finite element thermal model was employed to calculate the cooling rate and temperature gradient by Wang and Chou. (2018). The results were applied as input parameters for the phase-field model to investigate the evolution of microstructures. The simulated columnar dendrite arm spacing is consistent with the experimental results. Xiao et al. (2019) also combined the finite element model with the PFM to establish a multi-scale model to analyze the solidification behavior and dendrite growth during the direct energy deposition process of Inconel 718 alloy. The predicted results of columnar dendrite morphology and dendrite arm spacing provided a good fit to experimental results. Kumara et al. (2019); Kumara et al. (2020) proposed to simulate Laves phase and δ phase of Inconel 718 alloy during laser direct energy deposition and subsequent heat treatment *via* a phase-field model, but the accurate prediction of secondary phases was not realized.

In summary, PFM has been well applied in the simulation of microstructure in additive manufacturing. But it only focuses on microstructure morphology of dendrite and secondary phases, and does not simulate the evolution of microstructure characteristics in the subsequent heat treatment (Wang and Chou, 2018; Kumara et al., 2019; Kumara et al., 2020; Cao et al., 2021; Zhao et al., 2021). The microstructure in solidification and subsequent heat treatment jointly determines the performance of Inconel 718 samples fabricated by the L-PBF. In this paper, the solidification and subsequent heat treatment are connected to optimize the process and explore the feasibility of the whole process organization simulation. The solidified microstructure model of Inconel 718 alloy fabricated *via* L-PBF is established by multiphase field model. Then, based on the solidified microstructure model and HSA standard heat treatment (AMS 5383) proposed for casting Inconel 718, the microstructure evolution of Inconel 718 fabricated by the L-PBF during homogenization is simulated by the multiphase-field method coupled with CALPHAD data. Together with experimental research, the effects of homogenization time on microstructure evolution and mechanical properties of Inconel 718 samples with HSA heat treatment are analyzed. It lays a foundation for the formulation of a heat treatment recipe suitable for Inconel 718 alloy fabricated *via* L-PBF. The research strategy in this paper is illustrated in Figure 1. This research can provide guidance and reference for the microstructural control as well as the TMP parameters design of the additive manufactured alloys.

2 Phase field modeling

2.1 Multiphase-field model

Phase field method is a microstructure-level simulation technique often used in the ICME approach to materials design. The multiphase-field model, as implemented in the commercial phase field software MICRESS (Access e.V. Aachen, Germany) (Steinbach et al., 1996; Eiken et al., 2006; Steinbach, 2009), is adopted in this paper. The evolution of multiphase field variables ϕ_α in time and space is described in the multi-phase model. Within the interface thickness (η) between phase α and another phase, the value of ϕ_α varies from 0 to one continuously. A free energy model is applied as an part of the density functional *F*, which is a function of phase fields $\{\phi_\alpha\}$ and composition fields $\{\vec{c}_\alpha\}$ over the domain Ω and divided into the interface energy density f^{intf} and the chemical free energy density f^{chem} (Eiken et al., 2006), i.e.,

$$F\left(\{\phi_\alpha\},\{\vec{c}_\alpha\}\right) = \int_\Omega f^{intf}\{\phi_\alpha\} + f^{chem}\left(\{\phi_\alpha\},\{\vec{c}_\alpha\}\right) \quad (1)$$

The bracket { } denotes all phases, $\vec{c}_\alpha$ is the concentration field variable. The specific formula of each parameter has been given

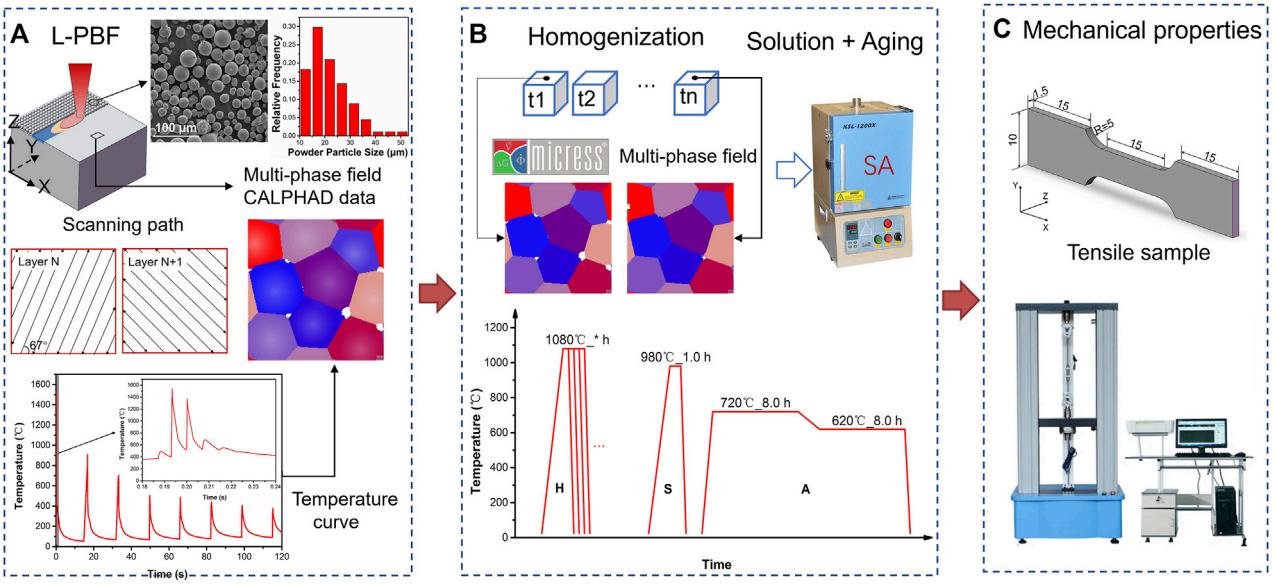

FIGURE 1
The research strategy of the L-PBF and subsequent homogenization heat treatment of Inconel 718 alloy, **(A)** phase-field modeling of the microstructure of as-built samples, **(B)** phase-field modeling under different homogenization time, and parameters of subsequent solution and double aging process, **(C)** mechanical properties.

in the literature (Eiken et al., 2006). According to the thin interface theory (Karma, 2001), the interface width is smaller than the scale of the microstructure, but larger than the distance between atoms. Furthermore, the minimum interface thickness should be set twice the cell size in the multiphase-field model.

In addition, molar Gibbs free energy densities are employed to evaluate the chemical contribution combined with CALculation of PHase Diagram (CALPHAD) databases. With the assumption of all interface widths being the same, the multi-phase field equations are derived for general multi-phase transformations according to the principle of minimizing free energy (Eiken et al., 2006).

$$\dot{\phi}_\alpha = \sum_{\beta=1}^{\tilde{\nu}} \frac{M_{\alpha\beta}}{\tilde{\nu}} \left(\sum_{\gamma=1}^{\tilde{\nu}} \left(\sigma_{\beta\gamma} - \sigma_{\alpha\gamma} \right) K + \frac{\pi^2}{8\eta} \Delta G_{\alpha\beta} \right) \tag{2}$$

Here, $\tilde{\nu}$ is the number of phases. $M_{\alpha\beta}$ is the interface mobility of the α/β. $\sigma_{\beta\gamma}$ and $\sigma_{\alpha\gamma}$ are the interface energy of the β/γ interface and α/γ interface respectively. K is the generalized curvature term. $\Delta G_{\alpha\beta}$ is the thermodynamic driving force, which could be obtained from CALPHAD database.

In the model, the interfacial energy σ_0 and the mobility M_0 are adjusted to be anisotropic as $\sigma(\theta)$, $M(\theta)$ respectively. θ is the angle between the crystal orientation and the growth direction (Böttger et al., 2006). For a simple 2D cubic symmetry, $\sigma(\theta) = \sigma_0(1 - cos(4\theta))$ and $M(\theta) = M_0(1 - cos(4\theta))$. In addition, some nucleation models have been employed in MICRESS (Steinbach, 2009), e.g., seed undercooling model and seed density model. Thus, the secondary phases with different shapes or crystal symmetry could be predicted by MICRESS software. For a multicomponent system, the multi-component diffusion equations considered the constraint of quasi-equilibrium, as shown in Eq. 3 (Eiken et al., 2006).

$$\dot{\vec{c}} = \nabla \sum_{\alpha=1}^{\tilde{\nu}} \phi_\alpha \mathbf{D}_\alpha \nabla \vec{c}_\alpha \tag{3}$$

Here $\mathbf{D}_\alpha$ is the diffusion matrix, which can be obtained from the CALPHAD database. For a given composition and phase state, the compositions $\vec{c}_\alpha$ can be calculated from the Gibbs energies by the quasi-equilibrium. In addition, the model is combined with the CALPHAD database, and some physical parameters, such as $\Delta G_{\alpha\beta}$, $\mathbf{D}_\alpha$, $\vec{c}_\alpha$, $M_{\alpha\beta}$, and molar volume fraction of phases, are calculated by CALPHAD method. Therefore, the phase field and solute field of multi-phases and multi-components could be calculated by coupling CALPHAD database. The coupled method has been successfully employed to investigate the microstructure evolution of multi-components alloy in the sub-rapid solidification process, additive manufacturing process, and heat treatment process (Boussinot et al., 2019; Kumara et al., 2019; Park et al., 2020a; Park et al., 2020b; Kumara et al., 2020; Rahul et al., 2020; Du et al., 2022).

2.2 Model parameters

The thermodynamic and kinetic data, such as $\Delta G_{\alpha\beta}$, $\mathbf{D}_\alpha$, $\vec{c}_\alpha$, $M_{\alpha\beta}$, and molar volume fraction of phases, are obtained from

TABLE 1 Simplified composition of Inconel 718 alloy in multiphase-field model.

Element	Ni	Cr	Fe	Mo	Nb	Ti	Al
Content (wt%)	54.7	19.0	16.7	3.2	5.0	1.0	0.5

TCNI9 and MOBNI5 databases provided by Thermo-Calc software. In the two-dimensional phase-field calculation domain, the solidification conditions during laser powder bed fusion are set as the temperature curve (Luo and Zhao, 2019) shown in Figure 1A to obtain the microstructure characteristics of Inconel 718 samples fabricated *via* L-PBF. The periodic boundary condition is employed in all borders. The focus of this model is to reproduce the evolution of Laves phase distributed at cellular substructure. Therefore, the following assumptions are adopted in phase field model. 1) In the computational domain, a temperature curve under the L-PBF solidification conditions is applied to control the evolution of temperature. 2) The effect of temperature gradient, fluid flow and material shrinkage on cellular structure is ignored. 3) The evolutions of size of cellular structure and NbC phase are ignored in the calculation.

According to the preliminary experimental results, the secondary phases of the as-built samples are a large amount of white Laves and a small amount of bright white NbC phase. On the basis of the standard heat treatment of AMS5383 for casting Inconel 718, the homogenized temperature is determined as 1,080°C. Therefore, the NbC phase with a dissolution temperature of 1,265°C will not be dissolved in the homogenization process. In addition, the area fraction of the NbC phase is lower. Therefore, we mainly take the Laves phase as the research target phase and analyze its evolution during the homogenization process. According to the element content and the main constituent elements of the Laves phase, the chemical composition of Inconel 718 is simplified for simulation, as shown in Table 1.

In L-PBF process, the powders are melted through the laser beam and then solidified into components. Taking the cellular structure of the XY plane (perpendicular to the building direction Z), as shown in Figure 1A, as the simulation domain, the evolution of Laves phase and solute distribution during L-PBF process of Inconel 718 alloy are simulated. Five SEM images along the scanning track, are analyzed to obtain the cellular substructure size and its number density. The average diameter of the cellular substructure is 0.8 μm and the number density is about 2.18/μm^2. Therefore, nine nucleation seeds of γ phase are placed in simulation domain with the size of 2 μm × 2 μm, and the grid size is set to 0.01 μm. Laves phase nucleates in the undercooling model at the interface of liquid/γ, which is set as an anisotropic interface with the cubic crystal structure. All boundaries are set as periodic boundary conditions. The

TABLE 2 Parameters in multiphase-field model.

Parameters	Value
Grain size Δx (μm)	0.01
Interface width (μm)	3.5 Δx
Interfacial energy—liquid/γ (J/cm2)	1.2E-5
Interfacial energy—liquid/Laves (J/cm2)	6E-6
Interfacial energy—γ/Laves (J/cm2)	5E-6
Kinetic coefficient—liquid/γ (cm4/Js)	0.025
Kinetic coefficient—liquid/Laves (cm4/Js)	1.0
Kinetic coefficient—γ/Laves (cm4/Js)	2.5E-11
The average factor of the driving force	0.3
Minimum phase fraction	5E-5

numerical parameters such as interface thickness, minimum phase fraction, and average factor of driving force are adjusted to correct the effect of non-equilibrium solute trapping. The appropriate values are determined based on whether the solidification is completed and the distribution law of the discrete distribution of the laves phase along with the substructure as the evaluation criteria. The calculated the microstructure results of -Inconel 718 samples fabricated *via* L-PBF are extracted as initial parameters for the simulation of microstructure evolution in the homogenization process. The parameters adopted in reference (Kumara et al., 2019) and the final simulation parameters of this study are shown in Table 2.

3 Experiment

3.1 L-PBF process and homogenization

The spherical powders of Inconel 718 with the size range of 15–53 μm are prepared by gas atomization technology as shown in Figure 1A, and their chemical compositions are listed in Table 3. The powders are dried at 100°C for 8 h and then deposited on a 304 L stainless steel substrate with a size of 250 mm × 250 mm for L-PBF. As-built Inconel 718 samples are fabricated on a BLT A300 equipped with a maximum 500 W fiber laser with a Gaussian intensity distribution and spot size (1/e2) of 76 μm. The process is carried out under a flow of ultra-high purity Ar gas (99.999%) to reduce the oxygen content below 200 ppm. The parameters applied in our work are the results of AM equipment manufacturer's recommendation and our own lab practices for Inconel 718 alloy. The zigzag scan is selected, the scanning path as shown in Figure 1A. The other parameters are as follows, laser power of 275 W, scanning speed of 960 mm/s, the powder layer thickness of 40 μm, scanning spacing of 100 μm.

The heat treatment experiments are carried out with a muffle furnace (KSL-1200X). According to the HSA standard heat

TABLE 3 Nominal chemical composition of the gas atomized Inconel 718 powder.

Element	Ni	Cr	Fe	Mo	Nb	Ti	Al	Co.	Si	Cu	Mn	C
Content (wt%)	54.66	18.98	Bal	3.15	5.0	0.98	0.48	0.12	0.07	0.034	0.027	0.024

treatment, i.e., homogenization treatment at 1,080°C for 1.5 h/AC, solution treatment at 980°C for 1 h/AC and then double aging at 720°C for 8 h/FC at 50°C/h to 620°C for 8 h, AC, proposed for casting Inconel 718, the homogenization temperature is set at 1,080°C. The microstructure evolution with different holding times (0.5 h–4.0 h) is analyzed. The subsequent heat treatments (Solution treatment at 980°C for 1 h/AC and then double Aging at 720°C for 8 h/FC at 50°C/h to 620°C for 8 h, AC) of HSA heat treatment (AMS 5383) are carried out to investigate the effect of homogenization time on microstructure and mechanical properties of Inconel 718 samples fabricated *via* L-PBF.

3.2 Microstructural observation and properties

To reveal the microstructure of XY planes, the polished samples are etched for 20 s using Kalling's reagent (HCl (100 ml) +CuCl2 (5 g) + C2H5OH (100 ml)). A ZEISS Gemini SEM 500 scanning electron microscope (SEM) and a Mira 3 LMH SEM equipped with electron backscatter diffraction (EBSD) from Oxford Instrument are employed to examine the microstructure. The area fractions of Laves phase and NbC phase are measured by ImageJ according to the different grayscale values of the phases from fifteen SEM - SE (secondary electron) images. To resolve the secondary phase boundaries, SEM images of etched samples are employed for area fraction measurement. The contrast and brightness of all pictures are adjusted to ensure that the gray values of the matrix phases in the pictures are consistent. ImageJ software is used to get area fractions of Laves phase and NbC phase from the different grayscale values of the phases.

The grain morphology, size, orientation of the samples, and polar diagrams are obtained by channel 5 software. Electron Probe Micro Analysis (EPMA) (JXA-8230) is used to analyze the solutes segregation in the cellular substructure of finely polished samples. Three rectangular regions with a size of 4 × 8 points are randomly selected in the cellular substructure of samples, and the point spacing is set to about 0.1 μm. A Titan ETEM G2 transmission electron microscope (TEM) is applied to investigate the solute distribution and precipitation particles distribution of deposited and HSA heat treatment samples, prepared by double jet technology. TEM samples etched in 90% C2H5OH+10% HClO4 solution at −25°C and 20 V using a dual jet system.

The size of tensile samples at room temperature is shown in Figure 1C, with a thickness of 1.5 mm. According to the standard of GB/T2281-2010, mechanical properties are measured by a CTM2500 microcomputer controlled electronic universal testing machine equipped with an extensometer.

4 Results and discussion

4.1 Microstructure of as-built inconel 718 samples fabricated *via* L-PBF

Figures 2A, B shows EBSD images of the microstructure on XZ plane, parallel to building direction Z, and XY plane, perpendicular to building direction Z, of as-built Inconel 718 sample with columnar dendritic morphology. During the laser scanning in L-PBF process, the partially remelting of the solidified part of the lower layer leads to the epitaxial growth to form columnar dendritic morphology. The microstructure shows stronger texture on the (Zhang et al., 2019) crystallographic plane than that on XY plane. Strip-shaped grains are arranged in parallel across the width of the melt channel, and there are some fine grains at the edge of the scanning track. In order to analyze the distribution of solutes along the center to the edge of substructures, the XY plane has be chosen to show the entire surface of substructures. Along the substructure from center to edge, the XY plane should be choice to display the whole surface of the substructure. Therefore, the microstructure characteristics and solute distribution behavior on XY plane of the Inconel 718 samples in the L-PBF process are analyzed in the current work.

The high cooling rate and cyclic temperature profile are the main reasons for the formation of columnar grains, which exhibit as cellular substructures in the range of 0.5–1.5 μm on the XY plane of Inconel 718 alloy fabricated by L-PBF, as shown in Figure 2C. The main secondary phase of as-built Inconel 718 is the fine white Laves phase and a little amount of bright NbC phase, according to Figure 2D–F. The results indicate that the dispersed Laves phase and NbC phase are mainly distributed on cellular substructure boundaries. The area fractions of Laves phase and NbC phase are 2.24% ± 0.25, and 0.23% ± 0.06, respectively. During the L-PBF process, the molten metal is solidified after laser scanning, and solutes at the solid/liquid (S/L) interface are redistributed. With the movement of the S/L interface, solutes (Nb, Mo, Ti, Al) are accumulated at the front of the interface, and most of the solutes are partitioned to the

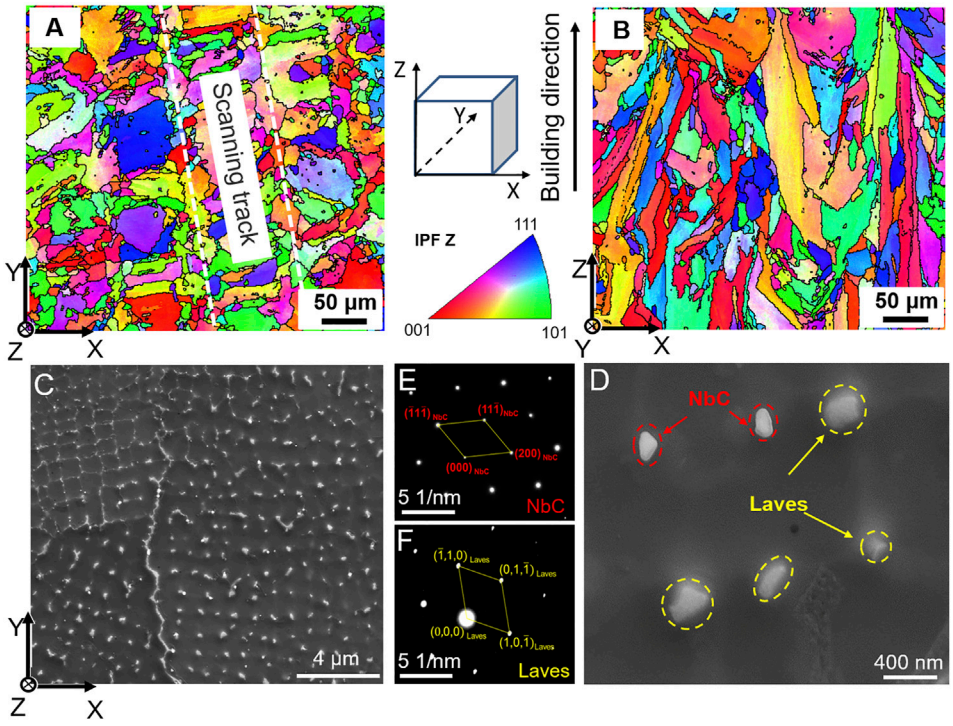

FIGURE 2
EBSD maps of as-built Inconel 718 samples, **(A)** IPF Z color mappings on XY plane, **(B)** IPF Z color mappings on XZ plane, SEM images on XY plane, **(C)** lower magnification, **(D)** higher magnification, **(E,F)** electron diffractions of Laves phase and NbC phase.

residual liquid phase. Due to insufficient back diffusion, significant solute segregation was observed in the solid. The solutes remaining in the residual liquid diffuse and enrich between the dendrites. Therefore, NbC phase with higher melting points and Laves phase with lower melting points are precipitated from the residual liquid phase, which consumes a large number of the Nb elements required by the formation of γ′ and γ″ strengthening phases. The amount of strengthening phases precipitated in aging is reduced, which is unfavorable to the mechanical properties. The microstructure evolution of solute distribution and secondary phase (Laves) of Inconel 718 alloy during L-PBF process and homogenization are analyzed.

4.2 Solidified microstructure model established by phase field

The several cellular substructures of as-built Inconel 718 fabricated *via* the L-PBF are simulated to describe its characteristics in the MICRESS software with the multiphase-field model. The solute trapping and secondary phases in the L-PBF solidification microstructure are analyzed. The simulation results of cellular substructure and Laves phase distribution on XY plane are shown in Table 4; Figure 3A. The white Laves phases are distributed on the boundary of cellular substructure, and its area fraction is about 2.19%, which is much coincided with the experimental measurement results (area fraction of 2.24% ± 0.25). Figure 3B shows that, in the as-built Inconel 718 sample, the solutes with equilibrium partition coefficients (obtain from Thermo-Calc) less than 1, such as Mo, Nb, Ti, and Al, are segregated between cellular substructures, and the segregation of Nb is the most significant. The solutes with equilibrium partition coefficient greater than 1, such as Cr and Fe, are segregated in cellular substructures. The SEM-EDS maps of solute distribution are shown in Figure 4, which qualitatively verifies the segregation of each element in the simulated results. As shown in Figure 3C, the calculation results (dashed lines) agree well with the overall trends of EPMA measurement results (solid lines), which shows that the multiphase-field model can effectively calculate the solute distribution in the rapid solidification. Nb element is an important component of γ′ and γ″ strengthening phases of Inconel 718 alloy, and its concentration and distribution in the matrix directly determine the strengthening effect. Therefore, the evolution of the Nb element is used as one of the important indicators for measuring the homogenization effect in current work.

TABLE 4 Experiment and simulation of microstructural characteristics.

	Diameter of cellular substructure (μm)	Area fraction of laves phase (%)	Area fraction of NbC phase (%)
Experiment	0.79 ± 0.32	2.24 ± 0.25	0.23% ± 0.06
Simulation	0.76 ± 0.18	2.19%	—

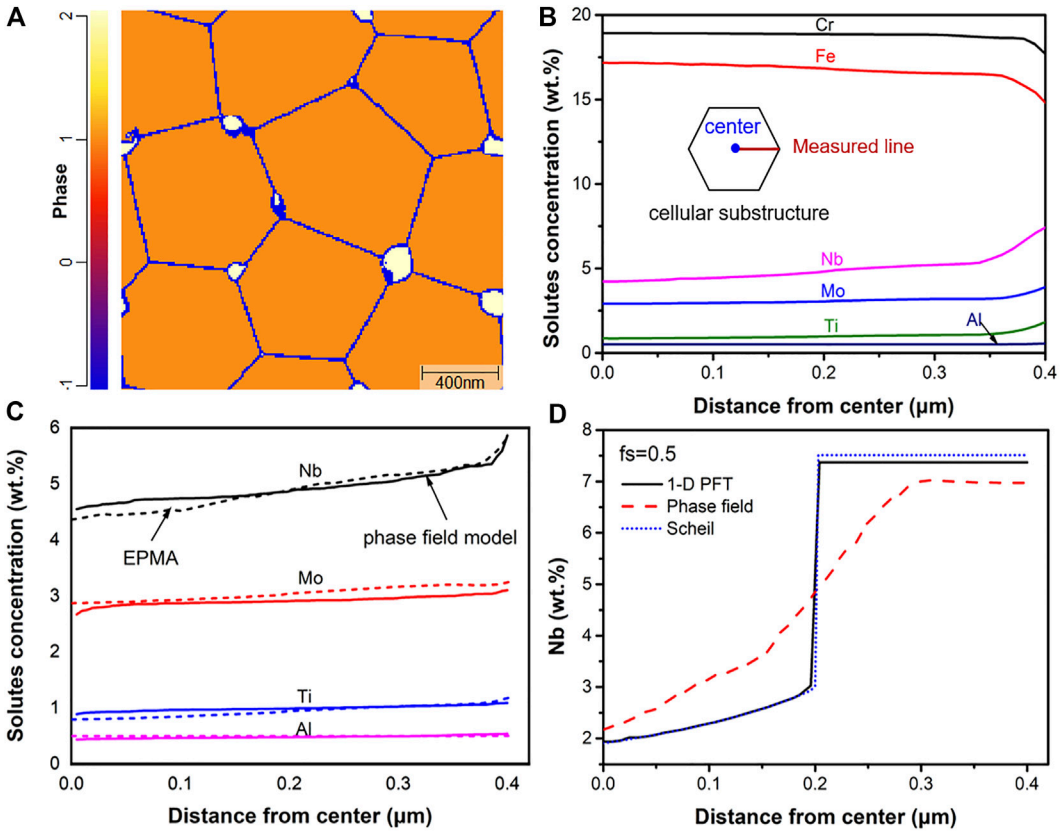

FIGURE 3
Simulation results of **(A)** cellular substructure and Laves phase distribution, **(B)** solute distribution curves from center to edge in cellular substructure. Solutes distribution curves, **(C)** EPMA measurements and multiphase-field model simulation results, **(D)** Nb distribution calculated by 1-D PFT model, multiphase-field model, and Scheil model when fs = 0.5.

The solute trapping effect in the solute distribution process is the main feature that distinguishes the L-PBF process from other conventional casting processes. To confirm the solute trapping effect in the calculated results by multiphase-field model, the solutes partition behavior is compared with that calculated by Scheil model and Pseudo Front Tracking (PFT) model (Du and Jacot, 2005), as shown in Figure 3D. Scheil is a classic model of non-equilibrium solidification, in where there is no diffusion in solid phase and infinite diffusion in liquid phase. The PFT model is a sharp interface model developed by (Jacot and Rappaz. (2002); Du and Jacot. (2005); Du et al. (2007), which considers the limited diffusion in solid and liquid phases. The 1-D PFT model is based on the assumption of local equilibrium at S/L interface, which is suitable for microstructure simulation in sub rapid solidification process without solute trapping. The quasi-equilibrium is assumed at the interface on the multiphase-field model, which make it possible to capture solute trapping. The solute concentration in primary phase gradually increases from the center to the edge of the cellular substructure under the effect of local equilibrium at S/L interface and back diffusion in the primary phase. Therefore, the solute concentration in solid calculated by Scheil is higher than that in

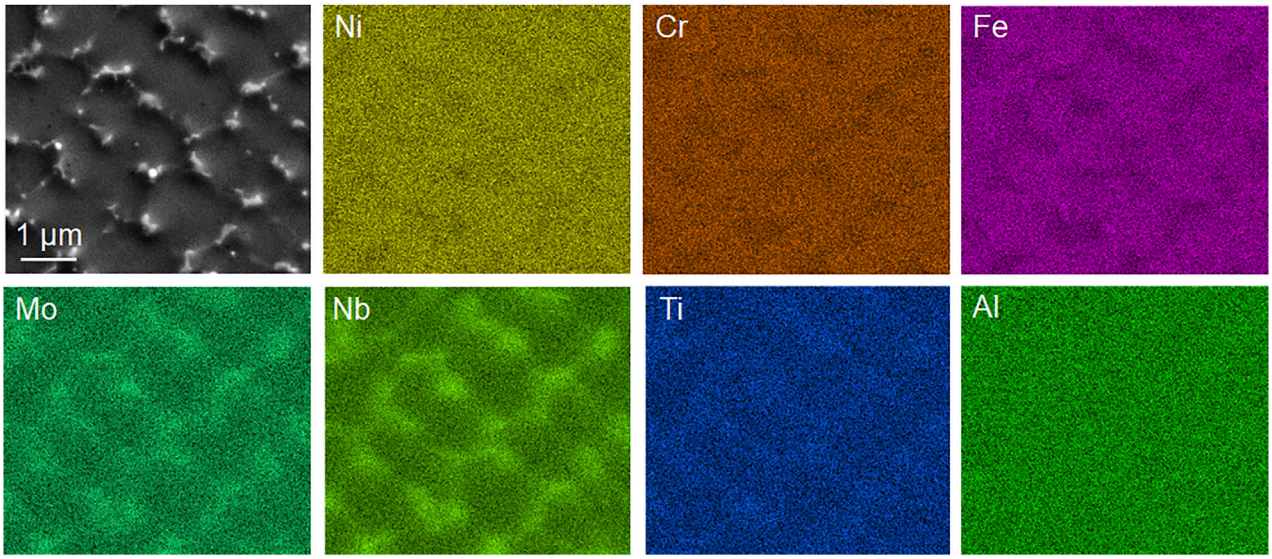

FIGURE 4
SEM-EDS maps of solutes in cellular substructures of as-built Inconel 718 sample.

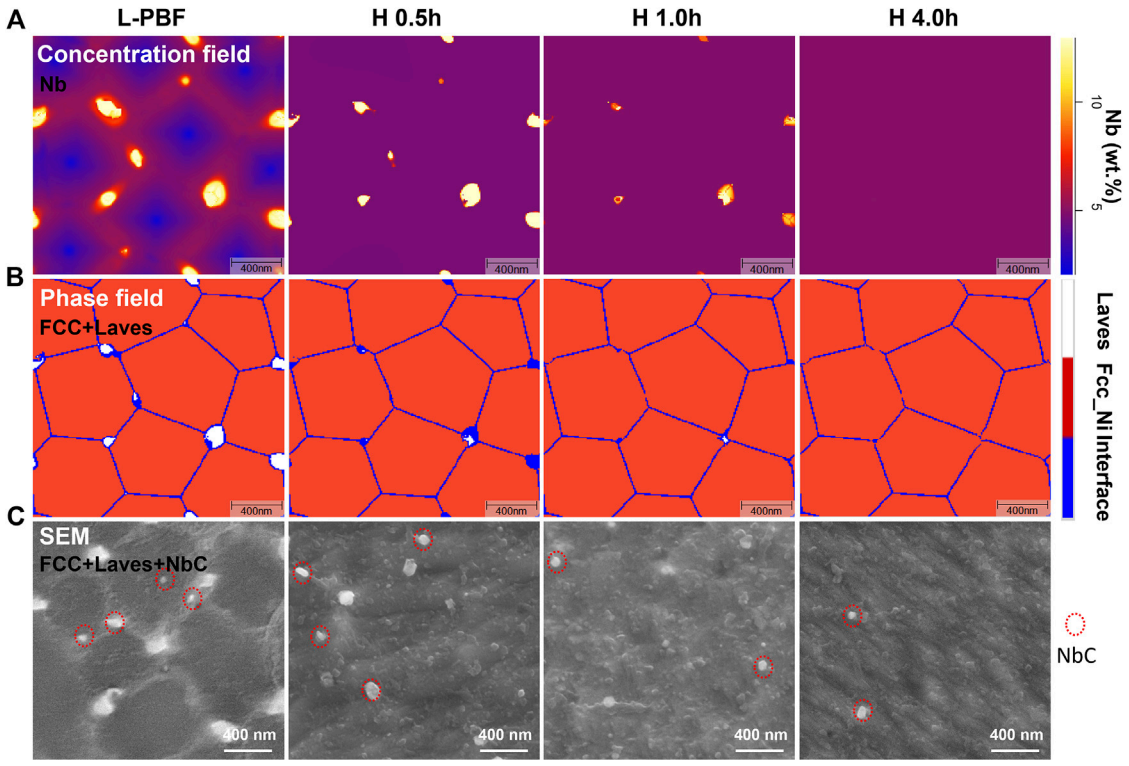

FIGURE 5
(A) Simulated concentration fields of Nb, **(B)** phase field, and **(C)** SEM images at the homogenization temperature of 1,080°C for 0–4.0 h.

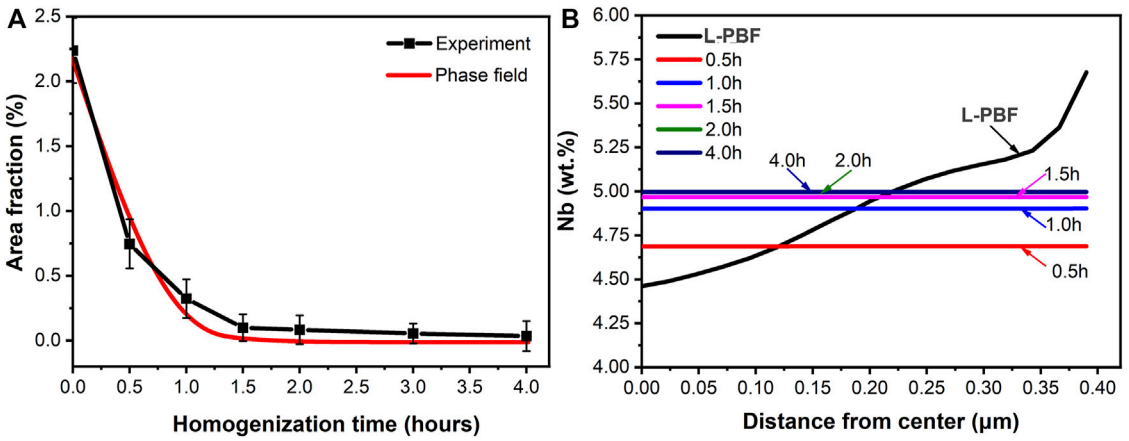

FIGURE 6
At the homogenization temperature of 1,080°C for 0.5–4.0 h, **(A)** area fractions of Laves phase in simulation and experimental results, **(B)** distribution curves of Nb element along the radius of cellular substructure simulated by phase-field.

the 1-D PFT model due to the absence of diffusion in primary phase. The S/L interface of the multiphase-field model is a dispersion interface with a certain thickness, and no obvious solid/liquid boundary in the calculation results of Nb solute distribution showing an increasing trend as a whole. As shown in Figure 3D that in the solidified matrix phase, the Nb solute concentration calculated *via* the multiphase-field model is higher than that calculated by PFT model. The higher part is the difference of Nb concentration calculated by PFT and multiphase-field models due to the solute trapping in the rapid solidification, which proves that multiphase-field simulation can effectively capture solute trapping. The phase filed model provides the possibility for the accurate simulation of solidification microstructure characteristics, which is an essential foundation for optimizing the subsequent heat treatment process.

4.3 Effect of homogenization time on microstructure and mechanical properties

Based on the simulated results of as-built Inconel 718 samples, the evolution of microstructure in subsequent homogenization process is carried out to analyze the effect of homogenization time on its microstructure evolution and mechanical properties. As shown in Figures 5A, B, the solute fields of Nb and phase field in the cellular substructure are simulated at the homogenization temperature of 1,080°C for 0.5–4.0 h by phase-field method. The results indicate that the solute distribution gradually tends to be uniform, and the fraction of Laves phase is significantly reduced during the homogenization process. Under the same conditions, the experimental results are also shown in Figure 5C, which also indicate the reduction of Laves phase particles in size and number density. Since the NbC phase will not dissolve in the homogenization process, it is ignored in the phase field calculation. Therefore, compared with the calculated results, it seems that there are more second phases in the experimental results. Some solutes, such as Nb, Ti, Al, required for strengthening phase are contained in brittle Laves phase, which would result in initiation and propagation of cracks. Therefore, one of the purposes of homogenization is to dissolve Laves phase particles as many as possible, so as to release the solutes required for strengthening phases and improve the effect of subsequent aging strengthening.

The area fractions of Laves phase and homogenization time in the simulation and experimental results show a nonlinear relationship as shown in Figure 6A. The distribution trend of the calculated results agrees with the experimental results, which proves the reliability of the calculated results. Although the measurement method has been standardized as much as possible, it will inevitably lead to measurement error and hinder its validation of the simulation results. However, it does not affect the analysis of the microstructure evolution during the homogenization process. During the short-time homogenization process (less than 1.0 h), the area fraction of Laves decreases rapidly with the increase of homogenization time. However, with the increase of the homogenization time, the Laves area fraction decreases slightly during a longer homogenization time (above 1.0 h). According to Figure 6B, the solute diffusion is promoted by high concentration gradient of as-built Inconel 718 samples at the beginning of homogenization, and the dissolution rate of the secondary phase (Laves phase) is higher. The solutes in the substructure have been evenly distributed at the homogenization time of 0.5 h. With the increase of homogenization time (more than 0.5 h), the solute

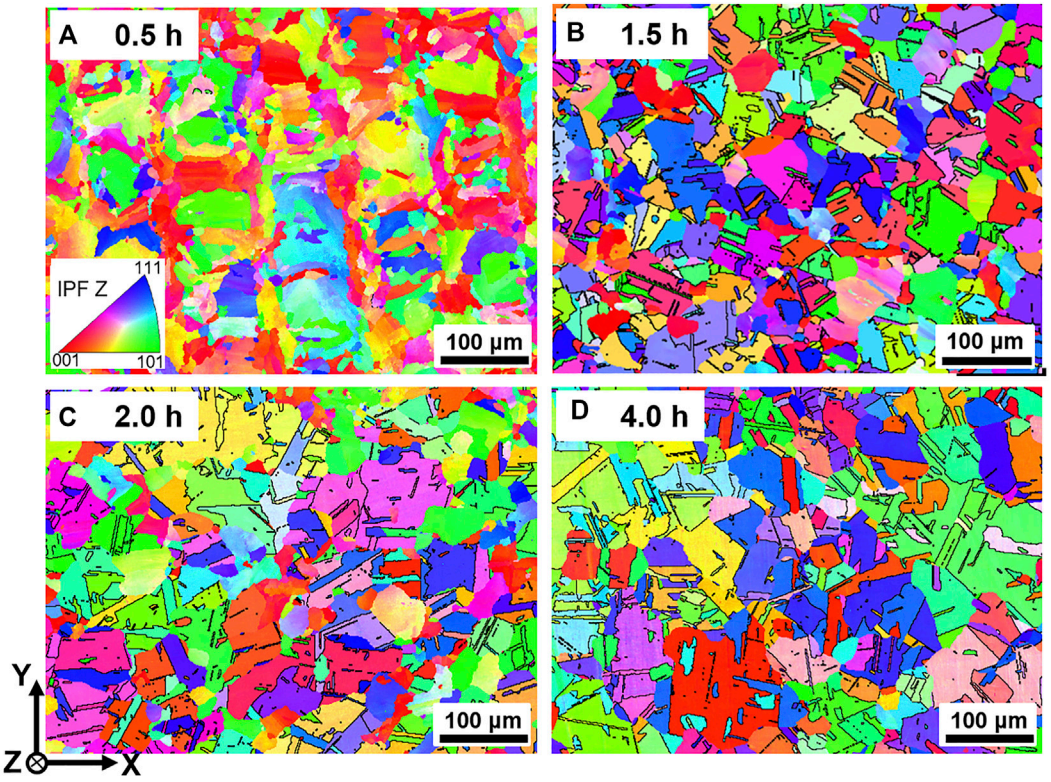

FIGURE 7
EBSD IPF images of Inconel 718 samples fabricated *via* the L-PBF at homogenization temperature of 1,080°C for different times **(A)** 0.5 h, **(B)** 1.5 h, **(C)** 2.0 h, and **(D)** 4.0 h.

concentration distribution in the substructure becomes uniform, so that solutes diffusion rate decreases, and dissolution rate of the secondary phase decreases.

The grain orientation evolution under conditions with different homogenization times (0.5 h–4.0 h) at 1,080°C was analyzed by EBSD maps, as shown in Figures 7A–D, and twin grain boundaries are marked by black lines. With the increase of the homogenization time, the morphology of the strip-shaped grains on the XY plane no longer exhibit the regularity of parallel arrangement gradually. The grains are merged and keep growing, and the average grain radius increase from 4.9 μm of the as-built sample to 13.5 μm of the homogenized sample at 1,080°C for 4.0 h, as shown in Figure 8A. There are about 67% area fraction of the Laves phase generated during L-PBF process are dissolved at homogenization time of 0.5 h. After a longer time (more than 1.0 h) of homogenization, the twins grow significantly. The area fractions of twins under the homogenization conditions of 1.5 h, 2.0 h, and 4.0 h are 22.43%, 27.78%, and 46.41%, respectively. The subsequent solid solution (S: 980 °C/1 h) and double aging (A: 720°C/8 h + 620°C/8 h) treatments are carried out for the samples homogenized with different time to analyze the effect of homogenization time on the final mechanical properties of Inconel 718 samples fabricated *via* L-PBF. The evolution of the microstructure during homogenization process will also affect the microstructure characteristics and mechanical properties of the final aged samples.

Figures 8B, C shows stress-strain curves, ultimate tensile strength and yield strength of the aging-heat-treated Inconel 718 samples. The results indicates that with the increase of homogenization time, the strength also increases initially and then decreases, reaching the maximum at homogenization time of 0.5 h. The ultimate tensile strength is 1,465 ± 9 MPa, which is about 6% higher than that of 1,378 ± 5 MPa at the homogenization time of 1.5 h. The yield strength is 1,334 ± 12 MPa, which is 14% higher than that of 1,165 ± 7 MPa when the homogenization time is 1.5 h. However, the elongation of the final aging-heat-treated Inconel 718 samples under the condition of homogenization time of 0.5 h decreased from 23.6 ± 0.8% to 17.9 ± 0.5% in reference to the condition of homogenization time of 0.5 h. Although the ductility at the homogenization time of 0.5 h is significantly reduced, it is still higher than the minimum value of 12% specified in the AMS5663 M (for Inconel 718 components, ultimate tensile strength and the yield strength are 1,276 MPa and 1,034 MPa respectively).

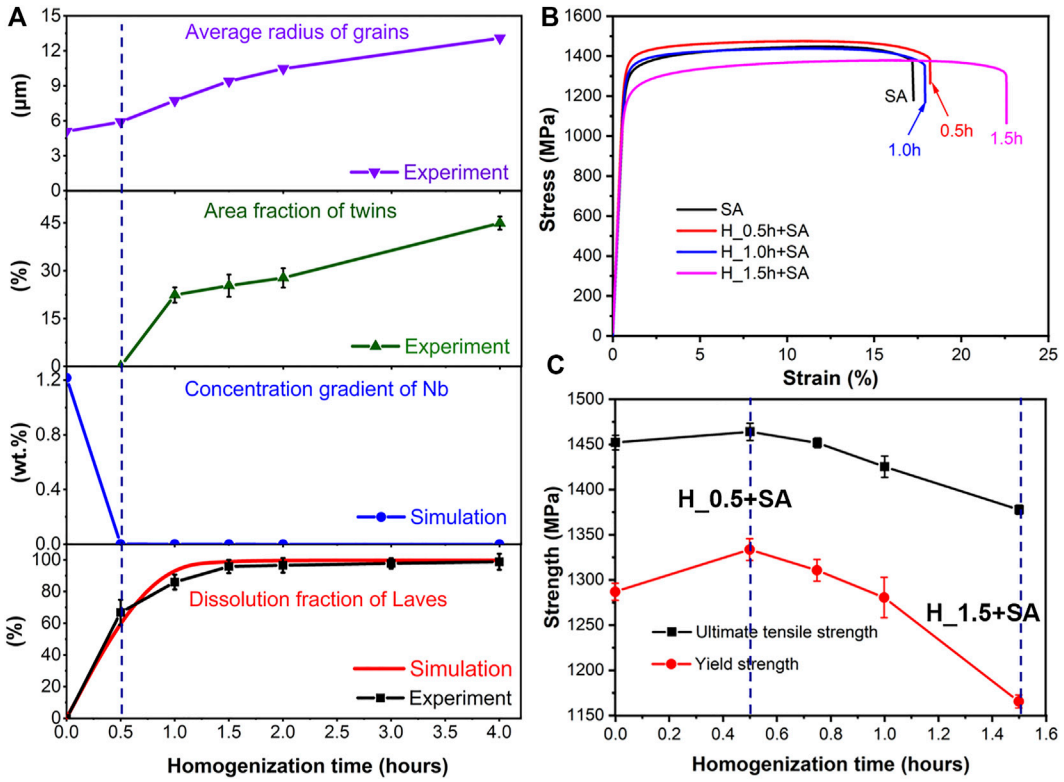

FIGURE 8
(A) Average grain size, area fraction of twins, simulated concentration gradient of Nb, and area fraction of laves phase at homogenization temperature of 1,080°C for different times, **(B,C)** ultimate tensile strength and yield strength of HSA heated Inconel 718 samples at different homogenization time.

The distribution and electron diffraction patterns of strengthening phases (γ′, γ″) along the [011] and [$\bar{1}$ 10] zone axes of HSA heated samples at the homogenization time of 0.5 h and 1.5 h are shown in Figures 9A, B. The superlattice reflections (100) and (010) of γ′ precipitates, and (110) arose both from γ′ and γ″ phases. The reflections of (1 1/2 0) and (1/2 1 0) belong only to γ″ precipitates. Figure 9B indicate that more and finer strengthening phases particles precipitate from matrix phase with longer homogenization time. The average length of γ″ phase particles decreases from 22.6 nm to 14.6 nm as the homogenization time increase from 0.5 h to 1.5 h, and its number density increases from 1.36 × 10^3/μm^2 to 2.54 × 10^3/μm^2. The results show that long-time homogenization is beneficial to improve the effect of aging strengthening. Figures 9C, D shows the fracture morphologies of tensile specimens of the final aging-heat-treated at different homogenization times. All of them are dominated by ductile fractures. The results indicated that at the homogenization time of 1.5 h, there are many finer and uniform dimples. However, at the homogenization time of 0.5 h, the fracture presents dimples with uneven depth and size, and a small amount of quasi-cleavage fracture morphology appears locally. The above fracture patterns are consistent with the change of elongation after fracture under corresponding conditions.

The simulation and experimental results show that a large number of Laves phase particles at cellular substructure and grain boundaries are dissolved. When the homogenization time increases to 0.5 h, the solutes, such as Mo and Nb, Ti, are greatly increased and evenly distributed gradually. The increase and uniform distribution of solutes in the matrix phase are beneficial to achieve high yield strength. Therefore, strength increase as the homogenization time increases when the homogenized time is less than 0.5 h, as shown in Figure 8C. However, when the homogenized time is greater than 1.0 h, the strength of the aged Inconel 718 samples decreases with the increase of homogenization time. One reason is that many annealing twins are generated and growth. The other reason is that the grains grow significantly as the homogenization time increases, which also adversely affects the strength. According to the simulated results in the homogenization, a large number of Laves phase particles have been dissolved and the solutes have been distributed evenly at the homogenization time of 0.5 h. In addition, when the homogenization time is 0.5 h, there is no obvious grain evolution according to experimental results.

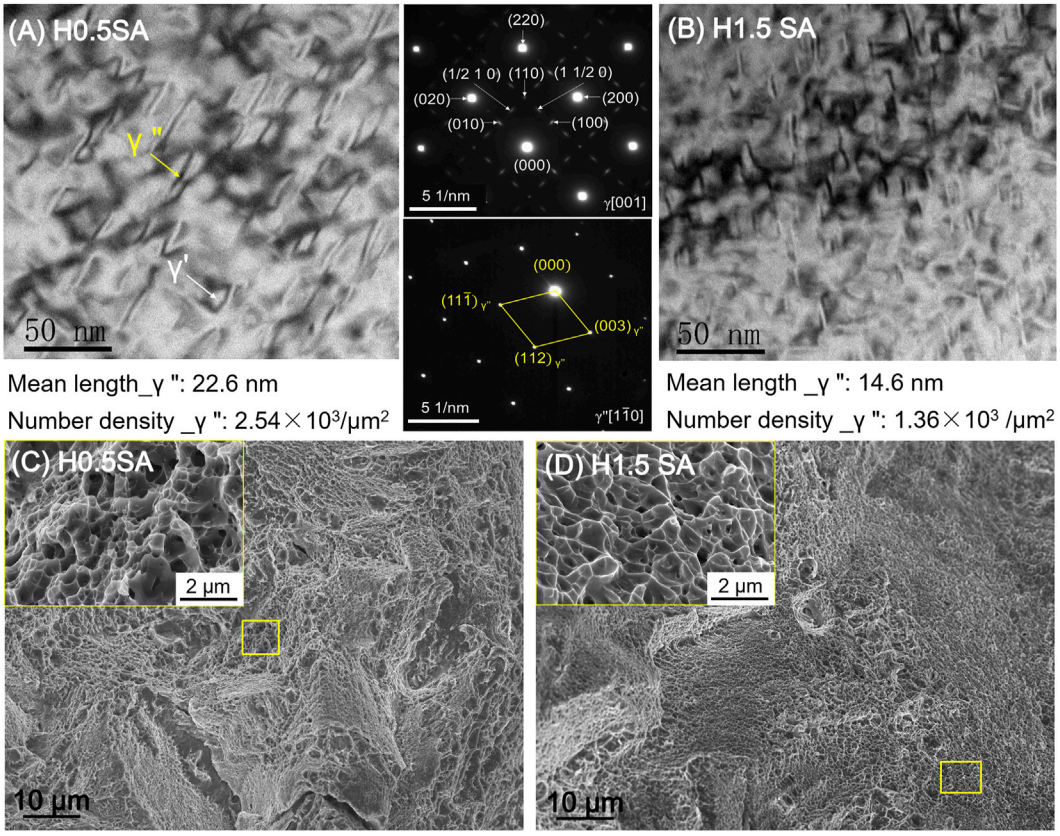

FIGURE 9
(A,B) Bright-field TEM micrographs and electron diffraction patterns of strengthening phases (γ′, γ″) along the [001] and [$\bar{1}$ 10] zone axes, **(C,D)** fracture surfaces of HSA heated Inconel 718 samples at homogenization time of 0.5 h and 1.5 h.

Therefore, under the combined effects of solute concentration evolution, secondary phase dissolution, annealing twin evolution, and grain growth, the strength shows non-monotonic trends. They increase initially and then decrease with the increase of homogenization time, reaching the maximum at the homogenization time of 0.5 h.

Based on the homogenization simulation results, δ phase (Ni_3(Nb, Ti)) and strengthening phases (γ″, γ′) precipitated in solution and double aging heat treatments with different process parameters will be modeled in our future study. The δ phase precipitated at the grain boundaries during the solid solution can strengthen grain boundaries, but it also consumes the solutes required for strengthening phases. Microstructure simulation method are useful to study the precipitation and evolution of δ phase under different solution parameters to balance the effects of grain boundary strengthening and aging strengthening. According to the precipitation strengthening mechanism and mechanical property test results, the effects of size and volume fraction of precipitate phases on mechanical properties are valuable for obtaining the most suitable heat treatment parameters.

5 Conclusion

In this paper, based on the solidified microstructure model established by multiphase field simulation, the effects of homogenization time on microstructural evolution and mechanical properties are analyzed and optimized. The following conclusions are obtained:

1) Considering the solute trapping in the solidified microstructure model, the simulated results are consistent with the experimental results, such as solute distribution and area fraction of the secondary phase (Laves). The advantages of the multiphase-field model in calculating solutes distribution in L-PBF printed Inconel 718 are demonstrated.
2) Combining phase field simulations and experimental studies, it is found that when the homogenization time is 0.5 h, 67% area fraction of the laves phase are dissolved and the concentration gradient of Nb along the radius of the cellular substructure decreases from the initial 1.217 wt% to 0.001 wt%, which have achieved the homogenization purpose.

3) Under the condition of homogenization time of 0.5 h optimized by phase filed simulation, the yield strength (YS) is 1,334 ± 12 MPa, and the ultimate tensile strength (UTS) is 1,465 ± 9 MPa. Compared with that at the homogenization time of 1.5 h, i.e., standard HSA heat treatment (AMS 5383), the YS and UTS are increased by 14% and 6%, respectively.

Data availability statement

The original contributions presented in the study are included in the article/supplementary material, further inquiries can be directed to the corresponding authors.

Author contributions

MC: Investigation, Conceptualization, Methodology, Writing—original draft. QD: Conceptualization, Methodology, Supervision, Resources, Writing—review and editing. RS: Supervision, Resources, Writing—review and editing. HF: Supervision, Resources, Writing—review and editing. ZL: Supervision, Resources, Writing—review and editing. JX: Supervision, Resources, Writing—review and editing, Funding acquisition, Project administration.

Funding

This work was supported by the following fund projects: National Natural Science Foundation of China (Nos. 52090041, 52022011), National Major Science and Technology Projects of China (No. J2019-VI-0009-0123), and Key-area Research and Development Program of Guangdong Province (No. 2019b010943001).

Conflict of interest

The authors declare that the research was conducted in the absence of any commercial or financial relationships that could be construed as a potential conflict of interest.

Publisher's note

All claims expressed in this article are solely those of the authors and do not necessarily represent those of their affiliated organizations, or those of the publisher, the editors and the reviewers. Any product that may be evaluated in this article, or claim that may be made by its manufacturer, is not guaranteed or endorsed by the publisher.

References

Blackwell, P. L. (2005). The mechanical and microstructural characteristics of LaserDeposited IN718. *J. Mat. Process. Technol.* 170, 240–246. doi:10.1016/j.jmatprotec.2005.05.005

Böttger, B., Eiken, J., and Steinbach, I. (2006). Phase field simulation of equiaxed solidification in technical alloys. *Acta Mat.* 54, 2697–2704. doi:10.1016/j.actamat.2006.02.008

Boussinot, G., Apel, M., Zielinski, J., Hecht, U., and Schleifenbaum, J. H. (2019). Strongly out-of-Equilibrium columnar solidification during laser powder-bed fusion in additive manufacturing. *Phys. Rev. Appl.* 11, 014025. doi:10.1103/PhysRevApplied.11.014025

Cao, M., Zhang, D. Y., Gao, Y., Chen, R. P., Huang, G. L., Feng, Z., et al. (2021). The effect of homogenization temperature on the microstructure and high temperature mechanical performance of SLM-fabricated IN718 alloy. *Mater. Sci. Eng. A* 801, 140427. doi:10.1016/j.msea.2020.140427

Chen, D., Chen, W., Liu, Y., and Sun, D. (2022). A two-relaxation-time lattice Boltzmann model for electron beam selective melting additive manufacturing. *Front. Mat.* 9. doi:10.3389/fmats.2022.885481

Chen, L. Q., and Zhao, Y. (2022). From classical thermodynamics to phase-field method. *Prog. Mat. Sci.* 124, 100868. doi:10.1016/j.pmatsci.2021.100868

Dai, R., Yang, S., Zhang, T., Zhong, J., Chen, L., Deng, C., et al. (2022). High-throughput screening of optimal process parameters for PVD TiN coatings with best properties through a combination of 3-D quantitative phase-field simulation and hierarchical multi-objective optimization strategy. *Front. Mat.* 9. doi:10.3389/fmats.2022.924294

De Bartolomeis, A., Newman, S. T., Jawahir, I. S., Biermann, D., and Shokrani, A. (2021). Future research directions in the machining of Inconel 718. *J. Mat. Process. Technol.* 297, 117260. doi:10.1016/j.jmatprotec.2021.117260

Du, Q., Azar, A. S., and M'Hamdi, M. (2022). Kinetic interface condition phase diagram for the rapid solidification of multi-component alloys with an application to additive manufacturing. *Calphad* 76, 102365. doi:10.1016/j.calphad.2021.102365

Du, Q., Eskin, D., Jacot, A., and Katgerman, L. (2007). Two-dimensional modelling and experimental study on microsegregation during solidification of an Al-Cu binary alloy. *Acta Mat.* 55, 1523–1532. doi:10.1016/j.actamat.2006.10.035

Du, Q., and Jacot, A. (2005). A two-dimensional microsegregation model for the description of microstructure formation during solidification in multicomponent alloys: Formulation and behaviour of the model. *Acta Mat.* 53, 3479–3493. doi:10.1016/j.actamat.2005.04.004

Du, Q., Tang, K., Marioara, C. D., Andersen, S. J., Holmedal, B., and Holmestad, R. (2017). Modeling over-ageing in Al-Mg-Si alloys by a multi-phase CALPHAD-coupled kampmann-wagner numerical model. *Acta Mat.* 122, 178–186. doi:10.1016/j.actamat.2016.09.052

Eiken, J., Bottger, B., and Steinbach, I. (2006). Multiphase-field approach for multicomponent alloys with extrapolation scheme for numerical application. *Phys. Rev. E* 73, 066122. doi:10.1103/PhysRevE.73.066122

Hosseini, E., and Popovich, V. A. (2019). A review of mechanical properties of additively manufactured Inconel 718. *Addit. Manuf.* 30, 100877. doi:10.1016/j.addma.2019.100877

Hu, Y. S., Wang, G., Ji, Y. Z., Wang, L. P., Rong, Y. M., and Chen, L. Q. (2019). Study of θ' precipitation behavior in Al-Cu-Cd alloys by phase-field modeling. *Mater. Sci. Eng. A* 746, 105–114. doi:10.1016/j.msea.2019.01.012

Jacot, A., and Rappaz, M. (2002). A pseudo-front tracking technique for the modelling of solidification microstructures in multi-component alloys. *Acta Mat.* 50, 1909–1926. doi:10.1016/S1359-6454(01)00442-6

Karma, A. (2001). Phase-field formulation for quantitative modeling of alloy solidification. *Phys. Rev. Lett.* 87, 115701. doi:10.1103/physrevlett.87.115701

Kumara, C., Balachandramurthi, A. R., Goel, S., Hanning, F., and Moverare, J. (2020). Toward a better understanding of phase transformations in additive manufacturing of alloy 718. *Materialia* 13, 100862. doi:10.1016/j.mtla.2020.100862

Kumara, C., Segerstark, A., Hanning, F., Dixit, N., Joshi, S., Moverare, J., et al. (2019). Microstructure modelling of laser metal powder directed energy deposition of alloy 718. *Addit. Manuf.* 25, 357–364. doi:10.1016/j.addma.2018.11.024

Luo, Z. b., and Zhao, Y. y. (2019). Efficient thermal finite element modeling of selective laser melting of Inconel 718. *Comput. Mech.* 65, 763–787. doi:10.1007/s00466-019-01794-0

Luu, D. N., Zhou, W., and Nai, S. M. L. (2022). Mitigation of liquation cracking in selective laser melted Inconel 718 through optimization of layer thickness and laser energy density. *J. Mat. Process. Technol.* 299, 117374. doi:10.1016/j.jmatprotec.2021.117374

Nabavizadeh, S. A., Eshraghi, M., and Felicelli, S. D. (2020). Three-dimensional phase field modeling of columnar to equiaxed transition in directional solidification of Inconel 718 alloy. *J. Cryst. Growth* 549, 125879. doi:10.1016/j.jcrysgro.2020.125879

Nandy, J., Sarangi, H., and Sahoo, S. (2019). A review on direct metal laser sintering: Process features and microstructure modeling. *Lasers Manuf. Mat. Process.* 6, 280–316. doi:10.1007/s40516-019-00094-y

Park, J., Kang, J. H., and Oh, C. S. (2020a). Phase-field simulations and microstructural analysis of epitaxial growth during rapid solidification of additively manufactured AlSi10Mg alloy. *Mat. Des.* 195, 108985. doi:10.1016/j.matdes.2020.108985

Park, J., Oh, C. S., Kang, J. H., Jung, J. G., and Lee, J. M. (2020b). Solidification and precipitation microstructure simulation of a hypereutectic Al-Mn-Fe-Si alloy in semi-quantitative phase-field modeling with experimental aid. *Metals* 10, 1325. doi:10.3390/met10101325

Paturi, U. M. R., Vidhya, D. B., and Reddy, N. S. (2021). Progress of machinability on the machining of Inconel 718: A comprehensive review on the perception of cleaner machining. *Clean. Eng. Technol.* 5, 100323. doi:10.1016/j.clet.2021.100323

Rahul, M. R., Samal, S., and Phanikumar, G. (2020). Metastable microstructures in the solidification of undercooled high entropy alloys. *J. Alloys Compd.* 821, 153488. doi:10.1016/j.jallcom.2019.153488

Rao, G. A., Kumar, M., Srinivas, M., and Sarma, D. S. (2003). Effect of standard heat treatment on the microstructure and mechanical properties of hot isostatically pressed superalloy Inconel 718. *Mater. Sci. Eng. A* 355, 114–125. doi:10.1016/s0921-5093(03)00079-0

Reed, R. C. (2006). *The superalloys: Fundamentals and applications*. Cambridge: Cambridge University Press.

Sahoo, S., and Chou, K. (2016). Phase-field simulation of microstructure evolution of Ti-6Al-4V in electron beam additive manufacturing process. *Addit. Manuf.* 9, 14–24. doi:10.1016/j.addma.2015.12.005

Sahoo, S., and Chou, K. (2014). "Review on phase-field modeling of microstructure evolutions: Application to electron beam additive manufacturing," in *ASME 2014 int. Manuf. Sci. Eng. Conf., proc. MSEC2014-3901, V002T02A020*, 9. doi:10.1115/MSEC2014-3901

Sahoo, S. (2022). Prognostication of microstructure evolution during laser powder bed fusion of aluminum alloy using phase-field method. *J. Laser Appl.* 34, 022014. doi:10.2351/7.0000658

Seiz, M., and Nestler, B. (2021). Modelling and simulation of the freeze casting process with the phase-field method. *Comput. Mat. Sci.* 193, 110410. doi:10.1016/j.commatsci.2021.110410

Steinbach, I., Pezzolla, F., Nestler, B., Seeßelberg, M., Prieler, R., Schmitz, G. J., et al. (1996). A phase field concept for multiphase systems. *Phys. D. Nonlinear Phenom.* 94, 135–147. doi:10.1016/0167-2789(95)00298-7

Steinbach, I. (2009). Phase-field models in materials science. *Model. Simul. Mat. Sci. Eng.* 17, 073001. doi:10.1088/0965-0393/17/7/073001

Sui, S., Chen, J., Fan, E. X., Yang, H. O., Lin, X., and Huang, W. (2017). The influence of laves phases on the high-cycle fatigue behavior of laser additive manufactured Inconel 718. *Mater. Sci. Eng. A* 695, 6–13. doi:10.1016/j.msea.2017.03.098

Trosch, T., Strößner, J., Völkl, R., and Glatzel, U. (2016). Microstructure and mechanical properties of selective laser melted Inconel 718 compared to forging and casting. *Mat. Lett.* 164, 428–431. doi:10.1016/j.matlet.2015.10.136

Wang, X. Q., and Chou, K. (2018). Microstructure simulations of Inconel 718 during selective laser melting using a phase field model. *Int. J. Adv. Manuf. Technol.* 100, 2147–2162. doi:10.1007/s00170-018-2814-z

Xiao, W. J., Li, S. M., Wang, C. S., Shi, Y., Mazumder, J., Xing, H., et al. (2019). Multi-scale simulation of dendrite growth for direct energy deposition of nickel-based superalloys. *Mat. Des.* 164, 107553. doi:10.1016/j.matdes.2018.107553

Yuan, K. B., Guo, W. G., Li, P. H., Wang, J., Su, Y., Lin, X., et al. (2018). Influence of process parameters and heat treatments on the microstructures and dynamic mechanical behaviors of Inconel 718 superalloy manufactured by laser metal deposition. *Mater. Sci. Eng. A* 721, 215–225. doi:10.1016/j.msea.2018.02.014

Zeng, Y., Mittnacht, T., Werner, W., Du, Y., Schneider, D., and Nestler, B. (2021). Gibbs energy and phase-field modeling of ferromagnetic ferrite (α)→ paramagnetic austenite (γ) transformation in Fe-C alloys under an external magnetic field. *Acta Mat.* 225, 117595. doi:10.1016/j.actamat.2021.117595

Zhang, D. Y., Niu, W., Cao, X. Y., and Liu, Z. (2015). Effect of standard heat treatment on the microstructure and mechanical properties of selective laser melting manufactured Inconel 718 superalloy. *Mater. Sci. Eng. A* 644, 32–40. doi:10.1016/j.msea.2015.06.021

Zhang, M., Wang, J., Han, J., Sui, H., Huang, H., Jin, K., et al. (2019). Optimization of heat treatment process of Al-Mg-Si cast alloys with Zn additions by simulation and experimental investigations. *Calphad* 67, 101684. doi:10.1016/j.calphad.2019.101684

Zhao, X. M., Chen, J., Lin, X., and Huang, W. D. (2008). Study on microstructure and mechanical properties of laser rapid forming Inconel 718. *Mater. Sci. Eng. A* 478, 119–124. doi:10.1016/j.msea.2007.05.079

Zhao, Y., Meng, F., Liu, C., Tan, S., and Xiong, W. (2021). Impact of homogenization on microstructure-property relationships of Inconel 718 alloy prepared by laser powder bed fusion. *Mater. Sci. Eng. A* 826, 141973. doi:10.1016/j.msea.2021.141973

Frontiers in Materials

Investigates the discovery and design of materials for future application

A multidisciplinary journal that explores the breadth of materials science, engineering and mechanics - from carbon-based materials to smart materials.

Discover the latest Research Topics

See more →

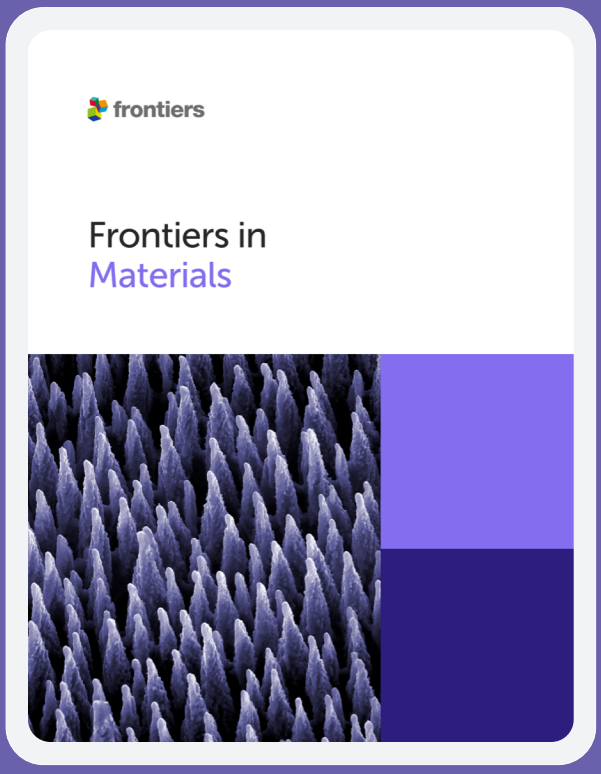

Frontiers

Avenue du Tribunal-Fédéral 34
1005 Lausanne, Switzerland
frontiersin.org

Contact us

+41 (0)21 510 17 00
frontiersin.org/about/contact